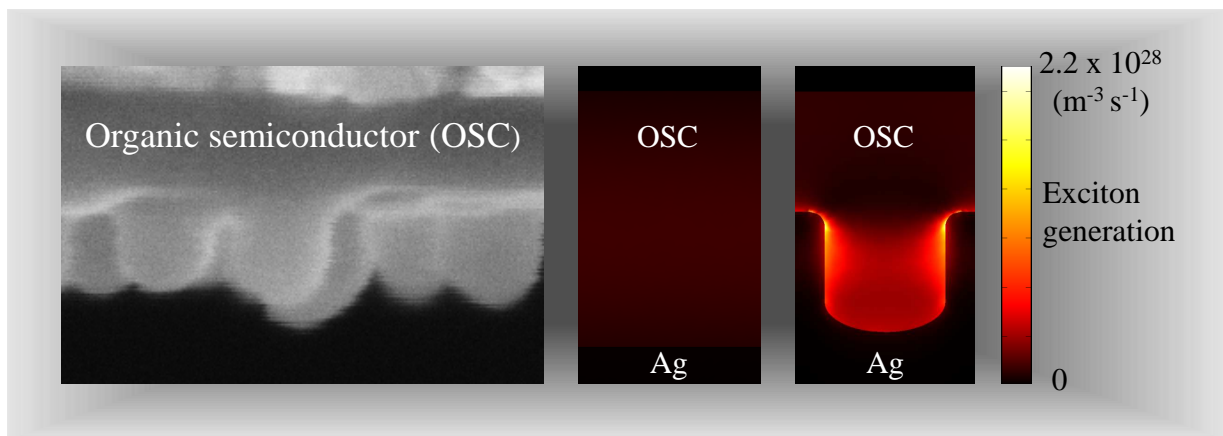


Using metallic nanostructures to trap light and enhance absorption in organic solar cells



Doctoral Thesis

vorgelegt von

Ricky Dunbar

angefertigt in der Arbeitsgruppe
Hybrid Nanostructures
Prof. Dr. Lukas Schmidt-Mende

Fakultät für Physik
Ludwig-Maximilians-Universität München
April 4, 2012

Tag der mündlichen Prüfung: 03.04.2012

Erstgutachter: Prof. Dr. Lukas Schmidt-Mende

Zweitgutachter: P.D. Dr. Bert Nickel

Contents

Abstract	vi
Related publications	ix
List of abbreviations and symbols	xi
1 Introduction	1
2 Background	5
2.1 The solar cell	5
2.2 Organic solar cells	9
2.3 Plasmonic Theory	18
2.3.1 Optical properties of noble metals	18
2.3.2 Surface Plasmon Polaritons (SPPs)	19
2.3.3 Localized Surface Plasmons (LSPs)	24
2.3.4 Void plasmons	27
2.4 Light-trapping in thin-film solar cells	29
2.4.1 Highly absorbing organic solar cells	29
2.4.2 How much can be gained?	31
2.4.3 The connection between enhanced absorption and enhanced efficiency .	32
2.5 Prominent light-trapping architectures	34
2.5.1 Scattering dielectric structures	34
2.5.2 Plasmonic light-trapping	36
2.6 Summarizing remarks	40
3 Experimental Techniques	43
3.1 Fabrication of organic solar cells	43
3.2 Fabrication of organic solar cells with structured metallic electrodes	46
3.2.1 Anodization	46
3.2.2 Stamp geometry	52
3.2.3 Imprint	54

3.3	Characterization	56
3.3.1	Morphology	56
3.3.2	Spectroscopy of solar cell architectures	57
3.3.3	Solar cell characterization	59
3.4	Summarizing remarks	61
4	Simulation using the finite element method	63
4.1	Finite element method in 1D	63
4.2	Finite element method in higher dimensions	67
4.3	Summarizing remarks	69
5	Absorption enhancement in solar cell architectures	71
5.1	Reflectometry	71
5.2	Angle-sensitive reflectometry	77
5.3	Summarizing remarks	82
6	Experiment and simulation compared	83
6.1	Sample preparation	84
6.2	Reflectivity measurements	86
6.3	Finite element simulations	88
6.4	Summarizing remarks	97
7	Photoluminescence measurements of light trapping architecture samples	99
7.1	Sample preparation	99
7.2	Measurement	101
7.3	Photoluminescence quenching	103
7.4	Polymer ordering	104
7.5	Summarizing remarks	108
8	Solar cell performance	109
8.1	Analysis	109
8.2	Flat imprint	113
8.3	100 nm period nanovoids	114
8.4	500 nm period nanovoids	121
8.5	Summarizing remarks	122
9	Optimization of plasmonic solar cells	123
9.1	Plasmonic solar cells	123
9.2	Method	125

9.3 Optimization study	127
9.4 Dependence on semiconductor layer thickness	130
9.5 Spectral characteristics of light-trapping	132
9.6 Ideal vs. non-ideal conductors	135
9.7 Practical considerations for plasmonic solar cell fabrication	136
9.8 Summarizing remarks	138
10 Outlook and conclusion	139
Appendix A - Sample finite element simulation code	155
Bibliography	155
Acknowledgements	171

Abstract

Solar cells generate clean electricity from sunlight. However, they remain significantly more expensive than other, less environmentally-friendly, energy generation technologies. Although the emergence of thin-film solar cells, low-cost alternatives to the prevailing crystalline silicon solar cells, has been a significant advance in photovoltaic technology, these devices typically suffer from low absorption. If this absorption could be enhanced, it would enable an increase in power conversion efficiency and hence a reduction in cost/kW of generating capacity. This is the motivation of the work presented in this doctoral thesis. Metallic nanostructures are used to trap light within the semiconductor film in organic solar cells. By increasing the optical path length, the probability that photons are absorbed before exiting the film is increased. A novel process is developed to fabricate nanostructured metallic electrode organic solar cells. These devices feature a nanovoid array interface between the metallic electrode and the semiconductor film. Absorption enhancements over conventional, planar architectures as high as 45% are demonstrated. This light-trapping is found to be largely enabled by localized void plasmons. The experimental investigations are supported by finite element simulations of absorption in solar cells, which display very good agreement with experimental results. It is found that light trapped in organic solar cell architectures is very efficiently absorbed by the organic film - increases in the exciton generation rate per unit volume of semiconductor material of up to 17% are observed. The simulation routine is additionally used to compare and contrast common plasmonic architectures in organic solar cells. The role of the metallic nanostructure geometry on the dominant light-trapping mechanism is assessed for various size domains and optimum architectures are identified. When implemented according to the findings of this thesis, light-trapping will have the potential to vastly increase the efficiency and hence decrease the price of thin-film solar cells.

Zusammenfassung

Solarzellen, Bauelemente die Sonnenlicht in Strom umwandeln können, sind im Vergleich zu herkömmlichen, weniger umweltfreundlichen Energietechnologien noch sehr teuer. Obwohl Dünnschichtsolarzellen eine preisgünstige Alternative zu den marktdominierenden hochkristallinen Siliziumsolarzellen darstellen, sind sie durch ihre geringe Absorption beschränkt. Eine höhere Absorption würde es ermöglichen, den Wirkungsgrad zu verbessern und gleichzeitig die Modulpreise zu reduzieren. Das ist die Motivation für die vorgelegte Arbeit. Metallische Nanostrukturen werden verwendet, um Licht in der Halbleiterschicht organischer Solarzellen einzufangen. Die Photonabsorptionswahrscheinlichkeit steigt durch die Verlängerung des optischen Wegs. Das Ziel des effizienten Lichteinfangs in organischen Solarzellen wird sowohl experimentell als auch durch computergestützte Modellierung verfolgt. Ein neuartiges Verfahren wird entwickelt. Die Struktur dieser Elektroden ist eine periodische Anordnung nanoskaliger Vertiefungen an der Grenzfläche zwischen Metallelektrode und halbleitendem Film. Diese Zellgeometrie zeigt eine 45% höhere Absorption als vergleichbare Bauformen mit ebener Elektrode. Der Lichteinfang an Vertiefungsstrukturen wird weitgehend durch Anregung lokalisierter Oberflächenplasmonen ermöglicht. Zur Unterstützung dieser Studien werden Finite-Elemente-Simulationen durchgeführt, die eine sehr gute Übereinstimmung mit den experimentellen Ergebnissen zeigen. Wir berechnen eine Erhöhung der Exzitonengenerationsrate mittels einer metallischen Vertiefungsstruktur von 17%. Das Simulationsprogramm wird darüber hinaus verwendet, um die Lichteinfangeneigenschaften verschiedener plasmonischer Strukturen quantitativ zu vergleichen. Dadurch wird eine optimale Geometrie errechnet: Silbernanoteilchen, die in der organischen Schicht mit einer Periodizität von 330 nm eingebettet sind. Die Entwicklungen, die diese Forschung ermöglicht hat, sind extrem wichtig für die zukünftige Design von Dünnschichtsolarzellen

Related publications

- **Dunbar, R. B.**, Hesse, H. C., Lembke, D. S. and Schmidt-Mende, L. *Light-trapping plasmonic nanovoid arrays*. Phys Rev B 85, 035301 (2012).
- **Dunbar, R. B.**, Pfadler, T. and Schmidt-Mende, L. *Highly absorbing solar cells - a survey of plasmonic nanostructures*. Opt. Express 20, A177-A189 (2012).
- Y. Jiao, C. Peng, F. Guo, Z. Bao, J. Yang, L. Schmidt-Mende, **Dunbar, R. B.**, Y. Qin, and Z. Deng *Facile Synthesis and Photocatalysis of Size-Distributed TiO₂ Hollow Spheres Consisting of 116 Plane-Oriented Nanocrystallites*. The Journal of Physical Chemistry C 115, 6405-6409, (2011).
- Weickert, J., **Dunbar, R. B.**, Hesse, H. C., Wiedemann, W. and Schmidt-Mende, L. *Nanostructured Organic and Hybrid Solar Cells*. Adv Mater 23, 1810-1828, (2011).
- **Dunbar, R. B.**, Pfadler, T., Lal, N., Baumberg, J.J and Schmidt-Mende, L. *Imprinted localized plasmons for enhanced solar cells*. (2012, *Journal of Applied Physics*, submitted).
- Handloser, M., **Dunbar, R. B.**, Wisnet, A., Altpeter, P., Scheu, C., Schmidt-Mende, L. and Hartschuh, A. *Influence of metallic and dielectric nanowire arrays on the photoluminescence properties of P3HT thin films*. (2012, *Nanotechnology*, submitted).

Conference presentations

- **Dunbar, R. B.**, and Schmidt-Mende, L, *High performance new generation solar cells with metal nanostructures*, Sustainable Energy Technologies Conference, Istanbul, Turkey, 2011.
- **Dunbar, R. B.**, Handloser, M., Altpeter, P and Schmidt-Mende, L, *Energy transfer between nanostructured silver surfaces and materials for organic photovoltaics*, European Optical Society Annual Meeting, Paris, France, 2010.
- **Dunbar, R. B.**, Yang, J., Lembke, D. and Schmidt-Mende, L, *Enhancement of light absorption in organic solar cells with structured silver electrodes*, Hybrid Organic Photovoltaics Conference, Assisi, Italy, 2010.

List of abbreviations and symbols

η	power conversion efficiency
τ	decay lifetime
μ	charge-carrier mobility
$A(\lambda)$	absorption (absorptivity)
AAO	anodic aluminum oxide
AFM	atomic force microscopy
Ag	silver
Au	gold
Al	aluminium
Al_2O_3	aluminum oxide
AM1.5	air mass 1.5 (solar zenith angle 48°) global solar spectrum
DSSC	dye-sensitized solar cell
ECP	electrochemical polishing
EQE	external quantum efficiency
EtOH	ethanol
FF	fill factor
FEM	finite element method
ITO	tin-oxide doped indium-oxide
$HClO_4$	perchloric acid
$H_2C_2O_4$	oxalic acid
H_2CrO_4	chromic acid
HOMO	highest occupied molecular orbital
H_3PO_4	phosphoric acid
H_2SO_4	sulfuric acid
IQE	internal quantum efficiency
J_{ph}	photocurrent density
J_{SC}	short circuit current density
LSP	localized surface plasmon
LUMO	lowest unoccupied molecular orbital

MDMO-PPV	Poly(2-methoxy-5-(3'-7'-dimethyloctyloxy)-1,4-phenylenevinylene)
N ₂	nitrogen
NP	nanoparticle
OSC	organic semiconductor
P3HT	poly (3-hexylthiophene)
PCBM	[6,6]-phenyl-C ₆₁ -butyric acid methyl ester (PC ₆₁ BM)
PC ₇₀ BM	[6,6]-phenyl-C ₇₁ -butyric acid methyl ester
PCPDTBT	Poly[2,1,3-benzothiadiazole-4,7-diyl[4,4-bis(2-ethylhexyl)-4H-cyclopenta[2,1-b:3,4-b']dithiophene-2,6-diyl]]
PMMA	Poly(methyl methacrylate)
PSC	plasmonic solar cell
P _{in}	input power
PL	photoluminescence
P _{out}	output power
PV	photovoltaics
Pt	platinum
R _s	series resistance
R _{sh}	shunt resistance
SEM	scanning electron microscopy
Si	silicon
SPP	surface plasmon polariton
TE	transverse electric polarization
TiO ₂	titanium(IV) dioxide
TM	transverse magnetic polarization
V _{OC}	open circuit voltage
WO ₃	tungsten(VI) oxide

1 Introduction

Robust, renewable energy technologies are critical for a secure global energy future. An abundant source of renewable energy is solar radiation. The word ‘abundant’ is more than apt in describing the magnitude of usable energy - around 10^{15} J is absorbed by the Earth (after around 30% is reflected) each second. This power is approximately 1000 times more than the global energy consumption per second and around 10000 times more than the energy generated by the global consumption of (primarily carbon-based) fuel per second. [1] However, this seemingly endless supply of energy remains largely untapped¹.

Market penetration of solar technology is held back by the high (mostly material) costs - it costs around 3 times more to generate electricity via photovoltaics (solar cells) than via the consumption of coal (Fig. 1.1). [4] To “unlock” the abundant supply of solar energy, and hence ensure a more secure energy future, the cost-competitiveness of solar technology must first be improved by reducing the cost per kW of generating capacity. Methods to do this include reducing the material costs and inexpensively improving the power conversion efficiency such that the cost/kW generating capacity decreases. With the solution proposed in this thesis, it will be possible to do both.

Solar thermal concentrators, one leading type of solar technology, are typically located in remote locations and require solar tracking equipment. In this work, we will focus on a second type of solar technology: solar cells - devices that convert solar energy to electricity at the location of the end consumer. Currently, more than 80% of all solar cells manufactured are based on crystalline or polycrystalline silicon. [5] Such devices are notoriously expensive to produce as they use highly crystalline semiconductor films of up to $100\mu\text{m}$ in thickness. Given the monopoly of these devices over the photovoltaics market, the cost of generating electricity with these devices can be considered to be similar to that shown in Fig. 1.1.

Solar cell researchers have made a number of innovations in order to reduce device costs. Arguably the most important has been the development of thin-film devices which feature semiconductor thicknesses of $10\mu\text{m}$ or less. In addition to reduced manufacturing costs arising from

¹In Germany, solar energy (primarily photovoltaics) currently accounts for 1.9% of the total electricity generation [2]. In the U.S.A. the value is 0.07% (whereas 43% is generated by coal) [3]

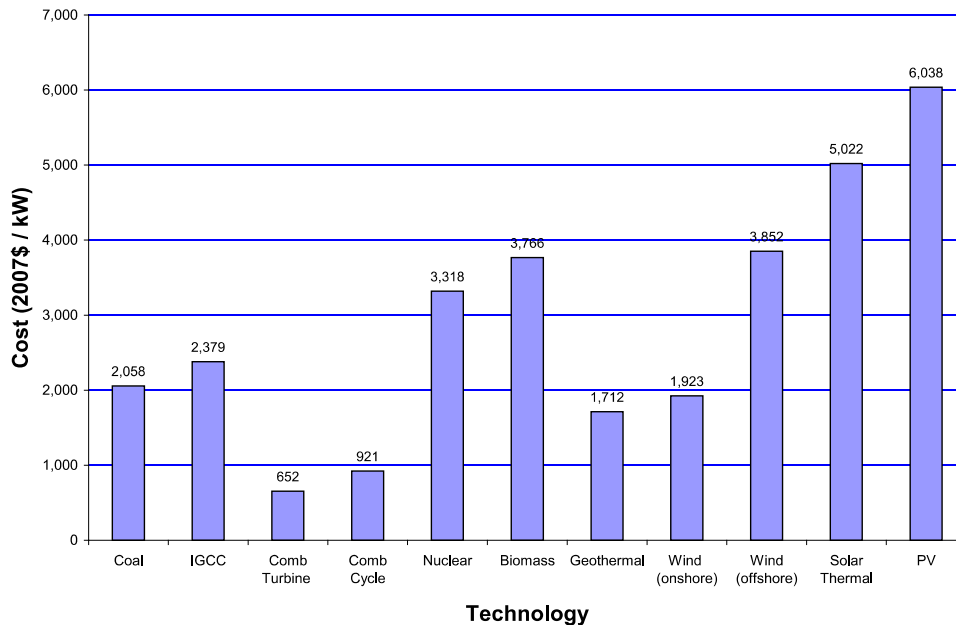


Figure 1.1: The overnight capital costs, per kW of generation capacity, of power plants based on the indicated power sources in 2007. Findings from the *Annual Energy Outlook 2009*, U.S. Energy Information Administration. [4] Overnight capital costs comprise the cost of engineering, procurement and construction plus owner's costs such as infrastructure and cooling. Financing and predicted escalation in prices are not included. PV stands for photovoltaics and IGCC stands for integrated gasification combined cycle.

lower material consumption, devices with thin semiconductor films can have the advantage of reduced electrical losses.²

However, thin-films absorb less light. The consequence of this is that the power conversion efficiency is limited. Thus, two contradicting design rules for solar cells emerge:

1. Maximize semiconductor film thickness to maximize light absorption.
2. Minimize semiconductor film thickness to improve electrical properties and minimize cost.

Thankfully, a solution to this conundrum exists: light-trapping. We demonstrate that it is possible to allow incident light to enter a semiconductor film and prevent it from escaping again. In this way we demonstrate that thin films can absorb as much as a much thicker layer, and nevertheless retain their good charge transport properties. In this thesis, we will implement

² As charge carriers can only travel a finite distance before they inevitably recombine (mutual annihilation with a carrier of opposite charge), the probability of extracting the carriers and hence a current from the semiconductor can improve for thinner films.

light-trapping structures in thin-film organic solar cells and demonstrate that both reduced semiconductor material consumption and an enhanced absorption is possible.

2 Background

In this chapter, the theoretical background of light-trapping in solar cells is outlined. We begin with a general discussion of solar cells (Section 2.1). Although many of the techniques explored in this thesis can be adapted for all thin-film solar cell types, we shall focus on organic solar cells, which have inherently low production costs. As such, we will follow the general discussion of solar cells with a description of the mechanisms governing the operation of organic solar cells (Section 2.2). We will then proceed to describe the theory behind an important phenomenon that will allow us to achieve light trapping: plasmonics (Section 2.3). A general section on light-trapping will follow (Section 2.4), where we discuss the consequences of trapping light in organic films and the maximum absorption enhancement permitted by the laws of thermodynamics. We conclude this chapter with a review of light trapping in thin-film solar cells (Section 2.5), with an emphasis on results pertaining to organic devices.

2.1 The solar cell

Solar cells are used to convert solar energy into electricity. In simple terms, a solar cell consists of a semiconductor film between two conducting electrodes. Upon absorption of incident photons, charge-carriers (electrons and holes) can be generated in the semiconductor film. If a bias V exists across the electrodes, which arises, for example, when the cell is connected to a load, the device is capable of producing electrical power $P = IV$. The total current I that flows is dependent on the number of photons absorbed, the bias V across the electrodes and the dynamics of the charge carriers within the semiconductor.¹

The operation of a solar cell can be approximated using an equivalent circuit (Fig. 2.1) with the following elements: a current source (representing the flow of photogenerated charge carriers, known as the photocurrent), a diode (just as in a regular diode, the flow of charge-carriers in the semiconductor film can be assisted or impeded depending on the bias across the film), a

¹This is true for most inorganic solar cells. However, in organic solar cells, the dynamics of excitons and charge transfer states are also critical (see Sec. 2.2)

2.1 The solar cell

shunt resistor (non-infinite values of which represent parasitic current between the electrodes) and a series resistor (the sum of series resistances of the semiconductor, electrodes and external loads and circuitry).

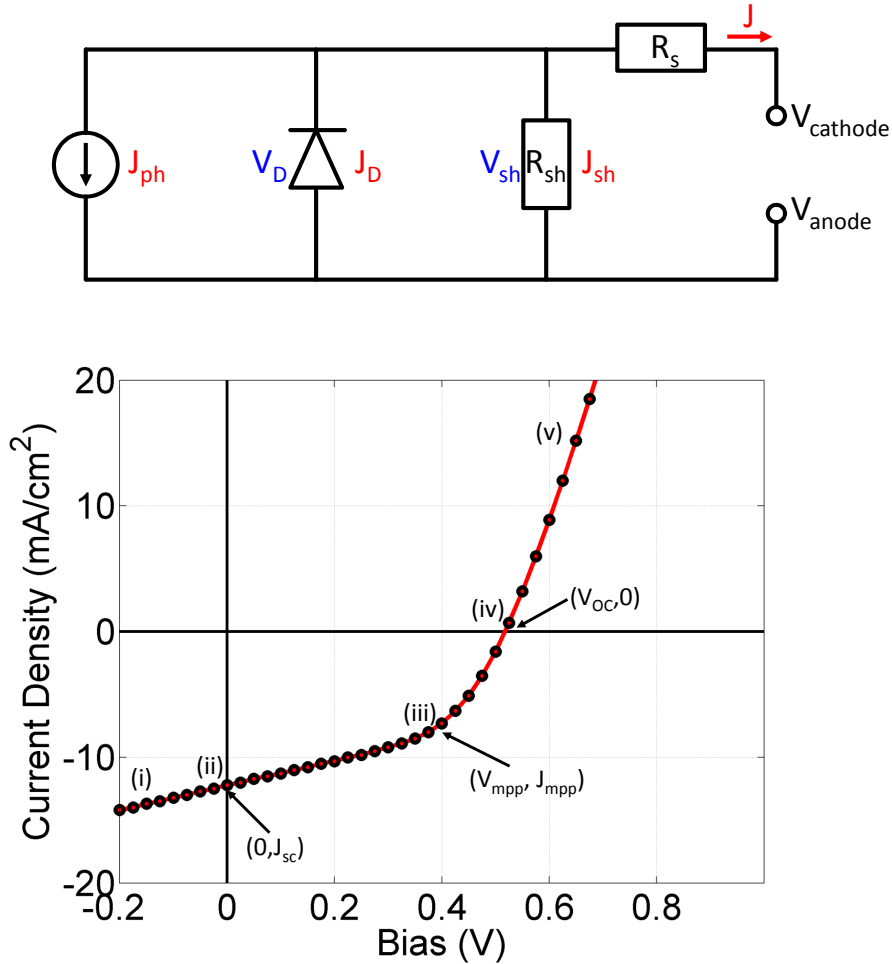


Figure 2.1: A simple model to describe the current-voltage characteristic of solar cells. (top): The solar cell equivalent circuit . An analysis of the current flowing through each of the components enables us to express the current-voltage characteristic as a solution of the generalized Shockley equation. (bottom): A solution representative of devices fabricated in this work (see also Tab. 2.1). Critical points on the curve are the short-circuit current density J_{SC} , the open-circuit voltage V_{OC} and the current density and voltage at the maximum power point J_{mpp} and V_{mpp} respectively.

The current density J observed at the indicated position on the circuit (which will flow through connected electrical loads, for example to power devices) is given by the sum of the current densities through each component:

$$J = J_D + J_{sh} - J_{ph} \quad (2.1)$$

We note that the total current I can be obtained from $I = JA$, where A is the device area. As we are dealing with current density (Am^{-2}) and not current (A), we will express the resistances in units of Ω multiplied by area. The current density through a diode is well known:

$$J_D = J_0 \left(\exp \left(\frac{qV_D}{nkT} \right) - 1 \right) \quad (2.2)$$

where q is the electronic charge, k is Boltzmann's constant, T is the temperature and J_0 is the saturation current density. The constant n is known as the diode ideality factor which takes values between 1 and 2. A small value of n corresponds to a diode that opens sharply over a narrow voltage range. Denoting the bias between the anode and cathode, $V_{\text{anode}} - V_{\text{cathode}}$ as V and applying Kirchoff's voltage law for the resistors connected in series:

$$V_{sh} = V - JR_s = V_D \quad (2.3)$$

where the last equality holds because the shunt resistor and the diode are connected in parallel. The current density across the shunt resistor is therefore:

$$J_{sh} = \frac{V - JR_s}{R_{sh}} \quad (2.4)$$

Combining equations (2.1), (2.2) and (2.3) we obtain the output current:

$$J = J_0 \left(\exp \left(\frac{q(V - JR_s)}{nkT} \right) - 1 \right) + \frac{V - JR_s}{R_{sh}} - J_{ph} \quad (2.5)$$

which is known as the *Generalized Shockley Equation*. This equation (which is transcendental) results in a current-voltage characteristic (also known as an IV curve) such as the one depicted in Fig. 2.1, constructed using the parameters in table 2.1. These parameters were chosen to approximate IV curves of typical organic solar cells in the literature and in this work. The photocurrent density J_{ph} is an approximate of the maximum that can be expected from a P3HT:PCBM cell [6]. J_0 and n are taken from [7], whereas R_s and R_{sh} are representative of typical devices used in this work, which have device area A as shown.

We identify a number of important biases and bias regimes (labeled in Fig. 2.1) .

- (i) In reverse bias ($V = V_{\text{anode}} - V_{\text{cathode}} < 0$), the diode is closed² and the main contributors to the current density are J_{ph} and J_{sh} . Under reverse bias, J_{sh} is directed in the same direction as J_{ph} and the two will therefore sum such that the magnitude of the total current

²The diode is closed for all moderate reverse biases. At very large reverse biases, e.g. of the order of -50 V for a silicon diode, breakdown occurs and large current flows. However, solar cells are never operated in this voltage region.

J_0	$10^{-11} \text{ mAcm}^{-2}$
J_{ph}	13 mAcm^{-2}
R_s	$50 \Omega \text{ cm}^2$
R_{sh}	$800 \Omega \text{ cm}^2$
A	0.12 cm^2
n	1.47

Table 2.1: Input parameters for the curve show in Fig. 2.1.

density exceeds that of J_{ph} alone for non-infinite values of R_{sh} , as observed in 2.1. The current density J , measured in the indicated direction, is negative.

- (ii) At $V = 0$, J_D is still negligible, we have $J \approx -J_{ph}$ under the assumption that $R_{sh} \gg R_s$ (valid for all robust devices). The current density at the short-circuit condition ($V = 0$) is denoted by J_{SC} .

At positive biases ($V = V_{anode} - V_{cathode} > 0$), we enter the domain where the diode opens up (somewhere between (ii) and (iii)) and a large current passes through.

- (iii) This point is of special importance: the power P generated by the solar cell ($P = AJV$) is maximal. We denote the bias and current density values at this maximum power point as V_{mpp} and J_{mpp} respectively.
- (iv) As the bias is further increased, we reach a point where J_D and J_{sh} sum to exactly cancel out the photocurrent density. The voltage at open-circuit condition ($J = 0$) is denoted by V_{OC} .
- (v) As the bias is increased further, the photocurrent becomes negligible compared to the injected current. Therefore, the IV curve of a solar cell in the dark $J_{ph} = 0$, known as the dark curve, approaches the IV curve under illumination at sufficiently high forward biases.

The shape of the curve between points (ii) and (iv) is typically quantified with the fill-factor FF , defined as:

$$FF = \frac{P_{out}}{P_{ideal}} = \frac{V_{mpp}J_{mpp}}{V_{OC}J_{SC}} \quad (2.6)$$

where P_{ideal} is the power produced by an ideal solar cell with an open-circuit voltage and short-circuit current of V_{OC} and J_{SC} respectively. We note that even for $R_s = 0$ and $R_{sh} = \infty$, a fill-factor of unity is impossible due because diodes open up over an extended voltage range, as

expressed with the exponential dependency on voltage. The current density through the shunt resistor is very important in determining the fill-factor: in forward bias, J_{sh} is directed in the opposite direction to J_{ph} and therefore acts to reduce the total current density J for a given bias V .

The energy conversion efficiency, defined as the fraction of incident power that is converted into electrical power, is defined as follows:

$$\eta = \frac{P_{out}}{P_{in}} = \frac{V_{OC}J_{SC}}{P_{in}} FF \quad (2.7)$$

This is the critical performance parameter for solar cell research. As explained in the Introduction, the value of this parameter is intimately linked with the cost of photovoltaic technology.

To illustrate the role of the parameters in the *Generalised Shockley Equation*, we show IV curves for incrementally less ideal values of series and shunt resistance, the saturation constant and the ideality constant (Figures 2.2 and 2.3). When we increase R_s , the current density is reduced at all biases. For very high values of R_s , the IV curve tends towards a straight line - the characteristic of a single resistor. When we decrease R_{sh} , parasitic current along the shunt resistor increases (see large, negative biases). The current becomes positive at lower positive biases because the (negative) photocurrent is dwarfed by the large positive current through the shunt resistor. As a result we observe a reduction in V_{OC} (Fig. 2.2). Similarly, increased values of J_0 and decreased values of n effectively mean that the diode opens at lower biases, which also reduces V_{OC} (Fig. 2.3).

Although the equivalent circuit (Fig. 2.1) was originally developed for inorganic solar cells, it can nevertheless be used to gain a qualitative understanding of the IV curves of organic cells. In fact, the *Generalized Shockley Equation* can closely match experimental measurements if appropriate additional considerations are made (see [8] and [9] for details).

2.2 Organic solar cells

Organic solar cells, which are intrinsically low cost because of their ease of processing and the low cost of organic (carbon-based) semiconductors, are currently undergoing impressive growth in demonstrated operating efficiency (Fig. 2.4). In the time taken to perform the research for this thesis, the world record efficiency has increased from around 5% (in 2008) to the current certified record of 8.3%. [10].

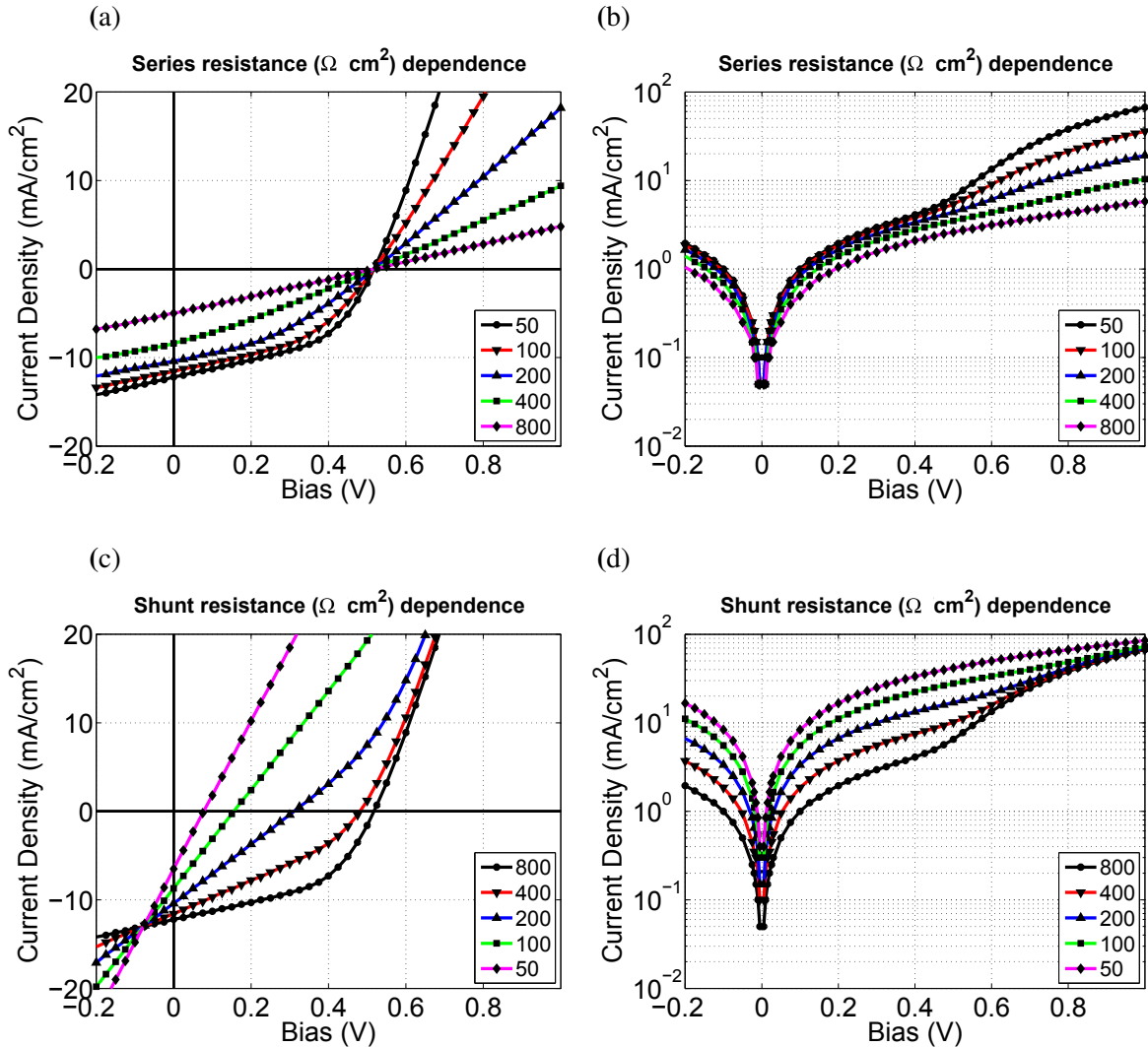


Figure 2.2: The effect of series (a-b) and shunt (c-d) resistance on IV curves under illumination (a,c) and in the dark (b,d). Curves for series and shunt resistance values in the range 50-800 $\Omega \text{ cm}^2$ are shown. Only the indicated variable is varied in each plot. All other variables are as given in Tab. 2.1.

Organic semiconductors

Organic semiconductors, like their inorganic counterparts, exhibit structures in which delocalized electrons can be excited into higher energy states and then undergo transport and collection. In the case of organic semiconductors, this is enabled by the electronic orbital structure established along alternating single and double bonds between carbon atoms (known as conjugated bonds). The π -orbitals (denoted p_z) overlap sufficiently such that electrons in these

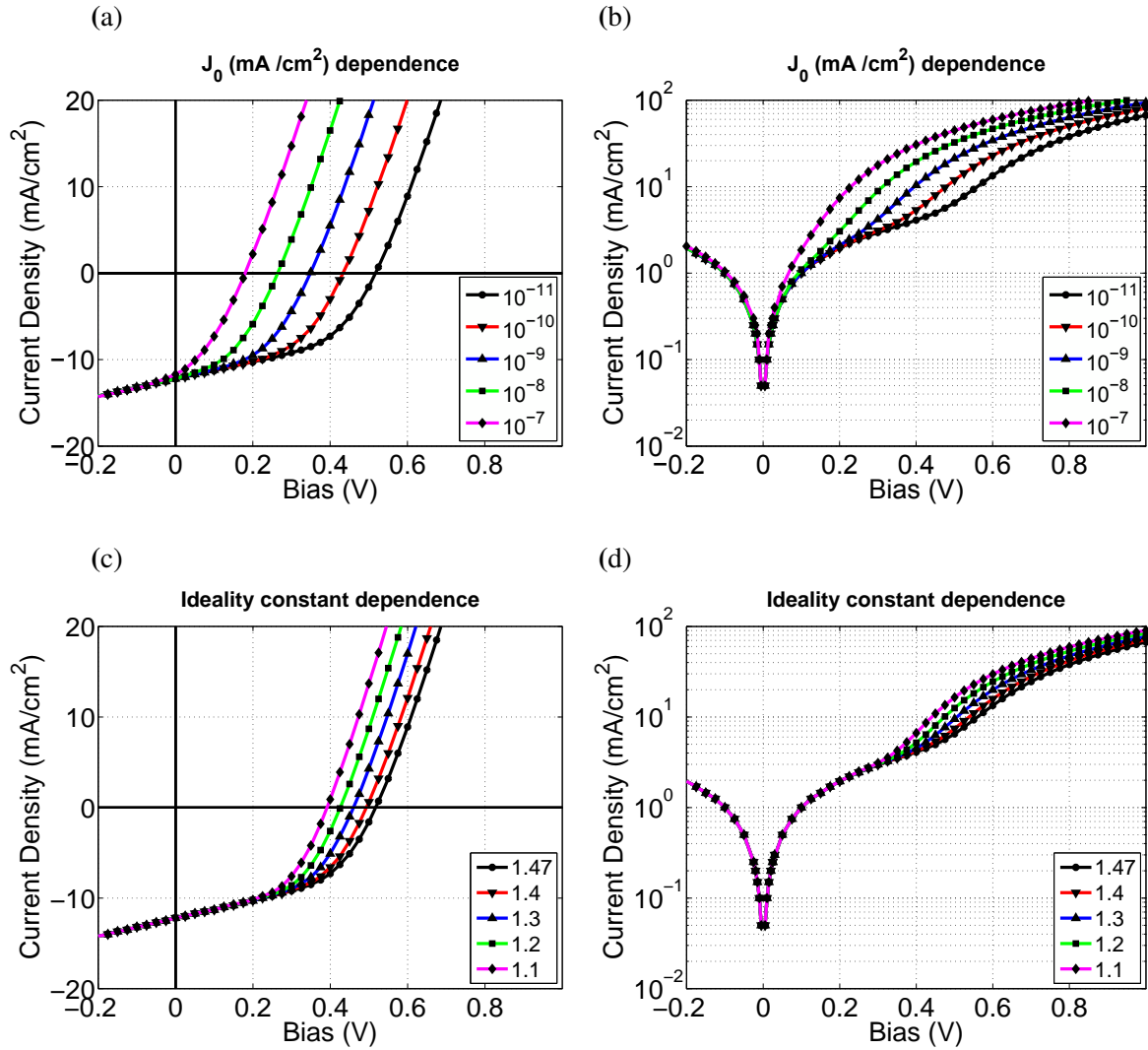


Figure 2.3: The effect of the saturation current (a-b) and ideality constant (c-d) on IV curves under illumination (a,c) and in the dark (b,d). (a-b) Curves for saturation current density values in the range 10^{-11} - 10^{-7} mA/cm² are shown. (c-d) Curves for diode ideality factor values in the range 1.1-1.47 are shown. Only the indicated variable is varied in each plot. All other variables are as given in Tab. 2.1.

orbitals become delocalized - hence materials with conjugated bonds can conduct electricity. Furthermore, the interaction of these orbitals forms bonding and antibonding orbitals π and π^* which provide two separate energy states in which electrons can reside, separated by a band-gap E_g - hence materials with conjugated bonds can act as semiconductors. These orbitals are commonly referred to as the highest occupied molecular orbital (HOMO) and lowest unoccupied molecular orbital (LUMO) respectively. The energy-levels of the respective orbitals are

2.2 Organic solar cells

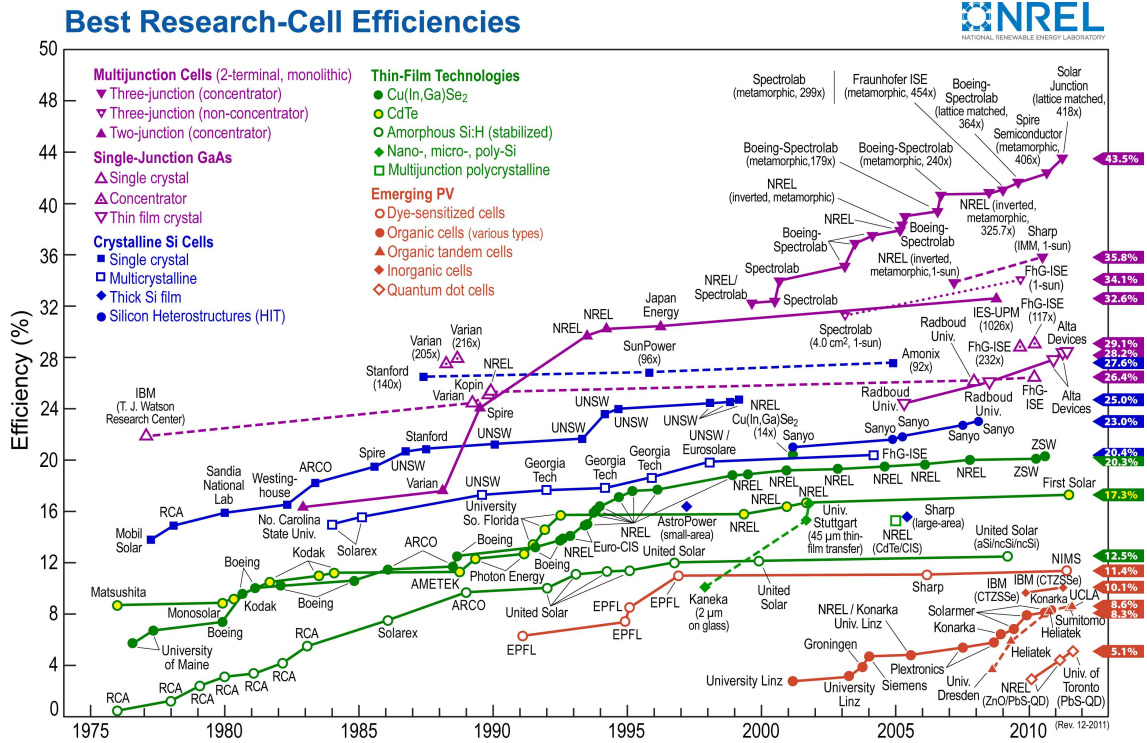


Figure 2.4: Timeline of record solar efficiencies. The rapid growth of organic solar cells is evident (filled orange circles). [11]

highly dependent on the molecular structure of the semiconductor. The molecular structure of all of the organic materials considered in this study are shown in Fig. 2.5. The materials are classified into two groups: electron donors, which are good hole conductors, and electron acceptors, which are good electron conductors.

We now explain the process of current generation in organic solar cells. The process consists of six steps (Fig. 2.6) which are explained below:

(i) Absorption

In order to excite electrons from the HOMO to the LUMO, energy is required. As E_g is of the order of one or more eV for commonly used organic semiconductors, thermal excitation of HOMO electrons is inefficient at room temperature ($kT = 0.0256$ eV at 298 K) - organic semiconductors are insulators under such conditions. Electrons can be excited into higher energy states upon the absorption of sufficiently energetic incident photons.

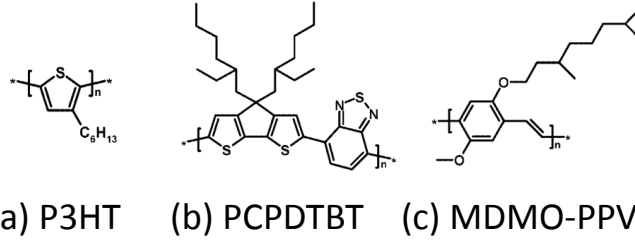
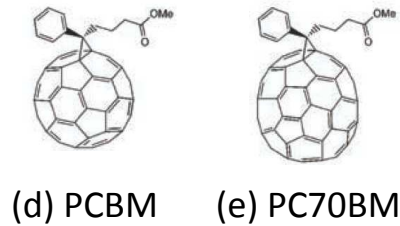
Electron donors:Electron acceptors:

Figure 2.5: The molecular structure of electron donors (a-c) and electron acceptors (d-e) used in this study. A device consisting of a combination of (a) P3HT and (d) PCBM is somewhat of a standard device in the organic solar cell community.

Organic semiconductors are typically efficient absorbers, with an absorption constant α within the range 10^6 - 10^8 m^{-1} at the absorption peak. Note that it is generally appropriate to assign common organic semiconductors macroscopic optical properties in this way, however larger organic molecules may require a more complex treatment accounting for inhomogeneity and optical anisotropy. To calculate the absorption in a slab of organic material with $\alpha(\lambda)$, we can make use of the Beer-Lambert law for the optical intensity $I(x, \lambda)$ of a light beam of wavelength λ after having propagated a distance x through the medium:

$$I(x, \lambda) = I_0(\lambda)e^{-\alpha(\lambda)x} \quad (2.8)$$

where $I_0(\lambda)$ is the intensity at $x = 0$. We see that the intensity of a light beam decreases exponentially with penetration into an absorbing medium. If we consider the intensity reduction occurring within a cylinder of volume $V = xS$, where S is the cross-sectional area of the cylinder, we can obtain the absorbed power $A(x, \lambda)$:

$$\begin{aligned} A(x, \lambda) &= (I_0(\lambda) - I(x, \lambda))S \\ &= I_0(\lambda)(1 - e^{-\alpha(\lambda)x})S \end{aligned} \quad (2.9)$$

2.2 Organic solar cells

Therefore, the absorption $A(x, \lambda)$ is directly proportional to the intensity of the incident beam. In order to calculate the absorption of a film with a more complicated geometry, such as a solar cell with a light-trapping system, more sophisticated techniques are required. This is one of the main focuses of this thesis (see Chapters 6 and 9).

In inorganic semiconductors, the absorption of a photon produces two free charges (an electron in the conduction band and a hole in the valence band). However, in organic semiconductors, the absorption of a photon produces two charges (an electron in the LUMO and a hole in the HOMO), but they are very much bound to each other. This is due to the lower dielectric constant typically observed in organic materials: compare $\epsilon_r \approx 3$ for P3HT [12] and $\epsilon_r \approx 18$ for monocrystalline silicon [13] at 500 nm.³ As evident from Coulomb's law for the electrostatic force F between two charges of charge q separated by d : $F = (1/4\pi\epsilon_r\epsilon_0)(q^2/d)$ where ϵ_0 is the permittivity of free space, a reduced dielectric constant corresponds to an increased Coulombic attraction between the excited electron and the hole in an organic semiconductor. In inorganic semiconductors, the high dielectric constant is said to "screen" the electrostatic force between the conduction band electron and the corresponding valence band hole. In organic semiconductors, the electrostatic force is not screened - the electron and hole experience a strong Coulombic attraction to each other. Before the charges can contribute to a photocurrent, they must first be separated.

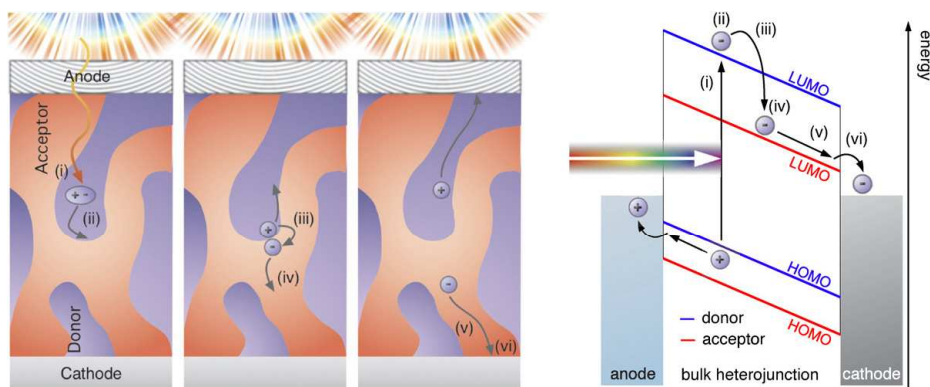


Figure 2.6: The steps involved in generation of photocurrent in bulk heterojunction devices. (i) Exciton generation arising from the absorption of a photon. Generation is shown here to occur in the (electron) donor, although generation in the acceptor also occurs. (ii) Exciton diffusion to a donor-acceptor interface. (iii) Exciton dissociation via electron transfer to the acceptor to form a charge transfer state (iv) Complete separation of the charge pair. (v) Charge transport to the respective electrodes. (vi) Charge collection. These processes are illustrated according to (left) the spatial location at which they occur and (right) on a simplified energy diagram. Taken from [9].

³The values given are the real part of dielectric constant as calculated from refractive index data in the indicated references.

(ii) Exciton diffusion

The tightly bound charge pair is commonly referred to as an exciton, a charge-neutral quasi-particle. The energy required to overcome the Coulombic attraction in order to separate the charges is known as the binding energy, which is typically several tenths of an electron volt. [14] Since the first report in 1986 [15], organic solar cells typically feature not one but two semiconductors: an electron donor and an electron acceptor (see Fig. 2.5). This interface between the two is known as a heterojunction. It is energetically favorable for excitons to dissociate at the heterojunction (which is explained in the next paragraph). The exciton must, however, first travel to the interface. Exciton transport in organic semiconductors is usually described as a diffusion process. In order to maximize the efficiency of exciton diffusion from the point of generation to the heterojunction, networks of interpenetrating phases of each material, known as bulk heterojunctions [16], are commonly used to maximize the interfacial area (illustrated schematically in the left panel of Fig. 2.6). Upon formation, excitons primarily reside along a conjugated chain segment. From there, excitons diffuse to progressively lower energy sites but have a limited lifetime before they recombine. Typical exciton diffusion lengths in P3HT range from 3-14 nm, although values up to 27 nm have been reported. [17] The large surface area of the semiconductor-semiconductor interface of bulk heterojunctions minimizes the nominal distance that an exciton must travel to reach the nearest interface, thereby ensuring that the probability that an exciton diffuses to an interface before recombining is high. In optimized bulk heterojunction networks, excitons in conjugated polymer materials can diffuse to the interface with a time scale of nanoseconds. [18]

(iii) Exciton and (iv) charge transfer state dissociation

The heterojunction of a correctly chosen electron donor and acceptor pair exhibits the property $\text{HOMO}_{\text{donor}} > \text{HOMO}_{\text{acceptor}}$ and $\text{LUMO}_{\text{donor}} > \text{LUMO}_{\text{acceptor}}$. This is shown in the right panel of Fig. 2.6. These conditions are favorable for exciton dissociation at the heterojunction: it is energetically favorable for the electron to be transferred from the $\text{LUMO}_{\text{donor}}$ to the lower energy $\text{LUMO}_{\text{acceptor}}$, whereas it is energetically favorable for the hole to remain in the higher energy $\text{HOMO}_{\text{donor}}$. However, even after the charges are separated, one on each side of the heterojunction, they are still Coulombically bound. This state is known as a charge transfer state (CTS) or a polaron pair.⁴ The dissociation probability of a CTS is commonly described using Onsager-Braun theory [19], and is a monotonically increasing function of the electric

⁴A polaron is a particle consisting of a charge and the deformation of the charge's environment. Unlike rigid atomic lattices in inorganic semiconductors, molecules in organic semiconductors can be significantly deformed due to the presence of a charge. This partially accounts for the reduced conductivity of organic materials.

field experienced at the CTS location. The probability is also increased for larger separation between the charges, which is heavily dependent on the organic materials in question. Improved agreement with experimental results can be obtained by taking energetic disorder and extended polymer chains into account. [20]

(v) Charge transport

Upon dissociation of the CTS, the charge-carriers can travel in opposite directions to the respective electrodes for collection. This transport is enabled by charge-carrier diffusion and the force experienced by the charges due to the bias across the electrodes (the component of current that flows due to this force is known as the drift current). The efficiency of the transport is typically quantified by the material mobility μ , defined as the average particle velocity in response to an electric force per unit electric field. The lack of long-range order in organic materials prevents efficient band transport. Instead, charges must move between localized states on neighboring molecules, referred to as hopping transport. The lifetime of a charge-carrier, τ , is finite. In addition, each semiconductor phase must exhibit contiguous pathways from the point of charge generation to the electrode for charge transport. If not, charges become trapped and cannot be collected. This represents a loss for the solar cell. One of the drawbacks in bulk heterojunction solar cells is the compromise that must be made with the phase inter-mixing: large intermixing ensures that the heterojunction has a large surface area but decreases the number of contiguous pathways available for charge transport.

Charge-carrier transport can be quantified with the transport length $L_{e,h}$ defined by:

$$L_{e,h} = \mu_{e,h} \tau_{e,h} E \quad (2.10)$$

for electrons and holes. E is the electric field strength and $\tau_{e,h}$ is the carrier lifetime. Measurements for standard P3HT:PCBM cells find values of $L_e > 340\text{nm}$ in PCBM and $L_h = 90\text{nm}$ in P3HT. [21] The limiting transport length (in this case, 90 nm) of the charge carriers may enforce a limit on the semiconductor film thickness. This could explain the observation that optimized devices based on similar materials tend to have thicknesses of around 100 nm or less. [22] In a recent publication, Sun et al. observed an increase in the FF from 59% to 61% when the film thickness was reduced from 180 to 100 nm. [23] An increase FF is an indication of reduced electrical losses.

(vi) Charge collection

Charges that reach the electrodes can then be extracted. Under ideal conditions, the charge is extracted immediately (infinite surface recombination). If the surface recombination is non-infinite, charges may collect at the electrode forming space charge which leads to increased bulk recombination and a potential barrier for charge collection. Under such conditions, kinks in the IV curve known as S-shapes can occur, particularly at voltages near the open-circuit voltage. [24] In the ideal case, no potential barrier exists and the electrode is said to form an ohmic contact with the semiconductor.

Loss mechanisms: electrical

A number of recombination (mutual annihilation of a positive and negative charge) processes can occur in bulk heterojunction solar cells. Upon recombination, the energy carried by the charges is lost via either a radiative or non-radiative mechanism. Therefore, recombination represents an efficiency loss mechanism for the device. We typically distinguish between two kinds of recombination:

- Geminant recombination is a term used to describe the recombination of two charges that exist in a CTS. This is therefore one of the two decay pathways for a CTS (the other being dissociation into free charges).
- Bimolecular recombination refers to the recombination of two free charges which typically do not originate from the same exciton. As is implicit in the design of heterojunction solar cells, positive charges primarily reside in the donor material and negative charges primarily in the acceptor material. This means that bimolecular recombination usually takes place at the heterojunction. Importantly, two free charges cannot recombine directly - they must first form a CTS. Therefore, a finite probability exists that the charges will once again become free (see above).

Other electrical losses can also occur in organic solar cells. Excitons can decay prior to reaching an interface to form a CTS. Excitons can decay non-radiatively (where the exciton's energy is converted to heat or transferred to lattice energy) or radiatively, in which case there is a finite probability that the photon emitted during radiative decay will be absorbed again by the semiconductor. Exciton-exciton annihilation, where the energy of one exciton is lost to a nearby exciton, can occur for high exciton generation densities (see [17]). Metal-induced exciton annihilation (also referred to as quenching) can also occur at metallic surfaces. This is investigated in Chap. 7.

Loss mechanisms: optical

The first source of optical loss in solar cells is reflection. In optically thick devices, where light is effectively absorbed upon one traversal, reflection occurs exclusively at the front interface. This is especially relevant to many inorganic solar cells such as those made from silicon. The high refractive index of silicon leads to high reflectance at the air-silicon interface unless anti-reflection films are used. Optically thin devices usually incorporate reflective metallic back electrodes made from silver or aluminum, such that a second propagation of light through the active layer is ensured. Therefore, out-coupling of this reflected light back out of the device as well as reflection at the front interface comprise reflection losses in optically thin cells. Measures taken to reduce reflection can increase absorption in the active layer.

Absorption in regions within the device where charge-pair generation is ultimately not possible (such as in the metallic electrode) represents another optical loss in solar cells. Gold, which absorbs significantly at optical wavelengths (due to a d orbital transition) can lead to a reduction in absorption in the active layer. In this sense, silver can be seen as a preferable alternative, as its highly reflecting properties at optical wavelengths can ensure that light absorbed in the device is almost exclusively absorbed by the semiconductor (see [25], flat device).

2.3 Plasmonic Theory

We now introduce the field of plasmonics: the study of electromagnetic modes that can exist on metallic interfaces or in metallic nanostructures. In subsequent chapters, we will demonstrate how the energy of incident light can be transferred to plasmonic modes that reside on an organic semiconductor - metallic interface. The energy in the mode can then be absorbed in the semiconductor. This is one method of achieving light-trapping.

2.3.1 Optical properties of noble metals

A useful model for describing the optical behavior of metals is the Drude or free electron gas model, which arises when we treat the metal as a gas of free electrons that moves against a background of fixed positive ions. Lattice potential and electron-electron repulsion are not taken into account. As shown in *Maier, 2007* [26], by assigning an electron collision frequency γ and solving for the motion of a single electron in an arbitrary external field with oscillation frequency ω , the dielectric constant is found to be:

$$\epsilon(\omega) = 1 - \frac{\omega_p^2}{\omega^2 + i\gamma\omega} \quad (2.11)$$

where ω_p is the plasma frequency. However this model is only of limited use for the two most important metals in optical plasmonics: silver and gold. This is due to readily occurring inter-band transitions, in which photons excite electrons from filled bands to higher level bands. One of the consequences of this is that the imaginary part of the dielectric constant (and hence the absorption of the metal) is higher than that predicted by Eq. 2.11.

In this work, experimentally determined complex dielectric constants are used for simulations which removes the need to make assumptions about the optical response of any material. Effects such as inter-band transitions in metals and semiconductors are elegantly contained in the dielectric constants themselves.

2.3.2 Surface Plasmon Polaritons (SPPs)

Surface plasmon polaritons (SPPs) are surface-bound electromagnetic waves which can propagate along metal-dielectric interfaces. It is possible to arrive at the fundamental dispersion relation for SPPs by analytically solving the wave equation in the electric field \mathbf{E} for solutions that propagate along the interface and decay exponentially in the direction perpendicular to the interface. As demonstrated by *Maier* [26], such solutions exist for TM modes only. The component of the mode wave vector in the direction of propagation along the interface (which we will assume is located along the x-axis) is denoted by the propagation constant $\beta = k_x$:

$$\beta = k_0 \sqrt{\frac{\epsilon_d \epsilon_m}{\epsilon_d + \epsilon_m}} = \frac{\omega}{c} \sqrt{\frac{\epsilon_d \epsilon_m}{\epsilon_d + \epsilon_m}} \quad (2.12)$$

where k_0 is the magnitude of the wave vector propagating in a vacuum, and ϵ_d and ϵ_m are the frequency dependent, complex-valued dielectric constants of the dielectric and the metal, respectively.

We now have the propagation constant for a SPP, a propagating surface mode, at the interface between a conductor and a dielectric. External excitation of this mode must respect both energy and momentum conservation. The component of the momentum of a freely propagating photon at grazing incidence to the interface is given by:

$$k_x^{photon} = \frac{\omega}{c} \quad (2.13)$$

For all typical combinations of ϵ_m and ϵ_d at visible and infra-red frequencies, the square root term is greater than one (for silver and gold, $\text{Re}(\epsilon_m)$ is large and negative [27] whereas ϵ_d is

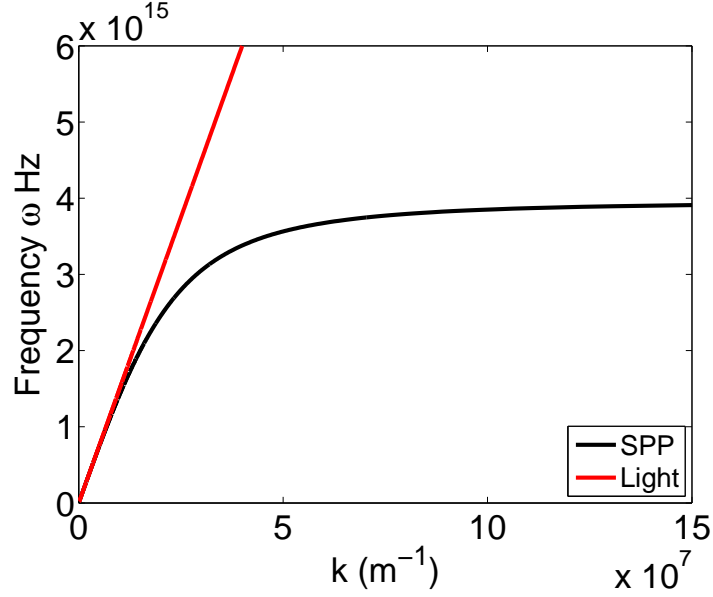


Figure 2.7: A surface plasmon polariton (SPP) dispersion curve at a silver (Drude approximation):dielectric interface and an accompanying light curve The SPP curve is calculated for a silver-dielectric interface where the dielectric has a (real) dielectric constant of 4. The dielectric constant of silver is approximated by the Drude form (Eq. 2.11). The wave vector refers k refers to the component along the interface in the direction of SPP propagation. Only the real component of the wave vector is plotted. Eq. 2.14 holds for all non-zero wave vectors. Therefore coupling between SPPs and photons from this light curve is forbidden.

positive and greater than 1) so we obtain:

$$k_x^{photon} < \beta \quad (2.14)$$

This is shown explicitly in Fig. 2.7 where the dispersion curve for $\epsilon_m = \epsilon_{silver}$. We will approximate the dielectric constant of silver with the Drude model (with $\omega_p = 8.85 \times 10^{18} s^{-1}$ (following [28]) and $\gamma = 10^{14} Hz$ [26]), and then show the effect of using the experimentally determined constant afterwards. The dielectric constant of the adjacent dielectric is taken to be $\epsilon_d = 4$ - typical for common organic semiconductors. We see that for all non-zero frequencies, the wave vector of light is smaller than the SPP propagation constant (2.14). We note that Fig. 2.7 is in actuality a plot of momentum $p_x = \hbar k_x$ v.s. energy $E = \hbar \omega$. As the SPP and light curves do not cross, there exists no energy-momentum state in which a photon can transfer its energy to a SPP without violating at least one of the conservation laws (energy or momentum). Therefore, excitation of SPPs by direct illumination of propagating light is not possible .

We emphasize that Eq. 2.13 shows the x-component of the photon wave vector for grazing incidence. If the angle of incidence θ is reduced, k_x^{photon} will decrease as $\sin \theta$. Therefore,

$k_x^{photon}(\omega)$ can be reduced by simply decreasing the incidence angle - which increases the slope of the light curve and moves it towards the y-axis. The indicated light curve depicts the maximum value (obtained at $\theta = 0$) of $k_x^{photon}(\omega)$. Therefore, all points to the left of the light curve are accessible with freely propagating photons. As we see, all points within this “light-cone” have wave vectors of insufficient magnitude to couple to a SPP mode.

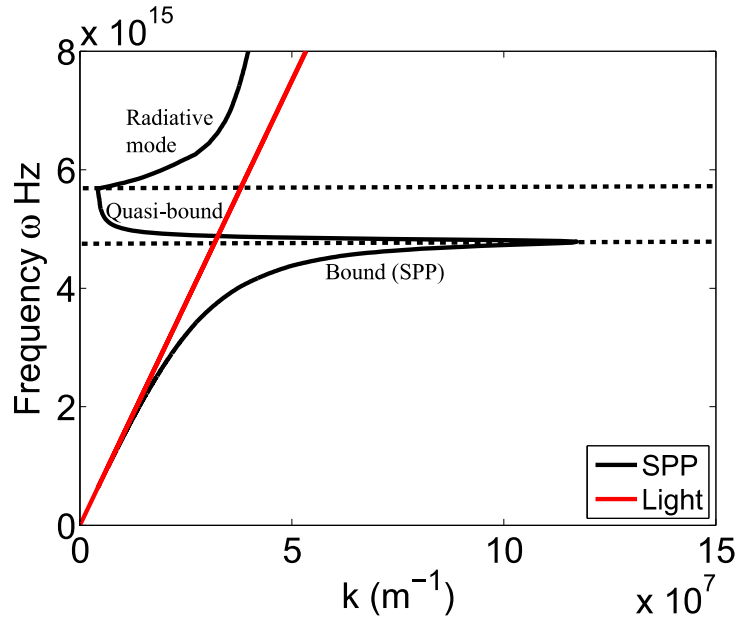


Figure 2.8: A surface plasmon polariton (SPP) dispersion curve at a silver:dielectric interface and an accompanying light curve The SPP curve is calculated for a silver-dielectric interface where the dielectric has a (real) dielectric constant of 4. The dielectric constant of silver is experimentally determined [27]. The wave vector k refers to the component along the interface in the direction of SPP propagation. Only the real component of the wave vector is plotted. The important regions of the dispersion curve are indicated. Only the bound SPP modes lie outside the light curve, and can therefore propagate along the surface without coupling to light. The radiative and quasi-bound modes are of less interest. For this reason, we will use the term SPP synonymously with bound SPP from now on.

This also holds true if we calculate the dispersion curve using the experimentally determined dielectric constant for silver (Fig. 2.8). The important regions of the plot are labeled. The only truly bound modes (SPPs) are below the dotted line. The dispersion curve appears to approach an asymptote (dotted line) but then bends back on itself. The frequency of this quasi-asymptote is known as the surface plasmon frequency ω_{sp} .⁵ Modes at this frequency can be considered to be SPPs in the limit $\beta \rightarrow \infty$. We see that for an interface between an organic-like material and silver, the surface plasmon frequency is around $4.9 \times 10^{15} \text{s}^{-1}$, equivalent to a wavelength

⁵This is the correct usage of the term surface plasmon. However, it is often used less precisely to refer to plasmonic excitations in general

of 380 nm. The radiative modes lie entirely within the light cone and therefore are not bound - the energy of these modes can be readily out-coupled in the form of photons. At frequencies between the dotted lines, the modes are said to be quasi-bound.

The fact that Eq. 2.14 holds for SPPs is essential for their bound nature; a SPP is able to propagate along the interface precisely because its wave vector is too large for it to couple to light. Nevertheless, it is highly desirable to excite SPPs with photons. In order to do this, one of the following methods can be used to impart extra momentum to the photons.

Attenuated total internal reflection

One method of exciting SPPs using an external photon source is excitation via attenuated total internal reflection. In this geometry, light is incident on a thin metal film through a high index medium such as glass ($k_{glass} = k_{vacuum} \sqrt{\epsilon_{glass}}$). The incidence angle is larger than the critical angle for total internal reflection. A component of the incident wave evanescently tunnels through the metal film to an interface with a lower dielectric constant medium such as air ($\epsilon_{air} = 1 < \epsilon_{glass}$). As the wave vector of the evanescent wave exceeds that of light in the low dielectric constant medium, SPP excitation at this interface is possible. Attenuated total internal reflection excitation is typically achieved using glass prisms [29] or highly focused optical beams [30].

Grating coupling

A second method, and arguably the most relevant for SPP excitation in solar cells, is known as grating coupling. As shown in Fig. 2.8, the photon wave vector is too small to excite SPPs at all frequencies. However, if the light interacts with a body near the interface, the component of the wave vector in the plane of the interface can be increased by a component due to scattering Δk_x :

$$k_x^{photon} = k \sin \theta \pm \Delta k_x \quad (2.15)$$

where θ is the angle of incidence of the incoming light measured from the normal.

The additional component Δk_x is exactly known if the scattering is provided by an array of scatterers, such as a shallow 1D line grating on the surface. The photon wave vector is then given by:

$$k_x^{photon} = k \sin \theta \pm G \quad (2.16)$$

where $G = \frac{2\pi m}{P}$ is the reciprocal vector of a grating of period P and m is the (integer-valued) mode number. Equation 2.16 can be generalized for 2D gratings. For example, for a 2D square grating, Eq. 2.16 holds with $G = \frac{2\pi}{P}\sqrt{m^2 + n^2}$ for mode numbers m and n .

For a virtuous choice of grating period P , the increase in the photon wave vector can suffice to allow coupling to a SPP:

$$k_x^{photon} = k \sin\theta \pm G = \beta \quad (2.17)$$

The resulting SPP is then said to be grating-coupled.

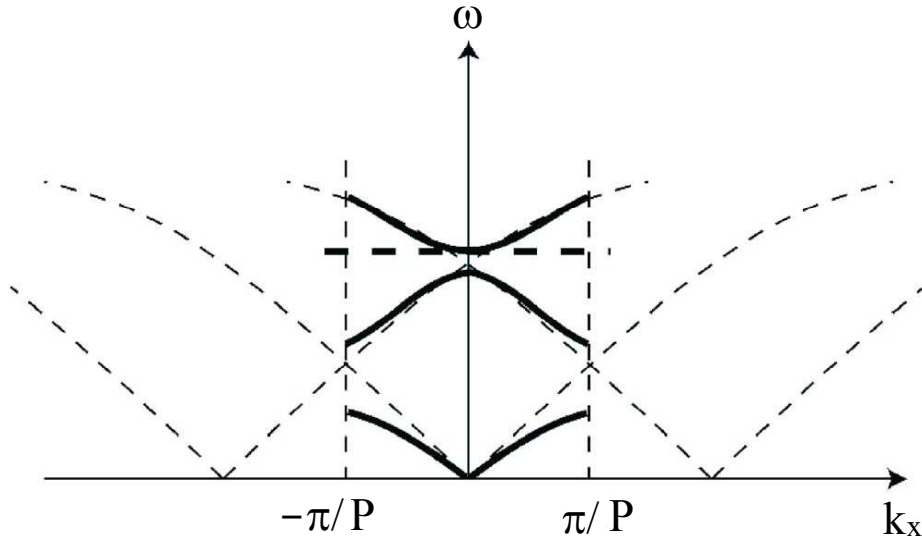


Figure 2.9: Dispersion curves (thick lines) for 1D grating-coupled SPPs. The relevant dispersion can be expressed within the first Brillouin zone ($-\frac{\pi}{P} \leq k_x \leq \frac{\pi}{P}$) and is obtained by folding the dispersion curves (dashed-lines) based at points located at integer multiples of the reciprocal lattice vector $\frac{2\pi}{P}$. Also shown are the plasmonic band gaps that arise near the zone edge. Adapted from [31].

From an alternative viewpoint, the effect of the gratings is to fold the SPP dispersion curve on itself in k space. For a 1D lattice, the first Brillouin zone is bounded by the wave vector values $-\frac{\pi}{P}$ and $\frac{\pi}{P}$ (Fig. 2.9). As shown, the SPP dispersion curve is repeated (dashed curves) at each lattice point $\frac{2\pi m}{P}$, as each point can arbitrarily be considered as an origin in reciprocal space. As the wave vector values of these curves are not unique, we can equivalently represent the corresponding ω values within the first Brillouin zone. Hence the lattice “folds” the SPP dispersion curve back on itself, which allows coupling to light.

In addition to folding, the lattice also affects the SPP wave vector itself, most prominently at the Brillouin zone edge (Fig. 2.9, black lines). This is due to the interaction between modes scattered by the grating and the formation of standing waves. [32] Two standing wave solutions

of different energy are established, leading to the formation of band-gaps. The nature of this deformation of the flat-surface SPP curve and the size of the band-gap depends strongly on the grating shape, as is investigated in detail by Hooper and Sambles [33].

Light-trapping with SPPs

Once a SPP has been excited at the interface between an organic semiconductor and a metal, the energy of the SPP mode is ultimately dissipated via absorption in one of the two media. As required for a bound mode, the electric field of the SPP drops sharply (exponentially) in the direction perpendicular to the direction of travel. In the semiconductor, the electric field drops as:

$$\frac{E_z(z)}{E_z(0)} = \frac{E_x(z)}{E_x(0)} = e^{-k_2 z} \quad (2.18)$$

where $k_2^2 = \beta^2 - k_0^2 \epsilon_d$ is the component of the wave vector in the z direction ([26]). The absorption of electromagnetic energy is proportional to the square of the modulus of the electric field (see Eq. 6.3 in Chap. 6). Therefore, the absorption of this mode will primarily occur closest to the interface, where the electric field is strongest. The fraction of SPP energy that is absorbed in the semiconductor (and not in the metal) is a strong function of frequency and the dielectric constants involved. This has been explicitly calculated by *Atwater and Polman* [34]. A high fraction of SPP energy is absorbed in the organic semiconductor, a result of its high absorption coefficient and low dielectric constant (Fig. 2.10).

This is encouraging for plasmonic light-trapping in solar cells: if additional light can be trapped into the device via SPPs (for example, light that would have otherwise been lost to reflection) then the majority of it will be ultimately absorbed in the semiconductor, thereby increasing the exciton generation rate. Under ideal conditions (see Sec. 2.4), this will lead to an increase in power conversion efficiency.

2.3.3 Localized Surface Plasmons (LSPs)

Localized surface plasmons are non-propagating excitations of conduction electrons within a metallic nanostructure. They can be thought of a cloud of negative charge being driven by an external electric field (the electric field of an incident light wave for example), relative to stationary positive charges which provide a restoring force. The combination of a driving force and a restoring force means that a resonant driving frequency (or frequencies) can exist at which the amplitude of the oscillation becomes large. In the classic example of LSPs, in

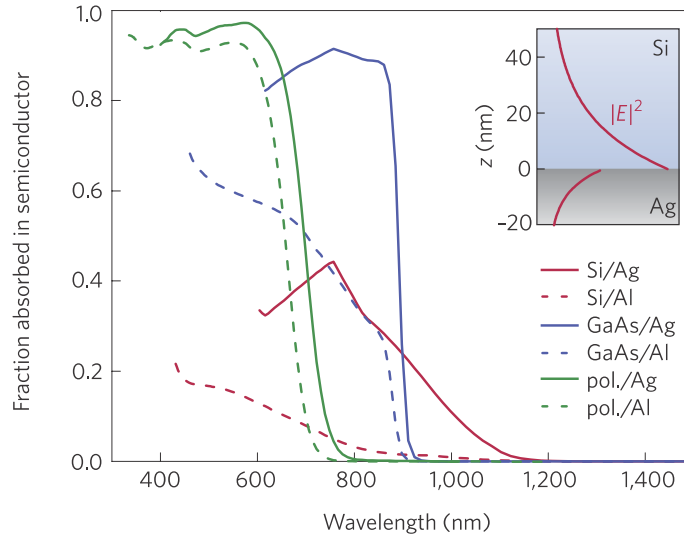


Figure 2.10: The fraction of SPP energy absorbed in a semiconductor adjacent to a metal surface. Shown is the fraction of the SPP energy absorbed in a film of silicon, gallium arsenide and organic polymer (PF10TBT:PCBM) adjacent to either a silver or aluminum film. The Taken from [34].

which a metallic nanoparticle is illuminated by an external field, enhanced absorption and or scattering can typically be observed at resonance.

The nanostructure geometry is critical to LSP excitation: the displaced electrons need to be spatially restricted in order for them to experience the restoring force of stationary positive charges, which is required to enable resonant oscillation. Below we present the formalism for obtaining the quasi-static approximation for the resonant frequency of a spherical particle in a uniform external electric field, following *Maier* [26]. We will find that this simple problem gives rise to dipole oscillation behavior with a single resonance.

Small particle, quasi-static approximation

Here we assume that the particle is sufficiently smaller than the wavelength of light ($2a \ll \lambda$, where a and λ are the particle radius and the wavelength of incident light, respectively) such that the electric field is uniform across the particle. Furthermore, we assume that the field changes slowly enough with time to allow a quasi-static treatment. The electric field is denoted as $\mathbf{E}_0 = E_0 \hat{z}$ and the dielectric constants of the sphere and the dielectric medium by ϵ and ϵ_d respectively. By solving the Laplace equation for the potential $\nabla^2 \Phi = 0$, the electric field E can be obtained via $\mathbf{E} = -\nabla \Phi$, defined separately for the inside and the outside of the sphere [26]:

$$\begin{aligned} \mathbf{E}_{\text{in}} &= \frac{3\varepsilon_d}{\varepsilon + 2\varepsilon_d} \mathbf{E}_0 \\ \mathbf{E}_{\text{out}} &= \mathbf{E}_0 + \frac{3\mathbf{n}(\mathbf{n} \cdot \mathbf{p}) - \mathbf{p}}{4\pi\varepsilon_0\varepsilon_d} \frac{1}{r^3} \end{aligned} \quad (2.19)$$

where \mathbf{r} is a radial vector from the center of the particle to a point P , θ is the angle subtended by \mathbf{r} and the z axis and ε_0 is the permittivity of free space. The field outside the sphere has been expressed as the sum of the contribution from the external field and a contribution from an induced dipole \mathbf{p} where

$$\mathbf{p} = 4\pi\varepsilon_0\varepsilon_d a^3 \frac{\varepsilon - \varepsilon_d}{\varepsilon + 2\varepsilon_d} \mathbf{E}_0 \quad (2.20)$$

Thus we observe that the external field induces a dipole moment in the sphere. If we further introduce the polarizability α via $\mathbf{p} = \varepsilon_0\varepsilon_d\alpha\mathbf{E}_0$, we can write:

$$\alpha = 4\pi a^3 \frac{\varepsilon - \varepsilon_d}{\varepsilon + 2\varepsilon_d} \quad (2.21)$$

This allows us to further express the scattering and absorption cross-sections of the sphere, C_{sca} and C_{abs} respectively, in terms of the polarizability (*Bohren and Huffman* [35]):

$$C_{sca} = \frac{k^4}{6\pi} |\alpha|^2 = \frac{2\pi^5}{3} \left(\frac{(2a)^6}{\lambda^4} \right) \left| \frac{\varepsilon - \varepsilon_d}{\varepsilon + 2\varepsilon_d} \right|^2 \quad (2.22)$$

$$C_{abs} = k \text{Im}(\alpha) = \pi^5 \left(\frac{(2a)^3}{\lambda} \right) \text{Im} \left(\frac{\varepsilon - \varepsilon_d}{\varepsilon + 2\varepsilon_d} \right) \quad (2.23)$$

where k is the magnitude of the wave vector of the incident light. We note that the polarizability becomes large when $|\varepsilon + 2\varepsilon_d|$ is a minimum, or, in other words, (for small or slowly-varying $\text{Im}(\varepsilon)$), when:

$$\text{Re}(\varepsilon(\omega)) = -2\varepsilon_d \quad (2.24)$$

This is known as the Fröhlich condition. We note that up until now, no restrictions on the dielectric constant of the sphere ε have been made. If the medium surrounding the sphere is an ordinary dielectric material, then ε_d is positive and the real part of ε must be negative to satisfy this condition. Obviously, it cannot be met by a dielectric sphere in a dielectric medium. However, a number of metals do have dielectric constants which exhibit negative real

parts at optical/near-optical wavelengths and hence there exists a resonance wavelength where α becomes large. At this wavelength, resonant values in C_{sca} and C_{ab} can be observed. This is known as the localized plasmon resonance.

As is obvious from the Fröhlich condition, the resonance wavelength is sensitive to the dielectric environment. This gives metallic nanoparticles great application as optical sensors of changes in local refractive index.

Beyond the small particle, quasi-static approximation

In order to extend beyond the small particle, quasi-static approximation, the Mie solutions to Maxwell's equations are required (see [36] for details). This allows a treatment of arbitrary excitation frequencies and particle sizes. The Mie solution for the scattering and absorption coefficients can be expressed as a power series. The small particle results (Equations 2.22 and 2.23) are recovered by retaining only the first term. Mie theory can also be used to treat spherical particles with arbitrary shells (e.g. dielectric coatings), which can be used to tune the plasmonic resonance.

2.3.4 Void plasmons

It is possible to use Eq. 2.24 to treat quasistatic void geometries. If we consider a spherical dielectric void in a metallic film, we can simply make the substitutions $\epsilon \rightarrow \epsilon_d$ and $\epsilon_d \rightarrow \epsilon$ in Eq. 2.21 to obtain the Fröhlich condition for voids:

$$\text{Re}(\epsilon(\omega)) = -\frac{1}{2}\epsilon_d \quad (2.25)$$

More complicated void geometries require individual treatment. A simple model of LSP excitation (non-propagating plasmonic mode) on voids treats the LSP as a SPP mode bound within the void. This leads to the formation of a standing SPP wave with nodes at the void rim where the wave is reflected. This model leads to good agreement with experimental data. [37]

A well-studied geometry is the so-called truncated nanovoid array (Fig. 2.11(a)), on which SPPs, LSPs and hybrids of the two can be excited. [37] SPP excitation is achieved via grating coupling (Sec. 2.3.2) whereas localized void plasmons couple easily to incident light. The angle-dependence of grating-coupled SPPs (Eq. 2.16) permits identification in experiments where the reflection from nanostructured surfaces is measured at different angles of incidence. This technique, described in Sec. 3.3.2, is used to characterize nanostructured solar cell architectures in this work.

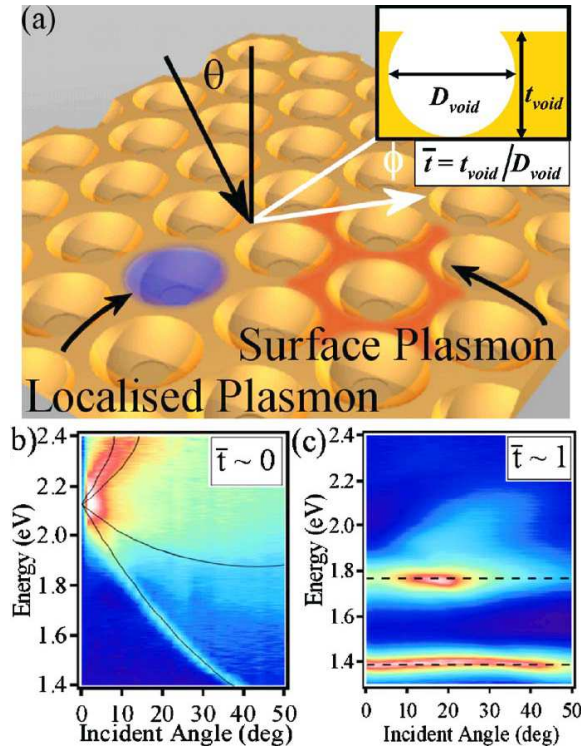


Figure 2.11: Localized plasmon (LSP) and surface plasmon (SPP) excitation on a nanovoid array. (a) A schematic of a nanovoid array showing LSP excitation within a void and SPP propagation along the planar inter-void space. The void geometry can be quantified by the normalized void depth \bar{t} . (b-c) Reflectivity spectra for incidence angle θ between 0 and 50° . Dark-blue corresponds to high reflection and red-white corresponds to low reflection (high absorption). (b) When $\bar{t} \sim 0$ the voids are shallow, promoting excitation of SPPs that are grating-coupled and therefore highly dependent on the photon incidence angle. (c) When $\bar{t} \sim 1$ the voids are almost completely sealed and LSP excitation is favored. LSPs on metallic nanovoids exhibit spectra that are largely independent of incident angle. Taken from [37]

Light-trapping with LSPs

Just as with the case of SPPs, the electric field of a LSP mode is partially distributed within the metal and partially in the surrounding dielectric. For small particles, the strength of these fields are given by Eq. 2.19. As expected, these fields are heavily dependent on the dielectric constants of the metal and the dielectric. If the surrounding dielectric is an absorbing material, such as an organic semiconductor, the absorption in this material is obtained using Eq. 6.3. Again, the high absorptivity of organic semiconductors promotes high dissipation of LSP energy in the organic semiconductor. This fraction will be calculated explicitly in Chap. 9 for a system in which scattering and LSP excitation is found to enable significant light-trapping.

2.4 Light-trapping in thin-film solar cells

2.4.1 Highly absorbing organic solar cells

Similar to most typical thin-film solar cells, organic solar cells suffer limited absorption. Unlike in inorganic CdTe or CIGS (Cu(In,G)Se_2) devices, where a major driving factor in using thin-films is to minimize costs, organic devices tend to feature thin-films out of necessity. As mentioned in Sec. 2.2, efficient charge transport in bulk heterojunctions is only possible if contiguous pathways for both charge-carriers in their respective phases (donor and acceptor) exist. Naturally, the existence of these pathways is less likely for thicker films. In addition, electrons and holes exhibit reduced transport lengths in organic semiconductors (compared to in silicon) due to the limitations in hopping transport. As a result, semiconductor thicknesses in optimized organic devices are typically around 100 nm or less (see Sec. 2.2).

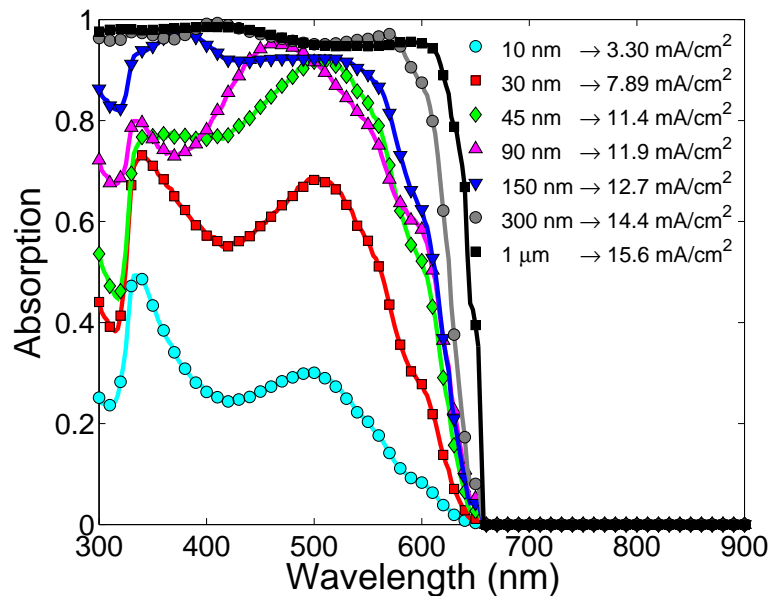


Figure 2.12: The absorption, and hence the maximum current that can be theoretically extracted, is limited in thin-film solar cells. Shown is the absorption in a P3HT:PCBM film of thickness between 10 nm and 1 μm in the following architecture: glass-P3HT:PCBM-silver. The maximum theoretical short-circuit current density $J_{SC_{max}}$ under AM1.5G illumination is indicated.

Figure 2.12 demonstrates the limited absorption that can be expected in thin films of P3HT:PCBM, mixed 1:1 by weight. The absorption spectra are obtained by performing finite element simulations (a technique that will be introduced in Chap. 4) of a P3HT:PCBM film located between a thick layer of glass ($\epsilon_{\text{glass}} = 1.96$) and a reflective silver film with light incidence from the

glass side. The optical constants of P3HT:PCBM and silver that are used for this calculation are experimentally determined. [38] [27] The general routine will be described in more detail later in this thesis.

We first note that the absorption drops sharply at around 650 nm for all layer thicknesses. This can be considered to be the effective band-gap of a P3HT:PCBM film. Photons of wavelength 650 nm or higher have insufficient energy to excite delocalized electrons into higher orbitals along the organic molecules and create excitons - the absorption of the film is zero regardless of the layer thickness. It is an ongoing challenge for the photovoltaic community (both organic and inorganic semiconductors) to fabricate materials with a broader absorption response.⁶ The absorption responsivity of state-of-the-art organic semiconductors such as the combination DTS(PTTh₂)₂:PC₇₀BM spans from 300 nm to around 1000 nm [23].

The maximum theoretical short-circuit current density, J_{SCmax} under AM1.5G illumination is also shown in Fig. 2.12. This is obtained directly from the absorption spectra with the assumption that every absorbed photon results in an electron delivered to the external circuit. These numbers compare well with calculations in the literature for a similar layer structure. [6] The short-circuit current density is the maximum current that flows through the device under the assumption of infinite shunt resistance (see Sec. 2.1). It is stressed that these values represent a theoretical maximum - recombination in the device will act to reduce this value. Furthermore, this simple model does not include additional layers which are present in working devices (such as a transparent electrode and interfacial layers), which would introduce additional optical losses and modify interference effects in the device.

Although organic semiconductors can absorb light very effectively the absorption coefficient is evidently not high enough to achieve complete absorption for layers of thickness < 100 nm. The J_{SCmax} for a 90 nm film is 11.9 mA/cm², which is almost 25% lower than the J_{SCmax} for a 1 μ m film. In other words, if poor charge transport dictates that the thickness of the film must be 90 nm or lower, the penalty is a 25% reduction in J_{SCmax} . We seek to implement light-trapping

⁶However, we note there is an added level of complexity associated with the design of more absorbing semiconductors. In order to increase the absorption at infra-red wavelengths, the semiconductor band-gap (for example, of one of the blend components) must be reduced. As all photons with energy greater than the band-gap energy can be absorbed, a reduction of the band gap results in an increase of the absorption response, but it also introduces additional loss. This loss has to do with the thermal relaxation of electrons: excited electrons, after gaining the energy of an absorbed photon, drop in energy back to the LUMO (in the case of organics) or conduction band (in the case of crystalline solar cells, with an accompanying loss of energy). Therefore, by reducing the band-gap, this energy loss channel is increased. The theoretical optimal band-gap for solar cells is 1.1 eV (corresponding to an absorption edge of 1100 nm). [39]. A consequence of this limitation is that the absorption edge of a semiconductor with an ideal band-gap lies in a spectral region of significant solar insolation. As the semiconductor absorption naturally becomes vanishingly small near the band-gap, light-trapping will always find application to counteract this. Electronic excitations arising from the absorption of near-band-gap photons suffer the smallest thermal relaxation loss when dropping back down to the LUMO/conduction band.

in thin-film organic devices with the goal of removing this limitation in absorption and hence J_{SCmax} , and consequently, power conversion efficiency.

2.4.2 How much can be gained?

In simple terms, light-trapping is ensuring that light, once having entered the semiconductor film, doesn't get out again. An important question is the maximum absorption enhancement via light-trapping permitted by the rules of thermodynamics. As predicted by Yablonovitch in 1982 for the ray optics regime [40], this value is $4n^2$, where n is the refractive index of the film in question. An important qualifier is that ergodic conditions must prevail: all of the occupied electromagnetic modes (states) within the film within a small frequency range must be equally occupied under steady-state conditions. In order to achieve these conditions, a structured interface which scatters incident light equally into all available modes is suggested. In addition, this value holds only for sufficiently thick films (see [41] for a discussion what constitutes a sufficiently thick film), as the density-of-states of an infinite dielectric is assumed in the derivation.

However, this limit can be exceeded. Callahan et al. argue that this is possible in systems which have local density of optical states (LDOS) greater than that considered in the ergodic limit. [42] Essentially, if additional states are made available to the radiation in the film, then the energy density and hence the absorption will increase. An elegant example of this is seen when the film is placed adjacent to a metallic surface - new states (SPP modes) become available for occupation. Under these conditions, photons in trapped states in the film can enter surface states (SPPs), bound to the metal interface. At frequencies sufficiently below the surface plasmon frequency, the maximum absorption enhancement that can be expected is $4n^2 + n\lambda/h$ where h is the film thickness. [43]

The same is true for the introduction of LSP and cavity modes, a system which has recently been investigated by Callahan et al. (Fig. 2.13). As can be seen, the absorption of an isolated 10 nm slab of P3HT:PCBM in air is limited at these (near-band-gap) wavelengths (yellow dotted line). Under ergodic light-trapping conditions, the absorption can be significantly increased. The absorption for the depicted plasmonic resonator structure, calculated via FDTD (finite difference time domain) simulation, greatly exceeds that of the slab in air and also exceeds the ergodic limit at some wavelengths.

One of the central aims of this thesis is to identify and fabricate light-trapping structures that will improve the absorption in organic films, just as we observe in Fig. 2.13. We investigate a large range of geometries and consistently demonstrate, both experimentally and using simulation, the ability to significantly improve the absorption in organic films over planar architec-

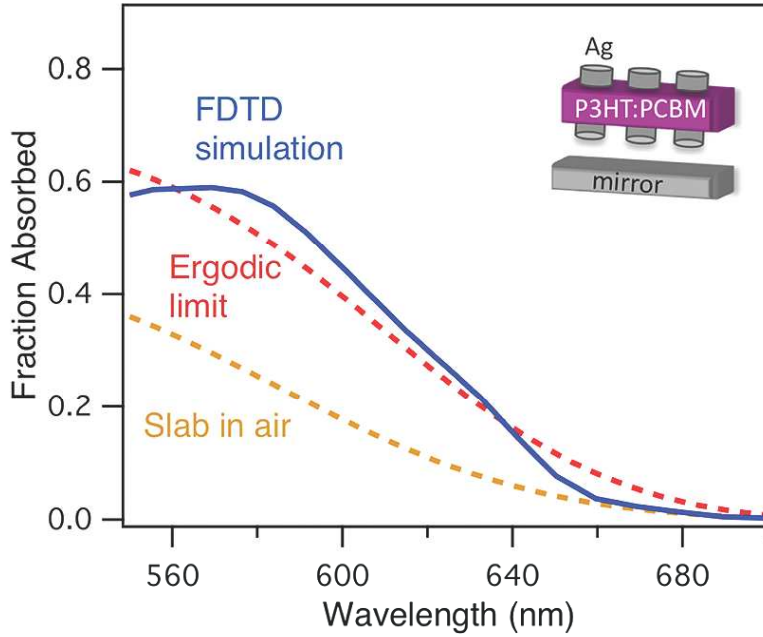


Figure 2.13: The ergodic limit of absorption of a slab of P3HT:PCBM, shown with the absorption of a slab in air and the simulated plasmonic resonator light-trapping system. The ergodic limit is exceeded by the FDTD (finite difference time domain)-simulated resonator in the 560-640 nm wavelength range. This corresponds to near-band-gap light, where P3HT:PCBM absorbs poorly. Taken from [42].

tures. Enhancements in absorption in the semiconductor as high as 19% across the wavelength range of 350-1000 nm are found (see Sec. 9). In the next section, we discuss the extent to which this enhanced absorption can be converted to an enhanced power conversion efficiency.

2.4.3 The connection between enhanced absorption and enhanced efficiency

In this section we wish to discuss the quantitative extent to which an improved absorption can lead to an improved efficiency. We consider that the implementation of a light-trapping system leads to an increase in the semiconductor absorption from A to A' . We assume that the relative increase in generated excitons is equal to the relative increase in absorbed photons and that the excitons are converted to electrons in the collected current with the same efficiency as without the light-trapping system. Under these conditions, the relative increase in the J_{SC} is given by:

$$\frac{J'_{SC}}{J_{SC}} = \frac{A'}{A} \quad (2.26)$$

Further assuming that the $FF' = FF$ and $V'_{OC} = V_{OC}$,⁷ Eq. 2.7 gives:

$$\frac{\eta'}{\eta} = \frac{J'_{SC}}{J_{SC}} = \frac{A'}{A} \quad (2.27)$$

Therefore, under these assumptions, the relative increase in the solar cell efficiency is equal to the relative increase in the absorption in the semiconductor. However, there are a number of conditions that need to be met if this is to hold, especially for organic solar cells.

An important question is the effect of light-trapping on exciton generation and separation. The interaction of excitons with plasmons in plasmonic solar cells is of particular importance, given the well-documented tendency of plasmons and excitons to couple [44, 45]. If a metallic nanostructure were to enhance exciton generation and yet simultaneously induce excitonic quenching⁸ then the presence of the metallic nanostructure would have the effect of increasing the absorption yet decreasing the efficiency. In this case, Eq. 2.27 would not hold. However, as shown by Kulkarni et al. [46], enhanced absorption in P3HT:PCBM films via near-field absorption enhancement can indeed lead to enhanced generation of long-lived charges. Therefore, there is no fundamental limitation which prevents plasmonic light-trapping from leading to enhanced free charge generation and hence to an enhanced efficiency.

Although Kulkarni et al. found that the charge yield increased linearly over an extended range of illumination intensities, it is expected that exciton annihilation [17] will become important at high generation densities. This is an important consideration for plasmonic light-trapping, where absorption enhancement is typically localized at the metallic interface. Exciton annihilation, in which the energy of one exciton is transferred to another upon annihilation (occurring at a separation distance of the order of nanometers), can be expected to lead to saturated charge generation in these regions, similar to the saturation of radiative excitonic decay in experiments where the illumination intensity is varied. [17]

Further studies are required to better understand the effects of highly localized absorption in organic solar cells. However, the performance of solar cells under illumination levels greater than one sun provides us with a good insight. Concentrated sunlight of up to multiple hundreds of suns is routinely used to achieve high power conversion efficiencies in inorganic solar cells. Organic solar cells can be operated under concentrated sunlight as well, but recent studies of P3HT:PCBM inverted cells have shown that the power conversion efficiency decreases signif-

⁷ The validity of this assumption is highly dependent on the quality of the solar cell. Setting $J = 0$ in Eq. 2.5, for $R_{sh} \rightarrow \infty$ and $R_s = 0$, we obtain $V_{OC} \approx \frac{kT}{q} \ln\left(\frac{J_{ph}}{J_0}\right)$. Therefore, for an ideal solar cell, we expect the the open-circuit voltage should actually increase with the current density, and not just stay constant.

⁸ Annihilation of an exciton, e.g. via non-radiative transfer of energy to a metal, see Sec. 7.3

icantly for illuminations of 10 suns or more. [47] Recombination seems to be the source of the decrease in performance, as the fill-factor undergoes a strong reduction despite the J_{SC} and V_{OC} increasing.

Importantly, however, the efficiency does remain relatively constant under illumination levels of 0.1-2.5 suns. This results are incredibly promising for the implementation of light trapping in organic solar cells, as they demonstrate that even for large absorption rates corresponding to that of up to 2.5 suns, the steps (ii-vi) of current generation (Sec. 2.2) still occur efficiently. Therefore, as a first approximation, Eq. 2.27 should hold for moderate absorption enhancements. We return to this point in Sec. 8.3 and discuss it for the magnitude of absorption enhancement that we observe.

2.5 Prominent light-trapping architectures

The following section is an updated version of my contribution to the review article *Weickert, Dunbar et al. Advanced Materials, 2011*. [48]

This section will review recent attempts to design nanostructures in thin-film solar cells that give rise to increased performance due to novel methods of light-trapping.

Light trapping constructions of various forms have been considered in the literature, and the interested reader is directed to the literature to read recent results on distributed Bragg reflectors [49] and on macroscopic structures such as lenses, microcavities and Winston cones [50–52] We will here however, limit our focus to two nanostructure-based light trapping approaches that are receiving current attention in organic photovoltaics: scattering dielectric structures and plasmonics. We also draw from results from the fields of dye-sensitized and inorganic solar cells to put the progress in organic solar cells in perspective.

2.5.1 Scattering dielectric structures

Promoting wide-angle scattering into the absorbing layers in solar cells is a robust way of increasing the optical path length and hence absorption of the light. The geometry of the scattering object plays a critical role in determining the intensity and angular distribution of the scattered radiation. For the regime $d < \lambda$, where $d = 2a$ is the diameter of the scattering object and λ the wavelength of incident light, the scattering and absorption cross-sections, C_{sca} and C_{ab} , are given by Equations 2.22 and 2.23, respectively. The scattering cross section is proportional to the particle diameter raised to the sixth power - highlighting the importance of the particle size. As in the case for scattering bodies embedded in solar cells, where absorption in

the scattering body may be an unwanted effect, it is often desirable to have scattering dominant interactions, i.e. it is desirable to ensure the ratio $Q = C_{sca}/C_{abs}$ is maximized. For particles of diameter $d \approx \lambda$ or $d > \lambda$, the Mie solution [36] to Maxwell's equations is required to provide an adequate description of the scattering.

In silicon solar cells, front electrodes featuring textured interfaces with a roughness of the order of several hundred nm have been successfully implemented to achieve light trapping. [53] The roughness of the interfaces, which could be controlled through an etching process, determines the feature size and spacing, and hence the scattering properties. In dye-sensitized solar cells (DSSCs), favorable light scattering can be achieved by exerting control over the titanium dioxide nanoparticles in the active layer. Conventional titanium dioxide electrodes used in this cell type have a nanocrystalline porous morphology obtained by sintering colloids of nanoparticles with sizes less than 30nm. [54] The optical scattering of particles of this size is negligible as the scattering cross-section is small compared to the geometric cross-section (easily shown using Eq. 2.22). That is also evident from the characteristic transparency of DSSCs, which demonstrates coherent propagation of light through the device. This would not be possible in the presence of significant scattering, which is non-coherent for randomly distributed particles. The scattering of optical light can be increased upon the introduction of large diameter (50 and 100nm) TiO₂ nanoparticles into the electrode, as shown by Wang et al.. [55] They were able to increase the power efficiency of a reference cell from 7.6 to 9.77 % by constructing TiO₂ electrodes that consisted of various nanoparticle sizes deposited in multiple layers. The larger particles, which scatter most strongly, were placed deeper into the electrode, to ensure that back-scattered radiation would not be lost through the front surface, but would be able to be absorbed by the intervening layers.

This concept has also been extended to scattering bodies of other shapes. Increased power conversion efficiency has been reported for DSSCs that have highly-scattering anatase nanorods or nanotubes incorporated into the standard nanocrystalline electrodes. [56] Regardless of the shape of the scatterer, the potential improvement obtainable by this approach is determined by a trade-off between the surface area of the porous electrode and the corresponding scattering capability. While larger particles provide more efficient scattering, they also have a reduced surface area which limits the amount of dye that can be adsorbed onto the surface of the electrode and therefore the light absorption. In organic solar cells, scattering with metallic nanoparticles has been more earnestly pursued. We will describe these developments in the next section.

2.5.2 Plasmonic light-trapping

This section addresses the results of recent attempts to harness the potential of Surface Plasmons (SPs) to achieve light trapping. The typical metals of choice for the excitation of SPs are Au, Ag, Al and Cu. Both SPPs and LSPs can give rise to near-field enhancement of electromagnetic radiation, and LSPs in particular can give rise to strong resonant light scattering. It is for these reasons that plasmonic solar cells are gaining a great deal of attention from research groups seeking to demonstrate light trapping in solar cells. [34, 57] Previous reports of plasmonic light trapping in organic solar cells have in general been based on one of three excitation geometries: external scattering metal nanoparticles, dispersed metal nanoparticles and nanostructured electrodes. The following sections will address each of these geometries in turn.

External scattering metal nanoparticles

Favorable plasmonic in-coupling of scattered light from an external layer of metallic nanoparticles into the absorbing medium in solar cells has been reported across multiple solar cell types. In a typical configuration, Ag or Au nanoparticles are deposited onto the front surface of the solar cell, either embedded into the front electrode or electronically isolated by an intermediate transparent dielectric layer. By selecting nanoparticle sizes that are favorable for scattering (of the order of 100 nm) and an appropriate nanoparticle area coverage, scattering can increase the light's path length in the absorbing medium. As a result, the light absorption can be improved, along with its power conversion efficiency. This configuration has been used to demonstrate photocurrent enhancements in thin-film silicon solar cells [58] and efficiency enhancements in gallium arsenide [59] and amorphous silicon [60] solar cells.

This light trapping mechanism has been implemented into organic solar cells with similar success. Enhancements in the power conversion efficiency compared to control devices have been reported by a number of groups. [61–64] Although the synthesis and deposition of the metal nanoparticles vary, all of the authors reported cells with Ag or Au nanoparticles embedded in a layer of PEDOT:PSS deposited on the ITO (tin-oxide doped indium-oxide) electrode. However, it is often difficult to confidently attribute photocurrent enhancements to plasmonic effects alone, and more consideration of the role of other effects such as the improved series resistance (due to the incorporation of Ag in ITO electrodes) [65] is required.

One important consideration is the role played by the order of the scattering bodies. Methods of depositing scattering particles with highly-ordered geometries [59, 65] are promising avenues to improve upon the performance of previously reported organic plasmonic devices

(see Table 2), which feature completely disordered arrays of scattering particles. Not only do highly ordered arrays offer the benefit of hosting additional, order-sensitive electromagnetic modes [66], but they are also more suitable candidates for simulation.

The approach of depositing nanoparticles onto the front electrode can also be extended to realize structures that promote the propagation of nanocavity modes within the organic layer. [67] In this configuration the front electrode is patterned by an array of 250 nm wide Ag stripes. The light scattered from the stripes then becomes confined in the space between the stripes and the opposing electrode. An increase in conversion efficiency was reported for test micrometer scale devices incorporating these electrodes.

In addition to coupling incident light to cavity modes, which travel in a direction perpendicular to the device plane, it is also possible to excite waveguide modes which propagate in the active layer parallel to the device plane. Arrays of Ag stripes oriented on the front electrode can also act as a suitable excitation geometry for this purpose, with efficient scattering into waveguide modes possible in addition to the near field enhancement. [68] Simulations indicate that photocurrent enhancements of up to 43 % are possible for thin-film silicon cells. In a study of a similar geometry for amorphous silicon cells [69], large enhancements in absorption were also predicted, citing large enhancements due to near-field plasmonic enhancement for TM excitation, and coupling to waveguide modes for both TE and TM excitation. Although the excitation of waveguide modes in 3D nanowire DSSCs has been considered [70], there have been no reports on waveguide excitation using metal nanostructures in either hybrid or organic solar cells to the best of our knowledge.

Dispersed nanoparticles

An alternative construction features metallic nanoparticles dispersed in the active layer itself, rather than situated on the electrode. In this configuration a number of additional processes must be considered. In comparison to the external scattering layer devices, back-scattering as well as forward scattering may lead to enhanced absorption in the active layer. A second important process is the LSP near-field enhancement of the electromagnetic field which may give rise to an absorption enhancement in the active material immediately surrounding the nanoparticles. A third important process is the charge recombination at the metal-organic interface, which must be minimized in order for the incorporation of the nanoparticles to have a net positive effect on the power conversion efficiency. In order to prevent dispersed metallic particles as acting as recombination centers within the active layer, coatings of insulating materials are recommended. [71, 72]

Interestingly, however, two recent publications from the *Heeger* group demonstrate considerable efficiency enhancements using un-coated gold [73] and silver [74] nanoparticles. Given that the FF of the PSCs is greater than that of the reference devices, no evidence is found that the metallic NPs act like recombination centers. The authors attribute the enhanced efficiencies to enhanced scattering and improved charge transport respectively - not to enhanced absorption due to LSP field enhancement. This is significant, as this effect has arguably been one of the motivations driving research for this device type. [65, 75, 76]

Simulations of metallic nanoparticles dispersed in organic films can estimate the maximum possible enhancement that can be provided by this light trapping configuration. One study reported absorption enhancements of the order of 1.5 for devices made from P3HT:PCBM featuring an array of 23 nm diameter nanoparticles with a spacing of 40 nm in a film. [75] The shape of the metallic nanoparticle has a large influence on its interaction with light. A recent study used nanoprisms as metallic additives to the active layer, in place of the conventional spherical nanoparticles. [46] Nanoprisms have the advantage that their plasmon resonances are highly tunable within the visible and near infra-red wavelengths. [77] This could enable tuning of the plasmonic resonance to optimize absorption enhancement for any given active material.

High efficiency “plasmonic tandem cells” have also been reported recently [78], following on from the first report in 2004. [72] The authors claim the 20% enhancement in efficiency from 5.22% to 6.24% is due to LSP near field absorption enhancement.

Structured electrodes

In a third geometry, plasmonic modes are directly excited on metallic (back) electrodes in solar cells. In order to achieve excitation from normally incident solar radiation, the electrode can be structured with either ordered features such as nanowires (Fig. 2.14) or random irregularities. Light scattered from these features can then be coupled to propagating SPPs at the interface between the semiconductor and the metallic electrode. The electromagnetic energy transferred to these SPPs is essentially “trapped” traveling parallel to the plane of the device, promoting enhanced absorption in the semiconductor layer. Calculations for a PF10TBT: PC60BM-Ag interface give the promising result that the bulk of the energy density of the SPP is absorbed in the semiconductor layer, corresponding to a low energy loss due ohmic damping of the mode in the Ag layer. [34] Ohmic damping of plasmonic modes in silver electrodes can also be reduced by using appropriately chosen dielectric layers between the semiconductor and the electrode. [79]

In addition, LSPs can also be excited in transverse and longitudinal directions along metal nanowires. [80] Similar to the case of the LSPs excited on metallic nanoparticles dispersed in

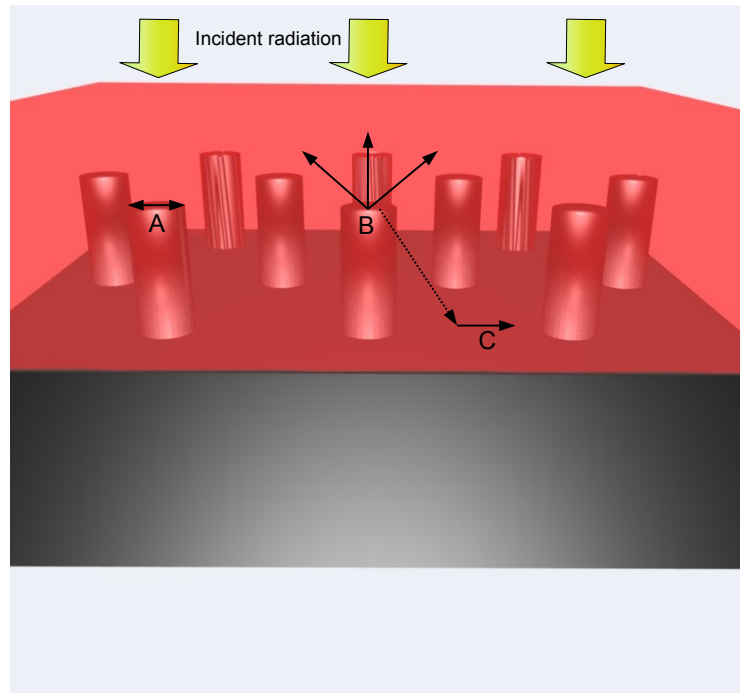


Figure 2.14: A semiconductor film deposited on a structured electrode, which consists of an array of free-standing metallic nanowires on a dense metal film. Light trapping can be achieved in the semiconductor film as a result of mechanisms such as A: excitation of Localized Surface Plasmons (LSPs) on the metal nanostructure, B: light scattering from sub-wavelength features and C: excitation (from scattered radiation) of Surface Plasmon Polaritons (SPPs).

the active layer from section 2.5.2, the plasmonic near field enhancement due to the LSP and SPP modes on structured electrodes have the potential to lead to significant enhancements in absorption in the active layer.

Structured metallic electrodes have been considered in inorganic solar cells [53, 81, 82] and they are also receiving increased attention from organic photovoltaic researchers. Sinusoidal Ca/Al electrodes have been shown to increase the conversion efficiency for P3HT:PC60BM cells [83][182], the improvement attributed to diffraction grating properties of the electrode. Higher order diffracted modes with larger angles of diffraction have increased path lengths in the active layer, with the possibility for total internal reflection at the active layer-front electrode interface. In another study, a device was constructed using a periodic Al grating with a height of 50nm and a period of 277 nm as the back electrode. [84] The enhancement in

2.6 Summarizing remarks

photocurrent was attributed to near-field plasmonic enhancement of the electromagnetic field at the metal-organic interface.

Simulations have given some insight to the light coupling that can occur at structured electrodes. For a given geometry, the amount of light coupled to SPPs, waveguide modes and Fabry-Pérot resonances can be calculated using the Finite Difference Time Domain method. [82]

Devices that are constructed by depositing active layers on top of a pre-structured electrode or substrate have the benefit that all of the subsequent layers adopt the structure of the underlying layer. Improved performance has been reported for such cells, whose authors cite favorable scattering into guided modes within the cell as a large contributing factor towards the enhancement. [85, 86]

Summary of prominent light-trapping architectures

Some notable reports of organic solar cell architectures featuring metallic nanostructures, covered in the previous paragraphs, are summarized in Tab. 2.2. All authors report a significant efficiency enhancement, primarily due to an enhancement in the J_{SC} . We note that not all of the enhancements are attributed to plasmonic effects. This highlights the benefits that metallic nanostructures can provide in solar cells, namely (non-resonant) scattering [83] and enhanced charge transport [74]. The effects of metallic nanostructures in organic solar cells, both plasmonic and otherwise, will be discussed throughout this thesis.

2.6 Summarizing remarks

In this chapter, we have presented vital information that we will need for the rest of this thesis. The fundamentals of solar cells, especially organic solar cells, have been outlined. A description of plasmonics followed. We have discussed how it is possible, via plasmonics or otherwise, to achieve high absorbing thin-film solar cells, and what special considerations need to be made for organic solar cells. The survey of the literature of light-trapping in thin-film solar cells has introduced the wide variety of ways to trap light. In the following chapter, we will describe the fabrication and characterization of plasmonic solar cells carried out in this research.

PSC	Org. semiconductors	Geom.	J_{SC} (mA/cm ²)	V_{OC} (V)	FF	η (%)	Effect	Ref.
In-scat. NPs	P3HT:PCBM	a	10.2 (9.2)	0.59 (0.59)	0.70 (0.66)	4.2 (3.6)	b	[61]
Disp. NPs	PCDTBT:PC ₇₀ BM	c	11.6 (10.8)	- (0.86)	0.69 (0.68)	7.1 (6.3)	d	[74]
Disp. NPs	PCDTBT:PC ₇₀ BM	e	11.2 (-)	0.89 (-)	0.65 (0.64)	6.5 (5.8)	f	[73]
Struc. elec.	P3HT:PCBM	g	10.9 (9.5)	0.62 (0.61)	0.64 (0.62)	4.3 (3.6)	h	[83]

a = 45 nm Au particles in external PEDOT:PSS layer

b = absorption enhancement via LSP excitation and enhanced exciton dissociation.

c = clusters of 40 nm Ag particles.

d = improved charge transport.

e = 70 nm Au particles.

f = enhanced scattering.

g = Ca/Al 2D relief grating pitch=500 nm, height \approx 20 nm.

h = enhanced scattering (diffraction modes).

Table 2.2: Notable reports of organic solar cells with enhanced efficiency due to metallic nanostructures. A selection of reports of in-scattering NP, dispersed NP and structured electrode plasmonic solar cells (PSCs). All devices are single-junction bulk heterojunctions - the blend of organic semiconductors used is indicated. Also shown is the geometry of the metallic structure and the effect to which the authors attribute the enhanced efficiency. A dash indicates that the value was not provided.

2.6 Summarizing remarks

3 Experimental Techniques

In the previous chapter, important background concepts for light-trapping in thin-film, especially organic, solar cells were outlined. In this chapter, we describe the fabrication of bulk heterojunction organic solar cells. We fabricate both planar reference devices (Section 3.1) and nanostructured electrode devices featuring a nanovoid array interface between the metallic electrode and the organic semiconductor film (Section 3.2). We will demonstrate in subsequent chapters that these nanostructured electrodes exhibit excellent light-trapping capabilities. The development of the technique used to fabricate nanostructured electrode organic solar cells represents one of the important results of this work. This low-cost technique can be used to generate large-area ordered metallic nanostructures in a semi-controlled way. To conclude the chapter, a description of the sample and device characterization methods is presented (Section 3.3).

3.1 Fabrication of organic solar cells

We begin with a description of the fabrication of reference (no light-trapping) solar cells with planar electrodes. The processes steps to deposit the layers that constitute the device in Fig. 3.1(a) are outlined below:

Substrate preparation

Devices are fabricated on quartz substrates (2 cm^2 , thickness 1.1 mm) which are purchased with a 100-200 nm coating of tin-doped indium oxide (ITO - In_2O_3 doped with SnO_2). The sheet resistance quoted by the manufacturer, *Kintec technologies*, is $10 \Omega/\text{sq}$. The quartz used for the substrate is stable at temperatures exceeding 500°C . The ITO film is the solar cell's cathode - it will collect electrons when the device is operating at its maximum power point. It is important that the ITO film is as transparent as possible at optical wavelengths, as light will be required to pass through the film to reach the semiconductor layer (Fig. 3.1).

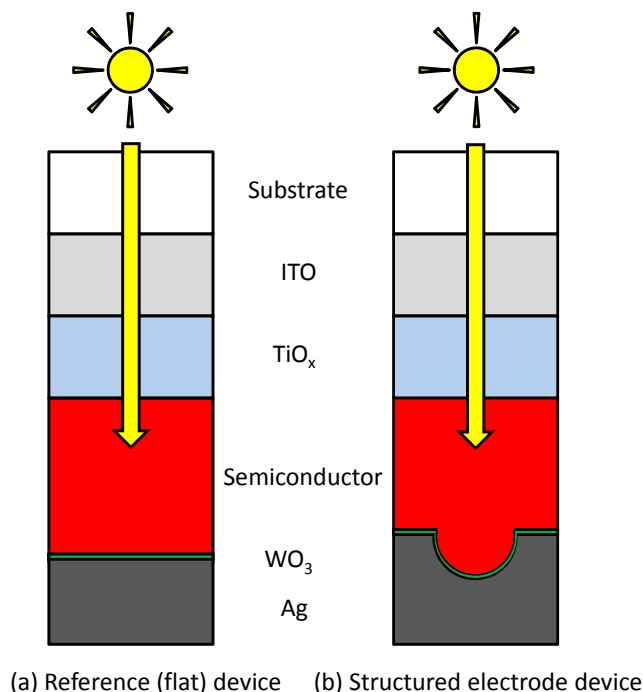


Figure 3.1: A schematic of the layer structure of the reference and structured electrode solar cells fabricated. The structured electrode device (b) is fabricated in an identical procedure to (a) the reference device, with an additional semiconductor imprinting step.

The ITO-coated substrates then undergo three thirty-minute cleaning steps in an ultrasonic bath: in distilled water with detergent, acetone and then finally isopropanol. The substrates are then dried with a stream of N_2 and further cleaned of any remaining loosely-bound impurities (such as organic molecules) in an O_2 plasma for 7 minutes. The substrates are then immediately transferred to a high vacuum sputter coater (typical base pressure 5×10^{-8} mbar) for TiO_x deposition.

Deposition of TiO_x layers

The next layer is known as an interfacial layer. It has the function of preventing direct contact between the electron donor and the cathode and therefore prevent recombination-inducing holes from reaching the cathode. TiO_2 is a commonly used hole-blocking layer [87] as the location of its orbitals inhibit hole transfer from most common organic materials.

Once inside the sputter coater, the substrates are further cleaned under vacuum using a 2-minute heat lamp treatment at 200°C. A film of approximately 80 nm is then deposited at 100 W at a process pressure of 6.7×10^{-3} mbar for one hour at room temperature using a TiO₂ target (99.99% purity) from *Testbourne materials*. Argon is used as the sputtering gas. The substrates are then removed and are heated at 450°C for 1 hour in air to improve the crystallinity of the film. This heat treatment has a rise and fall time of 1 hour and 10 hours respectively. The stoichiometry of the resulting film has not been determined. The TiO_x process parameters have been tailored towards producing films with optimal interfacial layer (hole-blocking) properties for our devices specifically.

Deposition of organic semiconductor

A bulk heterojunction organic semiconductor film is then applied.

The TiO_x-ITO-glass samples are then cleaned in ethanol in an ultrasonic bath for 10 minutes, dried with a stream of N₂ and heated at 110°C for 10 minutes to remove any water adsorbed onto the TiO_x surface. The samples are then allowed to cool to room temperature. A solution consisting of a mixture of electron donor and electron acceptor material dissolved in a mutual solvent is then spin-coated onto the TiO_x surface at 1000 rpm in air. A standard solution is a 1:0.8 mixture per weight of P3HT and PCBM, obtained by combining P3HT (30mg/ml) and PCBM (24mg/ml) solutions, where the solvent in each case is chlorobenzene. The components are prepared separately, and mixed overnight using an automated shaker. Equal volumes of two components are then blended, and the blend solution is shaken for a further hour. 50 μl of this solution is spin-coated onto each substrate. Under these conditions, P3HT:PCBM layers of thickness 100 nm result.

Deposition of WO₃ layer and top electrode

The WO₃ layer has the opposite function to the TiO_x layer - it serves as an electron-blocking layer between the bulk heterojunction film and the silver electrode (anode). It also serves as an exciton-blocking layer: excitons in the organic film are unable to diffuse to the metal electrode where metal-induced quenching could possibly occur (discussed in more detail in Chap. 7).

The organic semiconductor-TiO_x-ITO-glass samples are then transferred to a thermal evaporation deposition system. Upon pumping down to a base pressure of 8×10^{-6} mbar, 5 nm of WO₃ and 150 nm of Ag are evaporated without an intermediate vacuum break. Three separate solar cell devices are fabricated on each substrate by evaporating three electrically isolated electrodes onto the organic film.

Annealing

The completed devices are then transferred to a nitrogen atmosphere where they are heated on a hot plate (annealed) for 5 minutes at 140°C and then allowed to cool slowly. This step promotes alignment of P3HT chains [88], thereby improving the absorption and charge transport properties in the device (see [89]).

The resulting bulk heterojunction solar cells typically exhibit power conversion efficiencies of 1-2%, similar to comparable devices in the literature [90].

3.2 Fabrication of organic solar cells with structured metallic electrodes

The fabrication of nanostructured electrode devices (Fig. 3.1(b)) is identical to that of the reference devices with the addition of an imprinting step. In this step, which takes place after the deposition of the semiconductor film, a structured stamp is pressed into the film, thereby imprinting the inverse structure of the stamp. The subsequently deposited WO_3 and Ag layers conform to the nanostructured semiconductor film, resulting in a nanostructured electrode. The stamps are made in-house, which has allowed the optimization of the stamps for this specific purpose. A self-assembly process called anodization is used to make stamps with controlled nanostructured surfaces. This process is described below.

3.2.1 Anodization

Anodization can be thought of as a kind of controlled oxidation. In an electrochemical cell setup, a foil of aluminum can be submerged in an electrolyte across which a potential is placed. Under the correct conditions, the Al surface can be oxidized to form an Al_2O_3 film that features cylindrical pores perpendicular to the interface. The hexagonal ordering of these pores, which can in principle be achieved on arbitrarily large surfaces, and the fact that they form at all, is a result of a self-assembly process.

Anodization can be carried out under galvanostatic (constant current) or potentiostatic (constant voltage) conditions. The resulting time-dependent behavior of the voltage or current (Fig. 3.2 (a)-(b)) can reveal important information to the nature of the self-assembly process for galvanostatic and potentiostatic conditions respectively. In this study, we exclusively employ potentiostatic anodization. Starting with an aluminum film (with a native oxide layer), the application of an electropotential drives oxygen-containing ions (OH^- and O^{2-}) from the

electrolyte through the oxide film to the Al interface where oxidation occurs. As a result, the volume of the oxide film increases as the Al film is consumed. The increasing thickness of the Al_2O_3 film leads to a decreasing current between the electrodes, as can be readily observed in a plot of current vs. time (Fig. 3.2 I). The growth of the Al_2O_3 film is non-uniform - growth is accelerated near cracks or thinner regions in the oxide (where the propagation of ions through the film to the Al is more efficient) and near regions of high surface curvature on the Al (the enhancement of the applied field in such regions leads to increased rates of oxidation). Thus a film of variable Al_2O_3 thickness is established - featuring thick regions and thin regions (pores) as depicted in Fig. 3.2 II. The shortest distance between the electrolyte and the Al is through the base of the pores, therefore ions preferably reach the interface via this channel.

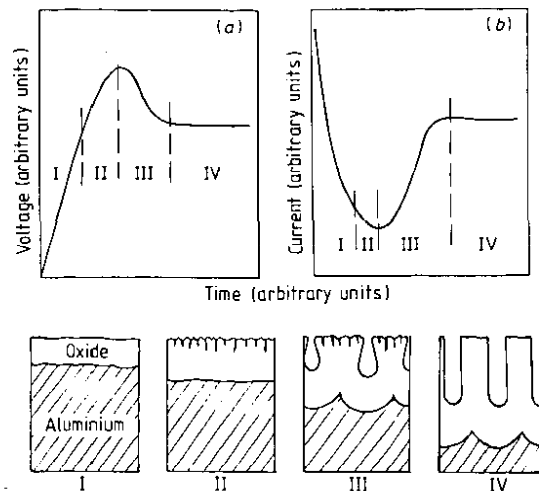


Figure 3.2: Pore growth process during anodic oxidation of aluminium. (a) Galvanostatic and (b) potentiostatic anodization. Schematics I-IV illustrate stages of pore growth. Taken from [91].

As the density of Al_2O_3 is close to half that of Al, the reaction leads to a significant volume expansion at the Al_2O_3 interface. According to proponents of the mechanical stress model for ordered pore formation, hexagonal ordering of the pores is established due to a repulsive force between the pores, which arises due to the mechanical stress of volume expansion at the bottom of the pores. [92, 93] Before steady-state is reached, the thickness of the barrier layer (the oxide film between the base of the pores and the Al film) is reduced which leads to an increase in current as oxidation is enabled via propagation through the barrier layer (Fig. 3.2 III). After a certain time, an equilibrium barrier layer thickness is reached, after which the barrier layer thickness remains unchanged. Beyond this time, the oxidation rate (and hence the observed current) is steady (Fig. 3.2 IV). The Al_2O_3 which is continuously produced is deposited in the inter-pore walls.

We note that in addition to the mechanical stress model, other theories have been proposed to explain the pore formation in steady-state, which incorporate thermal heating and electric field and anion concentration within the barrier layer (see [94]).

The fabrication of AAO membranes for use as imprinting stamps requires a total of 5 steps. We will now describe each of the steps in turn.

1. **Cleaning and electrochemical polishing**

Mechanically polished Al foils (99.999%, 50 μ m thick, Goodfellow) are cut into 25 \times 25mm chips and then cleaned with a lab-wipe with acetone to remove any excessive grease. They are then loaded into a custom-made holder (Fig. 3.3 B), where they undergo electrochemical polishing in a 1:4 volume ratio solution of perchloric acid in ethanol (> 95 %) for 8 minutes under a bias of 20 V. Electrochemical polishing can be thought of as the reverse of electroplating: the Al electrode is held at +20V relative to the opposing Pt electrode such that ions are removed from the surface of the Al. The highly ionic electrolyte enables a complete electrical circuit. Importantly, a higher density of surface charges will exist in regions of the Al surface with high curvature. Therefore, these areas will be ionized and removed first. This has the effect of smoothening the surface of the film (Fig. 3.4). During the electropolishing, it is important to stir the solution rapidly to prevent large spatial fluctuations in the distribution of ions in the electrolyte. Furthermore, it is advantageous to vary the direction of stirring (every 10 seconds), as otherwise radial defects develop on the foils. After an 8-minute treatment, approximately half of the 50 μ m thick Al film remains. A successful electropolishing should give the Al foil a uniform, mirror-like finish.

After the treatment, the foils are thoroughly rinsed in ethanol and water, and then loaded into the anodization holder (Fig. 3.3 A).

2. **First anodization**

The foils are now clean and smoothened. The first anodization step is the most important: here a self-assembly process will be initiated which will establish a hexagonal array of cylindrical pores. The values anodization voltage and temperature required for ordered membranes are electrolyte dependent (see Tab. 3.1). The anodization time is chosen depending on the order required - better order is obtained for longer anodization times. A typical duration in this study is between 6 and 16 hours. Although longer times may result in better pore ordering, care must be taken such that the pore growth (which under

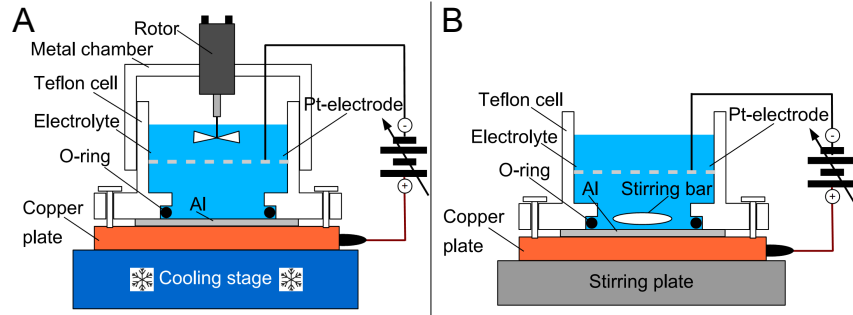


Figure 3.3: Schematic of the purpose-built anodization equipment. (A) The holder for anodization and (B) the holder for electrochemical polishing. Artist: Dominik Lembke.

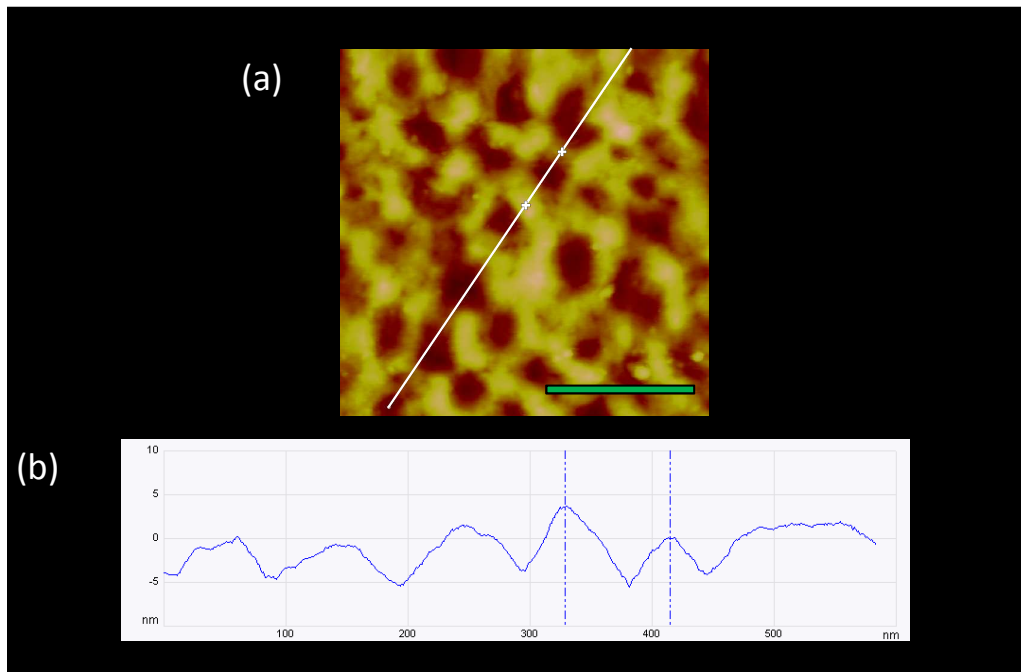


Figure 3.4: An electrochemically polished aluminum foil. (a) Atomic force microscope image of the surface and (b), the corresponding height profile along the line indicated. The green bar in (a) denotes a length of 200 nm

the standard conditions for anodization in oxalic acid (Tab. 3.1) has a rate of around $2\mu\text{m}/\text{hour}$ [95]) does not consume the entire Al foil. After the anodization is stopped, the samples are thoroughly rinsed with distilled water.

The resulting pore membrane exhibits increasingly high order towards the bottom of the pores. In order to access this high order, we next remove the entire Al_2O_3 film to

expose the highly ordered Al surface underneath that is established after anodization (Fig. 3.2IV).

3. Oxide removal

The oxide removed in a solution of phosphoric (6 wt. %) and chromic (1.8 wt. %) acid, leaving a highly ordered aluminum surface. Although the solution is somewhat selective in that it primarily consumes the oxide film, prolonged exposure of the sample to this solution will lead to a complete consumption of the oxide and a subsequent degradation of the (highly ordered) Al surface. In practice, this can be avoided if the oxide removal step is carried out for a shorter time than the first anodization under the indicated conditions (Tab. 3.1). Before the next step, the samples undergo a cleaning treatment in an ultrasonic bath for 10 minutes.

4. Second anodization

As a result of the previous two steps, the aluminum foil is now “pre-patterned”. Pore formation will tend to occur in the troughs of the aluminum surface - the location of the bottom of the pores established after the first anodization. As mentioned, the order at the bottom of the pores and hence of the structured aluminum film, is very high. The second anodization is typically carried out at an identical voltage and temperature as the first. However, the duration is typically a lot shorter (10 - 30 minutes). The depth of the pores can be directly controlled by the duration of this step. For our purposes, it is preferable to have shallow pores (< 500 nm). This enables an easy de-molding from the organic film after the imprint.

5. Pore widening

The resulting pores in the aluminum oxide membranes are then widened in dilute phosphoric acid. This step allows us to control the width of the pores. A typical duration for this step is 15-30 minutes..

Typical process parameters for anodization in sulfuric, oxalic and phosphoric acid are shown in Tab. 3.1. Special care is required for anodization in phosphoric acid to prevent catastrophic current flow at the aluminum substrate. In order to prevent this so-called “oxide burning”, a delicate transition from milder anodization conditions to those shown in Tab. 3.1 is required. [96, 97] Representative structures are shown in Figures 3.5, 3.6 and 3.7 for AAO membranes fabricated in oxalic, phosphoric and sulfuric acid respectively.

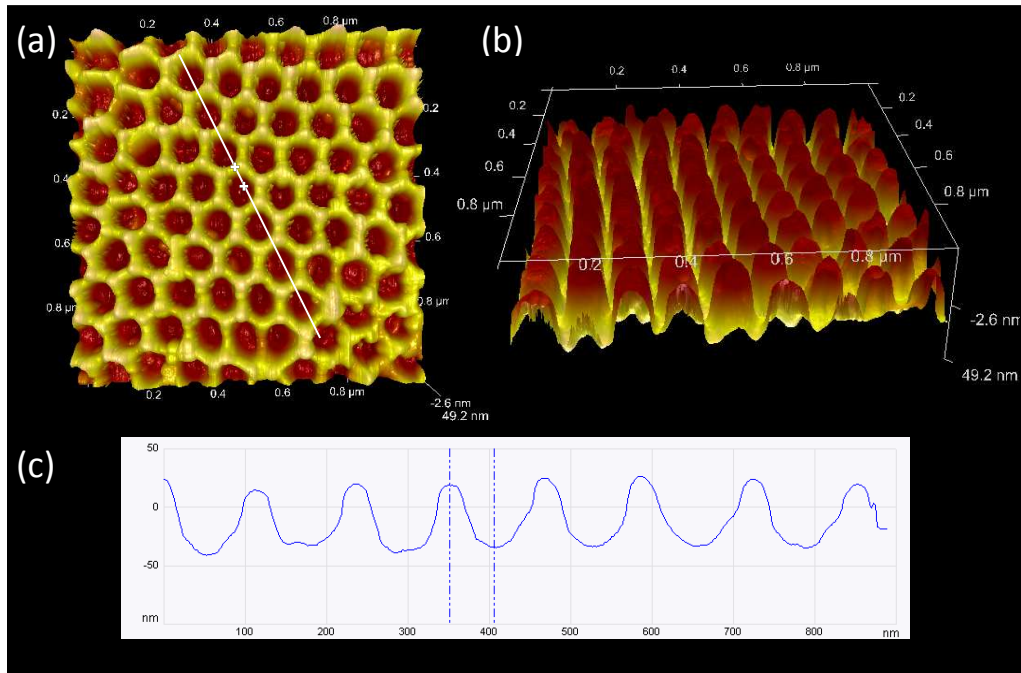


Figure 3.5: An anodized aluminum oxide membrane with a nominal periodicity of 100 nm. Anodization has been carried out in oxalic acid. (a-b) 3D views of atomic force microscopy images viewed from (a) above and (b) underneath. (c) The corresponding height profile.

Process step	Solution	Concentration	T [°C]	Time	Voltage [V]
ECP	HClO ₄ (EtOH)	1:4 (vol.:vol.)	10	8 min	20
1 st anod.	H ₂ SO ₄	0.3 M	3	6 h	25
Al ₂ O ₃ etch.	H ₃ PO ₄ /H ₂ CrO ₄	6wt%/1.8wt%	65	3 h	-
2 nd anod.	H ₂ SO ₄	0.3 M	3	60 s	25
PW	H ₃ PO ₄	5wt%	30	15 min	-
1 st anod.	H ₂ C ₂ O ₄	0.3 M	8	6 h	40
Al ₂ O ₃ etch.	H ₃ PO ₄ /H ₂ CrO ₄	6wt%/1.8wt%	65	4 h	-
2 nd anod.	H ₂ C ₂ O ₄	0.3 M	8	80 s	40
PW	H ₃ PO ₄	5wt%	30	30 min	-
1 st anod.	H ₃ PO ₄	0.5wt%	0.5	16 h	195
Al ₂ O ₃ etch.	H ₃ PO ₄ /H ₂ CrO ₄	6wt%/1.8wt%	43	8 h	-
2 nd anod.	H ₃ PO ₄	1wt%	2	80 s	195
PW	H ₃ PO ₄	10wt%	45	30 min	-

Table 3.1: Process parameters for AAO production. All solutions are aqueous except the perchloric acid solution which is dissolved in ethanol. ECP stands for electrochemical polishing and PW stands for pore-widening.

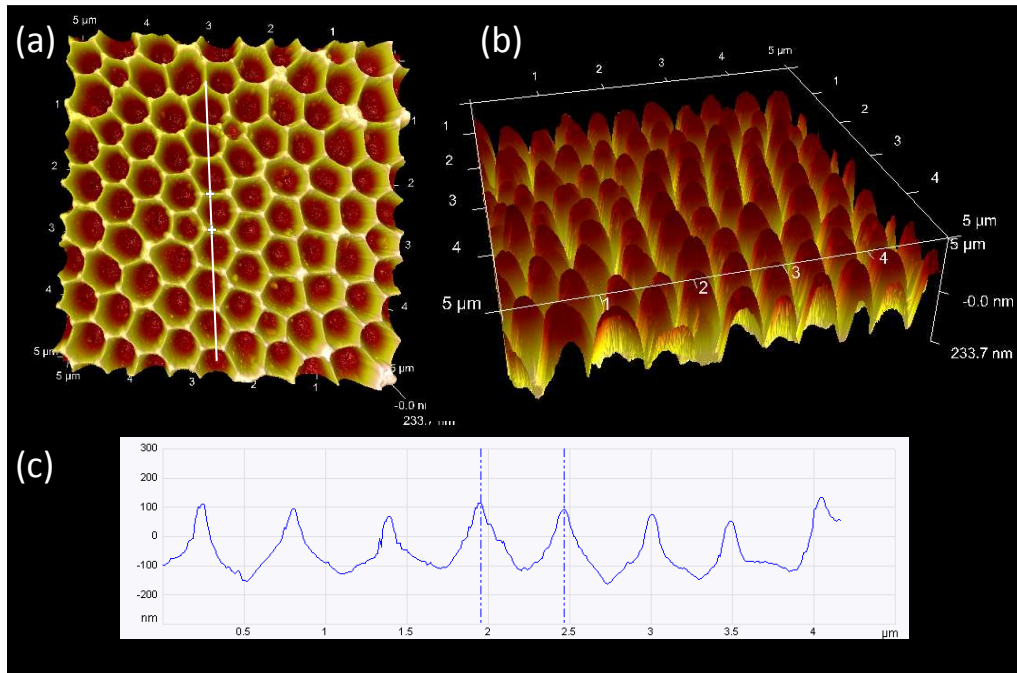


Figure 3.6: An anodized aluminum oxide membrane with a nominal periodicity of 500 nm. Anodization has been carried out in phosphoric acid. (a-b) 3D views of atomic force microscopy images viewed from (a) above and (b) underneath. (c) The corresponding height profile. We note that this stamp has not undergone a second anodization and pore-widening. This is done to minimize the pore depth.

3.2.2 Stamp geometry

The long-range geometry of the stamps fabricated in oxalic and sulfuric acid indicate a domain structure. Whereas high order is observed within each domain (around $1\mu\text{m}$ in size), neighboring domains are ordered in different crystallographic directions, with defects along the boundaries. No discernable ordering has yet been achieved for phosphoric stamps, although further optimization is underway.

Membranes that are fabricated according to the standard processing parameters (Tab. 3.1) exhibit characteristic feature sizes (pore period, width and depth) as displayed in Tab. 3.2. As high order phosphoric membranes have not yet been achieved in our lab, the establishment of characteristic void periods and widths is difficult (Fig. 3.6). The large uncertainty in the given values reflects this. In contrast, the sulfuric and oxalic membranes display reasonably ordered hexagonal void packing (Figures 3.5 and 3.7). By assuming perfect hexagonal ordering, the period of an array can be calculated by counting the number of voids (using *ImageJ*, an image analysis program) in a given area of an SEM image. The indicated error corresponds to the

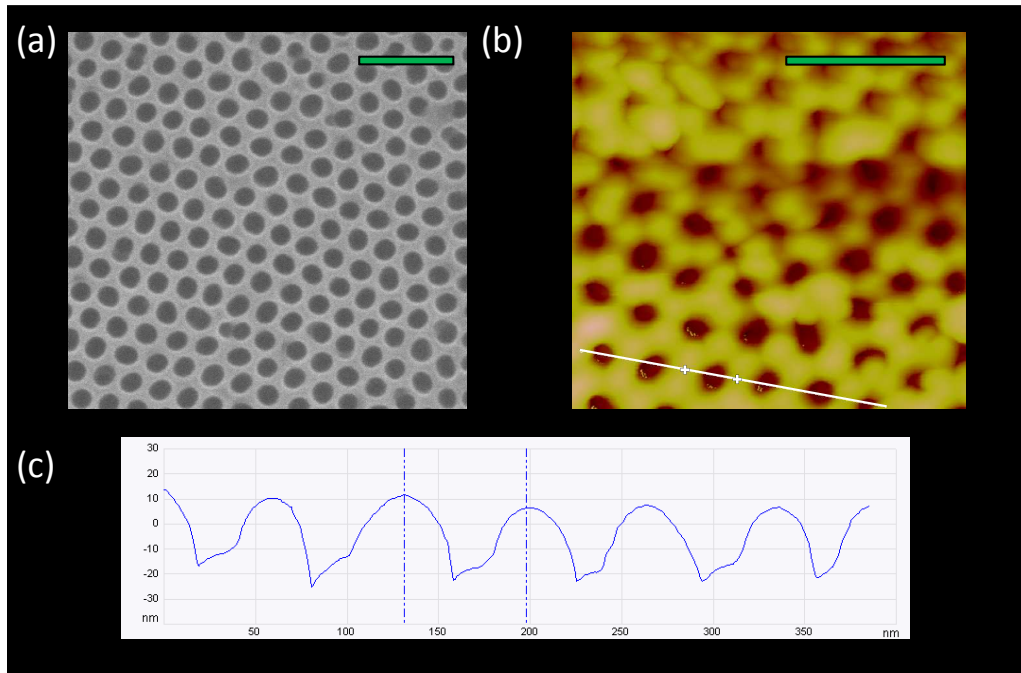


Figure 3.7: An anodized aluminum oxide membrane with a nominal periodicity of 60 nm. Anodization has been carried out in sulfuric acid. (a) A scanning electron microscope image. (b) An atomic force microscopy image and (c), the corresponding height profile. Incomplete penetration of the 30 nm diameter scanning tip into the pores (~ 30 nm diameter) is evident. The green bars in (a) and (b) denote a length of 200 nm.

approximate standard deviation of a number of such calculations for around 5 different images of a given sample. The width is obtained in a similar way: by assuming hexagonal ordering and the period obtained in the previous step and calculating the total area coverage of the pores (using *ImageJ*, an image analysis program). These measurements compare well with those observed in the AFM images.

	Period (nm)	Width (nm)	Depth (nm)
Sulfuric	60 ± 10	30 ± 10	> 30
Oxalic	100 ± 10	50 ± 10	60 ± 10
Phosphoric	400 – 500	400 – 500	200 ± 50

Table 3.2: Geometry of AAO membranes fabricated under the standard conditions presented in Tab. 3.1. Please see text for explanations on how the various values are determined and measured.

The values for the pore depth are read directly from Figures 3.5, 3.6 and 3.7. The indicated errors are associated with this reading. Accurate scanning of the the sulfuric acid stamp is difficult due to the fine size of the pores. The 30 nm wide AFM tip does not fully penetrate into the pores (indicated by the artifacts observed in Fig 3.7(c)), complicating the determination of the pore depth.

For the remainder of this thesis, we will refer to the stamps (and the corresponding structured devices) by their nominal periodicities: 60, 100 and 500 nm.

3.2.3 Imprint

The AAO membranes described in the previous section are used to structure organic films in a process known as nanoimprint lithography. Prior to the imprint, the membranes are placed in a desiccator where a small droplet of F₁₃-TCS silane solution placed by the stamps is allowed to evaporate.[98] A thin silane layer is formed on the surface of the stamps, which acts to reduce the adhesion with the organic material during imprinting.

The AAO stamp is then firmly pushed against the organic film using a mechanical press which can be heated to soften the film. As the AAO is pressed into the soft film, the film is deformed to fill the pores in the AAO membrane. If the surface of the AAO is appropriately treated to minimize adhesion to the organic film, the stamp can subsequently simply be lifted off the organic film. The resulting organic film exhibits the inverse structure of the stamp - mounds or standing wires in the positions corresponding to the AAO pores, and is relatively flat in positions corresponding to the inter-pore space of the AAO membrane. The deposition of WO₃ and Ag immediately follows the imprint to complete the fabrication of a nanostructured electrode device. Complete infiltration of the Ag into the contours of the nanostructure is observed in scanning electron microscope images of the resulting Ag film (see Fig. 6.1(d)). As such, the Ag film features nanovoids in positions corresponding to the organic nanowires of the underlying film. This metallic nanovoid surface was introduced in Sec. 2.3.4.

Scanning electron microscopy images of a typical nanoimprinted organic film are shown in Fig. 3.8. More images of nanostructured organic films will be presented together with the relevant experiments (Sec. 5.2 and Chap. 6). For standard devices, the imprinting temperature and pressure values are as shown in Tab. 3.3. The temperature used, 45°C, is chosen to be close to the glass transition temperature (the temperature at which the film makes the transition from a firm state to a molten or rubber state, without undergoing a phase transition) of a P3HT:PCBM film with a (1:0.8) mixing ratio. [99] As such, the imprinting parameters are specific to the organic film in question; we use the same parameters for MDMO-PPV:PCBM films, whereas significantly more extreme imprinting conditions are used for PCPDTBT:PCBM films

(Sec. 5.2). If the imprinting temperature is raised past the glass transition temperature, higher aspect-ratio structures can be fabricated, although stamp de-molding problems, where segments of the organic film may stick to the stamp and be detached from the substrate after the imprint, become more likely.

The AAO stamps are observed to macroscopically degrade due to the pressure applied during imprinting. For this reason, stamps are used for at most 10 imprints.

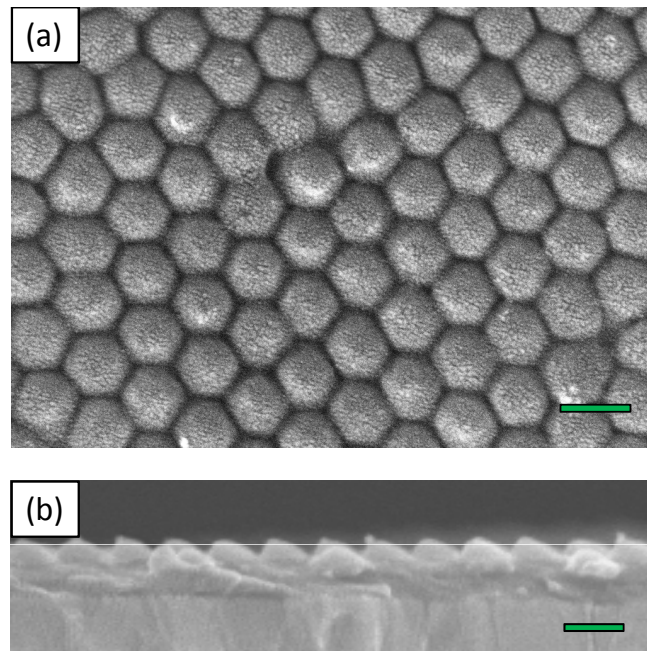


Figure 3.8: Nanostructured P3HT:PCBM film. An array of low aspect ratio nanowires fabricated via imprinting with a stamp with a 100 nm pore periodicity. (a) Top-view. (b) Side-view. The green bars in (a) and (b) denote a length of 100 nm.

Organic film	Stamp	T (°C)	Pressure (bar)
P3HT:PCBM	60 nm	45	250
P3HT:PCBM	100 nm	45	250
P3HT:PCBM	500 nm	45	150

Table 3.3: Standard imprinting parameters for nanovoid electrode solar cells. The duration is 5 minutes in each case.

“Flat-imprints” of organic films are also carried out in order to separate the influence of the electrode nanostructure with the effect of imprinting pressure and temperature. Accordingly, “flat imprint” devices are constructed in parallel with reference and structured electrode de-

vices. These flat-imprint devices are constructed via the standard imprinting procedure with the difference that the organic film is imprinted with a “flat” stamp. For this purpose, an Al chip that has undergone the standard electrochemical polishing is used as a stamp. The surface roughness of the flat stamp has a surface roughness of less than 5 nm (Fig. 3.4). The flat stamp has similar mechanical and thermal properties to the AAO stamps, identical aside from the porous aluminum oxide layer, and given that a (flat) layer of native oxide forms upon exposure to air, the surface can be functionalized and silanized using the same process as used in AAO stamp production. As we will show in Chap. 8, the performance of flat-imprint devices does not differ significantly from that of reference devices.

3.3 Characterization

3.3.1 Morphology

Scanning electron microscopy

Scanning electron microscopy (SEM) is used to obtain high resolution (of the order of nm) images of the surface topography of structured organic films and AAO membranes. A highly focused beam of electrons is scanned across the sample in a raster fashion. The interaction of these (primary) electrons with the sample produces a number of signals - for each of which a dedicated detector typically exists. Secondary electrons (with energies lower than 50 keV) are ejected from orbitals of sample atoms and are detected with a scintillator-photomultiplier system. Back-scattered electrons arising from elastic collisions with the sample typically reveal information about the atomic contrast of a sample, as the scattering cross-section of an atom is a strong function of the atomic number. Cathodoluminescence (emission when an electron returns to its previous energy level after being excited by a primary electron) and characteristic X-rays are also often typically detected.

In this work, a *Zeiss Ultra* scanning electron microscope is used. All images presented in this thesis are imaged using an InLens detector (a specialized secondary electron detector that enables high resolution due to its close proximity to the sample) using an accelerating voltage of 4-8 keV and working distances of 4-10 mm. In addition to images of samples from normal incidence, cross-section images are also obtained by cleaving samples and then placing them on their side on the sample holder. Organic films are typically coated with a thin (≈ 1 nm) layer of Au to improve conductivity (so that charge built up in the sample, “charging”, under illumination by the electron beam can dissipate) without significantly affected the topography.

AAO samples are typically not coated in Au prior to imaging - the conductivity is found to be sufficiently high such that charging is minimal.

Atomic force microscopy

Atomic force microscopy (AFM) is used to supplement SEM images. The central part of an atomic force microscope is the cantilever. The cantilever features a sharpened tip at its end which is used to scan the sample. In tapping mode, which is the mode used to produce the images presented in this thesis and the most commonly used AFM mode [100], the cantilever oscillates at a frequency close to its resonant frequency with an amplitude that allows the tip to lightly tap the sample surface. This amplitude changes with surface topography - a feedback control system adjusts the z position to maintain a fixed amplitude as the tip is scanned across the sample. In this way, an accurate measurement of the topography can be made.

A *Multimode 8 Atomic Force Microscope, Bruker* with a MC60 tip (30 nm diameter, provided by *Nanotools* [101]) with a tip velocity of 1 $\mu\text{m/s}$ is used in this work.

3.3.2 Spectroscopy of solar cell architectures

Reflection spectroscopy

Reflection spectroscopy (*Hitachi U-3501*) is used to measure the total absorption of planar and nanostructured electrode architectures at optical wavelengths. Measurements made in reflection mode, as opposed to transmission mode, are essential as the metallic electrode is non-transparent. To collect both specular and non-specular (diffuse and diffracted modes), the sample is mounted onto the side of a so-called integrating sphere. The operating principle of reflection spectroscopy with an integrating sphere is shown schematically for the incidence plane bisecting the center of the sphere (Fig. 3.9). The sample is mounted at a 10° angle to the incident beam such that the specularly reflected beam is deflected from the incidence aperture. The specularly reflected beam will then be diffusely reflected from the inner wall of the sphere, which is coated with BaSO_4 , a standard material in spectroscopy known for its near-unity (diffuse) reflective property at optical wavelengths. Recall that the schematic shows only the incidence plane - diffuse reflection will not be limited to this plane rather it will spread isotropically through the sphere. Subsequent reflections will ensue until the light is eventually entirely collected at the detector, located at the base of the sphere (indicated by the dashed circle).

Each measurement is normalized by a preceding background measurement where a white standard (composed of compressed Al_2O_3 which has similarly good diffuse reflective properties to

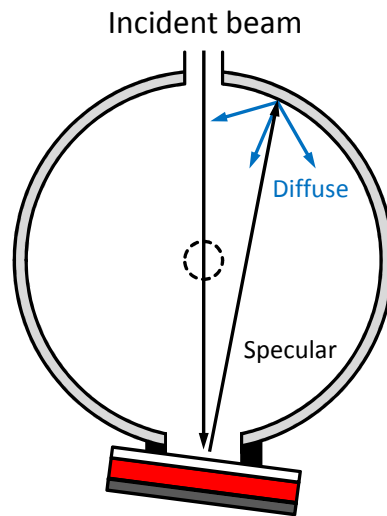


Figure 3.9: The working principle of reflection spectroscopy with an integrating sphere. The incident beam is first specularly reflected from the sample. It is then diffusely reflected from the inner sphere wall with a near-perfect efficiency. The light is collected at the detector located at the bottom of the sphere (dashed circle).

$BaSO_4$) is mounted in the sample position as shown. Systematic losses such as light absorption in the $BaSO_4$ layer lining the walls should be effectively canceled out by this normalization. The Teflon holder that is used to mount the sample has a beveled aperture of 13 mm^2 which is significantly larger than the beam spot size ($\approx 5 \text{ mm}$ in diameter).

The obtained reflectance spectrum $R(\lambda)$ contains both specular and non-specular components (any non-specular reflection of the incident beam at the sample is also collected). From this, the sample absorption $A(\lambda)$ is obtained via $A(\lambda) = 1 - R(\lambda)$. It is not possible to isolate the absorption of individual device components; as each layer is optically dependent on every other layer, the subtraction of the absorption of different layers to obtain the absorption of individual layers is invalid. Rather, the obtained absorption spectra pertains to the total sample absorption.

In order to investigate the absorption in individual layers, it is useful to supplement reflection spectroscopy measurements with numerical simulation (Chap. 4) and spectrally-sensitive electrical measurements of devices (Sec. 3.3.3).

Angle-sensitive reflection spectroscopy

Absorption spectra for incidence angles up to 45° are measured using a dedicated optical setup in the Nanophotonics Group in the University of Cambridge. In this setup, a supercontinuum white-light laser source (Fianium SC-450-6) passes through a polarizing filter onto the sample (Fig. 3.10). The beam has a diameter of around 1 mm. The sample is mounted onto the stage of a goniometer to allow rotation in the plane of Fig. 3.10 about an axis centered at a point on the sample surface. The direction of rotation is indicated by the arrows. Using this set-up, incident angles ranging from -30 to 90° can be accessed.

The detector is attached to an arm of the goniometer such that it can be rotated about the same axis as indicated by the arrows. An automated program rotates the arm to ensure that the detection angle is equal to twice the incidence angle (Fig. 3.10) so that specular reflection is collected. However if required, the detector can be positioned at any arbitrary angle. This is useful for determining the magnitude of non-specular reflection in the incidence plane.

The detected beam is fiber-collected, separated into visible and infra-red components by beam-splitters and collected by Ocean Optics QE65000 and NIRQuest spectrometers respectively. All spectra are normalized to reflection spectra of a silver mirror, as measured by placing the mirror in the sample position. For each sample, angle-dependent spectra are measured for multiple positions on the sample.

3.3.3 Solar cell characterization

Current-Voltage characteristic

In order to determine the power conversion efficiency of a solar cell, it is necessary to measure its current-voltage characteristic, or IV curve, to determine the maximum power point. The solar cell community uses the AM1.5G spectrum for device characterization, which is a standard illumination spectrum made available by the *National Renewable Energy Laboratory*. [102] Illumination that closely resembles the AM1.5G spectrum is provided by a 150 W solar simulator (*L.O.T. Oriel*). The light source is calibrated using a certified monocrystalline silicon diode (*Fraunhofer ISE WPVS Cell*) fitted with a bandpass filter (KG5, *Schott*) [103].

As described in section 2.1, important device characteristics (η , J_{SC} , FF and V_{OC}) are extracted from the IV curve. Values of R_{sh} and R_s can be obtained as a result of fitting the measured IV curves using the *Generalized Shockley Equation* (Eq. 2.5). In this study, R_{sh} and R_s are estimated by measuring the inverse of the slope at the IV curve at large reverse and large forward biases respectively.

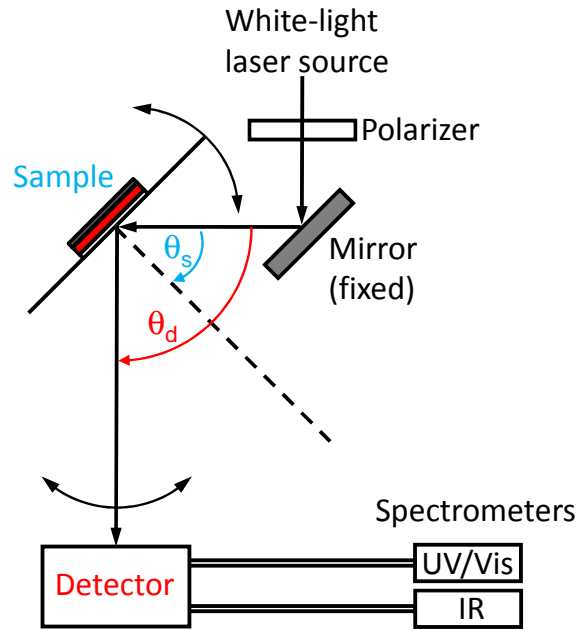


Figure 3.10: The working principle of angle-sensitive reflection spectroscopy. The reflected beam is detected by the detector as shown. The sample is positioned at the center of a rotation stage such that the angle of incidence of the incident beam θ_s can be varied. The allowed rotation is indicated by the double-headed arrows. The detector can be independently rotated about the same axis. An automated program is used to collect specular reflection by ensuring that the angle between the detector and the incident beam θ_d , satisfies $\theta_d = 2\theta_s$ (law of reflection). The sample and detector are located in the same plane (the plane of this page). The mirror is located slightly (2°) out of this plane to allow measurement at normal incidence $\theta_s = 0$.

External quantum efficiency

The external quantum efficiency, $EQE(\lambda)$, of a solar cell is defined as the number of electrons delivered to an external circuit divided by the number of incident photons at wavelength λ . In terms of easily measurable quantities:

$$EQE(\lambda) = \frac{J(\lambda)}{qP_{in}(\lambda)} \frac{hc}{\lambda} \quad (3.1)$$

where $J(\lambda)$ is the current density (Am^{-2}), q the electronic charge (C), $P_{in}(\lambda)$ the incident power flux (AM1.5 G) at wavelength λ (Wm^{-2}), h is Planck's constant and c is the speed of light in a vacuum. The $EQE(\lambda)$ is conventionally calculated under short-circuit conditions, although this is somewhat arbitrary.

Monochromatic illumination (FWHM ≈ 5 nm) is obtained using a 150 W xenon lamp (*L.O.T. Oriel*) and a *L.O.T. Omni 150* monochromator. The typical measured wavelength range is 280-800 nm. Calibration at each wavelength is carried out using a certified monocrystalline silicon diode (*Fraunhofer ISE WPVS Cell*). It is possible to spectrally integrate the obtained $EQE(\lambda)$ to arrive at the short circuit current J_{SC} as observed in Sec. 3.3.3 according to:

$$J_{SC} = \frac{q}{hc} \int_{\lambda_{min}}^{\lambda_{max}} EQE(\lambda) P_{in}(\lambda) \lambda \, d\lambda \quad (3.2)$$

3.4 Summarizing remarks

A novel method for fabricating nanostructured electrode devices, which was developed with the goal of achieving light-trapping in organic solar cells, was presented in this chapter. This is one of the important experimental accomplishments in this thesis. The fabrication and characterization of organic solar cells was also presented. In the next chapter, we will introduce the tool with which the computational component of this work is carried out: the finite element method.

3.4 Summarizing remarks

4 Simulation using the finite element method

In this chapter we describe the computational technique used to simulate absorption in solar cell architectures: the finite element method. The technique will be explained with the aid of a simple example: solving the wave equation to obtain the magnetic field strength on a one-dimensional domain.

Techniques that have been previously been invoked to address arbitrary metallic nanostructure geometries include the boundary element method [104] and the finite difference time domain method [82]. The finite element method (FEM) is appealing because it is a full wave technique and supports arbitrary geometries. In addition, as it is a method that operates in the frequency domain, experimentally-determined material dispersion can be conveniently incorporated without the need to model the optical constants as is required when using the finite difference time domain method. The FEM has been widely used to investigate plasmonic structures such as SPP waveguides, metallic nanoshells and nanorod arrays. [105–107]

4.1 Finite element method in 1D

The finite element technique will be explained using a simple example. In this example, we will obtain a solution to the wave equation in the magnetic field, \vec{H} , over a one-dimensional domain. We start with the wave equation:

$$\vec{\nabla} \times \left(\frac{1}{n^2} \vec{\nabla} \times \vec{H} \right) - k_0^2 \vec{H} = 0 \quad (4.1)$$

where n is the refractive index and k_0 is the magnitude of the wave vector in free space. We insist that the magnetic field $H = H_z$ varies with x only and that $H_x = H_y = 0$. This is consistent with a TM wave propagating along the x -axis. Under these conditions, equation (4.1) reduces to the following, which is a one-dimensional differential equation of the scalar quantity, H :

$$-\frac{1}{n^2} \frac{d^2 H(x)}{dx^2} - k_0^2 H(x) = 0 \quad (4.2)$$

which belongs to the family of *elliptical* equations. In order to obtain a numerical solution to equation (4.2) using the FEM [108], we take the following steps:

1. Define the geometry

We wish to solve (4.2) over the one-dimensional domain Ω of length L (Fig. 4.1(a)) for the case $n = 1$. Neumann boundary conditions will be enforced:

$$\vec{s} \cdot \frac{dH(x)}{dx} = g(x) \quad (4.3)$$

$$g(x) = \begin{cases} 1 & x = 0 \\ -1 & x = L \end{cases} \quad (4.4)$$

where \vec{s} is a vector normal to the boundary.

2. Formulate the weak form of the differential equation

Assuming H is a solution to (4.2), we multiply the equation with a test function v and integrate on the domain Ω :

$$\int_{\Omega} \left[-\frac{d^2 H(x)}{dx^2} v - k_0^2 H(x) v \right] dx = 0 \quad (4.5)$$

Applying integration by parts we obtain:

$$\int_{\Omega} \left[\frac{dH(x)}{dx} \frac{dv}{dx} - k_0^2 H(x) v \right] dx - \int_{\partial\Omega} \vec{s} \cdot \frac{dH(x)}{dx} v dS = 0 \quad (4.6)$$

Enforcing the boundary conditions (4.3):

$$\int_{\Omega} \left[\frac{dH(x)}{dx} \frac{dv}{dx} - k_0^2 H(x) v \right] dx - \int_{\partial\Omega} g v dS = 0 \quad (4.7)$$

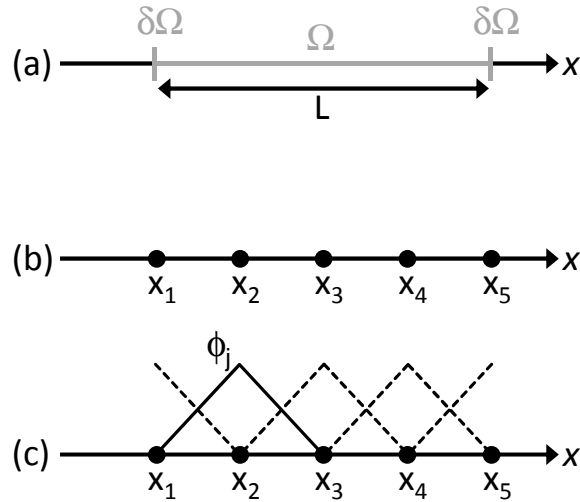


Figure 4.1: A one-dimensional finite-element problem. (a) The geometry in this problem is made up of domain Ω and boundary $\delta\Omega$. (b) The geometry is meshed into finite elements using 5 nodes x_1, \dots, x_5 . (c) Basis functions $\phi_j(x)$ are defined at each of the nodes. $\phi_2(x)$ is denoted with a full line.

Equation (4.7) is known as the variational or weak form of the initial differential equation. Any solution of the initial equation is also a solution of weak equation. **We seek $H(x)$ such that equation (4.7) holds $\forall v$.**

3. Discretize the weak form

$H(x)$ and $v(x)$ belong to function space V . In general, an infinite number of basis functions are required to span this space, c.f. modeling an arbitrary signal with a Fourier series composed of an infinite number of periodic functions. To proceed, we define a N -dimensional function subspace $V_N \subset V$ and insist that H and v exist in V_N . V_N is spanned by the basis functions $\phi_j(x)$, $j = 1, \dots, N$, and we can therefore write our solution in the form:

$$H(x) = \sum_{j=1}^N U_j \phi_j(x) \quad (4.8)$$

As the differential operator is linear and v is an arbitrary function in V_N , the following equations must hold if equation (4.7) holds:

$$\int_{\Omega} \left[\frac{dH(x)}{dx} \frac{d\phi_i(x)}{dx} - k_0^2 H(x) \phi_i(x) \right] dx - \int_{\partial\Omega} g(x) \phi_i(x) dS = 0 \quad i = 1, \dots, N \quad (4.9)$$

Combining (4.8) and (4.9) we obtain the linear system of equations:

$$\sum_{j=1}^N \left(\int_{\Omega} \left[\frac{d\phi_j(x)}{dx} \frac{d\phi_i(x)}{dx} - k_0^2 \phi_j(x) \phi_i(x) \right] dx \right) U_j - \int_{\partial\Omega} g(x) \phi_i(x) dS = 0 \quad i = 1, \dots, N \quad (4.10)$$

which can be expressed in matrix form:

$$(K + M)U = G \quad (4.11)$$

with matrix elements:

$$K_{ij} = \int_{\Omega} \frac{d\phi_j(x)}{dx} \frac{d\phi_i(x)}{dx} dx \quad (4.12)$$

$$M_{ij} = \int_{\Omega} -k_0^2 \phi_j(x) \phi_i(x) dx \quad (4.13)$$

$$G_i = \int_{\partial\Omega} g(x) \phi_i(x) dS \quad (4.14)$$

Now all that remains is to choose an appropriate set of basis functions, assemble the system matrices and then linearly solve them.

4. Assembly - evaluate system matrices

A set of basis functions enabling easy evaluation of the system matrices is the set of “tent” functions $\phi_i(x)$. The domain is divided into finite elements with N nodes. In this example, $N=5$. We will span our domain with tent functions centered at each node x_i (Fig. 4.1(b)) and require $\phi_i(x_i) = 1$, $\phi_i(x_j) = 0$ for $j \neq i$ and the value of $\phi_i(x)$ falls uniformly (constant slope) to 0 at x_{i-1} and x_{i+1} (Fig. 4.1(c)).

5. Linearly solve the system

The linear system can then be solved. In general, FEM systems require complex linear solvers. Here, we solve the linear system using MATLAB (Fig. 4.2) for $L = \lambda = 500$ nm, where $k = 2\pi/\lambda$. For this simple problem, it is possible to obtain an analytic solution. However in general, analytical solutions can not be found for even marginally more

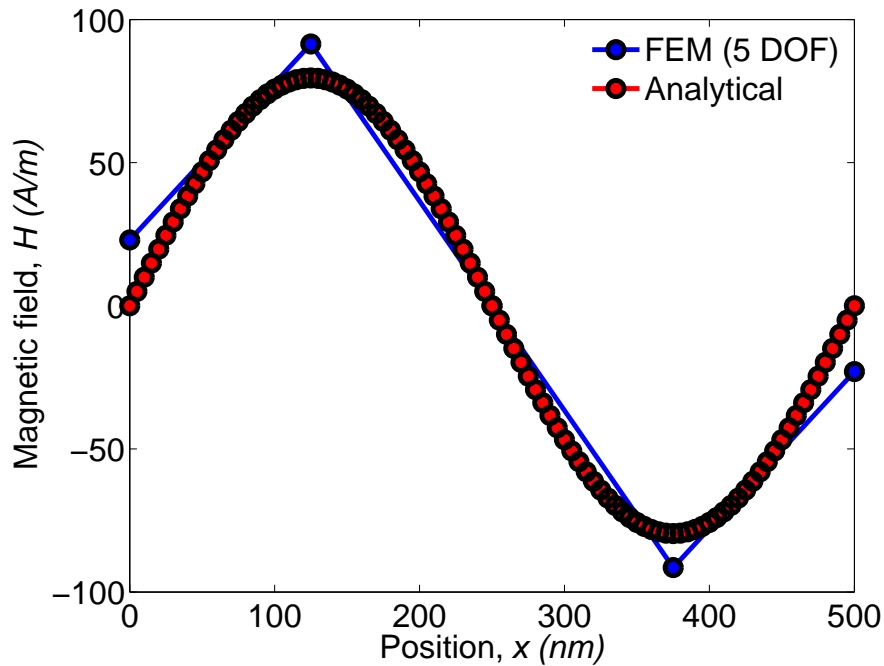


Figure 4.2: Finite element method and analytical solutions to the problem. The accuracy of the finite element solution can be increased by increasing the number of degrees of freedom (DOF). The FEM solution is defined at the nodes (blue circles). We interpolate between these points (blue line), here linearly, to approximate the solution over the entire domain.

complex problems. The general behavior of the sinusoidal analytical solution (obtained by taking an exponential trial solution) is present in the numerical solution. We note that the accuracy can be increased by increasing the number of nodes, which increases the number of basis functions available. The number of basis functions used to obtain the numerical solution is known as the number of degrees of freedom (DOF) of the linear system.

4.2 Finite element method in higher dimensions

This technique can be easily generalized to two and three dimensions. An important consideration for solvers is the numbering of nodes; two- and three-dimensional systems require robust algorithms to allocate and organize unique node indices. Matrix elements are then calculated using basis functions of appropriate dimension to arrive at the system matrices (i.e. $\phi_j(x,y)$ in two-dimensions). The main difficulty in three-dimensional FEM simulation is the sheer computational expense: a single model can require in excess of 200,000 DOF for accurate

computation, requiring tens of GByte of RAM and consuming up to four hours of computation time at 2.5 GHz . Linear basis functions such as the tent functions used in section Section 4.1 are usually replaced by quadratic functions for better accuracy (although at an increased computational cost).

Finite elements (with which we divide a domain) are line segments in 1D, finite areas in 2D and finite volumes in 3D. As a general rule, less fine meshes must be used in in higher dimensions to limit the DOF and hence computational time. For the 2D simulations in this work, a maximum element size of $\lambda/10$ is typically used for the domains with a maximum mesh size of around $\lambda/20$ along the boundaries. λ denotes the wavelength of the light in the relevant medium, not the vacuum wavelength. In 3D, the maximum mesh sizes are around $\lambda/5$ and $\lambda/10$ for the domain and boundaries respectively. Matched meshes (identical meshing of opposite boundaries) is always insisted upon to improve solver accuracy for periodic boundary conditions. Where perfectly matched layers (PMLs, boundary layers designed to absorb all incident radiation and minimize artificial reflections back into the system) are used, a thickness of λ is found to be sufficient to ensure negligible reflections for all incidence angles. A PML is essential when dealing with strongly scattering features. The PML is always located at a distance of at least λ from the system and is typically located within the glass substrate, which forms the top of the simulation boundary.

Simulations of solar cell geometries in 2D (Chap. 9) and 3D (Chap. 6) will be described later in this thesis. FEM solvers are typically invoked using a MATLAB script in which the geometry, boundary conditions and material properties can be defined. Solutions are obtained for vector-valued solutions of the electric and magnetic fields simultaneously. From these values, quantities such as the time-averaged absorbed energy and power fluxes through arbitrary boundaries can be obtained. It is also possible to obtain values at a fixed point in time, and then to vary this throughout a harmonic cycle by adjusting the phase of the incident illumination. The MATLAB script loops through incidence wavelength and typically one or two parameters such as material property or geometric size. An example script is included in Appendix A. This script calculates the absorption in a solar cell featuring semiconductor film in which a silver nanoparticle is placed. It performs an optimization study by looping through all valid combinations of incidence wavelength (varied from 350 nm to 1000 nm with a resolution of 2 nm), nanoparticle width (for values between 10 and 120 nm) and nanoparticle spacing (0-600 nm). This script was used to calculate the data for some of the figures in Chap. 9.

4.3 Summarizing remarks

The FEM has been introduced in this chapter. This framework will be the basis of the computational investigations that follow in this thesis, although the inner-workings of the FEM will not again be discussed in fine detail as they were here. The important inputs of subsequent simulations, such as selection of boundary conditions and object geometries, will be presented together with the findings of the studies themselves. We now move towards the first measurement results of the thesis - measurements confirming light-trapping in nanostructured electrode devices.

4.3 Summarizing remarks

5 Absorption enhancement in solar cell architectures

In the preceding two chapters the tools required for a rigorous experimental and computational investigation of light-trapping in solar cells have been described. We now present spectroscopic characterization measurements of reference and nanostructured electrode device architectures fabricated using the techniques introduced in Chapter 3. The strong interaction of light with the nanostructured electrode is evident: measurements indicate a destruction of coherence within the organic film. The first demonstration of light-trapping is introduced in this chapter: the nanostructure electrode architectures absorb up to 45% more incident light than the reference samples (Section 5.1). It is found that the absorption enhancement occurs primarily at wavelengths where the semiconductor absorbs poorly - efficiently absorbed photons do not propagate far enough into the organic film to reach the electrode. We show via angle-sensitive reflectometry that light-trapping for the most highly absorbing samples occurs due to the excitation of localized plasmonic modes (Section 5.2).

5.1 Reflectometry

An important consideration for light absorption in planar solar cells is Fabry-Pérot resonances - where incident light interferes constructively with its reflected beam to form a standing wave with spatial intensity and hence absorption maxima within the organic layer [109]. By introducing a thin layer of tungsten oxide (WO_3 , effectively transparent at optical wavelengths) between the semiconductor and the metal, the phase of the reflected beam and hence the nature of the interference can be altered. By varying the WO_3 thickness (Fig. 5.1(a)) we observe the effect of Fabry-Pérot resonances: for a given layer stack we can increase the absorption at certain wavelengths, typically at the expense of reduced absorption at other, non-resonant wavelengths. This effect is dramatically reduced for structured electrodes, which is an indica-

tion of disruption of coherence within the active layer (Fig. 5.1(a)).¹ This clearly demonstrates that light strongly interacts with the interface (for example by coupling to plasmonic or scattering modes) such that the formation of standing waves is inhibited.

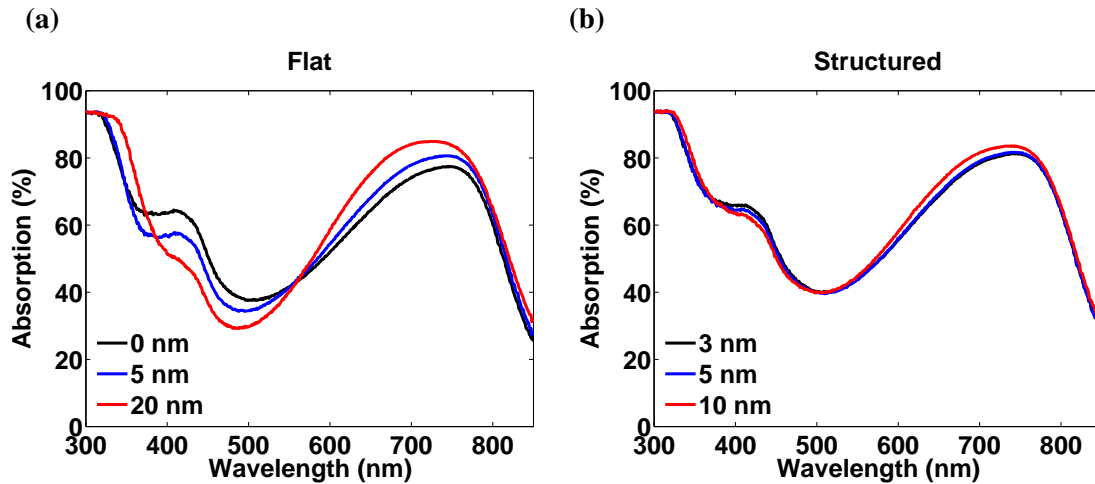


Figure 5.1: Absorption spectra for flat and structured electrode architectures for tungsten oxide thicknesses varying between 0 and 20 nm. The Fabry-Pérot resonances present in (a) the flat architecture are absent for (b), the structured electrode architecture. The sample structure is glass-PCPDTBT:PCBM-WO₃-Ag.

The central result of this thesis is presented in Fig. 5.2: significant light-trapping is achieved with nanostructured electrodes. An enhancement in the total absorption is observed consistently for a number organic semiconductor - silver nanovoid systems. The layer structure for these samples is: glass-semiconductor blend-Ag. This is a simplification of the layer structure of a complete solar cell - the ITO, TiO₂ and WO₃ layers have been omitted. This was done to obtain a targeted measurement of the effect of the nanostructured electrode. The effect of including these layers would be a reduction in the absorption in the semiconductor (although all of these layers are chosen for their high transparency, their absorption is nevertheless not negligible) and a modification of the interference pattern within the device. The mixing ratio of PCPDTBT:PCBM in Fig. 5.2(c) and Fig. 5.2(d) is 1:3 and 1:2 respectively. This explains the more pronounced peak at 750 nm, which is due to absorption in PCPDTBT.

¹Although the curves in Fig. 5.1(b) are strikingly similar despite the variation in WO₃ thickness, indicating that the Fabry-Pérot pattern evident in Fig. 5.1(a) has been destroyed, the range between of WO₃ film thicknesses is not strictly comparable. This experiment must be repeated in order to confirm this result

Figure 5.2(c) shows the absorption spectra for PCPDTBT:PCBM (1:3) devices, whereas Fig. 5.2(d) pertains to PCPDTBT:PCBM (The absorption over a finite wavelength domain, \mathbf{A} , is given by:

$$\mathbf{A} = \frac{1}{\lambda_{max} - \lambda_{min}} \int_{\lambda_{min}}^{\lambda_{max}} A(\lambda) d\lambda \quad (5.1)$$

where $A(\lambda)$ is the absorption at wavelength λ . The relative absorption enhancement of a structured architecture over a reference planar architecture will be defined as:

$$\mathbf{A}(\%)_{struc} = \frac{\mathbf{A}_{struc} - \mathbf{A}_{ref}}{\mathbf{A}_{ref}} \quad (5.2)$$

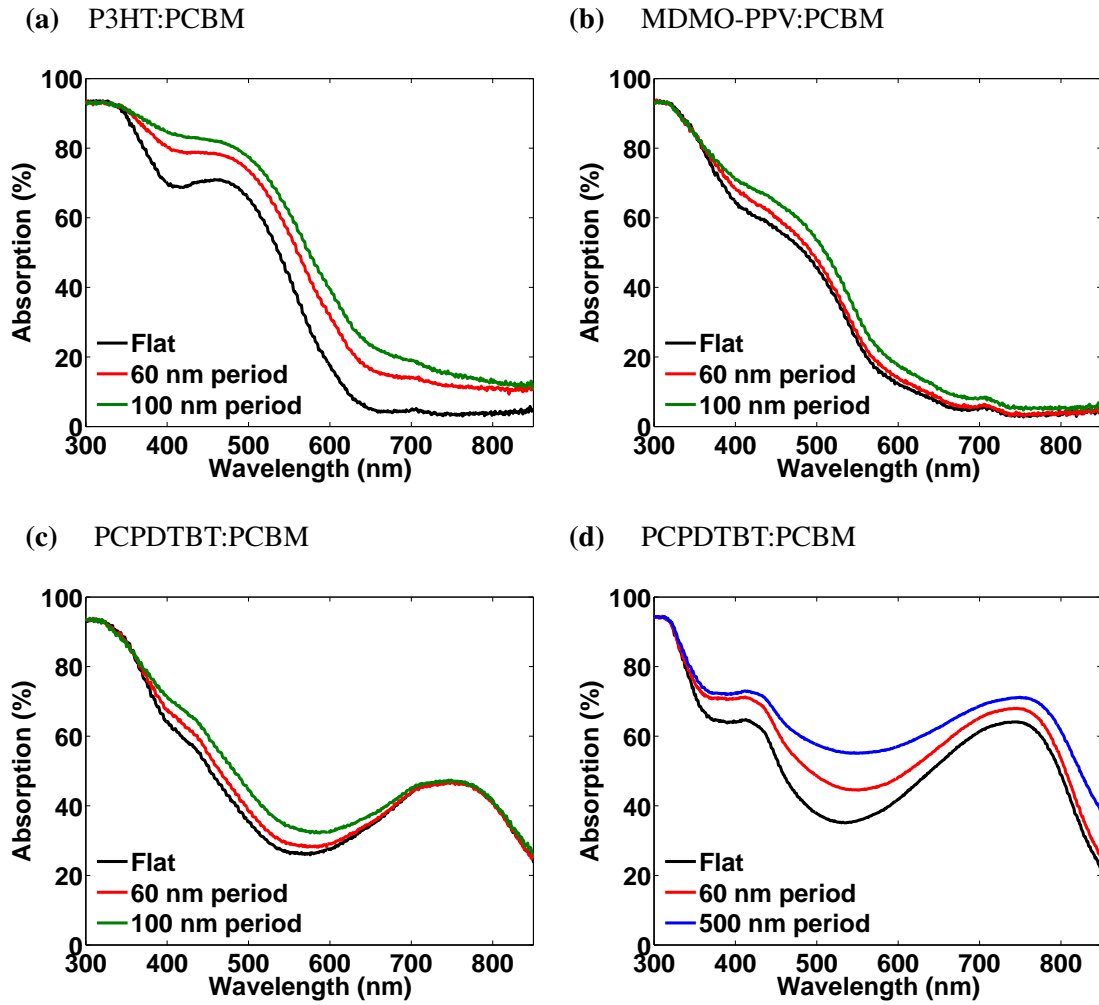
The relative absorption enhancements for all structured electrode architectures is shown in the table in Fig. 5.2. The enhancement is noticeably larger for larger void periods. We stress that nanovoid arrays produced with this technique (section 3.2) with larger periods typically have larger diameters and depths as well. As has been well documented, the response of nanovoid arrays is strongly dependent on all three parameters: void period, depth and height (see Sec. 5.2, Chap. 9 and Ref. [37]). It can, however, be seen that as the voids increase in size (in all three critical parameters), and become more comparable with the wavelength of incident light, a larger degree of light-trapping occurs.

It is difficult to discern the nature of light-trapping, and whether the light is trapped as absorption in the organic material or the metal, from these measurements alone. Direct simulation of nanovoids is used to gain large insights (section 6).

By comparing the effect of the nanovoid interface for three different adjacent blends of organic semiconductors (Fig. 5.2), we observe that the absorption enhancement is most prominent in spectral regions where the semiconductor absorption is low. This is attributed to a filter effect: as the light is incident through the glass side, it first propagates through the bulk semiconductor material before interacting with the nanovoid interface. Therefore, photons that are strongly absorbed by the semiconductor do not propagate to reach the interface; photons that are weakly absorbed are more likely to propagate to the organic-nanovoid interface where they can be subsequently trapped' in the system. This is shown explicitly in Fig. 5.3 for the PCPDTBT:PCBM-Ag interface (calculated directly from the data in Fig. 5.2(d)). The black dashed line is the reflectance of the flat sample. We observe the (absolute) absorption enhancement ($\Delta A(\%) = A_{struc}(\%) - A_{Flat}(\%)$) is predominately large in spectral regions where the reflectance of the flat sample is large, or conversely, where the absorption of the semiconductor is small.

5.1 Reflectometry

We do note however, that the spectral positions of these peaks do not exactly overlap. The difference in the spectral positions of the peaks of the flat reflectance and the absorption enhancement curves are a result of the dispersive nature of the light-trapping mechanism - the absorption enhancement does not only occur at wavelengths where the semiconductor absorbs poorly, there is also an additional tendency for certain wavelengths to be trapped. Absorption spectra such as these contain information on the nature of the light-trapping mechanism. This will be investigated in detail in Sec. 5.2, where we will identify LSP excitation as the primary light-trapping mechanism for these samples.



	60 nm	100 nm	500 nm
(a) P3HT:PCBM	0.19	0.28	-
(b) MDMO-PPV:PCBM	0.05	0.14	-
(c) PCPDTBT:PCBM	0.06	0.18	-
(d) PCPDTBT:PCBM	0.24	-	0.45

Figure 5.2: Enhanced absorption over flat architectures obtained for structured electrode architectures. The layer structure is glass-semiconductor blend-Ag. The nanostructured silver electrodes have periods of 60, 100 or 500 nm. Demonstrated for a variety of common organic semiconductors: (a) P3HT:PCBM, (b) MDMO-PPV:PCBM, (c) PCPDTBT:PCBM (1:3) and (d) PCPDTBT:PCBM (1:2). The absorption enhancement achieved by each nanostructured electrode architecture relative to the corresponding flat architecture, $A(\%)_{\text{struct}}$, is tabulated.

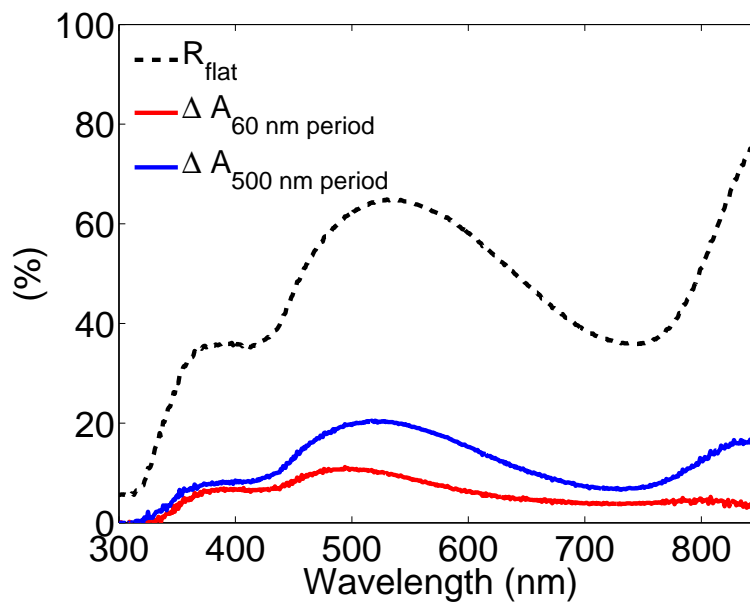


Figure 5.3: Light-trapping is greatest at wavelengths at which the semiconductor poorly absorbs. The reflectance spectrum of the flat architecture (R_{flat} , dashed black line) plotted alongside spectra of the absolute absorption enhancement over the flat architecture $\Delta A(\lambda)(\%) = A_{struc}(\lambda)(\%) - A_{flat}(\lambda)(\%)$ for the nanostructured samples with period 60 nm (red line) and 500 nm (blue line). At wavelengths where the flat sample absorbs poorly (R_{flat} is large), the enhancement provided by the nanostructured electrode is maximum.

5.2 Angle-sensitive reflectometry

This section is based on *Dunbar et al., 2012*, submitted to the *Journal of Applied Physics*, 2012.

Solar cells stand to benefit greatly from plasmonic light trapping, where plasmonic excitation leads to an increased absorption of light in the adjacent semiconductor film and a consequent enhancement in charge-carrier generation (or, in the case of organic semiconductors, exciton generation). [34, 48, 110] Previous reports have demonstrated that metallic nanovoid arrays are capable of hosting localized as well as propagating plasmonic excitations and are therefore extremely interesting for incorporation into solar cells in the form of nanostructured electrodes. [37, 111, 112] Here we investigate metallic nanovoid arrays fabricated using a simple, scalable, low-cost nanoimprint technique and assess their potential for trapping incident light in adjacent films. We first address plasmonic excitation on imprinted transparent dielectric - silver nanovoid interfaces. Then, in order to address the suitability of this method for manufacturing highly absorbing solar cells, we fabricate samples with organic semiconductor (OSC) - silver nanovoid interfaces. In such samples plasmonic excitations have two non-radiative loss channels: absorption in the silver and in the OSC film. Previous reports show that for organic-silver systems, light trapped in plasmonic excitations is preferentially absorbed in the OSC film, [25, 34] leading to an overall enhanced absorption compared to an unpatterned structure.

To elucidate the nature of the plasmonic excitation on imprinted nanovoids we first imprint silver nanovoid arrays adjacent to an optically transparent dielectric, PMMA (Polymethylmethacrylate). PMMA films of thickness around 300 nm are obtained by spin-coating from a toluene solution (96,9mg/ml) for 1 minute at 3000 rpm onto 2 cm² substrates. Quartz substrates are used for spectroscopy measurements and quartz substrates coated with indium tin oxide are used for SEM imaging. Nanoimprint lithography (NIL) [25, 86, 113, 114] (450 bar, 100°C, 5 minutes) is then used to structure the surface of the polymer film. The periodicity of the structured film is equal to that of the stamps, and the feature diameter and height are determined by the imprinting temperature, pressure and duration. Chips of anodized aluminum oxide (AAO) [93, 95] that feature large-area hexagonal lattices of pores are used as stamps. The nanostructured polymer films obtained (Fig. 5.4(a-d)) are then covered with a layer of silver via evaporation (nominally 150 nm thick) to produce samples with a nanovoid array interface (Fig. 5.4(e)). [25] Flat reference samples are fabricated in parallel under identical conditions without the imprinting step.

Stamps with two pore periodicities (490 and 95 nm) are used to fabricate nanovoid arrays of different pitch which we refer to as wavelength-scale and subwavelength-scale voids respectively. The voids can be well approximated by an array of hemispheres (Fig. 5.4(a)) with

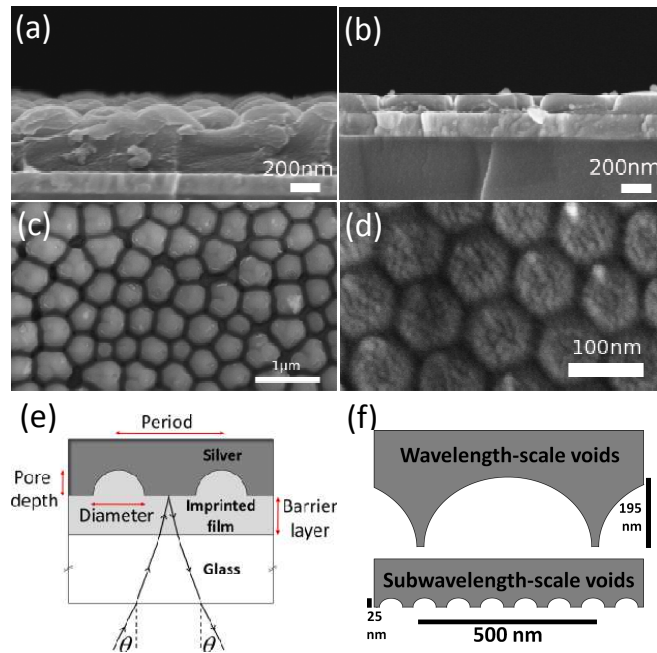


Figure 5.4: Angle-resolved reflectometry of imprinted nanostructures. (a-d) SEM images of imprinted nanostructures. A layer of indium tin oxide is visible between the structured polymer and the glass substrate in cross-sections images (a-b). (a) Transparent dielectric - and (b) organic semiconductor- wavelength-scale structures (490nm period) (c) Top-view of (a). (d) Organic semiconductor subwavelength-scale structure (95nm period). (e) Sample and measurement geometry. (f) Scale diagram of wavelength-scale and subwavelength-scale voids.

characteristic void diameters of 470 and 60 nm respectively. The pore depths are 195 and 25 nm respectively (Fig. 5.4(f)).

Specular reflectance spectra (Fig. 5.4(e)) are measured from 1.4-2.9 eV with a supercontinuum white-light laser source (Fianium SC-450-6) for incidence angles 0-45°. The incident beam is passed through a polarizer to obtain either TM or TE polarized light. The reflected beam is fiber-collected, separated into visible and IR wavelengths via beam-splitters and detected using Ocean Optics QE65000 and NIRQuest spectrometers respectively. [37] Reflectance R is normalized to a flat silver mirror and absorption A is obtained via $A = 1 - R$. Non-specular reflection is measured to be negligible - indicating that light trapping via coupling to surface modes [37] and multiple internal reflections dominates non-specular reflection. Similar results are found over the entire area of each sample.

Absorption in the structured dielectric-Ag samples (Fig. 5.5) occurs exclusively in the silver layer as the adjacent dielectric layer absorbs negligibly in this photon energy region. For the

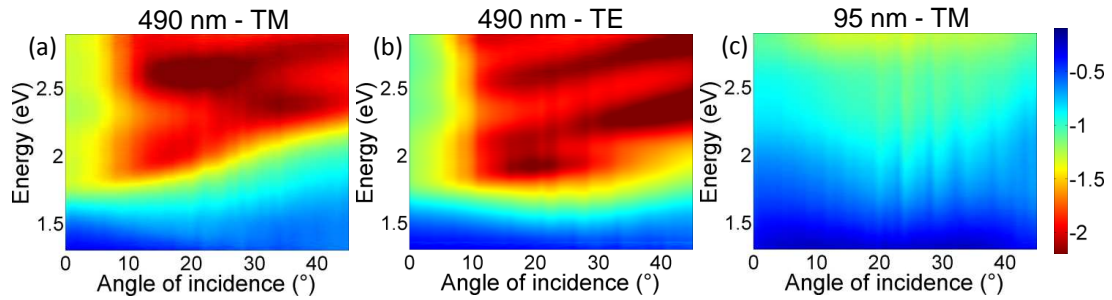


Figure 5.5: $\text{Log}_{10}(\text{Reflectance})$ spectra of transparent dielectric-Ag samples. Dark blue indicates high reflectance and red-black indicates low reflectance. The characteristic void period and polarization of incident light are indicated for each plot.

wavelength-scale voids, a number of broad, weakly dispersive absorption features can be seen between 1.9 and 2.9 eV (Fig. 5.5(a-b)), consistent with plasmonic excitation at the nanostructured dielectric-Ag interface. Similar absorption spectra for both TE and TM polarizations indicate that these modes are Localized Surface Plasmons (LSPs) which unlike Surface Plasmon Polaritons (SPPs) are polarization insensitive for hemispherical nanovoids. [26, 37] This is in qualitative agreement with measured and simulated spectra obtained for similar nanovoid arrays reported elsewhere. [37, 104, 112] Dispersive energy minibands (Fig. 5.5(b)) indicate coupling between localized plasmons in neighboring voids. [115] The absence of well-defined, strongly-dispersive TM absorption features, a signature of SPP excitation, indicates that SPP excitation is inhibited by the limited larger-scale order of the nanovoid array (Fig. 5.4(a),(c)). LSP modes are not observed for subwavelength-scale void samples with either TM (Fig. 5.5(c)) or TE (not shown) polarized light. The weaker absorption for the subwavelength-voids confirms the importance of LSP excitation for light trapping in nanovoid architectures.

To investigate imprinted nanovoid light trapping in solar cell geometries, we fabricate additional samples with organic semiconductor (OSC) - silver nanovoid interfaces. Here we use an OSC film of poly[2,6-(4,4-bis-(2-ethylhexyl)-4H-cyclopenta[2,1-b;3,4-b']dithiophene)-alt-4,7-(2,1,3-benzothiadiazole)] : phenyl-C61-butyric acid methyl ester (PCPDTBT:PCBM), two components commonly used in organic photovoltaics. [116] The absorption coefficient of this material features a prominent dip between 2 and 2.5 eV (Fig. 5.6(a)). [117] Precursor concentrations of 22,2 (PCPDTBT) and 24 mg/ml (PCBM) in chlorobenzene (mixed 1:2), and spin-coating conditions (1500rpm for 1 minute) are chosen to obtain films of 100 nm thickness, consistent with optimized solar cells of this type. [116] Nanoimprint lithography is then performed under identical conditions with the same stamps to fabricate samples that are directly comparable with the transparent dielectric samples. Due to the reduced thickness of the

OSC layer (necessary for efficient charge carrier extraction in solar cells), the voids imprinted with the wavelength-scale stamp have a truncated hemispherical shape (Fig. 5.4(b)) and hence a smaller depth (125 nm) than the voids in the dielectric sample (195 nm). Otherwise, the dielectric and OSC samples have equal void period, diameter and depth.

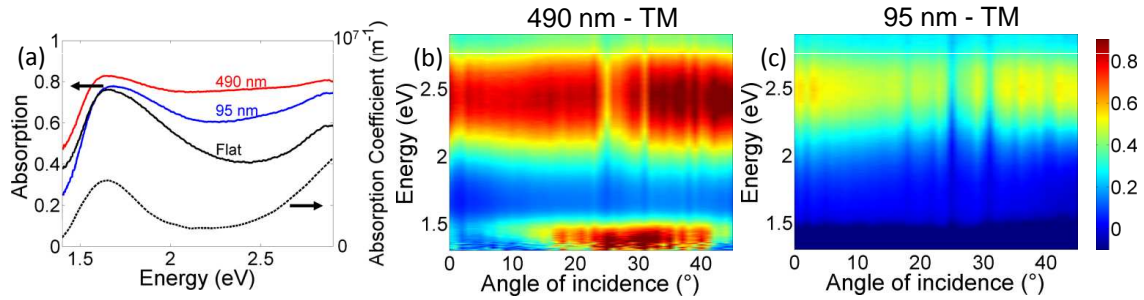


Figure 5.6: Absorption spectra of semiconductor-Ag samples. (a) Absorption of TM-polarized incident light for each of the sample geometries at 0° incidence (full lines) and the absorption coefficient of PCPDTBT:PCBM (dotted line). (b-c) Relative enhancement in absorption $(A_{\text{struc}} - A_{\text{flat}}) / A_{\text{flat}}$ for structured PCPDTBT:PCBM - Ag samples compared to the flat sample. The value of the enhancement is indicated by the linear color scale.

At 0° incidence we observe total absorption enhancements (integrated over the energy range between 2.9 and 1.4 eV (430 and 880 nm)) of 40 and 20% for the wavelength- and subwavelength-scale voids respectively (Fig. 5.6(a)). Spectra of relative absorption enhancement $((A_{\text{struc}} - A_{\text{flat}}) / A_{\text{flat}})$ do not display a strong angle-dependence (Fig. 5.6(b) and Fig. 3(c)) - the enhancement primarily occurs at energies where the OSC absorbs poorly (c.f. absorption coefficient, Fig. 5.6(a)). This is likely due to light filtering: photons that are inefficiently absorbed by the OSC film are more likely to propagate to the silver interface and benefit from plasmonic light trapping. In other words, the effect of the nanostructured electrode is to boost absorption of light at wavelengths where it is most needed.

Nevertheless, an absorption feature is observed for the wavelength-scale structure at 2.5 eV at large angles (Fig. 5.6(b)) which compares well with the wavelength-scale structure for the transparent dielectric film (Fig. 5.5(a)), although the feature is less pronounced and minibands dispersions are not resolved. This difference is attributed to absorption in the polymer (which has the effect of broadening the absorption features) and the truncated shape of the voids in the OSC sample. Previous studies have shown that the structure height of nanostructured metallic gratings has a strong influence on plasmonic resonances (both LSP and SPP) of the structure. [31, 104] Absorption of TE-polarized light (not shown) is similar to that of TM light, demonstrating the polarization independent plasmonic enhancement.

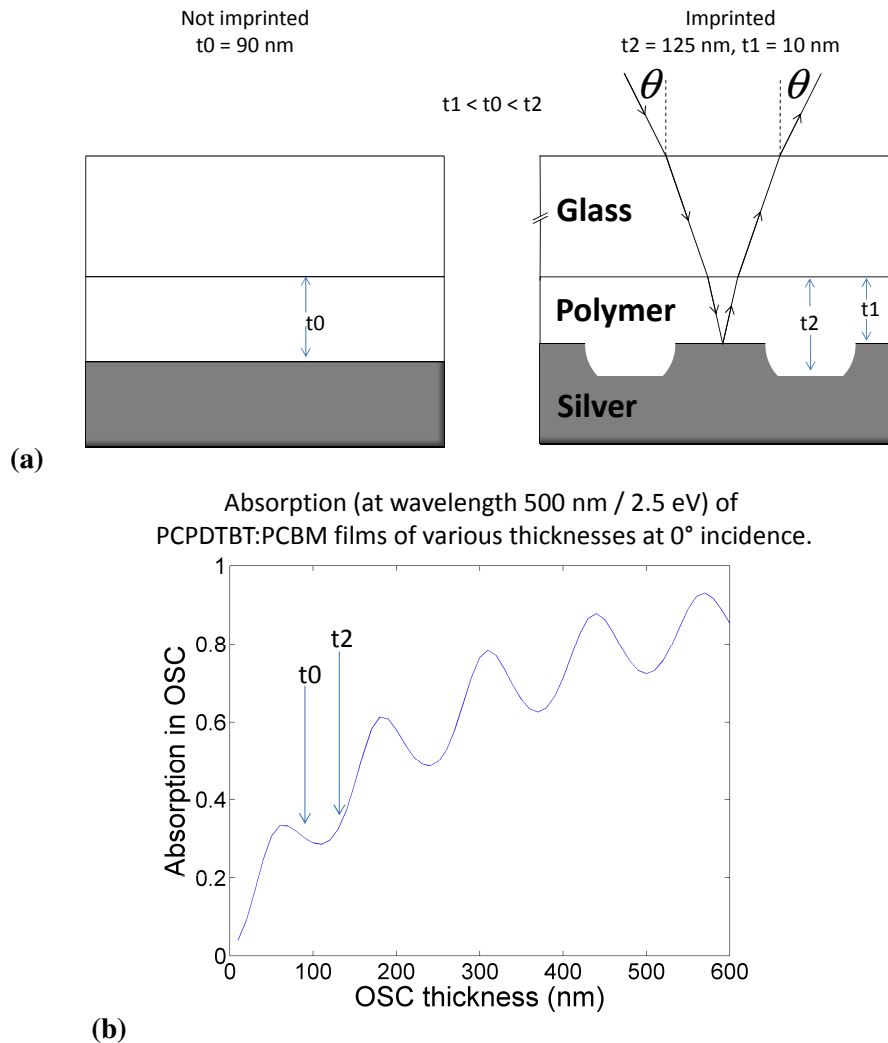


Figure 5.7: The resonant absorption observed in the imprinted polymer films is not due to a Fabry-Pérot resonance. (a) Schematics of the sample architecture before (left) and after (right) imprinting truncated hemispherical voids. The associated characteristic layer thicknesses are indicated. (b) Simulated absorption in the organic semiconductor (OSC) of the planar sample for film thicknesses between 0 and 600 nm. The absorption corresponding to the characteristic thicknesses is indicated.

Simple finite element simulations[25, 118] of absorption in a planar architecture (Fig. 5.7) are used to demonstrate that the enhancement at 2.5 eV cannot be attributed to a Fabry-Pérot resonance for the modified OSC film thickness (125 nm for the truncated voids, Fig. 5.4(b) compared to 100 nm for the flat film) after imprinting.

A second absorption feature at around 1.45 eV (Fig. 5.6(b)) is also correlated with a dip in the absorption coefficient of the OSC. The subwavelength-scale structure also provides an ab-

5.3 Summarizing remarks

sorption enhancement (Fig. 5.6(c)). No strong absorption features within the measured photon energy range are observed. This is consistent with the transparent dielectric companion sample.

In this work we have measured the angle-resolved specular reflectance spectra of imprinted nanovoid arrays. For samples featuring transparent dielectric - metal nanovoid interfaces we observe strong excitation of LSPs and evidence of plasmon-plasmon coupling for large structures (490 nm period) at visible wavelengths. We observe corresponding absorption enhancements in companion samples featuring OSC - metal nanovoid interfaces with evidence for LSP excitation in large structures (490 nm period). The absorption enhancement is found to be greatest at wavelengths where PCPDTBT:PCBM absorbs weakly. Nanostructured electrodes therefore have the potential to enhance solar cell performance by boosting absorption at wavelengths where it is most needed.

5.3 Summarizing remarks

In this chapter, one of the central results of this thesis has been presented: significant light trapping is enabled by the nanostructured metallic electrode architecture, the fabrication of which was presented in Chapter 3. We have already begun to characterize the nature of this light-trapping. In the next chapter, we delve deeper, with important insights enabled by finite element simulations of nanovoid electrode devices.

6 Experiment and simulation compared

In the previous chapter, light-trapping in nanostructured electrode architectures was demonstrated. However, the fraction of light that is absorbed in the semiconductor cannot be determined from reflectivity measurements alone. We turn to simulation to provide more insight. We demonstrate good agreement between simulated and experimental absorption spectra for samples featuring structured interfaces between PCBM and silver. Simulations indicate that the majority of the additional absorption indeed occurs within the organic semiconductor. This is a critical result - only if the additional trapped light is absorbed in the semiconductor will the absorption enhancement lead to an efficiency enhancement in thin-film solar cells. The simulations confirm the finding of the previous chapter - light-trapping is enabled by localized plasmonic modes. Two distinct modes are observed: one within the voids and one along the inter-void space. For the investigated geometry, it is found that the voids can be treated as independent antennas - a collective effect of neighboring voids is not observed.

The work in this section is based on *Dunbar et al., 2012, Physical Review B* [25].

In this study, high order nanovoid arrays are investigated for light trapping applications in organic solar cells. Organic solar cells, as well as other thin-film photovoltaic technologies based on materials such as amorphous silicon and GaAs, stand to benefit greatly from plasmonic light trapping, as it would enable the construction of devices with thinner active layers (which display better charge transport properties) without compromising total light absorption. This would correspond to a simultaneous increase in power conversion efficiency and a reduced consumption of the active material.

In order to fabricate highly ordered plasmonic structures across large areas with precise control over the geometry, we employ an imprinting technique. Here, an anodized aluminum oxide (AAO) stamp featuring highly ordered hexagonal pore geometry is used to imprint an organic film, forming an array of free-standing organic nanowires. A thick layer of metal (more than 200 nm, considerably larger than the typical height of the nanowires) is deposited on top via

6.1 Sample preparation

thermal evaporation. As the deposited silver structurally conforms to the underlying organic nanowire array, a metal-organic nanovoid interface is obtained. With this technique, the ordering, periodicity and diameter of the organic nanowires and hence the metallic nanovoids can be determined by adjusting the geometry of the AAO pore array through control of processing parameters. The pore diameter can be conveniently determined using a pore-widening step, and the pore periodicity can be set to a value within a broad range of 50-420 nm. [93] The height of the organic nanowires, corresponding to the depth of the nanovoids, is largely determined by the imprinting pressure, temperature and duration. The flexibility of this technique allows the fabrication of a wide variety of nanovoid array geometries, which can be adjusted to be application specific. In addition, this technique requires no electron-beam lithography, which is an expensive high-end technology with limited application for large-area manufacturing. The stamps used in this study are produced by anodization, which is a simple, fully scalable and inexpensive technique that can be immediately incorporated into commercial solar cell fabrication. In fact, it is conceivable that this technique could be incorporated into roll-to-roll assembly. Previous reports on the fabrication of structured organic interfaces via imprinting, which include a number in which AAO stamps were used, [119, 120] demonstrate the potential of this technique. [121, 122] These studies were primarily focused on using imprinting to improve the morphology in bulk heterojunction solar cells.

6.1 Sample preparation

Two stamps are fabricated with pore-pore periodicities of 60 (stamp A) and 100 nm (stamp B). Mechanically polished Al foils (99.999%, Goodfellow) first undergo electrochemical polishing in a 1:3 volume ratio solution of perchloric acid in ethanol (> 95 %) for 8 minutes under a bias of 20 V. The polished foils are then anodized following a two-step anodization process. [93, 95] The pore periodicity can be controlled by varying the electrolyte and the potential under which the anodization is carried out. Stamp A is produced by anodizing polished Al foil in sulphuric acid (0.3M) at a potential of 25V. The anodization for stamp B is carried out in oxalic acid (0.3M) at a potential of 40 V. The porous oxide is then removed in a solution of phosphoric (6 wt.%) and chromic (1.8 wt.%) acid, leaving a highly ordered aluminum surface. The first anodization and oxide removal steps have the function of patterning the aluminum foil in preparation for the second anodization step. This is conducted for 1 and 5 minutes for stamp A and B respectively. The resulting pores in the aluminum oxide membranes are then widened in phosphoric acid (5 wt.%) for 15 minutes (stamp A) and 30 minutes (stamp B). The resulting membranes are then placed in a desiccator where a small droplet of F13-TCS silane solution placed by the stamps is allowed to evaporate. [98] A thin silane layer

is formed on the surface of the stamps, which acts to reduce the adhesion with the organic material during imprinting. A SEM image of stamp A is shown in Fig. 6.1(a), and a side-on schematic is shown in Fig. 6.1(e). PCBM films are spin-coated on 2 cm² glass substrates. The silanized AAO membrane is cleaned via ultrasonification in chlorobenzene for 5 minutes, rinsed in isopropanol and dried with a stream of nitrogen. It is then used to imprint the PCBM film in a mechanical hot press at a pressure of 250 bar for 5 minutes at 120 °C. All samples are fabricated in duplicate: once on quartz glass substrates and once on conducting ITO (Indium Tin Oxide) -covered glass substrates. The samples on ITO are used for SEM imaging whilst the ITO-free layers are used for spectroscopy. A thin layer of ITO is undesirable in a spectroscopy sample due to thin-film interference effects and ITO's non-negligible absorption. The samples on ITO-covered glass and quartz glass otherwise undergo identical production. The structuring of the organic layer via imprinting is shown schematically in Fig. 6.1(f). Samples A and B (Figures 6.1(b) and 6.1(c)), imprinted with stamps A and B respectively, exhibit nanowire size, ordering and periodicity (60 and 100 nm) consistent with the hole array of the stamps. A third sample is produced under identical spin-coating conditions. Instead of an imprinting step, the sample undergoes an annealing treatment at the same temperature and for the same duration as the imprinting process, acting as a planar sample for comparison with samples A and B. Finally, silver is thermally evaporated on top of the structured (Fig. 6.1(g)) and planar PCBM layers. Despite depositing more than 200 nm of silver, a discernible hexagonally packed array of mounds across the top surface of the structured samples is observable in SEM pictures (not shown). This is consistent with surface modulation arising from deposition on a structured substrate. When samples are cleaved in preparation for cross section SEM imaging, the nanovoid array can be viewed directly in positions where the silver film has separated from the PCBM film during cleavage (Fig. 6.1(d)).

Samples A and B display striking differences in the geometry of the PCBM nanowire array. In addition to size and periodicity, the nanowires in sample A and B also vary in shape. Whereas the typical nanowire in sample A (Fig. 6.1(a)) approximates a cylinder with aspect ratio 1, the typical nanowire in sample B (Fig. 6.1(c)), more closely approximates a cone with slanted orientation in respect to the substrate. This shape is attributed to a slight deformation of the imprinted pattern in PCBM, which is in a molten and viscous state at 120 °C, [99] upon demolding. It is important to note the fine size of the features. Sample A exhibits a highly ordered array of nanovoids of diameter 40 nm, height 40 nm and periodicity 60 nm. An array of nanovoids of such small size with a high degree of order is beyond the capabilities of many other techniques. Highly ordered arrays of metallic nanovoids fabricated using the polystyrene sphere templating technique for example, typically feature nanovoids of diameter much greater than 100 nm. [37]

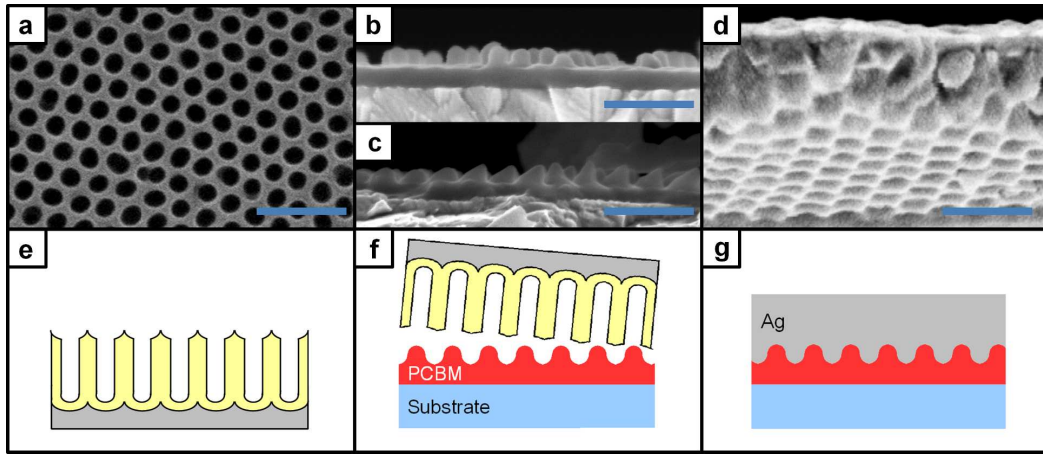


Figure 6.1: Fabrication of PCBM-Ag nanovoid arrays. Sample preparation (a-d) SEM images. All scale bars are 200 nm long. (a) Top view of a stamp: highly ordered porous AAO. The hexagonal packing is evident. (b) Sample A. PCBM nanowire array produced after imprinting a PCBM film with a stamp with 60 nm pore periodicity. (c) Sample B. PCBM nanowire array produced after imprinting a PCBM film with a stamp with 100 nm pore periodicity. (d) Ordered silver nanovoid array, as observed from underneath (the PCBM nanowires have been removed in this position, see text). (e-g) Schematic of sample preparation. (e) Side-on view of a finished stamp. (f) Imprinting of a PCBM film to produce ordered nanowires with diameter and periodicity corresponding to that of the stamp. (g) A finished sample: a silver nanovoid array in intimate contact with a layer of PCBM.

The reflectance of the samples is measured using a UV-Vis spectrometer (U-3501, Hitachi) fitted with an integrating sphere. The sample is positioned at an angle of 10° to the incident beam. In order to minimize silver oxidation, the samples are not exposed to air between the silver deposition and the measurement. Optical and UV illumination is provided by tungsten and deuterium lamps respectively. The light is incident on the sample through the glass side, and under the assumption that the transmission is zero, the absorbance A of the system can be obtained from the reflectance R using $A=1-R$.

6.2 Reflectivity measurements

The experimentally obtained absorption spectra are shown in Fig. 6.2. Each spectrum exhibits maximum absorption in the range 300-330 nm, which is primarily attributed to absorption in silver. This spectral position corresponds to silver's bulk plasmon resonance. [123, 124] In the context of this system, the strong absorption in this wavelength range can be understood to arise from a sharp decrease in the real part of silver's refractive index and hence an increase in transmission at the PCBM-Ag interface. At wavelengths beyond this peak, where (planar)

silver typically exhibits near-perfect reflection, absorption features that are attributed to PCBM are observed.

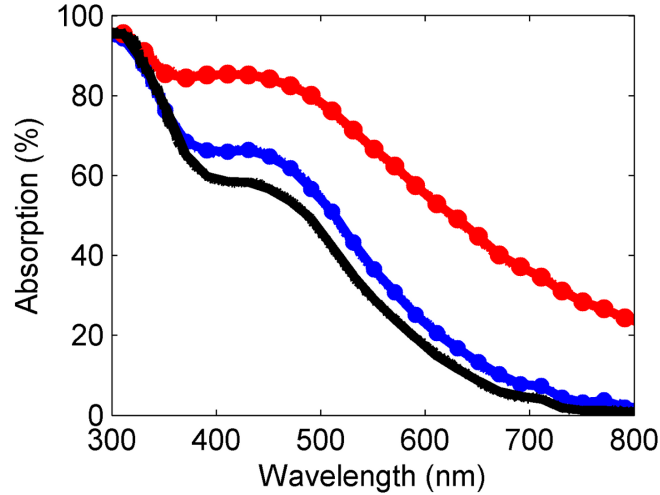


Figure 6.2: Absorption spectra of planar (black line), nanostructured with feature periodicity 60 nm (small blue circles) and nanostructured with feature periodicity 100 nm (large red circles) samples as obtained from reflection spectroscopy measurements.

A clear enhancement in total absorption over the planar sample is observed for both of the nanostructured samples. For the 300-800 nm wavelength range, the absorption is increased in samples A and B by 15% and 80% respectively. It is important to note that the total volume of PCBM in the nanostructured sample does not exceed that of the planar sample. In fact it is slightly less, as a small amount of PCBM invariably adheres to the stamp during demolding, despite anti-adhesion measures being taken. Nevertheless, broad enhancements in total absorption (the contribution of which is attributed to PCBM will be discussed later in this letter) are observed for the nanostructured samples. In sample A, with 60 nm feature periodicity, the enhancement is concentrated within the absorption range of PCBM, with a peak enhancement at 430 nm. For sample B, which has 100 nm feature periodicity, a significantly higher level of light trapping is observed. The absorption enhancement observed for sample B extends well beyond the absorption edge of PCBM (around 750 nm). We conclude therefore that both the absorption beyond the absorption edge and a significant amount of absorption below it must occur within the silver layer. This significant coupling to the silver layer as a result of the interface nanostructure could be facilitated by excitation of surface modes or an enhanced transmission through the interface. In order to obtain an insight into the absorption enhancement mechanisms governing the behavior of a PCBM-silver nanovoid interface, three-dimensional full wave simulations have been carried out.

6.3 Finite element simulations

The Finite Element Method (FEM), invoked with commercially available software (COM-SOL), is used to numerically solve the time-harmonic wave equations in the electric field E and the magnetic field H :

$$\vec{\nabla} \times \vec{\nabla} \times \vec{E} - n^2 k_0^2 \vec{E} = 0 \quad (6.1)$$

$$\vec{\nabla} \times \left(\frac{1}{n^2} \vec{\nabla} \times \vec{H} \right) - k_0^2 \vec{H} = 0 \quad (6.2)$$

where n is the complex refractive index and k_0 is the magnitude of the free-space wave vector. The optical field distributions in systems featuring planar and nanvoid interfaces between silver and PCBM are compared. Whereas a completely enclosed void can be accurately treated using Mie theory, numerical techniques are generally required to investigate plasmonic behavior in metallic nanovoids with more arbitrary geometries. The system consists of three layers: glass, PCBM and silver. Values for the complex refractive indices of PCBM and silver are obtained from the literature, [27, 125] and the glass is assigned a refractive index of 1.4. Surface roughness at the two interfaces is neglected and the materials are assumed to be optically isotropic.

The PCBM-silver interface is defined in the x-y plane, with plane wave illumination from normal incidence (along the z direction) as shown in Fig. 6.3(a). Circularly polarized incident light is used. As the magnitude of the electric field vector in circularly polarized light is preserved as it rotates in the plane of polarization, this is a close approximation of the unpolarized illumination of the lamp (and sunlight) - the time averaged polarization is zero in both cases. Periodic boundary conditions are applied to all four side boundaries. The system is terminated at the illumination side with a perfectly matched layer, [126] designed to absorb all reflected light and thus minimize artificial reflections. The planar interface is modeled with a PCBM layer thickness of 75 nm. The structured interface is modeled with size parameters chosen to resemble sample A (Fig. 6.3(b)), whose symmetric structure is conducive to accurate simulation (corresponding simulations of the asymmetric nanovoids, sample B, are addressed later in this section). The PCBM nanowire is modeled as a cylinder with a height and diameter of 40 nm. The tip is rounded using a 10 nm high oblate spheroid cap, and the join to the bulk PCBM layer is softened with a curved beveled edge of radius 5 nm. The thickness of the underlying, planar PCBM layer is set to 40 nm. All of these values are based on an analysis of SEM pictures (such as 6.3(c)) using an image analysis software (ImageJ). Square and hexagonal lattices are simulated by via appropriate placement of one or multiple nanovoids (one and

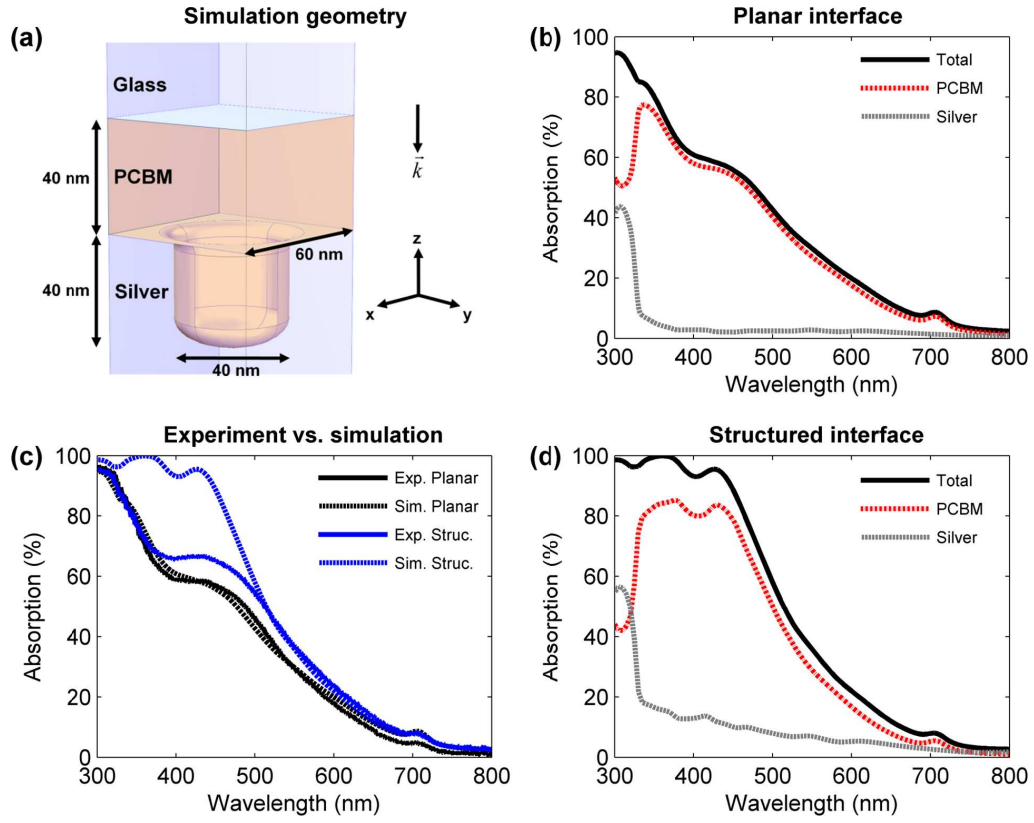


Figure 6.3: Simulated absorption spectra for hexagonally ordered void arrays with void periodicity 60 nm. (a) The simulation geometry of a single void. The plane wave is incident from the glass side. (b) The agreement between the experimental and simulated total absorption for the planar and structured system, where the structured system refers to sample A (60 nm feature periodicity). (c-d) The simulated contributions from PCBM and silver to the total absorption in the systems featuring a planar (c) and structured (d) interface. Important features that arise due to the structured interface include the emergence of two new peaks in PCBM absorption: at 375 and 430 nm.

four respectively) in appropriate periodic cells. Unless otherwise indicated, a hexagonal lattice is used, resembling the void ordering observed in experiment.

The time-averaged energy absorption rate in each material is calculated using the expression:

$$\frac{1}{2} \int_V \omega \epsilon_2 |E|^2 dV \quad (6.3)$$

where the integral is evaluated over the material volume V , ϵ_2 is the imaginary part of the permittivity and ω and E the angular frequency and electric field strength of the electromagnetic field respectively. As a check, the reflectance of the composite system is calculated independently as a flux integral over the boundary separating the system and the perfectly matched

layer. The sum of the independently calculated absorption and reflection is well within 0.1% of unity for all simulated wavelengths for planar as well as structured interface geometries.

The routine was rigorously tested to confirm the validity of the calculations and to quantify the strength of the conclusions that can be drawn from the results. Absorption and reflection spectra for arbitrary planar multi-layer systems agree exactly with those calculated using transfer-matrix formalism.¹ Excellent agreement with experimentally determined total absorption of the planar system is observed (see Fig. 6.3(b), black curves). The slight discrepancy between the experimental and simulated spectra can be attributed to a number of factors including the small offset in incidence angle between the experimental and modeled system, and the assumption of smooth interfacial surfaces. The relative contributions of the PCBM and silver layers to the total absorption are plotted in Fig. 6.3(c). The typical mirror-like nature of planar silver is observed, with excellent reflection properties in the optical and NIR wavelength region. Accordingly, absorption in the PCBM at these wavelengths accounts for almost all of the total absorption. At lower wavelengths the mirror-like property is no longer as observable. As mentioned earlier, the transmittance at the PCBM-Ag interface becomes large at wavelengths close to the bulk plasmon frequency, contributing to a sharp peak in absorption in the silver layer. This causes a corresponding dip in the PCBM absorption at these wavelengths. Above 330 nm, the PCBM absorption spectrum displays the typical shape that is observed in the complex part of its refractive index, [125] including the main peak at around 340 nm, a shoulder at around 450 nm and a small peak at around 700 nm. Given the very good agreement between simulation and experiment for the planar case, it is reasonable to infer that the PCBM and silver absorption contributions to the experimentally determined total absorption (Fig. 6.2) are similar as those shown in Fig. 6.3(c).

As shown in Fig. 6.3(b), we also observe good agreement between the simulated and experimentally determined absorption spectra for the structured interface (blue lines), although the agreement is not as close as it is for the planar case. This discrepancy will be discussed in more detail later in this subsection. We note however, that the enhancement in absorption over the planar case is clearly reproduced. Importantly, the wavelength of the maximum enhancement in absorption, 430 nm, coincides exactly with the position of a peak in the simulated spectrum. The relative contributions of the PCBM and silver layers to the total absorption for the structured case are plotted in 6.3(d). The general behavior is similar to that of the planar system, although there are some important differences. Given that the structured interface is capable of hosting localized plasmonic modes, the observed overall increase in the absorption of the system is expected. The spatial distribution of this additional absorption is

¹Transfer-matrix calculations are performed with FreeSnell, a thin-film optical simulator. <http://people.csail.mit.edu/jaffer/FreeSnell/>

highly dependent on the nature of the excitation and the refractive indices of the two materials. This has been calculated to be strongly concentrated in the organic layer for SPP modes on silver-organic semiconductor interfaces.⁴ In the system simulated here, the absorption in silver has increased significantly across the spectrum, in particular in the UV region. Importantly however, the PCBM absorption has also significantly increased. Two additional peaks are evident, one at 375 nm, which is easily resolved from the 340 nm PCBM absorption peak; and a second at 430 nm, which, as mentioned above, coincides with the wavelength of maximum enhancement in the experimental absorption spectrum.

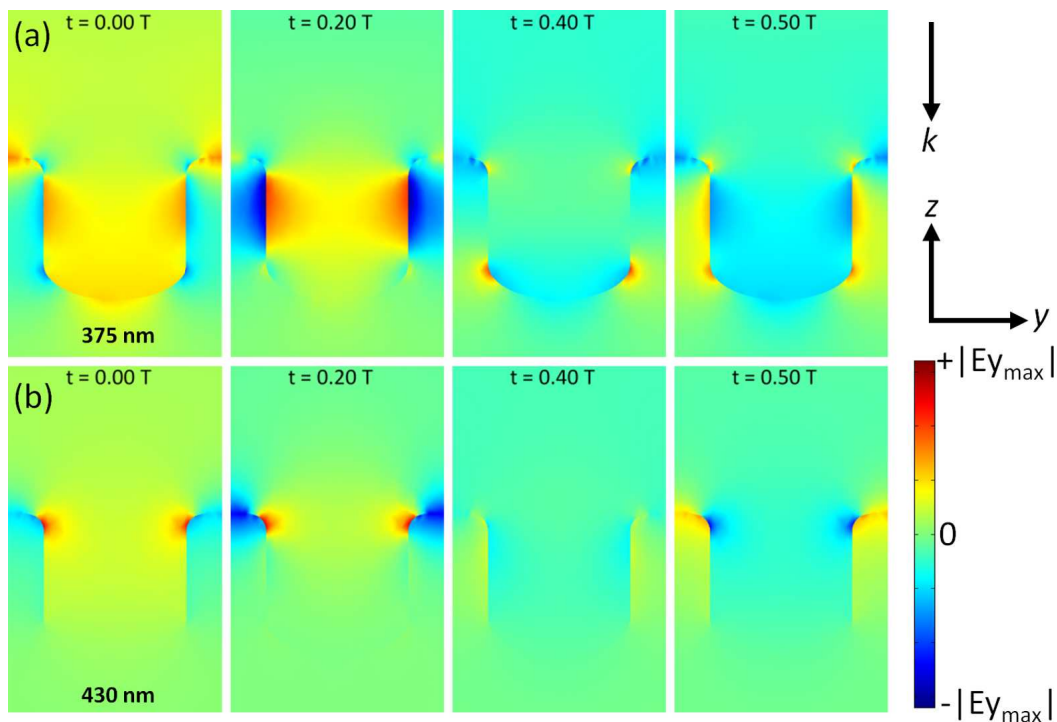


Figure 6.4: Temporal variation of the electric field strength. Simulated y-component of the electric field at (a) 375 nm and (b) 430 nm for times $0T$, $0.2T$, $0.4T$ and $0.5T$ respectively, where T is the period of the oscillation of the incident wave. The linear color scale indicates the strength of the field relative to the maximum and minimum values observed at each wavelength.

The variation of the y-component of the electric field (Fig. 6.4) over time reveals the nature of the peaks observed in Fig. 6.3. These profiles, displaying the behavior at four points in time across half of the periodic cycle T , are taken across a plane $x = \text{constant}$ which bisects a row of nanovoids separated by the lattice period. Similar plots are obtained regardless of whether the voids are ordered in square or hexagonal lattices. Absorption at wavelengths corresponding

to peaks in the PCBM absorption spectrum is highly localized at the interface, characteristic of surface-bound plasmonic excitation. The short wavelength peak (Fig. 6.4(a)) corresponds to enhanced electric field strength along the inner walls of the voids. The localization at this wavelength is evidently achieved via the excitation of a standing wave along the rim of the nanovoid, which has been proposed previously, but for much larger voids. [37, 127] Antinodes are observed on the nanovoid sides and “shoulders”, separated by nodes. The amplitude of the surface mode decreases along the length of the void, which we attribute to absorption in the semiconductor and metal (plotted explicitly in Fig. 6.7). We note that the void diameter is much smaller than the wavelength of incident light; penetration is only possible due to the excitation of the surface mode. At the longer wavelength (Fig. 6.4(b)), light does not significantly penetrate into the voids, rather, an enhanced electric field is observed along the inter-void space.

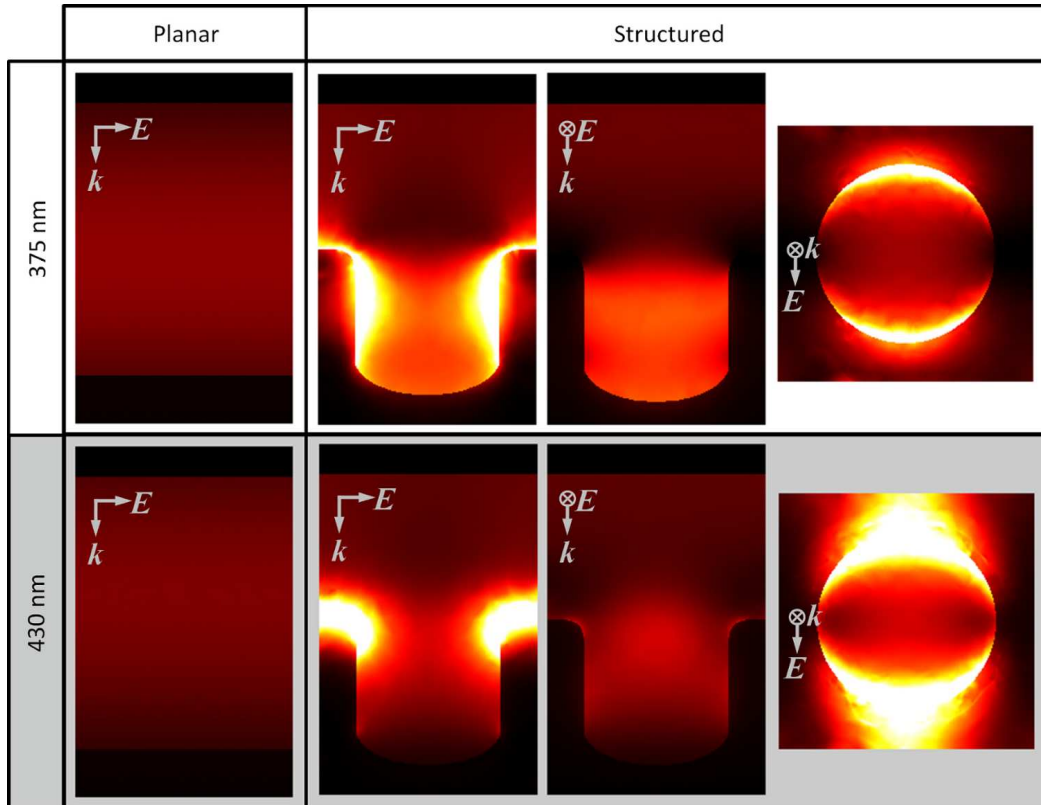


Figure 6.5: Absorption rate profiles (linear color scale) for wavelengths 375 and 430 nm. Black indicates areas of zero absorption and white indicates areas of maximum absorption. For each wavelength, the planar and structured interfaces are compared. For the structured interface, the absorption rate profile is shown in three different planes, as indicated relative to the electric field vector E and propagation vector k . For each wavelength displayed, significantly larger absorption, which is strongly spatially localized in nature, is observed in the structured system.

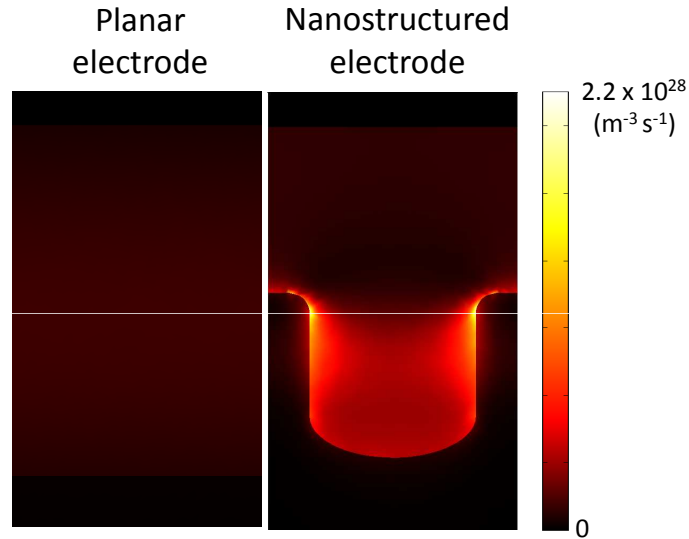


Figure 6.6: The absorbed photon density at 375 nm for a planar and nanostructured electrode architecture. In the semiconductor region, it can be understood as the exciton generation rate if it is assumed that one exciton is generated for every absorbed photon. The illumination intensity is that prescribed by the AM1.5G spectrum at this wavelength. The maximum exciton generation density in the semiconductor adjacent to the nanostructured electrode is 17% larger than the corresponding maximum in the planar electrode case.

Time-averaged absorption profiles for polarization along the (10) crystal direction are extracted to illustrate the relationship between the mode absorption and the orientation of the electric field vector of the incident light (Fig. 6.5). The profiles are plotted in three different planes for the structured case: the y - z plane ($x=0$), x - z plane ($y=0$) and the x - y plane ($z=-2$ nm) respectively. The profile in the x - y plane is taken within the silver layer, as opposed to directly at the interface. The antinodes of the standing wave responsible (Fig. 6.4) for the short wavelength peak (375 nm) can be observed but not clearly resolved and the amplitude of the wave (and hence the mode absorption) is seen to decrease along the length of the void towards the base. The relatively insignificant penetration of the long-wavelength mode (430 nm) compared to the short-wavelength mode can clearly be seen. Localized absorption is entirely absent in the system with the planar interface. Excitation of both void and inter-void modes is observed most prominently along the direction of the electric field. The absorption profile for circularly polarized incident light (not shown) is accordingly symmetric about the z -axis. The exciton generation density can be calculated from the absorption profile by first converting to an absorbed photon density and then assuming that one exciton is generated for every absorbed photon (Fig 6.6). It is observed that the maximum exciton generation density in PCBM at

375 nm is up to 17% larger for the nanostructured electrode than the corresponding maximum density for the planar case under AM1.5G illumination levels.

Similar behavior is observed regardless of whether the voids are ordered in square or hexagonal arrays (Fig. 6.7). The short wavelength peak has been shown to be due to strong localized absorption within the void (Fig. 6.4(a)), and therefore its spectral position is insensitive to the void ordering. We see that the magnitude of this peak is identical for square and hexagonal lattices despite the increased (15%) void packing density of the hexagonal lattice. This is because the total absorption at this wavelength is already saturated for the square lattice; increasing the density of voids cannot increase the total absorption of the system beyond 100%. In the hexagonal case the light trapped in this mode per void decreases compared to the square case, with the relative absorption in the semiconductor and silver remaining unchanged. The long-wavelength peak corresponds to localization between the voids (Fig. 6.4(b)) and we observe a weak dependency on lattice order, or in other words, on the position of the nearest neighboring voids. The width of this peak is slightly broadened for the square array: a result of the reduced rotational symmetry of the square array compared to the hexagonal array. However it must be stressed that the overall difference between the two configurations is small: the total absorption for the hexagonal lattice, spectrally integrated over the investigated wavelength region, is higher than that of the square lattice by less than 1%.

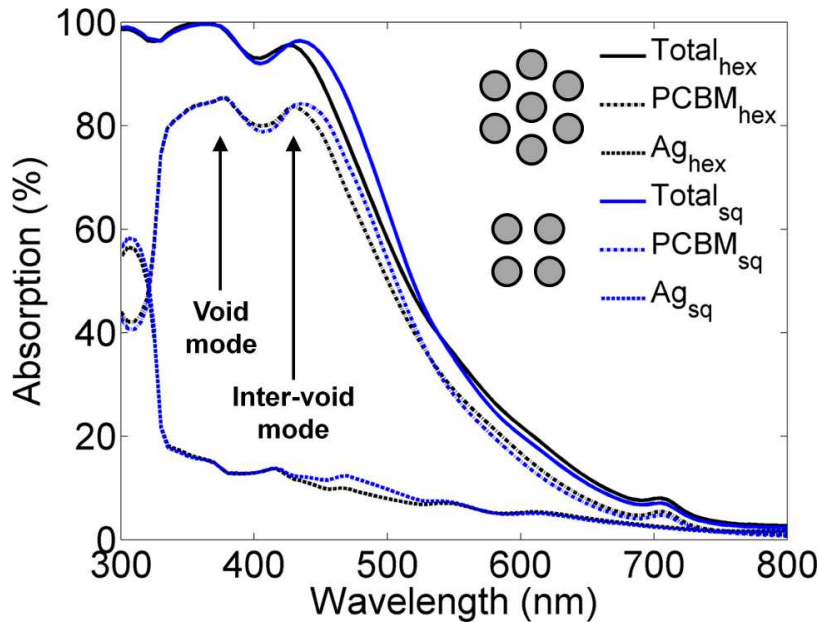


Figure 6.7: The effect of the void lattice type (hexagonal or square) on light dissipation.

Simulations (for the square lattice for example) where the polarization vector is held constant over time indicate an identical response regardless of whether the electric field is aligned along

the (1,0) (void spacing of the lattice constant a) or (1,1) (void spacing of $a/\sqrt{2}$) crystal directions. Polarization independence (at normal incidence) has also been observed in similar systems such as square arrays of holes [128] in metal films and hexagonal arrays of silver nanoparticles [129]. Combined with the result of Fig. 6.7 - the response is similar for square and hexagonal lattices - we see that the placement of neighboring nanovoids is of minor importance for this configuration (60 nm lattice constant and 40 nm void diameter): the long wavelength mode does not significantly extend beyond the distance to the next void to the extent that the lattice order is of major importance and the short-wavelength mode exists entirely within the voids themselves. The response can effectively be considered as the sum of the responses of non-interacting nanovoids rather than a collective response of interacting nanovoids.

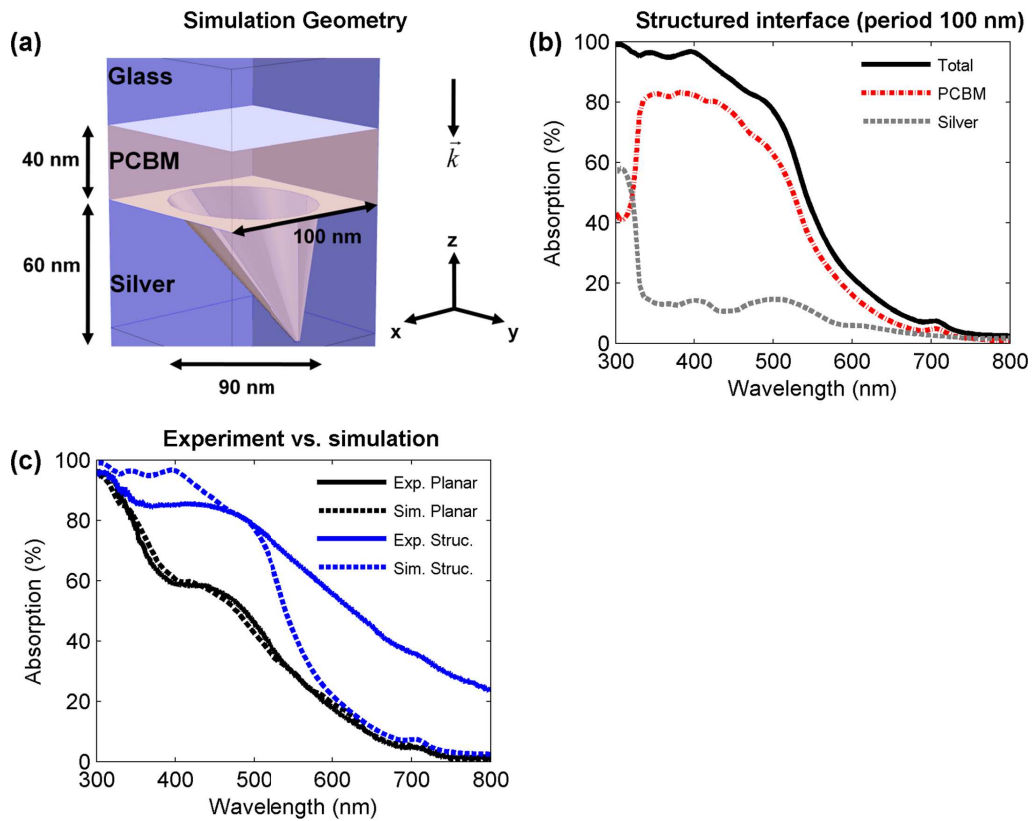


Figure 6.8: Simulated absorption spectra for square-packed void arrays with void periodicity 100 nm. (a) The simulation geometry of a single void representative of sample B. (b) The agreement between the experimental and simulated total absorption for the planar and structured system. (c) The simulated contributions from PCBM and silver to the total absorption in the system.

Sample B (Fig. 6.1(c)) is modeled using a square array of slanted cones with half-angle 35° which penetrates into the silver layer to a depth of 60 nm and has an opening diameter of 90 nm (Fig. 6.8(a)). The tip is softened with a 3 nm diameter circle. The total volume of PCBM is the

same as in sample A however due to the structure, the total absorption (Fig 6.8(b) and 6.8(c)) is about 20% higher than that what is simulated for sample A, This increase is more pronounced at longer wavelengths as observed experimentally, and the “smoother ”(compared to sample A) absorption curves indicates a larger number of resonances because of the non-symmetric void shape. It is expected that the large variation in cone size, symmetry and orientation in the experimental structure is fundamental for the broad band light-trapping experimentally observed for sample B. However, given the extremely computationally expensive nature of three-dimensional finite element simulations, a treatment of all of these effects is beyond the scope of this paper.

We will now discuss the agreement between experimentally-determined and simulated absorption spectra for the structured interface system, and attempt to account for the discrepancy (Fig. 6.3(b), blue lines). Deviations between experimental and simulated structures is proposed as the primary cause of this discrepancy. As stated earlier, the most significant enhancement in absorption occurs at around 430 nm for both the simulated and experimental spectra. However, the absorption peak at this wavelength is decidedly sharper in the simulated spectrum - a consequence of the perfect uniformity in the shape of the simulated voids and the irregularity of the voids across the experimental sample. The wavelengths at which plasmonic modes can be efficiently excited in nanovoid systems is highly dependent on the void geometry. [37] Therefore, a distribution in void size and shape around a mean value, and a corresponding distribution of wavelengths at which the plasmonic modes are efficiently excited, would have the observed effect of broadening the absorption peak. This effect is expected to be exacerbated for sample B, where the asymmetry and variation in shape is increased (Fig. 6.1(c)). This significantly increases the difficulty of simulation. The higher absorption of sample B is an indication that increased variation of plasmonic hosting features is advantageous for obtaining broad-band light trapping, which is the principle behind tandem plasmonic devices. [34] For rigorous reports on the effect of void shape and size on plasmonic excitation, we refer the reader to the literature. [37, 104] A second reason for the discrepancy is that due to inherent surface modulation in both the PCBM film and the stamp, a finite area of PCBM will have insufficient contact to the stamp during imprinting. The sample area is therefore made up of positions displaying a perfect imprint and positions where the imprint is either less prominent or absent. The absorption of such a system could be given as an average of the absorption of the structured and planar systems, appropriately weighted by the fractional area of each. This correction would have the effect of making the absorption spectrum for the structured case more similar to that of the planar case, as is observed in the measured data. Despite these difficulties, the observed overall agreement between experiment and simulation is quite strong.

Even better agreement is expected if the order and regularity of the experimental structures is further improved.

Conclusion

In conclusion, significant light trapping has been demonstrated in a system featuring an organic semiconductor adjacent to an ordered metallic nanovoid array. In order to realize these structures, an imprinting technique was employed. The applicability of this technique extends to all materials that are soft enough to be imprinted, and the flexibility in pore diameter, depth and periodicity allows a degree of application-specific “tuning”. The fabricated nanostructured interfaces feature hexagonally packed arrays of silver nanovoids, upon which localized and propagating surface plasmons can be excited. Using two different nanovoid geometries, featuring nominal void periodicity of 60 and 100 nm respectively, we observed total absorption enhancements of 15 and 80% across the wavelength region 300-800 nm. Three-dimensional, full-wave simulations using the finite element method were invoked to contrast and gain insight into the mechanisms governing absorption in nanovoid- and planar- interface geometries. Very good agreement is observed between experimentally-determined and simulated absorption spectra. Simulation results indicate that a significant fraction of the total additional absorption occurs in the organic semiconductor. Energy absorption rate profiles obtained from the simulations, which reveal strongly localized absorption at the metal-semiconductor interface, provide strong evidence that the origin of the observed light trapping is indeed due to the excitation of surface-bound plasmonic modes. These results suggest that by substituting planar metallic electrodes in organic solar cells with the nanostructured electrodes presented here, the exciton generation rate can be strongly increased.

6.4 Summarizing remarks

In this chapter, we have seen further demonstrations of light-trapping with nanovoid array electrode geometries. The validity of the FEM routine has also been established. This enables us to extend the routine further to address different kinds of plasmonic architectures (in Chapter 9). Before that, we conduct an important investigation into the dynamics of excitons in close vicinity to metallic nanostructures. This is presented in the next chapter (Chapter 7). This is extremely relevant for the construction of nanostructured electrode organic solar cells, which will be presented in Chapter 8.

6.4 Summarizing remarks

7 Photoluminescence measurements of light trapping architecture samples

In the previous two chapters, the effective light-trapping of nanostructured electrode architectures was demonstrated via reflectometry and finite element simulation. The simulations further indicated that the overall absorption in the semiconductor film can be increased - the exciton generation rate can be increased up to 17% by using a nanostructured electrode. We now take a closer look at the interaction between excitons and metallic nanostructures. Using two-photon time-resolved photoluminescence spectroscopy, we investigate the radiative decay of excitons in organic semiconductors in the vicinity of metallic nanogratings. We observe metal-induced exciton quenching and find that the presence of a grating (metallic or non-metallic) can lead to the existence of longer-lived excitonic states.

The following is my summary of the results of a collaboration with the Nano-optics group, led by Achim Hartschuh. A manuscript written by Mathias Handloser (*Handloser, Dunbar et al., 2012*) has been submitted for publication in *Nanotechnology* [130]. In this work, my contribution was experiment design and sample preparation (together with Philipp Altpeter). Measurements and data analysis were carried out by Mathias Handloser.

7.1 Sample preparation

Electron beam lithography is used to fabricate gratings on standard microscope cover slides. An organic semiconductor is then deposited onto the gratings via spin-coating and the sample is then sealed with a protective layer (Fig. 7.1).

Glass cover slides (17 mm × 17 mm, 100 μm thick, Schott) are first cleaned in acetone in an ultrasonic bath for 5 minutes. A layer electron-beam resist (PMMA, $M_w \sim 500k$, Sigma) of thickness around 100 nm is then deposited via spin coating for 3 seconds at 800 rpm and 30 seconds at 5000 rpm. The resulting film is then hardened in an oven at 170° for 2 minutes.

7.1 Sample preparation

Following this, a thin (3 nm) Cr discharge layer is thermally evaporated onto the PMMA. A focussed beam of electrons is then scanned across the sample following a pre-programmed pattern. In this work, the pattern is simply a series of parallel lines: a grating. The thin Cr layer serves to provide conductivity to the sample (to prevent charge build-up) whilst permitting electrons to reach the PMMA layer underneath. In illuminated regions, the PMMA becomes exposed - the chemical structure of the polymer is changed. After subsequent chemical removal of the Cr layer in ammonium nitrate, the sample now displays the desired pattern of exposed strips of PMMA within an otherwise unexposed PMMA film. In the following step, known as “development”, the sample is placed in a 1:3 solution of methyl isobutyl ketone and isopropanol for 50 seconds. This solution removes the exposed resist thereby exposing the substrate in the regions that were illuminated by the electron beam. All other regions are left in-tact.

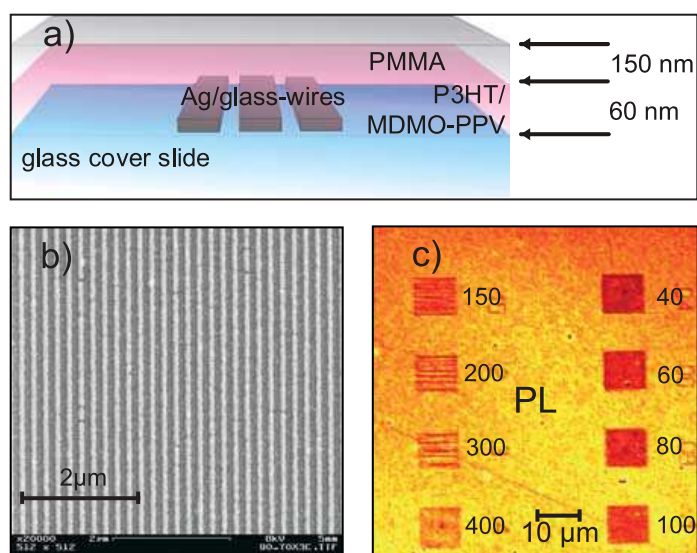


Figure 7.1: Organic semiconductor films fabricated on grating surfaces. (a) Schematic of the sample geometry. An organic semiconductor (P3HT or MDMO-PPV) is deposited on a grating surface where the strips consist of either Ag or glass. (b) A scanning electron microscope image of a Ag typical grating. (c) PL image of a set of Ag arrays. The spacing of each array (in nm) is indicated. Bright yellow indicates a high PL count, red indicates a low count.

Silver is then deposited onto the sample such that it fills the regions where the substrate is exposed - adhering directly to the substrate. A thin (2 nm) layer of Ti is typically deposited before the silver in order to improve adhesion. In the regions where the resist has not been removed, the silver simply forms deposits on top of the resist. In the final step, known as “lift-

off”, the sample is placed in acetone for at least 30 minutes at 40° during which all material aside from the silver that is directly deposited onto the substrate (the strip) is removed.

The final result is a precise metal grating on the substrate. The strips have a constant width of 100 nm and height 40 nm. In this work, 8 gratings are made in a grid separated from each other by $10\ \mu\text{m}$. Each grating is approximately square ($10\ \mu\text{m} \times 10\ \mu\text{m}$) in shape. The spacing between the strips is varied from grating to grating, taking values from 40 to 400 nm (Fig. 7.1(c)). Typically, many hundreds of copies of this 8-grating grid is made per sample such that the highest quality grid can be chosen for measurement.

A thin film of organic semiconductor, P3HT (Merck) or MDMO-PPV (Sigma-Aldrich), is then deposited onto the sample. Solutions of each semiconductor are prepared with a concentration 4 mg/ml in chlorobenzene and shaken overnight at room temperature. The semiconductor is then spin-coated onto the sample at 2000 rpm for one minute in a N_2 atmosphere to achieve film thickness of around 40 nm. Finally, a 150 nm thick film of PMMA ($M_w \sim 350k$, Sigma-Aldrich) is deposited onto the organic film from a 50 mg/ml solution in acetone to act as a protective layer against oxygen. Acetone, which is a poor solvent for organic semiconductors, is chosen as a solvent for the PMMA to minimize degradation of the underlying organic film during PMMA deposition.

Great care is taken to ensure that the finished samples are not exposed to air. This is done to minimize silver oxidization and degradation of the organic semiconductors. Samples are stored under vacuum and are measured in a holder which is continuously flooded with N_2 .

7.2 Measurement

Time-resolved, two-photon photoluminescence (PL) spectroscopy is used to investigate the samples. Electrons in metals can be excited from the d band to the sp conduction band via two-photon absorption (see [131]). The probability of this excitation scales with the square of the local field intensity. Therefore this technique can achieve high signal-to-noise ratios and is well-suited for investigating local plasmonic field enhancements. Two-photon PL measurements have also been used to investigate P3HT exciton dynamics. [132]. Radiative decay from excitons in the organic film is the predominate PL signal detected in this experiment (characterized by decay lifetimes of the order of picoseconds, much slower than the lifetime of excitations in metal, which are of the order of femtoseconds).

A schematic of the set-up is shown in Fig. 7.2. A Ti:Sapphire oscillator provides a pulsed (76 MHz repetition rate, 150 fs pulse duration) laser source at a wavelength of 800 nm. The beam is focussed onto the sample using a high numerical aperture objective (NA=1.3) to obtain a

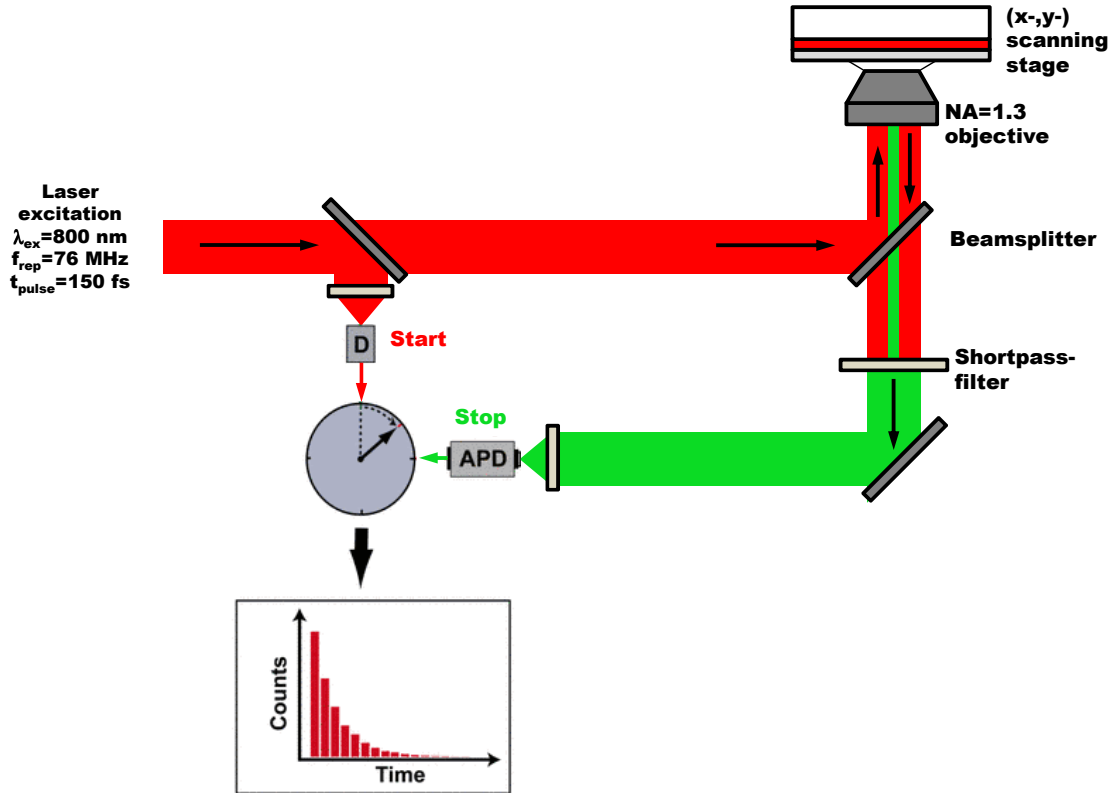


Figure 7.2: Measurement set-up for time-resolved, two-photon photoluminescence spectroscopy.

PL intensity and lifetime measurements can be made for the illuminated area of the sample. The sample is located on a stage which can be raster scanned in the x-y plane to produce PL images such as that shown in Fig. 7.1(c). NA stands for numerical aperture and APD stands for avalanche photodiode.

diffraction-limited beam spot of around 400 nm. The signal is collected with the same objective. The excitation light that is back-scattered from the sample (indicated in red in Fig. 7.2) is removed via a short-pass filter to leave only the PL signal of the sample (indicated in green). The intensity of the collected signal is measured with an avalanche photodiode, a single photon counting device. A beam splitter is placed in the incident beam path to allow the time of arrival of the beam to be logged. For each laser pulse, the time between the sample illumination and the emission of PL is recorded. In this way, both the intensity and the decay lifetime of the radiative decay of excitons in the sample can be measured.

The primary excitation in this experiment takes the form of exciton generation in the semiconductor film. Using time-resolved PL measurements, we investigate the influence of metallic and dielectric gratings on these excitations.

7.3 Photoluminescence quenching

The electrical contact between silver and the organic film can lead to PL quenching, where excitons non-radiatively transfer their energy to the metal. [133] In our samples, we illuminate through the semiconductor side first - excitons generated in the organic film are able to travel to the metal surface via diffusion. By varying the organic film thickness, we obtain an estimate of the range over which excitons efficiently diffuse to the metal to be quenched.

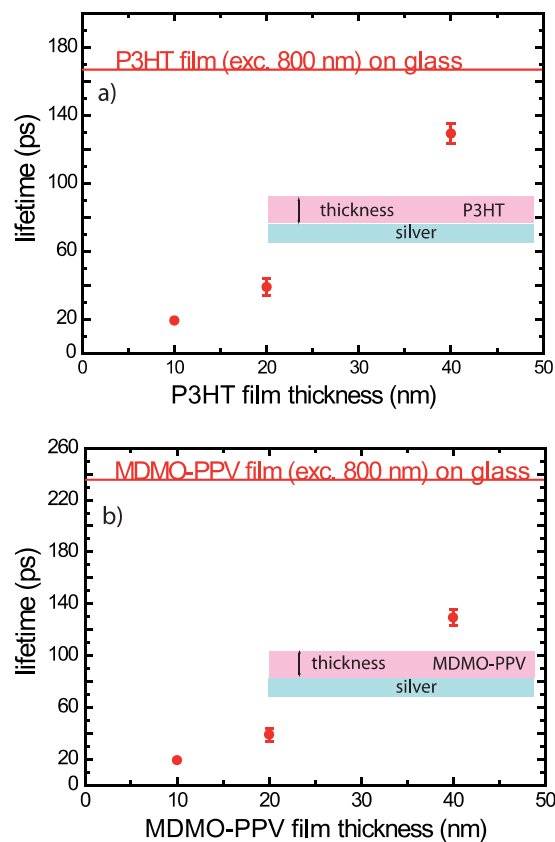


Figure 7.3: A reduced lifetime of radiative states for closer proximity to a metal surface. The metal surface has a strong influence on exciton dynamics out to a distance of 40-50 nm for both organic polymers (a) P3HT and (b) MDMO-PPV.

For thin film thicknesses, the excitation lifetime is significantly shorter than that observed for films where silver is absent (deposited on glass) (Fig. 7.3). This is an indication that for excitons with longer lifetimes, there is a high probability that they will diffuse to the metal interface within their lifetime and non-radiatively decay. Therefore only PL from shorter lifetime states is detected. This is observed for both tested semiconductors - indicating that decay via diffu-

sion and energy transfer to the metal (a non-radiative process) strongly influences the PL for semiconductor film thicknesses of up to 40-50 nm, which is in good agreement with literature values for similar polymers [133]. For greater thicknesses, the majority of excitons are generated at a sufficient distance from the metal (recall the exponential dependence of absorption with penetration depth, Eq. 2.9) such that radiative decay dominates.

7.4 Polymer ordering

The reduced lifetime behavior (which is attributed to quenching at the silver surface) is also observable for the case of semiconductor films deposited on silver gratings on glass (Fig. 7.4). Here we see that both the PL intensity (Fig. 7.4(a)) and lifetime (Fig. 7.4(b)) decreases sharply when the spacing is reduced beyond around 100 nm. When the spacing is reduced (density of strips increased), it has the effect that the volume of the semiconductor within the nominal exciton diffusion length from a metal surface increases.

The behavior at larger spacings (> 100 nm) is somewhat surprising. Distinctly larger intensities and longer lifetimes are observed when the illumination polarization is directed along the wires than when it is perpendicular to it. Especially striking is the peak in PL intensity and lifetime for spacings between 100 and 300 nm, which only occurs for parallel polarization. This means that the presence of the stripes with this spacing increases both the number of excitons that radiatively decay and their lifetime. In order to investigate this further, we compare to corresponding samples which feature SiO_2 strips instead of silver.

The fabrication of SiO_2 gratings is similar to that of silver gratings with the inclusion of an additional etching step. Prior to the deposition of the resist, a 175 nm film of SiO_2 is deposited onto the quartz substrate, as the quartz typically contains a high concentration of impurities which is difficult to etch. Instead of silver, Cr is evaporated in the deposition step, such that an array of Cr strips is formed. After lift-off, reactive ion etching with sulfur hexafluoride is used to etch 75 nm of the SiO_2 substrate underneath (the Cr mask protects the regions between the strips). The Cr layer is then chemically removed, leaving a SiO_2 grating array with grating height 75 nm and width and spacing chosen such that the width and spacing of the glass gratings are equal to that of the metal gratings.

The PL behavior of the glass grating (Fig. 7.5) reveals two important pieces of information. Firstly, the PL lifetime and intensity does not decrease for strip spacings below 100 nm as observed for silver gratings (Fig. 7.4). This supports our claim that this behavior is due to non-radiative decay of the excitons at the metal surface. Secondly, the peaks in lifetime and intensity for parallel polarization, observed for metal gratings, are present for glass gratings as

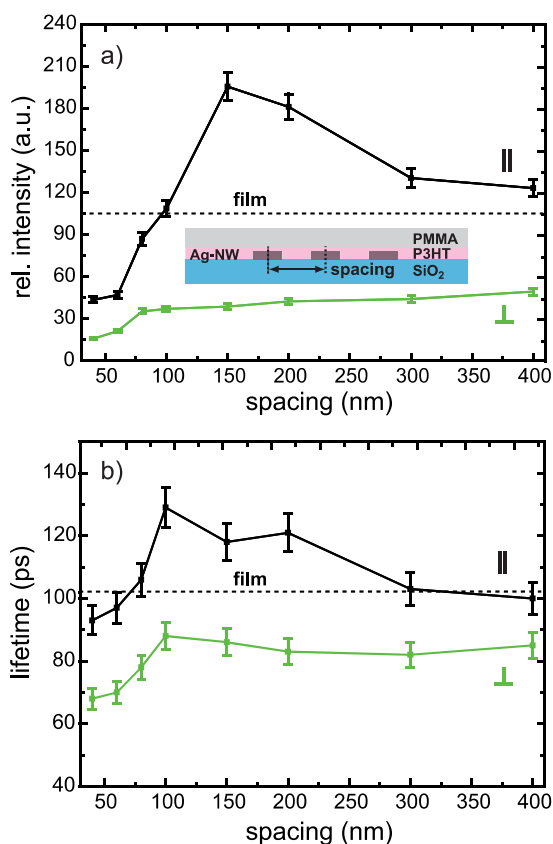


Figure 7.4: The polarization dependence of (a) the PL intensity and (b) lifetime for P3HT deposited on Ag gratings. A distinctive peak in the intensity and lifetime is observed for spacings between 100 and 300 nm, but only for illumination polarized parallel to the grating. The reduction in the intensity and lifetime for both polarizations is attributed to efficient quenching of excitons generated in close proximity of the metal strips.

well. Therefore, the peak cannot be caused by plasmonic enhancement on the metallic gratings. Rather, we consider this as an indication that the volume restriction imposed on the film due to the presence of the strips induces an ordering in the polymer film with a subsequent change in excited state lifetimes. Enhanced ordering, where P3HT chains can become aligned, has been observed in volume-restricted P3HT films such as P3HT nanoparticles [134] and films that have undergone nanoimprint lithography [135].

To confirm whether the aforementioned PL peak observed for P3HT excitons can be attributed to polymer ordering, we directly compare samples in which P3HT and MDMO-PPV are used as the organic semiconductor. Whereas the ordering of P3HT films (typically by annealing) is well-documented [88], it is generally agreed that MDMO-PPV films are amorphous and not amenable to ordering. We note that the P3HT sample whose data is shown in Fig. 7.6 is

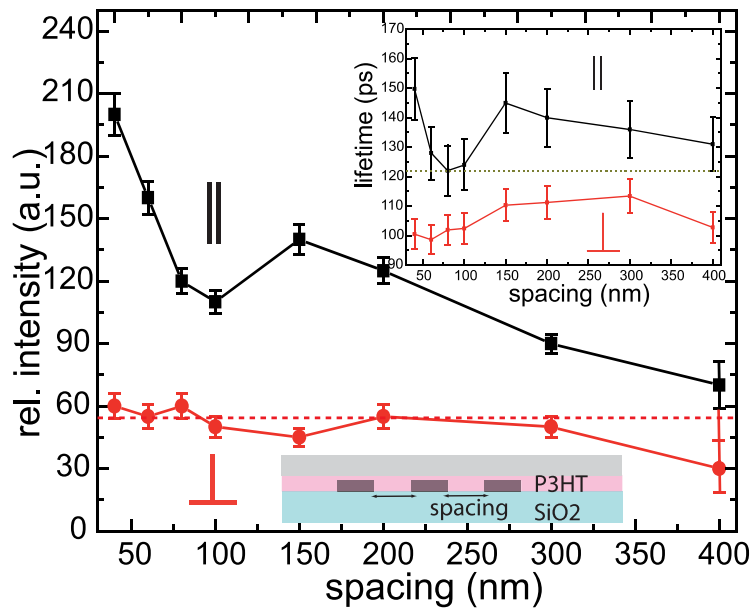


Figure 7.5: The polarization dependence of the PL intensity of excitons in P3HT deposited on glass gratings. The dip in PL intensity (Fig. 7.4 is absent for the glass grating. The peak for medium-valued spacings is still observed for parallel polarization.

fabricated under the same similar conditions to the sample whose data is shown in Fig. 7.4; the qualitative behavior is the same but the absolute numbers vary due to sample-to-sample variations.

The peaks in the PL lifetime and intensity are entirely absent in the MDMO-PPV sample. This is strong evidence that the peaks are associated with ordering in the P3HT film.

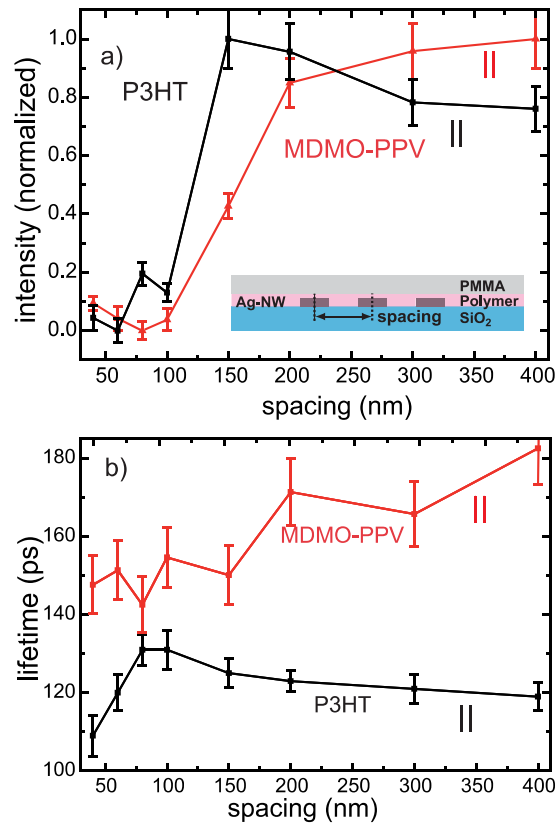


Figure 7.6: The PL intensity (a) and lifetime (b) for P3HT and MDMO-PPV deposited on Ag gratings with incident light polarized parallel to the gratings. The peak in the PL intensity and lifetime for P3HT which is attributed to volume-restricted polymer chain ordering, is absent for MDMO-PPV.

Conclusion

We have found that deposition of P3HT onto grating substrates can lead to a significant reduction of non-radiative losses. This effect is observed for both metallic and dielectric gratings. The absence of this effect for MDMO-PPV films, which are not amenable to induced ordering, suggests that ordering of the P3HT via volume confinement, which has already been documented in the literature, is responsible for this. These results underline the importance of chain ordering in P3HT films. Efficient exciton quenching at metallic surfaces is observed for finely spaced metal gratings.

7.5 Summarizing remarks

The findings of this chapter are of relevance for device fabrication. Firstly, the efficient quenching of excitons at metallic surfaces emphasizes the importance of exciton-blocking layers between the organic film and the metallic electrode. We will use 5 nm films of WO_3 for this purpose. Conversely, it is unlikely that the ordering phenomena is directly applicable to solar cell devices that will be presented in the next chapter, as any ordering induced by volume restriction is likely to be overshadowed by the effect of annealing, which is known to effectively promote ordered domains. In the next chapter, we will construct solar cells with nanostructured electrode architectures. We will use the findings of this and preceding chapters to assist in the analysis.

8 Solar cell performance

In this chapter we will characterize the effect of nanostructured electrodes on solar cell performance. As we have established, nanostructured electrode architectures exhibit considerable light trapping - total absorption enhancements of up to 45% (integrated across the wavelength range 300 - 850 nm) are observed (Section 5.1). Angle-sensitive reflectometry shows that this arises due to the excitation of localized plasmonic modes (Section 5.2). Finite element simulations, which exhibit good agreement with experimental data, indicate that the majority of the additional absorption occurs within the semiconductor and that the exciton generation density is increased (Chapter 6). An extended study of almost 100 solar cells is carried out to compare the performance of reference devices to three imprinted device types (Section 8.1). The results for each of the device types, the flat imprint (Section 8.2), nanostructured electrode device with a void periodicity of 100 nm (Section 8.3) and 500 nm (Section 8.4), are discussed in turn.

8.1 Analysis

In this chapter the performance of imprinted plasmonic solar cells will be discussed. Bulk heterojunction P3HT:PCBM devices with planar (reference, flat-imprint) and nanostructured electrodes (with void periodicities of 100 and 500 nm) are fabricated according to the procedures outlined in Chap. 3. We wish to answer the question:

Do nanostructured electrode devices display an enhancement or reduction in performance compared to the reference devices?

To address this, a total of 8 experiments are performed in which devices are fabricated and characterized. The total number of devices characterized is 99. In each experiment, devices are fabricated such that the processing steps for all device types, aside from the imprinting step, are identical. We then compare the characteristic solar cell parameters of the imprinted devices to those of the reference devices. The total number of fabricated devices of each type is shown

8.1 Analysis

in Tab. 8.1. The low number of nanostructured electrode solar cells with void periodicity of 500 nm is a consequence of the extra difficulty involved in fabrication of the stamps (Sec. 3.2.1).

Reference	Flat imprint	100 nm	500nm
48 (8)	12 (4)	33 (4)	6 (1)

Table 8.1: The number of devices used in this analysis, per device type. The device types are: reference (planar electrode), flat imprint (planar electrode) and structured electrode devices with nanovoid periods of 100 and 500 nm. Eight experiments in total are included in this analysis. The number of experiments in which each device is fabricated is indicated in brackets.

Not all device types (aside from the reference) are fabricated in each experiment. Furthermore, within one experiment, the number of devices is not the same for all device types. It is therefore not meaningful to pool the devices from all experiments to make our comparison, as the significant spread in device performance from experiment to experiment that arises due to variations in ambient temperature, humidity and processing parameters would introduce a bias into the analysis. Instead, we only allow comparisons between device types within individual experiments. The method we will use is outline below:

1. We will first address the solar cell parameter η . Within a single experiment, we take the median power conversion efficiency of all reference devices, $\tilde{\eta}_{\text{ref}}$. We do the same for all other cell types t present in the experiment to obtain the quantity $\tilde{\eta}_{\text{flat-imp}}$, $\tilde{\eta}_{100\text{nm}}$ and $\tilde{\eta}_{500\text{nm}}$. The median is used to quantify the “representative” device in each set - preferred to the mean which strongly influenced by outliers such as short-circuited cells (which due to the direct contact between the conductive electrodes have the IV characteristic of a resistor resulting in η , J_{SC} , V_{OC} and FF all being zero or near zero).
2. We then divide each value $\tilde{\eta}_t$ by $\tilde{\eta}_{\text{ref}}$ to obtain $y_{\eta,t}$ for device type t . For example, for the 100 nm structured electrode device ($t = 100\text{nm}$):

$$y_{\eta,100\text{nm}} = \frac{\tilde{\eta}_{100\text{nm}}}{\tilde{\eta}_{\text{ref}}} \quad (8.1)$$

3. This value is calculated for all experiments which include device type t .

This procedure is carried out for all device parameters x , where $x = J_{SC}, V_{OC}, FF, \eta, R_s$ or R_{sh} . The general form is:

$$y_{x,t} = \frac{\tilde{x}_t}{\tilde{x}_{\text{ref}}} \quad \text{where } x = J_{SC}, V_{OC}, FF, \eta, R_s \text{ or } R_{sh} \quad (8.2)$$

The values $y_{x,t}$ are plotted in Fig. 8.1 - every red dot represents the value calculated for one experiment.

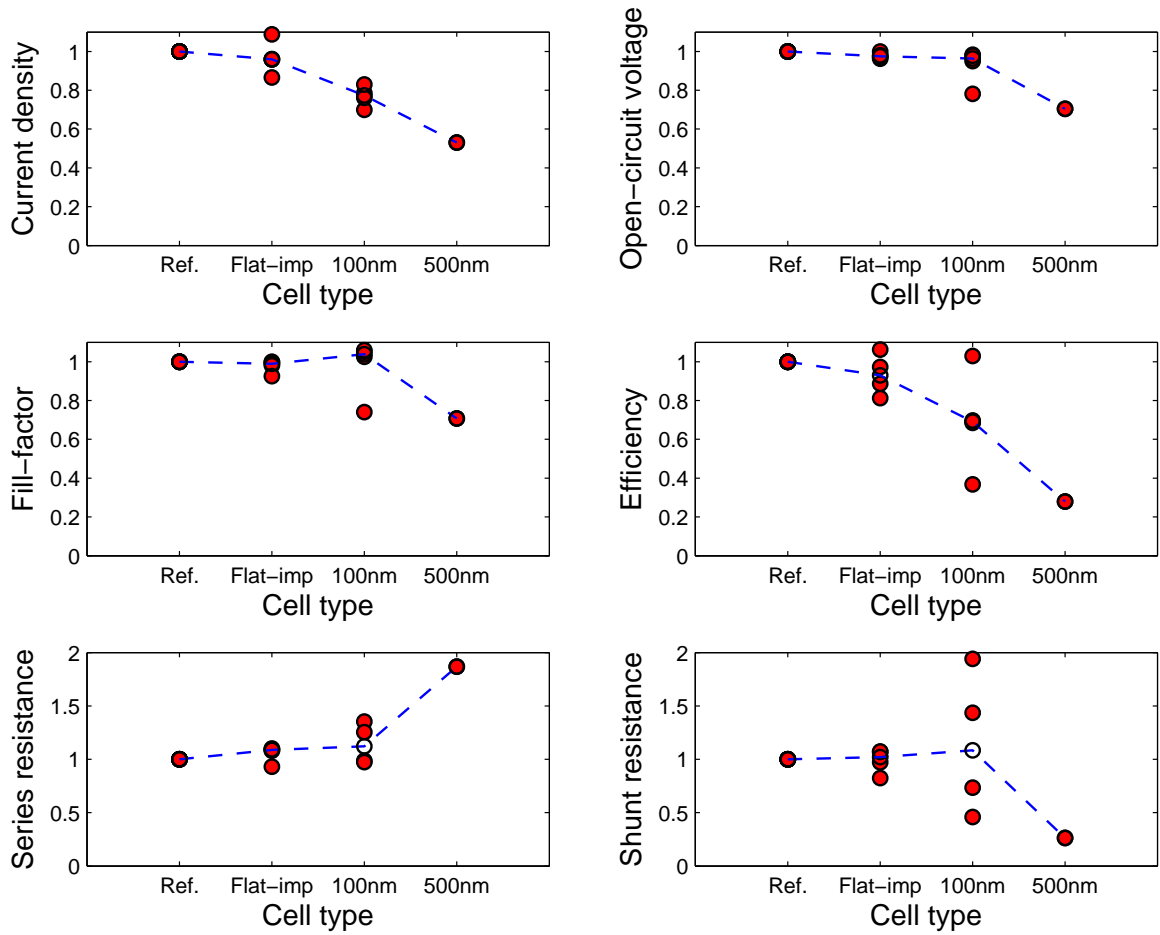
Values of $y_{x,t}$ exceeding 1 indicate that the value of x for the median device of type t exceeds that of the reference device. Values lower than one indicate that the value of x of the median reference device was larger. No attempt is made to quantify the “error” of the $y_{x,t}$ values themselves. The spread *between* the $y_{x,t}$ values is due to the variation of processing conditions between experiments.

As a guide for the eye, the median of the $y_{x,t}$ values are also indicated with hollow dots, joined by a dotted blue line (Fig. 8.1). These values, which we will denote as $\tilde{y}_{x,t}$, are also tabulated in the bottom pane. The $\tilde{y}_{x,\text{flat-imp}}$ values indicate a marginally reduced performance of the flat imprint devices relative to the reference devices. The $\tilde{y}_{x,100\text{nm}}$ and $\tilde{y}_{x,500\text{nm}}$ values indicate that the nanostructured electrodes exhibit a significantly reduced performance.

It would also be valid to consider the mean instead of the median to quantify the representative value of the device characteristics providing an appropriate data cut is applied, such as a minimum V_{OC} requirement. The fraction of devices that do not pass a cut requiring a minimum device V_{OC} of 0.1 V (deemed “short-circuited”) are as follows 6% (reference), 8% (flat imprint), 25% (100 nm void periodicity) and 0% (500 nm void periodicity). The fraction of “short-circuited” devices for each device type is revealing: we observe a significantly increased occurrence for devices imprinted with a (100 nm void periodicity) structured stamp, which likely arise when a stamp penetrates the entire organic film to expose the underlying layers. However, when the imprint is successful (for 75% of devices), excellent FF values are observed, indicating that the devices are indeed robust. Although all of the 500 nm periodicity voids pass this data cut, we emphasize that the sample size is small and may not reflect the true occurrence of short-circuited devices that would be observed in larger samples. We find, that if we insist on a minimum device V_{OC} of 0.1 V, and use the mean instead of the median as the representative value for a sample set, the same analysis yields similar results, with values for $\bar{y}_{\eta,t}$ of 0.94, 0.73 and 0.28 for the three non-reference cell types, respectively (to be compared with $\tilde{y}_{\eta,t}$ in Fig. 8.1). The introduction of a data cut can bias the results: the results of using the mean with no data cuts are identical to those obtained using the median to two decimal places. We shall exclusively refer to the results obtained using the median for the upcoming discussion.

We now consider representative experiments in which the devices exhibit solar cell parameters similar to the $\tilde{y}_{x,t}$ values tabulated in Fig. 8.1, so that we may scrutinize the behavior of individual devices within an experiment. We emphasize that within one experiment, planar and nanostructured electrode devices are fabricated under identical conditions with the exception of the imprinting step. We will aid our discussion with IV and EQE curves.

8.1 Analysis



	Flat imprint	100 nm	500 nm
J_{SC}	0.96	0.78	0.53
V_{OC}	0.98	0.96	0.70
FF	0.99	1.04	0.71
η	0.93	0.69	0.28
R_s	1.09	1.12	1.87
R_{sh}	1.02	1.09	0.26

Figure 8.1: Comparison of four device types: planar reference, flat imprint, nanostructured electrode (100 nm void periodicity) and nanostructured electrode (500 nm void periodicity). Each red dot pertains to one experiment, and represents the median value of the solar cell parameter for the device type, normalized by the corresponding value for the reference device. See text for details. The values in the table are the median values $\bar{y}_{x,t}$ of each set of red dots, indicated in the plots with hollow dots joined by blue dashed lines. The cell types are ordered along the axis by void size, from no voids (reference and flat-imprint) to the 500 nm periodicity voids which exhibit void diameters of 400-500 nm.

8.2 Flat imprint

The flat imprint - an imprint with a planar stamp - allows us to determine the effect of temperature and pressure on the solar cell performance. We observe only a marginal reduction in J_{SC} and V_{OC} (Fig. 8.2, Tab. 8.2). This is observed reproducibly over numerous experiments and is also found for experiments with PCPDTBT as a hole-conductor. Therefore the imprinting process alone (pressure, temperature and contact between the organic film and the silanized stamp) does not significantly reduce the device performance.

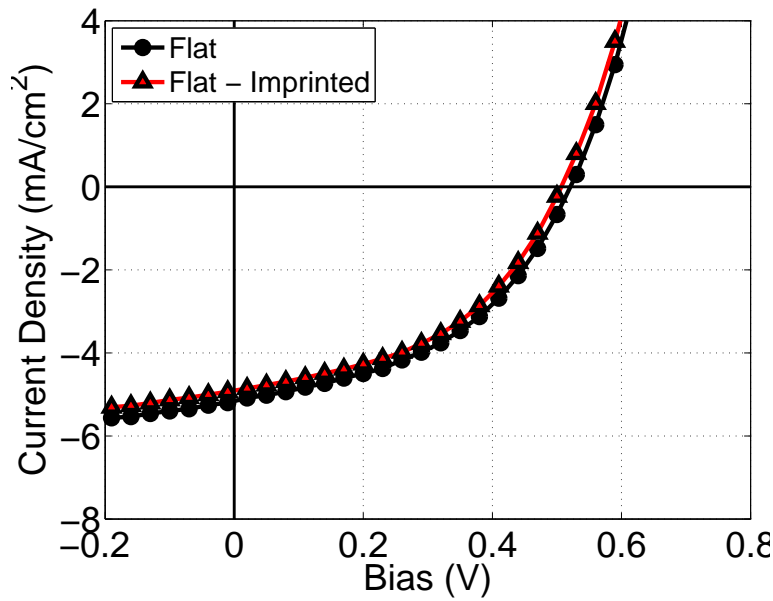


Figure 8.2: The device performance is not significantly altered by imprinting with a flat stamp.

	Reference	Flat imprint
J_{SC} (mA/cm ²)	-5.2	-4.9
V_{OC} (V)	0.52	0.51
FF	0.45	0.46
η (%)	1.21	1.14
R_s (Ω cm ²)	30	30
R_{sh} (Ω cm ²)	360	400

Table 8.2: Device parameters extracted from the IV curves in Fig. 8.2.

8.3 100 nm period nanovoids

A representative IV curve of a 100 nm nanostructured electrode device is shown in Fig. 8.3. The corresponding solar cell parameters are presented in Tab. 8.3. We note a considerable difference between the reference device from this experiment and the experiment of the previous section (compare Tables 8.2 and 8.3) - this justifies the approach taken in Sec. 8.1.

A significant reduction in efficiency relative to the reference is observed. This is primarily due to a reduction in the J_{SC} (Fig. 8.1), which, combined with the invariance of the other solar cell parameters, can be understood as a reduction in photocurrent. This is surprising, given that we consistently observe enhanced total absorption with structured interfaces (Sections 5.1 and 5.2) and simulations (Chapters 6 and 9) strongly indicate that the absorption in the semiconductor is enhanced. This should intuitively lead to an increase in J_{ph} . However, we observe the opposite.

	Reference	100 nm	500 nm
J_{SC} (mA/cm ²)	-6.20	-4.37	-3.39
V_{OC} (V)	0.56	0.53	0.45
FF	0.56	0.57	0.44
η (%)	1.90	1.31	0.65
R_s (Ω cm ²)	30	20	40
R_{sh} (Ω cm ²)	1110	1240	540

Table 8.3: Device parameters extracted from the IV curves in Fig. 8.3

Interestingly, the shunt resistance, R_{sh} is greater than that of the reference sample (Fig. 8.3). This indicates that additional protection against leakage current is introduced i.e. that the organic film remains intact after the imprint. However, Fig. 8.1 reminds us that there is a large spread in the $y_{R_{sh},100nm}$ values; the median value of R_{sh} relative to that of the reference devices varies greatly between experiments.

The reduction in J_{SC} is relatively constant over all illumination wavelengths, as indicated by the external quantum efficiency¹ (Fig. 8.4). The features in the relative reduction in the EQE for the structured electrode device between 300 and 400 nm and at 650 nm are not well understood, but we note they occur at spectral positions where the EQE starts to drop rapidly. Importantly, in the spectral region where the majority of the current is generated (between 400 and 600 nm)

¹The external quantum efficiency is measured on devices that underwent similar fabrication and display similar device performance to those for which the IV curves are shown in Fig. 8.3

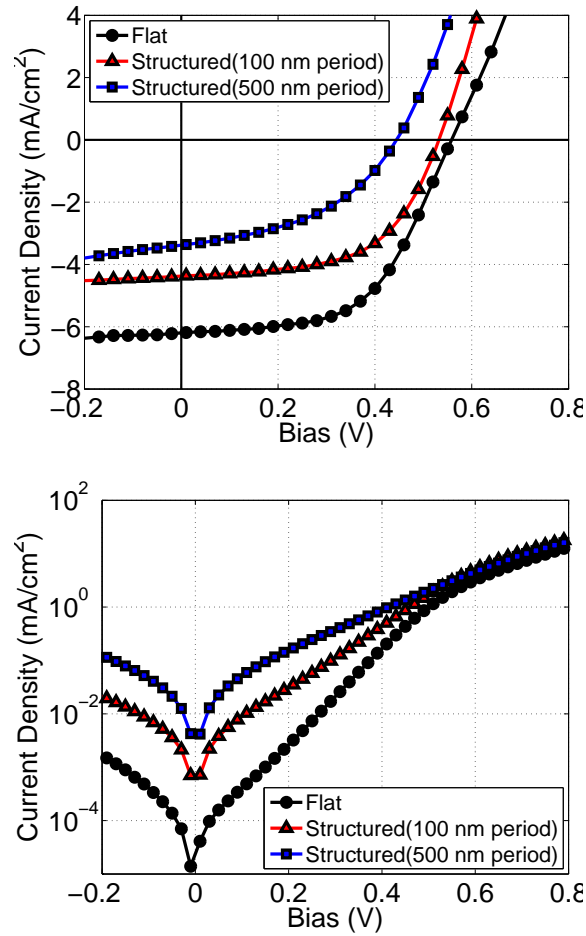


Figure 8.3: Current-voltage characteristics for nanostructured electrode devices. (Top) under AM1.5G illumination and (bottom) in the dark. The performance of both nanostructured electrode devices is reduced relative to the reference (flat) device.

the relative reduction is effectively wavelength-independent with a value of around 0.75 which is consistent with the value obtained for the representative reduction in J_{SC} ($\gamma_{J_{SC}} = 0.76$) in the extended study in Sec. 8.1. The spectral-independence of this curve strongly indicates that reduction in J_{SC} is not due to plasmonic quenching of excitons or other resonant mechanisms. In order to explain this behavior, explanations based on non-resonant loss mechanisms (which affect the EQE equally at all wavelengths) are required.

Below, we introduce and scrutinize a number of theories in more detail:

1. As discussed in Sec. 2.4.3, significant localized absorption can lead to exciton-exciton annihilation which would be expected to saturate the charge generation. It is possible to propose a scenario in which exciton annihilation could indeed lead to a reduction

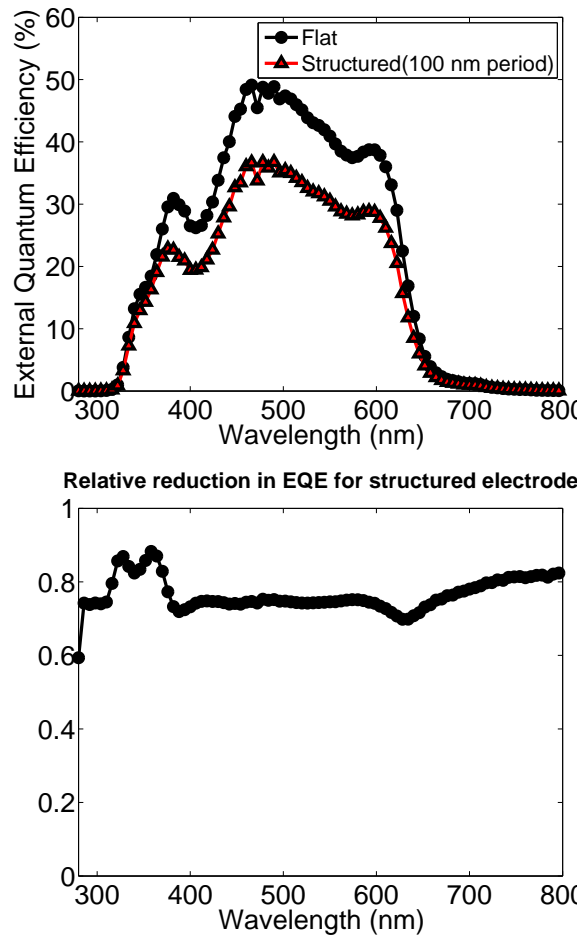


Figure 8.4: External quantum efficiency (EQE) of flat and nanostructured electrode (100 nm period) devices. (Top) Absolute values of EQE. The reduction in EQE of the structured electrode device relative to the flat device is shown (bottom) to be remarkably wavelength-independent.

in J_{SC} . Assume that at maximum saturation, the number of free charges that can be generated is limited to a in a unit volume V . In the extreme case, all of the incident light is absorbed in one unit V - producing a total of a free charges. However, in the case without light-trapping, exciton generation is more uniformly distributed across multiple volume units - producing a greater number of free charges from a smaller number of generated excitons. Critical to this argument is the exciton generation rate at which saturation becomes important.

Enhancements in the simulated exciton generation rate of up to 17% are observed for 60 nm nanovoid arrays adjacent to PCBM (Fig. 6.6). However as results for P3HT:PCBM solar cells under concentrated sunlight indicate, the fundamental photocurrent mecha-

nism remains efficient (and the FF remains constant) for illumination intensities of up to 2.5 suns, evident in the linear increase in J_{SC} . [47]. Recalling the proportional relationship between absorption and illumination intensity (Eq. 2.9), this means that the photocurrent mechanism remains effective in P3HT:PCBM devices for exciton generation rates of up to around 250% greater than what is observed under 1 sun. This dwarfs the local enhancement in exciton efficiency that we expect in our devices. Of course, simulations of 100 nm void arrays adjacent to P3HT:PCBM are required to facilitate a direct comparison to the solar cells presented here. However, based on the reasoning above, it is highly unlikely that the exciton generation density has been increased so greatly that exciton-exciton annihilation becomes significant.

2. Another mechanism that could account for a reduced J_{SC} is recombination at defect sites that are possibly introduced by the imprint. Although we observe minimal reduction in performance after the flat imprint, any damage done to the polymer will be correspondingly increased for the structured imprint because of the larger area over which the film makes contact with the stamp. If the imprint introduces defect sites (either by damaging the P3HT chains or PCBM molecules themselves or disturbing phase crystallinity), charges may collect there until they eventually recombine. Such defects (due to the imprint) would therefore act as charge traps and cause the build-up of significant space charge. This would reduce the current even if exciton generation is increased. However, the reduction in current that arises from a build-up of space charge at the interface is typically not uniform, rather, the field-dependence introduced by charges having to overcome a potential barrier at the interface modifies the IV in such a way that so called S-shapes are established. [24] No evidence of this is observed, therefore we cannot assume that additional interfacial recombination is primarily responsible for the reduced J_{SC} .
3. It is possible that the blend morphology of the film could be altered via the imprint: for example the varying chemical affinity of the two phases for the silanized stamp could result in one phase or the other preferentially occupying the region near the interface. If the interface region were to become significantly more PCBM-rich after the imprint, this would act as a hole-blocking layer adjacent to the hole-collecting contact. Similarly to the reasoning in the above paragraph, this would lead to a build-up of space charge and hence a strongly altered field dependence of the IV curve (e.g. an S-shape). No evidence of this is observed, hence this can be ruled out. If the region became significantly P3HT-rich, we would expect better electron blocking properties and hence a larger shunt resistance. As the shunt resistance is only slightly larger, we suspect that the imprint has no large influence on the blend morphology at the interface. This is especially likely

given that the films have been annealed at the melt crystallization temperature (140°) for 10 minutes before measurement, and it well established that P3HT and PCBM rapidly interdiffuse at this temperature, [99] which would reverse any disruption to the film morphology introduced by the imprint. We discount a change in the blend morphology as a reason for the reduced J_{SC} .

4. Due to the difficulties in depositing a uniform film on structured surfaces it is possible that the WO_3 film between the organic semiconductor and silver is non-continuous (in this study, WO_3 is deposited via thermal evaporation). The WO_3 film acts as an exciton-blocking layer, and to prevent parasitic currents between electrodes and charge recombination at the organic-metal interface (here, by preventing contact between the electron-conducting PCBM and the hole-collecting Ag electrode). The complete absence of WO_3 in this solar cell type typically results in a sharp reduction in R_{sh} (Fig. 8.5(b)) although *Tao et al.* claim that layers as thin as 1 nm suffice to ensure minimal losses to recombination and parasitic currents (Fig. 8.5(b)) [90]. *Tao et al.* explain that thin WO_3 films (less than 5-10 nm, the optimal thickness) are not uniform and this incomplete coverage cannot effectively prevent recombination at the interface. The effect of an incomplete coverage of the cell is the same as observed in Fig. 8.3: J_{SC} is reduced. The small reduction in V_{OC} (Fig. 8.3) is also observed in Fig. 8.5(b). We also note the importance of an exciton-blocking layer to prevent metal-induced quenching of excitons (Chap. 7). Exciton quenching is consistent with a reduction in J_{SC} without a corresponding reduction in the FF . The recommended course of action is to use atomic layer deposition instead of evaporation to fabricate the WO_3 films. This technique, which can deposit films with perfect conformality on the nanometer scale, [136] is capable of uniformly coating finely structured surfaces such as the nanostructured organic films used here.
5. The nanostructured electrode also deforms the electric field established via the external potential (shown schematically in Fig. 8.6). Whereas the field distribution is symmetric within the plane of the solar cell for the flat architecture, the introduction of the nanostructured electrode complicates this significantly. As silver is a good conductor, field lines emerge from the silver surface at right angles as shown, creating areas of higher and lower electric field strength (the field strength is indicated by the density of field lines). This is of no consequence to exciton transport, as excitons are electronically neutral, but the electric field dependence of the dissociation of charge transfer states is well-documented (a widely accepted model for the (field-dependent) dissociation probability is due to Onsager and Braun [19]). The influence of the non-trivial electric field distribution on charge transfer state dissociation is not understood. Furthermore, the drift current (the component of the current which flows due to electrostatic forces) will

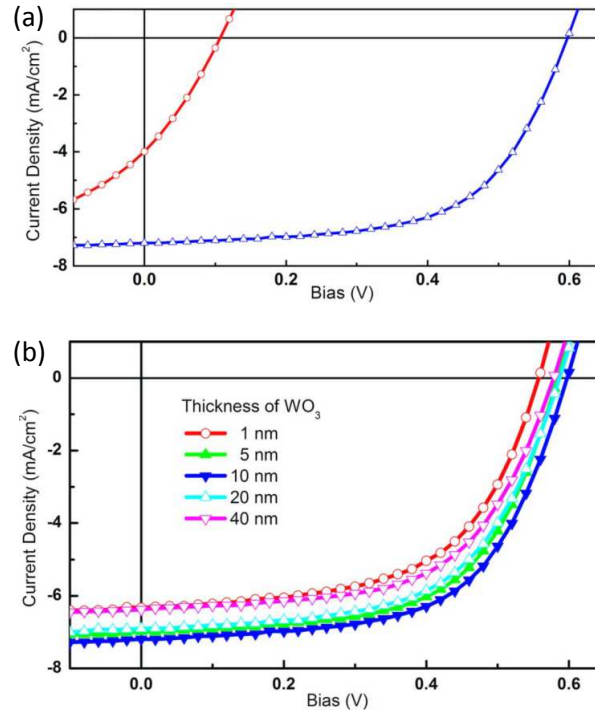


Figure 8.5: The effect of WO₃ thickness on the IV curve. (top) Dramatically reduced performance is observed when no WO₃ film (red circles) compared to a 10 nm WO₃ film (blue triangles). (bottom) The optimal layer thickness is 5-10 nm. Taken from [90]

be strongly affected by the deformed electric field. As noted by Hoppe et al. drift current is especially important in thin (< 100 nm) organic solar cells, as the electrical force due to the bias across the external contacts is poorly screened and therefore of a significant magnitude at all points within the cell. [89]

It is possible that the deformed electric field introduced by the nanostructured electrode affects the drift current and or the CTS dissociation efficiency. Reports of the electrical effects of plasmonic architectures in organic solar cells have recently emerged, but deal only with gold nanoparticles dispersed in the active layer [137] and in an interfacial layer [138]. A great deal of further investigation is required to ascertain the effect of the deformed electric field induced by nanovoid electrodes on the electrical properties of organic solar cells.

6. An important consequence of the nanovoid structure is that free charges formed within the voids face a very different percolation landscape than those formed in the inter-void space. Upon imprinting a film of thickness t_0 , two characteristic lengths are established:

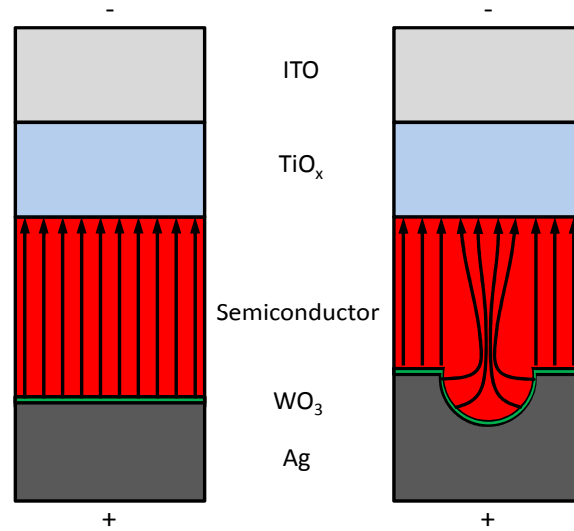


Figure 8.6: Nanostructured metallic electrodes lead to a deformation of the electric field lines between the electrodes. The arrows indicate the direction of the force imparted on positive charges in the field due to the electropotential. The field strength is indicated by the spacing of the field lines - more densely space lines indicates a stronger field.

t_1 , the distance between the inter-void region and the far electrode and t_2 , the distance between the deepest point in the void and the far electrode (see Fig. 5.7), with $t_1 < t_0 < t_2$. Electrons that are generated from excitons formed in the voids must travel a length t_2 to reach the far electrode for collection, which is longer than t_0 , the longest distance that electrons must travel in the flat case. For these devices, $t_0 = 100$ nm and $t_2 \approx 160$ nm (see Tab. 3.2). Thus electrons that form within the voids may have a reduced collection efficiency. Given that, as is the nature of plasmonic light trapping, a large amount of light is absorbed near the interface, at the expense of absorption in regions closer to the far electrode, this could account for a reduced current of the solar cell despite an increased absorption. This is, however, not consistent with measurements (with non-localized exciton generation) of > 300 nm for the electron transport in PCBM. [21] In order to verify this theory, further experiments need to be done to better understand electron transport in solar cells with non-trivial generation profiles. In addition, we note that the increased dark current (albeit by a small amount - around $2 \times 10^{-2} \text{ mA/cm}^2$ at -0.2V) could be due to increased parasitic current enabled by the shorter distance $t_1 < t_0$ between the far electrode and the intervoid space on the silver electrode.

After presenting six explanations for the reduced J_{SC} and discussing them in detail, two explanations seem highly implausible and one seems unlikely. A highly implausible explanation is exciton-exciton annihilation. As was argued, P3HT:PCBM cells are known exhibit a linear relationship between incident intensity (and hence exciton generation rate) and J_{SC} that extends well beyond the exciton generation rates that can reasonably be expected from these devices. An imprint-induced change in morphology or crystallization is also highly implausible, as both reference and imprinted devices are annealed to above the melt crystallization temperature for 10 minutes, which should undo any crystallization or morphology change introduced by the imprint. The discussion of the explanation involving extending electron transport paths for the nanostructured devices concluded that this was unlikely, as the electron transport length in PCBM is believed to be 300 nm, significantly longer than the longest distance between the electrodes (around 160 nm). However, we will not rule this explanation out, and experiments to verify its validity are outlined in Chap. 10. Similarly, we will describe experiments to scrutinize the three remaining plausible explanations: defect sites introduced by the imprint, a non-continuous WO_3 film and modified charge dynamics due to a deformed electric field.

8.4 500 nm period nanovoids

The performance of the nanostructured devices with 500 nm period nanovoids is reduced more significantly than the 100 nm period nanovoid devices (Fig. 8.3). The increase in dark current as well as the reduction in shunt resistance ($y_{R_{sh}} = 0.26$) is significant. As with the case of the 100 nm period voids, the deposited WO_3 is likely non-continuous, even more so given the increased height of the organic nanowires. In addition, the value of t_1 for these devices is typically quite small (of the order of a few tens of nm or less) due to the large void depth of the stamps (see, for example, Fig. 5.4). This enables, especially in combination with a poor WO_3 coverage, large parasitic current to flow. The observed reduction in V_{OC} can be attributed to the reduced R_{sh} (see Fig. 2.2(c) and [139]).

Thus in order to improve these devices, a uniform WO_3 film is required. In addition the penetration of the stamp into the film must be reduced so that the thickness of the imprinted organic film at its thinnest points is increased. The devices in question are imprinted with a lower pressure (150 bar) than the standard imprint (250 bar) in an attempt to reduce the depth of the imprint. However these results demonstrate that full stamp penetration cannot be prevented simply by controlling the pressure alone (the soft organic film is easily penetrated, even with moderate imprinting pressures). Shallower stamps are required.

8.5 Summarizing remarks

In this chapter, the performance of nanostructured electrode solar cells has been analyzed. The results raise many interesting questions - experiments are described in Chapter 10 which will provide further insight. In the next chapter, we compare the light-trapping properties of structured electrode architectures with two other plasmonic nanostructures: in-scattering nanoparticles and nanoparticles dispersed in the semiconductor layer. We perform an optimization study to identify the geometry parameters which provide maximum semiconductor absorption enhancement. Studies such as this are highly relevant to the further optimization of the devices presented in this chapter.

9 Optimization of plasmonic solar cells

In this final chapter, we perform a computational study of plasmonic solar cells to identify the maximum absorption enhancement that can be expected and which physical mechanisms make the most important contributions to the-light trapping. Absorption in the semiconductor layer with three standard plasmonic solar cell geometries is compared to absorption in a flat layer. We identify near-field absorption enhancement due to the excitation of localized surface plasmons but find that it is not necessary for strong light trapping in these configurations: significant enhancements are also found if the real metal is replaced by a perfect conductor, where scattering is the only available enhancement mechanism. The absorption in a 60 nm thick organic semiconductor film is found to be enhanced by up to 19% using dispersed silver nanoparticles, and up to 13% using a nanostructured electrode. External in-scattering nanoparticles strongly limit semiconductor absorption via back-reflection.

This chapter is based on *Dunbar et al., 2012, Optics Express* [118].

9.1 Plasmonic solar cells

We will start with a brief review of the three main metallic light-trapping nanostructures in solar cells. A more detailed treatment is given in Sec. 2.5.

Light-trapping structures can take many forms as outlined in recent publications. [48, 50] Of particular interest is plasmonic light-trapping, where metallic (typically Ag or Au) nanostructures enable excitation of localized surface plasmons (LSPs, non-propagating excitations of conduction electrons within a metallic nanostructure) and or surface plasmon polaritons (SPPs, surface bound electromagnetic waves that propagate along metal-dielectric interfaces) which traps light at the respective metal-semiconductor interface. For a number of typical semiconductor-metal configurations, this light is preferentially absorbed in the semiconductor,[34] leading to an overall enhancement in the absorption over the flat (no metallic nanostructure) case. Providing the implementation of the light-trapping structure does not modify the solar

cell's internal quantum efficiency (a measure of charge transport properties), the absorption enhancement corresponds to an enhancement in the power conversion efficiency.

A wide variety of plasmonic solar cells (PSCs) has been investigated experimentally and theoretically towards achieving performance superior to that of a flat layer solar cell (Fig. 9.1(a)). It is possible to group PSCs into three main classes: nanoparticles dispersed in the semiconductor layer (Fig. 9.1(b)), the nanostructured metallic electrode (Fig. 9.1(c)) and in-scattering nanoparticles (Fig. 9.1(d)).[48][34] Each PSC is fundamentally different in terms of absorption enhancement mechanisms.

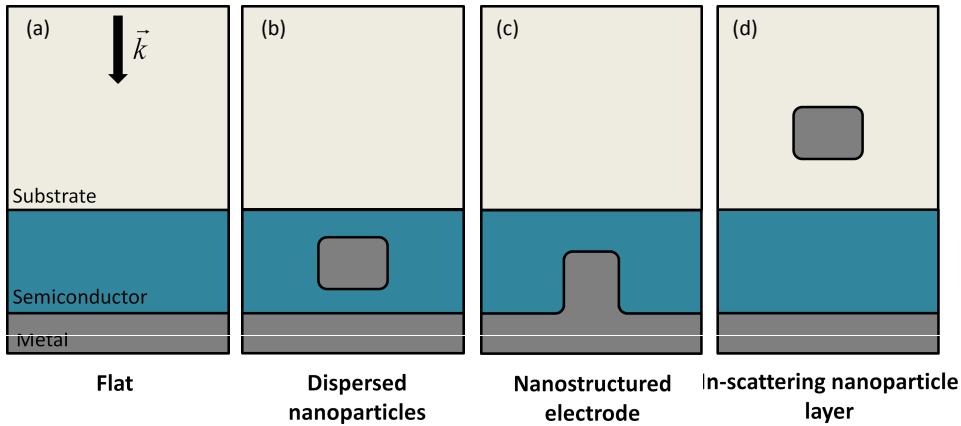


Figure 9.1: Solar cell architectures considered in this study. (a) Standard (flat) solar cell architecture. The direction of incident light is indicated. (b-d) Three classes of plasmonic solar cells designed to achieve enhanced semiconductor light absorption.

Nanoparticles (NPs) dispersed in the semiconductor layer (Fig. 9.1(b)) can, in addition to enhancing the absorption, also improve the series resistance. [140] Absorption enhancement is typically observed in the near-field of the NP and it has recently been argued that this enhancement arises primarily due to the excitation of scattered modes at the NP (rapidly absorbed in highly absorbing materials), as opposed to excitation of LSP modes. [73, 141] However, Zhu et al. found that light trapping in this geometry relies heavily on plasmonic excitation, by showing a strong fall-off in enhancement for nanometer-thin NP dielectric shells. [129] Excitation of SPPs on the flat back-electrode is also possible in this PSC via scattering at the NPs. The relative importance of NP scattering and absorption is highly size- and shape-dependent. [57, 141] Dispersed NP organic PSCs using nanowires, [142] truncated octahedral NPs [73] and NP clusters [74] have recently been reported with significant efficiency enhancements of up to 23%. [73]

Nanostructured electrodes (Fig. 9.1(c)) can be easily incorporated into standard solar cell design in place of the planar metallic electrode. Design of nanostructured electrodes can draw greatly from research in metallic nanostructures such as gratings [31], void [37, 104] and hole arrays [143, 144]. It is possible to excite both LSPs on the protrusions/voids and SPPs on the intervening planar surface. The role of the nanostructured electrode is two-fold: one, to enhance absorption in the active layer and two, to collect charge carriers. A number of reports demonstrate enhanced efficiencies of up to 20% [83] and attribute the enhancements to scattering as well as the excitation of plasmonic modes. [83, 86, 112, 145]

The in-scattering NPs geometry (Fig. 9.1(d)) can achieve light-trapping by scattering incident light at wide angles into the active layer. This increases the light path length in the cell and can lead to total internal reflection. It is also possible for this scattered light to excite SPPs on the back interface and photonic modes in the active layer. An efficiency enhancement of 8% has been reported for amorphous silicon solar cells with Ag NPs separated from the active layer by a 20 nm intervening indium tin oxide layer. [60] Near-field absorption enhancement due to the NPs is also possible if their separation from the semiconductor is sufficiently small. A number of groups have recently reported efficiency enhancements by embedding metallic nanoparticles in a layer of a hole-conducting polymer, PEDOT:PSS, adjacent to an organic semiconductor film. [62–64] For the purposes of this paper, we consider this geometry as a hybrid of the dispersed NP and in-scattering NPs PSC geometries and instead refer the interested reader to a recent report. [146]

We note that dielectric particles can also be used to excite SPPs on metal surfaces [147] and to provide scattering. However, metallic nanoparticles (mainly Au and Ag) have primarily been considered for this application, largely because of their ability to exhibit strong resonant scattering (e.g. the resonance scattering cross-section of a 20 nm Ag NP embedded in Si is 30 times larger than its geometric cross section). [142] Previous optimization studies have focused on individual PSC geometries in detail. [129, 146, 148] We aim to directly compare three fundamentally different PSCs in order to identify the most promising geometry, understand the nature of the absorption enhancement and estimate the likely maximum absorption enhancement that can be expected. To the best of our knowledge this is the first instance of such a report.

9.2 Method

The Finite Element Method (FEM) is invoked using commercially available software (COM-SOL) to model light absorption in the flat SC and the three PSC geometries. The suitability of

the FEM for reproducing experimental results in light trapping solar cells has been established previously. [118] We numerically solve the time-harmonic wave equations in the electric field E and the magnetic field H (equations 6.1 and 6.2).

The simulated area encompasses a single cell of the periodic structure (Fig. 9.2(a-b)). Symmetry is imposed along the direction perpendicular to the plane of incidence. This enables a 2D treatment of the problem, which compared to 3D FEM simulation, achieves numerical accuracy at a small computational expense. As a result, an investigation over a large parameter space is possible. An infinite 2D array of adjacent cells is simulated by invoking periodic boundary conditions on the sides, (Fig. 9.2(b)), which takes the influence of neighboring cells into account. The top and bottom boundaries of the simulation geometries are terminated with perfectly matched layers to ensure minimum artificial reflections from the boundaries. The outcome of each simulation is the electromagnetic field profile defined for all wavelengths in the range 350 - 1000 nm. From this profile, the absorption $A(\lambda)$ in the active layer, the (planar) electrode and the NPs can be calculated by integrating the energy dissipation density within the appropriate 2D volume according to equation 6.3. The reflectance is calculated by directly integrating the reflected flux at the top simulation boundary. The spectrum is then scaled using the AM1.5G solar spectrum and then integrated over wavelength to obtain the total absorption in the respective layer under one sun. [118] This is performed for illumination with polarization perpendicular (TM) and parallel (TE) to the nanostructure (Fig. 9.2(a)). In this configuration, plasmonic excitation is possible under TM illumination only. In order to quantify the absorption properties of the nanostructures under non-polarized illumination (such as sunlight), we also calculate a polarization-averaged absorption A_{av} , an equally-weighted sum of total absorptions (integrated over the investigated spectral range) A_{TM} and A_{TE} under TM- and TE-polarized illumination respectively:

$$A_{av} = \frac{A_{TM} + A_{TE}}{2} \quad (9.1)$$

A blend of two common organic semiconductors: PCPDTBT/PC₇₀BM (poly[2,6-(4,4-bis-(2-ethylhexyl)-4H-cyclopenta[2,1-b;3,4-b']-dithiophene)-alt-4,7-(2,1,3-benzothiadiazole)]/[6,6]-phenyl-C₇₁-butyric acid methyl ester, is chosen as the active material. Silver is used for both the nanoparticle and electrode material. The active layer thickness is fixed at 60 nm. The NP shape is chosen to be rectangular, as much of the literature in plasmonics is based on the use of rectangular gratings [31, 67–69] and the same shape is used for all three PSC geometries to facilitate a direct comparison. The corners of the NP are rounded (2 nm radius) to eliminate inaccuracies that arise when performing FEM simulation on geometries with sharp corners. [149] The height of the nanostructure is fixed at 30 nm, which is comparable to the dimensions of

nanoparticles commonly reported in PSCs and relevant plasmonic structures. [31, 57, 64, 69] The period of the array and the width of the NPs are varied independently, allowing an optimization of light absorption in the active layer (Fig. 9.2(a)). We model a simplified solar cell: a glass substrate ($n=1.4$), a semiconductor/active layer and a metallic electrode and nanostructure. In order to ensure clear conclusions about the mechanisms facilitating light-trapping can be drawn, we do not consider additional layers, such as charge transport layers, in the simulation geometry. A perfect antireflection coating at the air-glass interface is assumed - we illuminate at normal incidence from within the glass (Fig. 9.2(b)) at a distance of 250 nm from the active layer. The three PSC geometries can be realized by modifying the flat geometry (Fig. 9.1(a)) by placing the NP at the appropriate location in the layer stack: centered in the active layer (Fig. 9.1(b)), on the back electrode (Fig. 9.1(c)) or embedded in the substrate above the active layer (Fig. 9.1(d)). The spacing between the active layer and the NP in the in-scattering geometry is fixed at 30 nm, chosen to be consistent with experimental reports of this geometry. [58, 60] Values of complex refractive indices are obtained from the literature. [27, 117]

9.3 Optimization study

The absorption in the active layer for the dispersed NP geometry under TM polarized illumination is shown in Fig. 9.2(c) for NP widths ranging from 10 - 120 nm and periods ranging up to 600 nm. Absorption enhancements (relative to a flat solar cell (Fig. 9.1(a))) exceeding 1 are observed for a large range of NP widths and periods. It is important to note that the volume of active material in this configuration is decreased due to the presence of the NP. Despite this, the total amount of light absorbed in the active layer is increased - the absorption enhancement due to the presence of the NP outweighs the reduction in absorption due to the omitted semiconductor material. A maximum absorption enhancement of 45% (enhancement factor of 1.45) is observed for a NP width of 40 nm and a period of 190 nm. At low periods the content of active material rapidly decreases (the active layer is crowded with silver) and the active absorption drops correspondingly. At large periods, where the density of features becomes small, the absorption enhancements tend towards 1, as expected. The peak of the curve is located at a value of feature width and period for which the culmination of light-trapping effects integrated across the investigated spectrum is maximized. Under TE illumination the absorption is less than that of a flat layer for all values of NP width and period (Fig. 9.3(a)). No plasmonic excitation is possible with this polarization, and scattering from the particle does not compensate for the reduction in semiconductor volume.

9.3 Optimization study

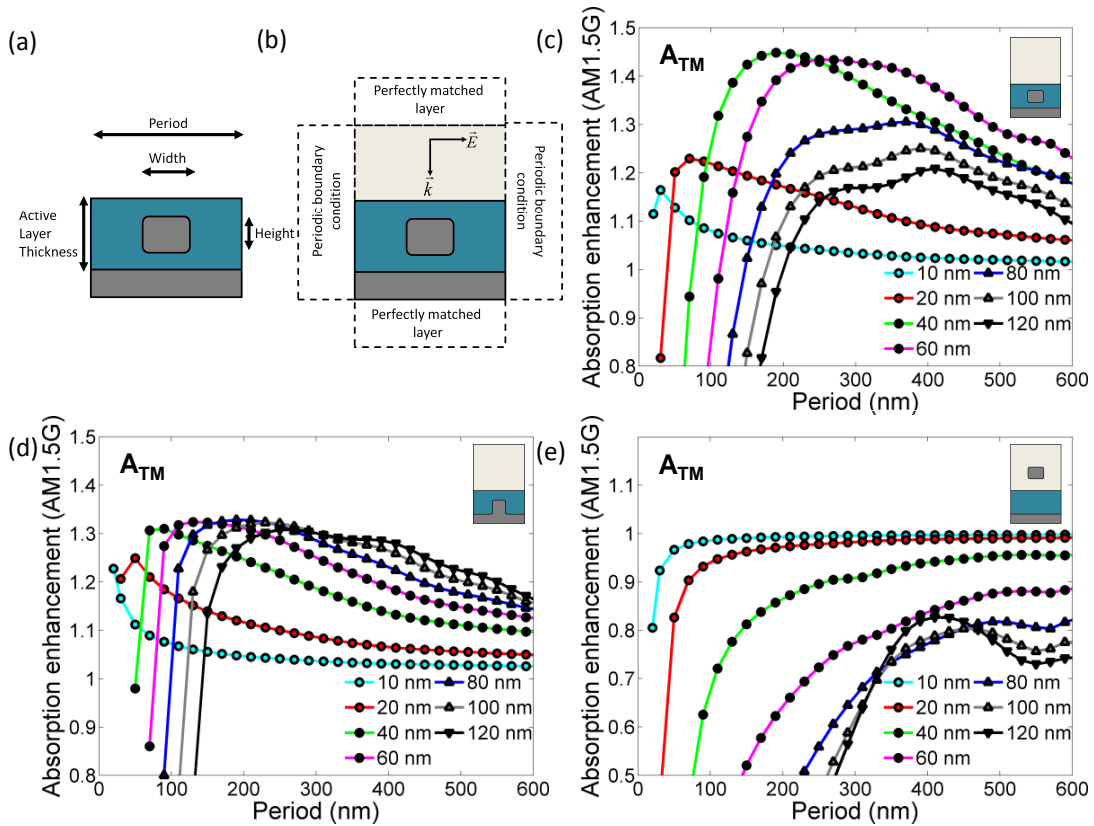


Figure 9.2: Optimization of plasmonic architectures for TM polarization. (a) Relevant geometry parameters for the simulations, shown here for the dispersed nanoparticle plasmonic solar cell. They can be similarly applied to the other two geometries. (b) Boundary conditions. (c-e) Absorption enhancement exhibited by plasmonic solar cells relative to a planar solar cell. The values are calculated by integrating semiconductor absorption spectra within the wavelength range 350-1000 nm with AM1.5G illumination intensity. (c) Dispersed nanoparticles. (d) Nanostructured electrode. (e) In-scattering nanoparticles.

A maximum enhancement in absorption in the OSC of 33% is observed for the nanostructured electrode PSC with a NP width of 80 nm and a period of 190 nm (Fig. 9.2 (d)) under TM illumination. Like the dispersed NP case, this is despite the 2D volume of semiconductor being reduced. The absorption under TE illumination is reduced for most combinations of NP width and periods, although a small absorption enhancement (1%) is observed for NP width 10 nm and period 600 nm. The higher performance of the nanostructured electrode PSC compared to the dispersed NP PSC for TE polarized light is likely due to the shadow effect present in the dispersed NP PSC.

The absorption enhancement provided by the in-scattering NP geometry with TM illumination is less than one for all simulated values of period and NP width (Fig. 9.2(e)) - the active

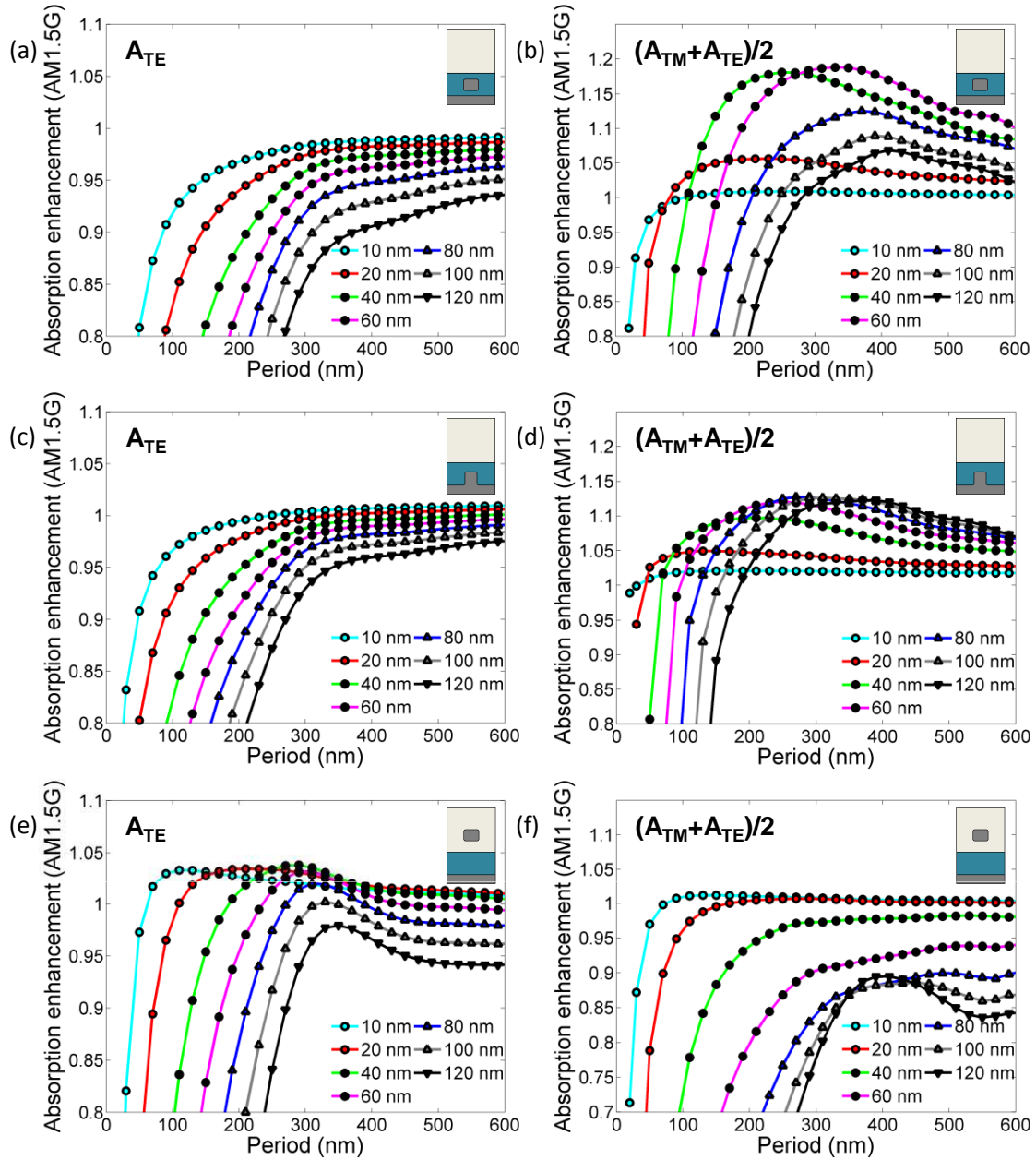


Figure 9.3: Optimization of plasmonic architectures for TE and averaged polarization. (a,c,e) Absorption enhancement exhibited by plasmonic solar cells relative to a planar solar cell for TE-polarized light. (b,d,f) Polarization-averaged absorption enhancement.

layer absorption of all simulated configurations are lower than that of the flat layer. The reasons for this will be discussed in the following section. However, an absorption enhancement of up to 4% is observed for TE polarization; absorption of TE-polarized light exceeds that

PSC Geometry	NP width (nm)	Period (nm)	Absorption enhancement (%)
Dispersed NPs	60	330	19
Struct. electrode	80	290	13
In-scattering NPs	10	130	1

Table 9.1: Optimized plasmonic solar cell geometries. Shown is the enhancement in polarization-averaged absorption over a flat architecture.

of TM-polarized light for this PSC geometry. We identify more efficient scattering into the semiconductor layer in the absence of localized plasmonic excitation at the nanoparticles as an important contributing mechanism for this. Excitation of low-order TE waveguide modes within the semiconductor layer [68] is not observed upon a rigorous inspection of the spectra - which is to be expected given the small difference in refractive index between the organic material ($n \approx 2$) and glass ($n = 1.4$), leading to poor mode confinement within the semiconductor material.

By combining the absorption enhancements for TM- and TE- polarized light according to equation 4, we obtain the polarization-averaged absorption enhancement of these devices (Fig 3(b,d,f)). These results apply for three-dimensional structures with an axis of symmetry as described in section 2 (c.f. line gratings). The optimized value for each PSC is shown in Table 9.1.

9.4 Dependence on semiconductor layer thickness

The previous optimization was carried out for a fixed value of the active layer thickness of 60 nm. The absorption enhancement of a PSC over a planar cell is highly dependent on this value. Taking the optimized dispersed NP geometry (NP width = 60 nm, period = 330 nm), we vary the thickness of the active layer, maintaining the center of the 30 nm high NP at a distance of 30 nm above the electrode. In doing so we effectively increase the amount of semiconductor material that the light must pass through before it can interact with the NPs. The absorption values (integrated across the 350-1000 nm wavelength range under 1 sun) of a flat and a PSC geometry are shown in Fig. 9.4 for active layer thicknesses up to 600 nm. The flat curve demonstrates a typical oscillatory dependence on active layer thickness, which arises from Fabry-Pérot resonances. [109] This oscillatory behavior is also observed for the PSC. We

note that the peaks of the PSC pattern are slightly shifted from those of the flat geometry. This confirms that the NPs affect the coherent interference of the light in the active layer. [150]

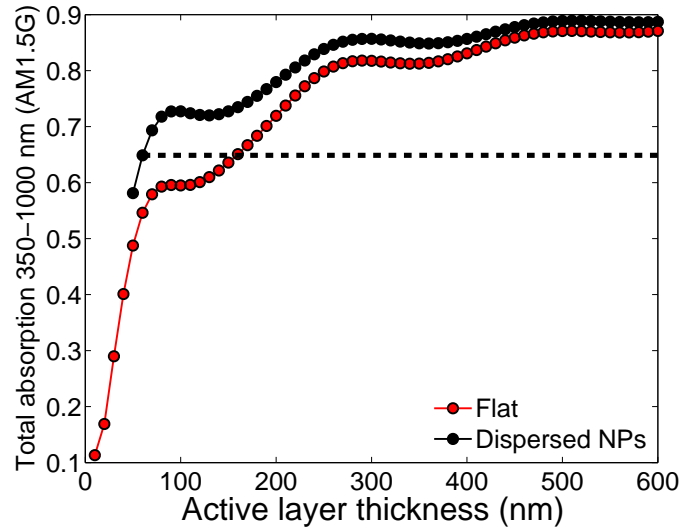


Figure 9.4: Plasmonic architectures can achieve absorption in thin-film solar cells equivalent to that of much thicker layers. Dependence of the active layer thickness on A_{av} for the dispersed nanoparticle and flat solar cells.

For an active layer thickness of 60 nm, we observe an absorption enhancement of 19% as shown in Table 1. Even higher enhancements are possible - a maximum of 22% is observed for an active layer thickness of 100 nm. As the active layer thickness further increases, the PSC curve converges with that of the flat geometry. This is consistent with a filter effect: the majority of light is absorbed before it reaches the NPs. Non-negligible enhancement is observed for active layer thicknesses as large as 600 nm. Finally we note that the active layer absorption for a 60 nm PSC exceeds that of all flat SCs with active layers thinner than 160 nm (indicated by the dashed line in Fig. 9.4). In other words, light trapping enables the absorption of a 60 nm thick semiconductor film in a PSC to be equivalent to that of a 160 nm flat film. By considering the area of the unit cell in each case, and accounting for the reduction in active material due to the presence of the NP, it follows that light-trapping enables an active material volume reduction of 65%.

9.5 Spectral characteristics of light-trapping

In order to focus on the role of plasmonic excitation on light trapping, we restrict our attention to TM illumination for the remainder of this paper. The absorption and reflection spectra of the flat and (TM-) optimized PSC structures are directly compared in Fig. 9.5, and corresponding spatial absorption profiles for selected wavelengths are shown in Fig. 9.7. Similar results are observed for the polarization-averaged optimized PSCs. The spectra have not been scaled by the solar spectrum. As the in-scattering geometry indicates a reduction of absorption in the active layer for all simulated values of period and NP width, there is no optimum configuration with non-zero NP width. In order to nevertheless compare the spectra with that of the other geometries to gain an insight into the loss mechanisms, we choose period = 40 nm and NP width = 190 nm (the same as those of the dispersed NP geometry).

The dispersed NP geometry semiconductor absorption exceeds the absorption in the flat geometry at all simulated wavelengths (Fig. 9.5(a)). Two main peaks are seen at 570 and 750 nm. A LSP resonance is observed as a sharp increase in the NP absorption at low wavelengths (the peak lies below 350 nm) (Fig. 9.5(c)). We see high active absorption at the same spectral position (Fig. 9.5(a)) - implying that light-trapping at this wavelength could be due to resonant near-field enhancement due to LSP excitation. No other LSP resonances are identified via peaks in the NP absorption spectrum. However, a spectrally broad enhancement in the semiconductor absorption is seen which cannot be solely accounted for by near-field enhancement due to (resonant) LSP excitation; scattering must play a large role. In section 3.3 we directly show that scattering alone can account for large absorption enhancements of the order observed here. We note that the small peak in the NP absorption at 600-650 nm (Fig. 9.5(c)) does not indicate a LSP resonance; it coincides with a dip in the absorption spectrum of the semiconductor (Fig. 9.5(a)), also observed in the electrode absorption (Fig. 5(d)). The absorption at 470 nm (Fig. 9.7(a)) is significantly more localized than in a flat SC (Fig. 9.7(c)), predominately occurring about the two front corners of the NP. This absorption pattern is similar with that observed for scattering into a highly absorbing material (see section 3.4). The absorption at 700 nm is preferentially localized at the back corners, which leads to intense absorption between the NP and the back electrode (Fig. 9.7(d)). This suggests that this structure could also be optimized to excite nanocavity modes. [67] The peak at 550 nm features localization (not shown) at both the front and back corners.

An impressive fraction of the additional absorption in the device (trapped light) is absorbed in the organic film (Fig. 9.6). This reaches a maximum of 97% at 750 nm. The spectrally-averaged enhancement, or alternately, the effective total enhancement, in device absorptivity due to the light-trapping enabled by the nanostructure is 26%.

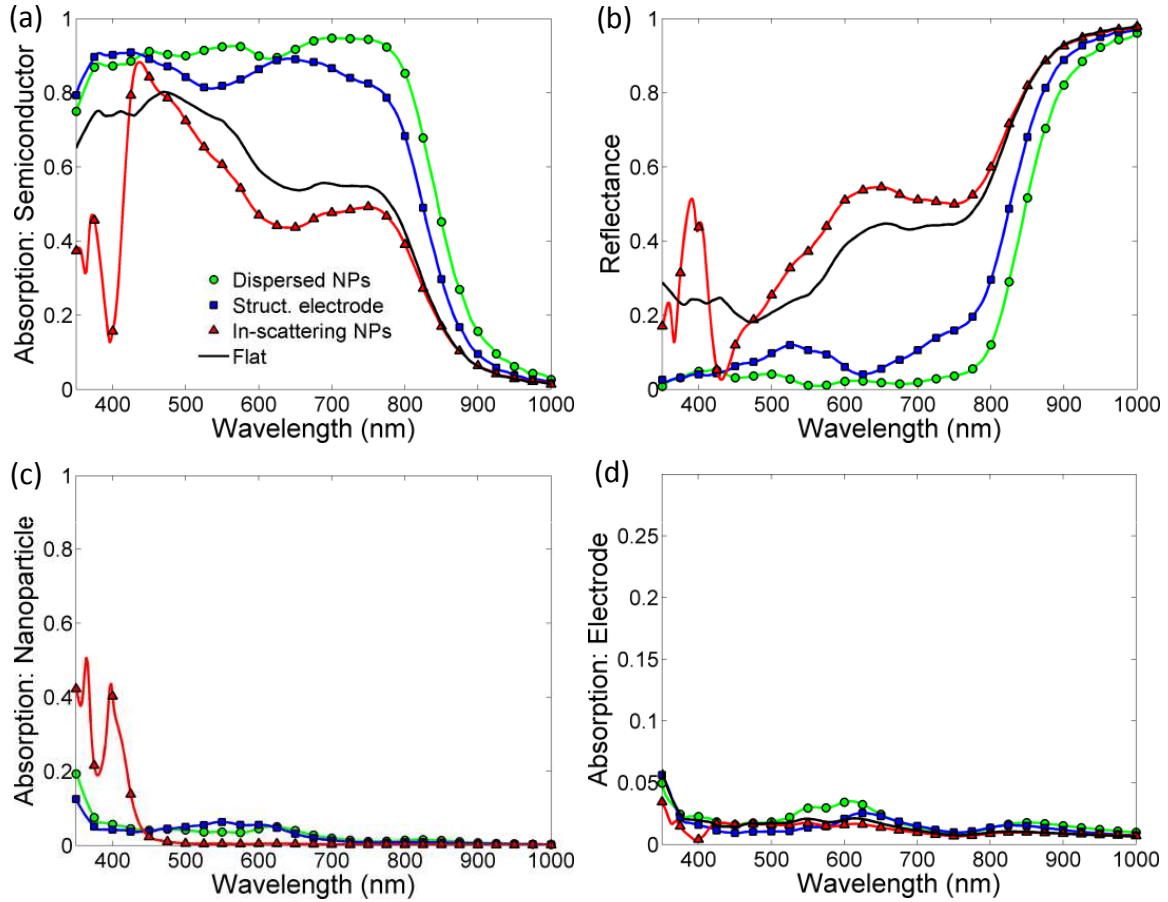


Figure 9.5: Redistribution of incident light (TM polarized) for the dispersed NP (circles, NP width = 40 nm, period = 190 nm), nanostructured electrode (squares, NP width = 80 nm, period = 190 nm) and in-scattering NP (triangles, NP width = 40 nm, period = 190 nm) plasmonic solar cells and the flat solar cell (black line). (a) Absorption in organic semiconductor. (b) Reflectance. (c) Absorption in the nanoparticle. (d) Absorption in the electrode. Note for the nanostructured electrode, the absorption in the planar electrode and the (attached) nanoparticle are calculated separately.

Like the dispersed NP geometry the active layer absorption for the nanostructured electrode geometry is significantly larger than that for the flat geometry (Fig. 9.5(a)) across the entire wavelength range addressed in this study. Strong absorption occurs between the NP and the top of the active layer at 470 nm (Fig. 9.7(b)). This is not however, due to a Fabry-Pérot resonance for this reduced active layer thickness (30 nm, between the NP and the edge of the active layer). Simulations where the thickness of the active layer for planar SCs is varied (Fig. 9.4), reveal no resonance for a layer thickness of 30 nm at the wavelength 470 nm (Fig. 9.7(b)). Therefore the NP itself must be fundamental to this absorption enhancement. As the absorption is quite

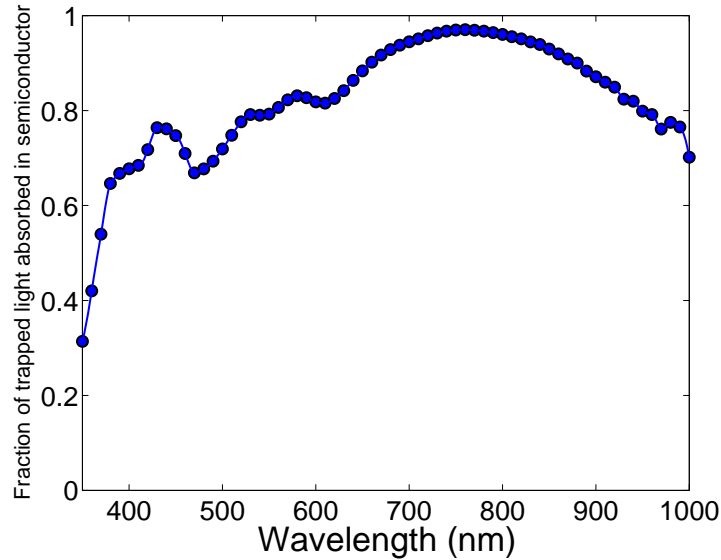


Figure 9.6: The majority of trapped light is absorbed in the semiconductor. For the (TM) optimized dispersed NP geometry: this graph shows the total additional light absorbed in the organic semiconductor due to the metallic nanostructure divided by the total additional light absorbed by the device.

delocalized and plasmonic absorption enhancement only extends into organic materials from a few to 10 nm, [72, 85] we attribute this delocalized absorption to back-scattering provided by the NP and not to near-field enhancement due to LSP excitation. The bulk of the absorption at 700 nm is similarly delocalized although localized absorption is also observed along the sides of the NP (Fig. 9.7(e)). The origin of the poor performance of the in-scattering layer in this study is largely due to enhanced reflection. The back-scattering that occurs due to the NPs has the effect of dramatically increasing the reflectance for a wide wavelength range (Fig. 9.5(b)), leading to a reduction in absorption in the active layer (Fig. 9.5(a)). Given the large spacing between the NP and the active material, near-field enhancement is also unavailable. We see therefore, that the wide angle in-scattering provided by the NPs does not outweigh the detrimental effect of back-scattering. The absorption in the NPs due to LSP resonances (Fig. 9.5(c)) at 360 (Fig. 9.7(f)) and 400 nm also represents a loss, although only over a narrow wavelength range. It is expected that further simulation studies of this PSC would indeed find an enhancement if other geometries and material combinations are considered. [34, 57]

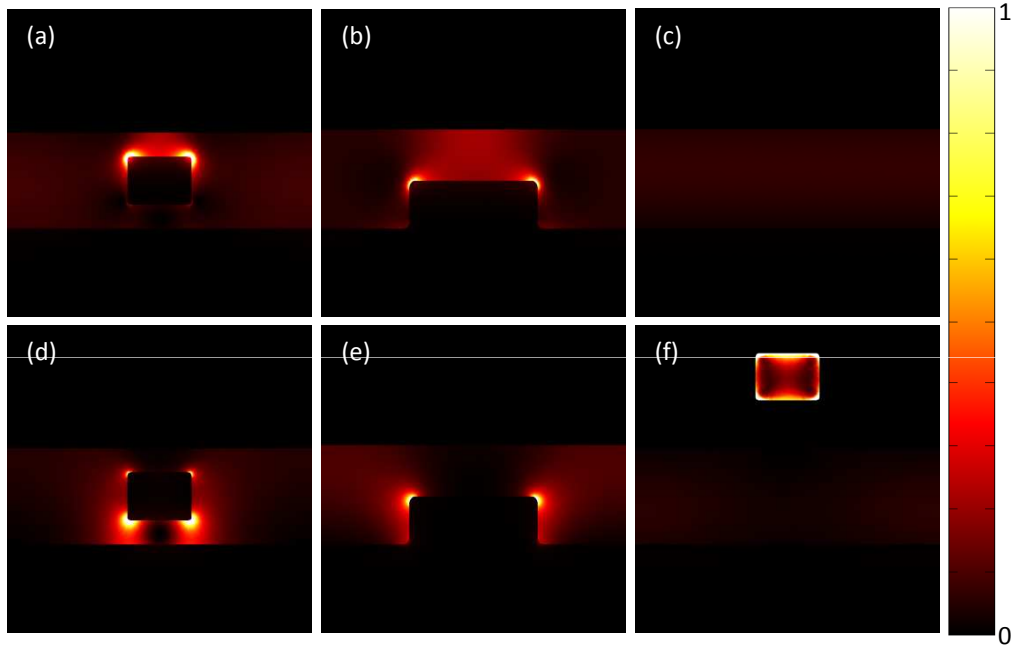


Figure 9.7: Spatial absorption profiles under TM polarization for selected wavelengths. (a,d): Dispersed nanoparticle solar cell (nanoparticle width = 40 nm, period = 190 nm) at wavelengths 470 nm (a) and 700 nm (d). (b,e) Nanostructured electrode (nanoparticle width = 80 nm, period = 190 nm) at wavelengths 470 nm (b) and 700 nm (e). (c) Flat solar cell at wavelength 470 nm. (f) In-scattering nanoparticle solar cell (nanoparticle width = 40 nm, period = 190 nm) at wavelength 360 nm. The color scale indicates the power dissipation density relative to the maximum in (a).

9.6 Ideal vs. non-ideal conductors

The importance of scattering in the absorption enhancement is explored further by comparing silver NPs with perfectly conducting NPs for the dispersed NP PSC. Plasmonic excitation is not possible for the perfectly conducting NPs; the only available enhancement mechanism is scattering. The semiconductor absorption spectra for period = 190 nm and NP width = 40 nm (as optimized for silver in section 3.1 for TM-polarized light) are shown in Fig. 9.8(a). A large absorption enhancement of 20% is seen for perfectly conducting NPs, which demonstrates that plasmonic excitation is not necessary for significant light trapping with this geometry. The localization of the absorption at the corners (Fig. 9.8(b)) closely resembles that observed in the case of silver NPs (Fig. 9.7(a-b)). The localization of the light arises because the scattered modes are absorbed before propagating more than a few nanometers into the high absorbing

material. This demonstrates that near-field enhancement due to LSP excitation is not necessary for light-trapping using metallic nanostructures: significant enhancements are possible via scattering alone. This corroborates the findings of previous reports. [73, 141] We note that even higher enhancement values are possible via scattering alone; 35% is observed for a perfectly conducting NP of width 60 nm and period 230 nm.

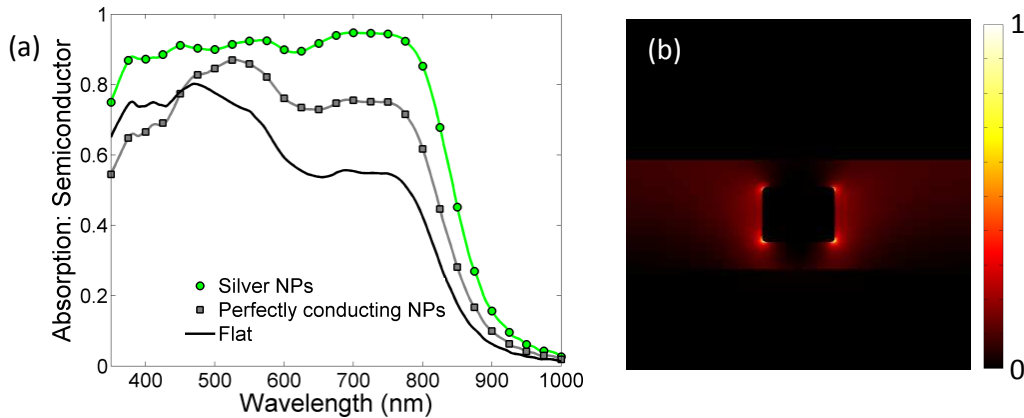


Figure 9.8: Plasmonic excitation is not necessary for effective light-trapping - scattering alone is sufficient. (a) TM semiconductor absorption for a flat solar cell (black line) and dispersed nanoparticle plasmonic solar cells with silver (circles) and perfectly conducting nanoparticles (squares), period = 190 nm, nanoparticle width = 40 nm. (b) Spatial absorption profiles with a perfectly conducting nanoparticle at 700 nm. The color scale indicates the power dissipation density relative to the maximum in 6(a).

9.7 Practical considerations for plasmonic solar cell fabrication

The above investigation finds excellent light-trapping properties for both dispersed nanoparticle and structured electrode organic solar cell architectures. Methods for fabricating ordered structured electrodes in solar cells have been well documented [83, 84]. Conversely, the ordered deposition of metal nanoparticles such that they rest in the middle of a solution-processed organic layer has not yet, to the best of our knowledge, been experimentally demonstrated (although very conceivable for organic solar cells featuring materials that can be evaporated, such as CuPc). However, high order is not critical for strong light trapping in this configuration, as observed experimentally with nanoparticles randomly dispersed within the active layer [73, 142?]. We find (Fig. 9.3(b)) the nanoparticles in the optimized configuration have a spacing of 330 nm, which far exceeds the distance over which LSP-LSP interaction takes place in an organic semiconductor (the plasmonic near field of a small nanoparticle extends to a distance of the order of 10 nm from the nanoparticle [72]). Therefore, light-trapping due to

LSP excitation at sufficiently widely spaced nanoparticles can be considered independent of the degree of order, and only on the density of the nanoparticles. A similar argument applies for scattering. Although excitation of diffraction modes is order sensitive, random arrays of metallic nanoparticles are known to (incoherently) scatter strongly due to the large scattering coefficient of individual particles [57, 58]. Therefore, the important parameter is the density of nanoparticles [129], implicitly defined here by the period of the nanoparticle array.

We also note that the presence of additional layers between the substrate and the organic layer such as the transparent electrode (typically indium tin oxide or aluminum-doped zinc oxide) and charge transport layers (PEDOT:PSS in non-inverted solar cells or TiO₂ or ZnO in inverted solar cells) affects the distribution of absorption within the semiconductor and as a result, the parameters of the optimal metallic nanostructure will vary between material system. Absorption in indium tin oxide electrodes represents an energy loss mechanism for both plasmonic and flat solar cells.

For the nanostructured electrode geometry, intervening layers between the semiconductor and the electrode could have a large effect, depending on the material and material thickness. In non-inverted solar cells, thin layers (< 1 nm) of LiF are often used. This would not be expected to strongly inhibit near-field effects (which extends out into the organic semiconductor up to around 10 nm from the metal surface) or light-trapping due to scattering at the electrode. A thick (5-10 nm) layer of Ca, which absorbs significantly and does not support plasmonic excitation, often used to modify the work function of the back-electrode, would significantly inhibit the absorption enhancement in the semiconductor. Conversely, a 5 - 10 nm layer of WO₃, which is optically transparent and often employed in inverted organic solar cells, may inhibit near-field enhancement but not light-trapping via scattering.

Conclusion

Plasmonic solar cells have been compared and optimized using finite element simulations to ascertain promising structures for high performance solar cells. The largest absorption enhancement observed for a 60 nm film of standard organic semiconductor is 19%, obtained by uniformly dispersing silver nanoparticles of width 60 nm with a periodicity of 330 nm. The absorption in a 60 nm film with this light trapping configuration is equivalent to that of a 160 nm flat film, representing a huge reduction in semiconductor consumption. Light-trapping is beneficial for all active layer thicknesses up to 600 nm. We find evidence of near-field plasmonic enhancement, but show that it is not necessary; strong absorption enhancement in the semiconductor is possible via scattering alone. This technique can be applied to a wide range

of low-cost semiconductors to find the critical device thickness below which light-trapping is required. If satisfactory charge transport is possible for thin films of this thickness, then light-trapping is unnecessary. If not, thinner films (with better charge transport properties) with light-trapping are preferable.

9.8 Summarizing remarks

In this chapter, an optimization study of three plasmonic solar cell architectures was presented. A particularly important result was obtained by comparing the light-trapping properties of silver nanoparticles and nanoparticles with infinite conductivity. Although localized surface plasmon excitation is certainly advantageous for light-trapping, it is not necessary. Significant light-trapping can be achieved via scattering alone. This is an important result for the design of future light-trapping architectures. The last and final chapter of this thesis, recommendations are provided for the continuation of this research. This is followed with a concise summary of the results and their implications.

10 Outlook and conclusion

Outlook

In the introduction (Chap. 1), the conundrum restricting the rise of inexpensive thin-film solar cells was introduced: thin semiconductor films are desirable to minimize costs and improve charge transport properties, yet suffer from limited absorption. In this thesis, it has been unequivocally demonstrated that appropriately designed nanostructures can be used to trap incident light and ensure that the absorption in a thin film can be equal to that of much thicker films. Key mechanisms relevant to this process in organic solar cells, such as exciton dynamics near metallic nanostructures and plasmonic excitations at metal-organic interfaces, have been examined. In addition, the sensitive relationship between light-trapping and nanostructure geometry has been characterized, and optimal metallic nanostructures for light-trapping in organic solar cells have been identified. This work has both laid the foundation for further studies and raised a number of interesting questions on the fundamentals of absorption enhancement in organic solar cells, such as the effect of a deformed electric field on charge transfer state dissociation. Precise recommendations for the continuation of this research, both experimentally and computationally, are presented in the following section.

Experimental

Stamp processing

The fabrication procedure for nanostructured electrode organic cells presented in this thesis is low-cost and scalable (Sec. 3.2). In this sense, it is suitable for mass-production manufacture in its current form. However, a shortcoming is that the anodized aluminum oxide (AAO) stamps are prone to wear and tear. While this is acceptable in a research and development setting, especially during process optimization when new stamps are regularly tested and compared, stamps made of more robust material will be required for industrialization.

It is nevertheless desirable to retain the significant amount of control that can be exerted over AAO stamp geometry. This versatility was one of the main motivations for using them. It is

therefore recommended that AAO stamps continue to be fabricated according to the current procedure (Sec. 3.2.1), but then undergo pattern replication. For instance, a flexible polymer film could be spin-coated onto an AAO stamp, such that it wholly or partially infiltrates the pores. This polymer film could then be peeled off, cured and optionally fixed to a flexible substrate. Such pattern replication processes have been demonstrated in the literature using polymers such as poly(methyl methacrylate) (PMMA) [151] and polydimethylsiloxane (PDMS) [83]. Specialized materials can be purchased commercially. [152] As part of this Ph.D, an internship project was supervised in which this was attempted. Promising demonstrations of pattern replication were achieved using the polymer *TOPAS 6013S-4*. This needs to be pursued further.

It is not possible to rule out whether the stamp damages the surface of the organic film during the imprint. Although the flat imprint displayed only a marginal reduction in performance (Fig. 8.2), the effect of any defects caused by the imprint is likely to be magnified for imprints with structured stamps due to the increased contact of the stamp with the organic film. It is therefore pertinent to continue to refine the surface functionalization of the stamp. In doing this, it is advisable to note the procedures taken by groups that have successfully imprinted organic films to obtain improved performance, such as *He et al*, who structured single semiconductor layers (not blend layers, as is done in this project) to improve the device morphology. [122]

Stamp geometry

As significant light-trapping (up to 45% over a range of 300-850 nm for a nanovoid architecture of periodicity 500 nm) has been consistently demonstrated (Sec. 5.1, Sec. 5.2, Chap. 6) with structured electrodes, the most pressing issue with the stamp geometry is not increasing the absorption. Rather, the most important step to be taken next is to ensure that the absorption enhancement can be converted to an efficiency enhancement in solar cells.

Evidence that the stamp penetrates too deeply into the organic film during imprinting with 500 nm period stamps is found as a reduced shunt resistance (Sec. 8.4). This is certainly partially due to the fact that the void depth (200 nm, shown in Fig. 3.6) exceeds the thickness of the organic film, which is 100 nm. A typical example of this is shown in Fig. 5.4(b), which shows that imprinted organic films can have a local thickness of 10 nm or less in some sections. It is recommended that for imprinting films of thickness 100 nm, stamps are produced with a pore depth of no more than 60 nm. Organic films imprinted with stamps of 60 nm void depth (observed for stamps with 100 nm void periodicity) remain in-tact, i.e. the stamp only partially penetrates the film, leaving a thick continuous, organic barrier layer between the substrate and the structured surface of the film, which can be seen in Fig. 3.8. This is confirmed by robust

device shunt resistances and fill-factors (Sec. 8.3). Therefore, it is essential to produce stamps with a 500 nm period (which have demonstrated the largest absorption enhancements so far) with shallower pores such that the thick organic barrier layers remain after imprinting. This will improve device performance dramatically.

Of course, as mentioned in Sec. 3.2.1, ordered AAO stamps with periodicity of 500 nm have not yet been achieved in our lab. An increased order is desirable, as it will enable effects such as more resonant localized surface plasmon excitations, and for ultra-high order, grating-coupled SPPs (Sec. 5.2).

Solar cells

The best nanostructured electrode devices constructed were with the 100 nm periodicity stamps. Despite this architecture exhibiting strong absorption enhancements of up to 28% over planar devices (Fig. 5.2), a 22% reduction in J_{SC} is observed (Fig. 8.1). As discussed in Sec. 8.3, a number of steps need to be taken to understand and overcome this. The first is to ensure that recombination and exciton annihilation at the silver surface is prevented by a continuous interfacial layer (Chap. 7). This can be done by depositing WO_3 films via atomic layer deposition. We note that efficient amorphous silicon solar cells with structured electrodes utilize a 130 nm thick, continuous barrier layer of aluminum doped zinc-oxide between the structured silver surface and the semiconductor. [86]

In addition, the thickness of the organic film can be varied to determine the effect of charge transport. As plasmonic excitation of nanovoids leads to significant localized absorption at the silver-organic interface (Chapters 6 and 9), the electrons have an increased distance to travel to reach the ITO electrode, compared to the planar case where light absorption is more uniform throughout the film. Conversely, holes, which are collected at the silver electrode, have a decidedly shorter distance to travel. The relationship between the current density and the organic film thickness may yield insights as to whether the device is limited by charge-transport.

Similarly, the mixing ratio of P3HT and PCBM may be varied: if the PCBM ratio in the bulk heterojunction is increased, electron percolation to the ITO electrode will improve. Any difference in the behavior between structured electrode and planar devices for varying PCBM content may provide further clues as to whether electron transport limits the performance of structured electrode devices.

It is possible to experimentally obtain an estimate of the exciton and charge transfer state dissociation probability following the method of *Mihaietchi et al.* [153] The probability that an

exciton will dissociate to form free charges (the probability that both an exciton and the corresponding charge transfer state will dissociate) is given by J_{ph}/J_{sat} at the short circuit condition, where J_{sat} is the current at which J_{ph} saturates at sufficiently high values of $V_{eff} = V_0 - V_a$ where V_0 is the voltage when $J_{ph} = 0$ and V_a is the applied voltage. It is recommended that these measurements are performed to compare the exciton and charge transfer state dissociation dynamics for nanostructured electrode and planar solar cells.

Typically, large applied biases (with a magnitude up to 15 V [154]) are required to obtain an accurate measurement of J_{sat} . The determination of the exciton-to-free charge dissociation efficiency will be invaluable in interpreting the performance of nanostructure electrode devices. A precedent exists for using this measurement for the characterization of plasmonic solar cells: it was found that the dissociation efficiency increases from 76% to 80% upon the incorporation of Au nanoparticles into a organic semiconductor layer. [137] Given the a nanovoid geometry will deform the device electric field (and hence influence the charge transfer state separation) in a different way to dispersed metallic nanoparticles, it is essential that this technique is applied to characterize the nanovoid electrode devices in this study.

Simulation

Absorption in solar cells

The simulation studies of absorption in plasmonic solar cells (Chapters 6 and 9) represent a rigorous treatment of the system. In order to extend this even further, a 3D equivalent of the optimization study in Chap. 9 could be carried out. This will require access to a much more powerful computing facility than was available during this research.

Charge dynamics in plasmonic solar cells

An understanding of how the deformed electric field introduced by the structured electrode affects charge transport and charge transfer state separation is vital for an improved understanding of the device performance in Chap. 8. The recommendation for investigating the experimentally was given above. Calculations of charge transfer state separation probabilities can be done with kinetic Monte Carlo simulations. [20] Simulations of charge transport in deformed electric fields could also be done with Monte Carlo methods. In order to carry out this investigation, a collaboration with a specialist group is recommended.

Nanvoid plasmons

An all-encompassing theory of plasmonic excitation on nanovoids still does not exist. One simple theory treats LSPs on voids as a standing wave pattern of SPPs bounded by the void rims. [37] Further 3D simulation studies such as the one in Chap. 6 could complement analytical and empirical models towards a deeper understanding of plasmons on nanovoids.

The origin of absorption enhancement

The influence of metallic nanoparticles in organic films is currently under intense discussion in the plasmonic solar cell community (see Sec. 2.5 and Chap. 9). The findings in this work support those in [73] and [141], indicating that the dominant mechanism in light-trapping with dispersed nanoparticles is scattering, and not near-field LSP enhancement. The effects can easily be confused in highly absorbing media - the distance from a nanoparticle within which scattered modes are strongly attenuated can be similar to the extent of the nanoparticle plasmon's near field (of the order of 10 nm in organic semiconductors, see [72, 85] and Figures 6.5, 9.7 and 9.8). This should be investigated further to determine the importance of each mechanism for various metallic nanostructures (including nanovoids) for different geometric domains. This would complement the findings of Sec. 5.2, where we observe efficient void LSP excitation in the wavelength range 430-800 nm for nanovoid arrays with a period of 500 nm, but not with 100 nm.

Conclusion

Light-trapping can strongly benefit the commercial development of thin-film solar cells. Low-cost and scalable fabrication methods, such as the ones developed in the course of this work, can be used to increase the efficiency and hence industrial cost-competitiveness of organic solar cells. In this thesis, a number of important steps have been made towards achieving this. We summarize the 10 most important achievements.

1. A technique was developed to fabricate nanostructured electrode solar cells (Sec. 3.2). Using anodized aluminum oxide stamps in a nanoimprint lithography process, nanostructured organic films were demonstrated (Sec. 3.2.3). A structured silver film is obtained when silver is thermally evaporated onto the structured organic surface. The silver film exhibits an ordered nanovoid surface (Fig. 6.1(d)). This technique can therefore be used to fabricate organic solar cells with structured (nanovoid geometry) metallic electrodes.

The process is low-cost, scalable and flexible. Moreover, it is conceivable that it could be incorporated into roll-to-roll processing.

2. Light-trapping was demonstrated using nanostructured electrode architectures fabricated using this technique. Total organic solar cell device absorption was demonstrated to increase by up to 45% over comparable planar architectures (Sec. 5.1). The robustness of this technique was demonstrated by presenting significant absorption enhancements for a range of nanovoid geometries and organic semiconductor blends (Fig. 5.2). As desired, the light-trapping was particularly effective for photon wavelengths that are poorly absorbed by the semiconductor.
3. Angle-sensitive reflectometry was used to ascertain the physical mechanisms responsible for the light-trapping (Sec. 5.2). Resonant, incident polarization-independent absorption peaks that were only weakly dependent on incident angle showed that localized surface plasmons are excited on the void surface for nanovoid arrays with 500 nm period periodicity. In contrast, no evidence of localized surface plasmon excitation is found for voids with 100 nm periodicity. We argue that it is likely that the plasmon resonance of these smaller voids lies at lower wavelengths than the minimum wavelength investigated (430 nm), consistent with simulation results for similar nanovoids (Chap. 6). Scanning plasmon polaritons were not observed, an indication of the limited long-range order of the nanovoids.

Similar results were found for both absorbing and non-absorbing organic films adjacent to the silver nanovoid surface.

4. Time-resolved two-photon photoluminescence spectroscopy was used to investigate the dynamics of excitons in the vicinity of metallic nanostructures (Chap. 7). It was found that volume-restricted P3HT films can exhibit exciton populations with higher radiative yield and longer lifetimes. This was attributed to ordering of P3HT chains within confined spaces. Significant metal-induced quenching of excitons is measured for excitons generated up to a distance of 40-50 nm from of a metallic surface (Fig. 7.3). As a result of this, we use films of WO_3 as exciton-blocking layers in all solar cell devices (Chap. 8).
5. Organic solar cells with nanostructured electrodes are fabricated using the technique developed in Sec. 3.2. A study of 99 devices is carried out to determine the performance of structured electrode devices relative to reference (planar electrode) devices (Fig. 8.1). The performance of devices where the organic film is imprinted with a flat stamp does not differ significantly from that of reference devices - demonstrating that the imprint (temperature and pressure) does not fundamentally damage the organic device (Sec. 8.2). Conversely, devices with a structured electrode with a periodicity of 100 nm exhibit a

reduced J_{SC} and hence a reduced efficiency (Sec. 8.3) despite having respectable values of FF and V_{OC} . We identify a number of plausible explanations and outline a short list of experiments that will clarify this. In addition, a number of recommendations are provided for the further refinement of the fabrication process.

6. The finite element method was used to simulate absorption of electromagnetic radiation in solar cells. Absorption spectra calculated using 3D models of experimentally-realized planar and structured electrodes architectures exhibited very good agreement with experimental spectra (Chap. 6).
7. Once it was established that the simulation routine reproduces experimental results satisfactorily, further investigations of nanovoid geometries were carried out (Chap. 6). Spatial absorption profiles revealed resonant localized absorption for void arrays with 60 and 100 nm periodicities. A thorough investigation of the 60 nm voids revealed that the two resonant peaks in absorption were fundamentally different: at the shorter wavelength, incident light was coupled to form a standing wave along the inner void rim whereas at the longer wavelength peak, light did not penetrate into the voids but excited localized modes on the planar intervoid space.

Importantly, we find that the majority of the additionally trapped light occurs in the semiconductor and not in the metal. Enhancements in the exciton generation rate per volume in nanovoid architectures is found to be up to 17% higher than in comparable planar architectures .

8. An optimization study was carried out to compare three plasmonic architectures that are commonly considered in the literature (Chap. 9). The values of nanoparticle width and height were varied independently, and the absorption within a 2D-symmetric solar cell device with a 60 nm thick organic film was simulated for each configuration. The most effective geometry featured silver nanoparticles of width 60 nm and a spacing of 330 nm dispersed in the active layer. An absorption enhancement of 19% is found for this configuration. It is found that this absorption enhancement is assisted by a very efficient absorption of the trapped light in the semiconductor. For TM-polarized incidence, the fraction of trapped light that is absorbed in the semiconductor is as high as 97%. The highest possible absorption enhancements for nanostructured electrode and in-scattering nanoparticle architectures are found to be 13% and 1%, respectively.
9. Although we find evidence of LSP excitation for the dispersed nanoparticles, we find that it is not necessary. Significant absorption enhancements are also demonstrated via non-plasmonic scattering alone (Sec. 9.6). This has important consequences for the future

design of light-trapping solar cells and confirms the findings of two recent reports in the literature [73, 141].

10. It is found that the absorption of a 60 nm thick organic film fitted with this optimized light-trapping system is equal to that of a 160 nm flat film (Sec. 9.4). In other words, the metallic nanostructure enables a semiconductor volume reduction of 65% without compromising the total absorption in the semiconductor. In real devices, this volume reduction translates into a reduction in semiconductor material cost and a possible improvement in charge transport.

Thin-film solar cells have the potential to play a big part in a secure global energy future based on renewable energy technology. However, they are typically encumbered by poor absorption of incident light, particularly near the semiconductor band-gap. The development of a low-cost, scalable process that can enable light-trapping in thin-films represents an important contribution toward a wider implementation of photovoltaics, as it can lead to an increase in device efficiency and a consequent reduction in the cost/kW generating capacity of the technology. Such a process has been developed in this work. We use it to demonstrate organic solar cells with structured (nanovoid) metallic electrodes. Devices with these electrodes exhibit absorption enhancements of up to 45% over devices with conventional, planar electrodes. The mechanisms responsible for this light-trapping are characterized. Computational studies are carried out to complement these experiments with the observation that localized plasmons are indeed excited on these nanovoid surfaces. A comprehensive simulation study of all important plasmonic geometries identifies ideal metallic nanostructures and demonstrates the massive potential of light-trapping. The results of this doctoral thesis unequivocally show that light-trapping, when correctly implemented, has the potential to vastly increase the efficiency and hence decrease the price of thin-film solar cells.

Appendix A - Sample finite element simulation code

Codes in Matlab have been written to define simulation geometries, material properties and boundary conditions, solve the problems by calling Comsol finite element solvers and to automate and cycle these processes. The code reproduced in the following pages simulates optical absorption in 2D solar cell architectures for a range of nanostructures by varying the period and width of a nanoparticle.

```

format long e;
%close all %closes open figures
fclose fem
clear all

% Functions
clear fns
%optical constants: (two are shown for illustrative purposes)
clear fns
fns(1,'type='interp');
fns(1,'name='johnsonagk');
fns(1,'method='piecewise cubic');
fns(1,'extmethod='interior');
fns(1,'x'={1.879E-7,1.917E-7,1.953E-7,1.994E-7,2.033E-7,2.074E-7,2.112E-7,2.148E-7,2.184E-7,2.263E-7,2.313E-7,2.371E-7,2.427E-7,2.49E-7,2.551E-7,2.616E-7,2.69E-7,2.762E-7,2.844E-7,2.925E-7,3.01E-7,3.108E-7,3.204E-7,3.316E-7,3.425E-7,3.543E-7,3.668E-7,3.815E-7,3.974E-7,4.133E-7,4.306E-7,4.509E-7,4.715E-7,4.96E-7,5.21E-7,5.487E-7,5.822E-7,6.169E-7,6.596E-7,7.045E-7,7.561E-7,8.212E-7,8.921E-7,9.841E-7,1.088E-6,1.216E-6,1.393E-6,1.61E-6,1.938E-6});
fns(1,'data'={1.07,1.1,1.12,1.14,1.15,1.18,1.2,1.22,1.25,1.26,1.28,1.3,1.31,1.33,1.35,1.38,1.41,1.41,1.39,1.34,1.34,1.13,0.81,0.17,0.14,0.1,0.07,0.05,0.05,0.05,0.04,0.04,0.04,0.05,0.05,0.05,0.06,0.06,0.05,0.05,0.04,0.03,0.03,0.04,0.04,0.04,0.04,0.04,0.09,0.13,0.15,0.24});
fns(2,'type='interp');
fns(2,'name='johnsonagk');
fns(2,'method='piecewise cubic');
fns(2,'extmethod='interior');
fns(2,'x'={1.879E-7,1.917E-7,1.953E-7,1.994E-7,2.033E-7,2.074E-7,2.112E-7,2.148E-7,2.184E-7,2.263E-7,2.313E-7,2.371E-7,2.427E-7,2.49E-7,2.551E-7,2.616E-7,2.69E-7,2.762E-7,2.844E-7,2.925E-7,3.01E-7,3.108E-7,3.204E-7,3.316E-7,3.425E-7,3.543E-7,3.668E-7,3.815E-7,3.974E-7,4.133E-7,4.306E-7,4.509E-7,4.715E-7,4.96E-7,5.21E-7,5.487E-7,5.822E-7,6.169E-7,6.596E-7,7.045E-7,7.561E-7,8.212E-7,8.921E-7,9.841E-7,1.088E-6,1.216E-6,1.393E-6,1.61E-6,1.938E-6});
fns(2,'data'={1.212,1.232,1.255,1.277,1.296,1.312,1.325,1.336,1.342,1.344,1.357,1.367,1.378,1.389,1.393,1.387,1.372,1.331,1.264,1.161,0.964,0.616,0.392,0.829,1.142,1.419,1.657,1.864,2.07,2.275,2.462,2.657,2.869,3.093,3.324,3.586,3.858,4.152,4.483,4.838,5.242,5.727,6.312,6.992,7.795,8.828,10.1,11.85,14.08});

fem.functions = fns;
%%%%%%%%%%%%%%%%%%%%%%%%%%%%%%%%%%%%%%%%%%%%%%%%%%%%%%%%%%%%%%%%%%%%%%%%
%%%%%%%%%%%%%%%%%%%%%%%%%%%%%%%%%%%%%%%%%%%%%%%%%%%%%%%%%%%%%%%%%%%%%%%%
%%%%%%%%%%%%%%%%%%%%%%%%%%%%%%%%%%%%%%%%%%%%%%%%%%%%%%%%%%%%%%%%%%%%%%%%
%input tested wavelength, flat/nanostructured electrode and polarization
%identifiers
wavemin=350e-9;
wavemax=1000e-9;
wavevals=326;
isitflat=0; %flat=1 structured=0
isitTM=1; % TM mode = 1, TE = 0

%Looping parameters - geometry of the nanostructure is varied
%accordingly. Here the period and xnanowire (NP width) is varied
periodmin=150e-9;

```

```

periodmax=610e-9;
periodstep=20e-9;

if isitflat==1
    periodvals=[200e-9];
else
    xnanowirevals=[10e-9,20e-9,40e-9,60e-9,80e-9,100e-9,120e-9];
end

[dummy xnanowirevals]=size(xnanowirevals);
mkdir('testoutput');
mkdir('testoutput\pictures');
for jii=1:nxnanowirevals
    Directoryname='testoutput\xnanowire-' num2str(round(1e9*xnanowirevals(jii)))
    'mm';
    mkdir(Directoryname)
end
mkdir('testoutput') %define directories to store output
mkdir('testoutput\pictures')
for jii=1:nxnanowirevals
    Directoryname='testoutput\xnanowire-' num2str(round(1e9*xnanowirevals(jii)))
    'mm';
    mkdir(Directoryname)
end

for jii=1:nxnanowirevals %loop through NP width values
    %%Geometry
    xnanowire=xnanowirevals(jii)
    if isitflat==0
        periodvals=[xnanowire+10e-9:periodstep:periodmax]; %for this NP width value,
        we select all suitable values of period
        if xnanowire==10e-9 %special case for xnanowire=10nm
            periodvals=[20e-9:10e-9:periodstep:periodmax];
        end
    end

    sizeperiodvals=size(periodvals);Nperiodsteps=sizeperiodvals(1,2); %define matrices
    to store data e.g. absorption for every wavelength
    reflmat=zeros(wavevals,Nperiodsteps+1);
    electrodesabmat=zeros(wavevals,(Nperiodsteps+1));
    nanostruconlyabmat=zeros(wavevals,(Nperiodsteps+1));
    activeabmat=zeros(wavevals,(Nperiodsteps+1));
    incenergymat=zeros(wavevals,(Nperiodsteps+1));
    leaksabmat=zeros(wavevals,(Nperiodsteps+1));

    %%Geometry of the solar cell explicitly defined for each simulation
    % xnanowire=75e-9;
    ynanowire=30e-9;
    % period=50e-9;
    filletradius=4.0e-9;
    nwelectrodespacing=15e-9;
    yactivescatgeom=5e-9;
    ycathode=200e-9; %silver layer

```

```

%
ytopPWL=400e-9;
yincmedtop=350e-9;
yincmedbottom=150e-9;

yactive=55e-9;
dwo3=5e-9;

powerin=100; %input power = 100 units

% Constants
fem.const = {'wave0', '5000e-9'};

for jj=1:Nperiodsteps
    %buffer=xbuffervals(1,jj);
    period=periodvals(1,jj)

    NewDirectoryName=['testoutput\pictures\' 'period' num2str(round(1e9*period))
    'mm'];
    mkdir(NewDirectoryName)

    %Constructing the geometry using simple shapes and functions
    % period=2*reilipsoid*2*xroundoff+xbuffer; %total width of period
    g1=rect2(xnanowire,ynanowire,'base','corner','pos',[-xnanowire/2,0]);
    g2=rect2((xnanowire+2*dwo3),(ynanowire+dwo3),'base','corner','pos',[-xnanowire/2-dwo3,0]);
    g3=fillet(g1,'radii',filletradius,'point',[3,4]);
    % g3=rect2(xnanowire,ynanowire,'base','corner','pos',[xnanowire/2,0]);
    % g3=fillet(g3,'radii',filletradius,'point',[1]);
    g3=rect2(xnanowire,ynanowire,'base','corner','pos',[xnanowire/2,0]);
    g4=rect2(filletradius,filletradius,'base','corner','pos',[xnanowire/2,0]);
    % g4=rect2(xnanowire,ynanowire,'base','corner','pos',[xnanowire/2,0]);
    g4=geomcomp([g4,g3],'ns',{'R4','CO3'],'sf','R4-CO3','edge','all');
    g5=mirror(g4,[xnanowire/2,0],[1,0]);
    g5=move(g5,[-xnanowire,0]);
    %
    g6=geomcomp([g1,g4,g5],'ns',{'R1','CO4','CO5'],'sf','R1-CO4+CO5','edge','all');
    %nanowire

    g6=geomcomp([g1,g4,g5],'ns',{'R1','CO4','CO5'],'sf','R1-CO4+CO5','edge','all');
    %nanowire
    xnanowire/2-dwo3,0];
    % g7=fillet(g7,'radii',(filletradius+dwo3),'point',[3,4]);
    g16=rect2(period,dwo3,'base','corner','pos',{(-period/2),0},'rot','0');
    %spacer
    layer
    g16flat=rect2(period,dwo3,'base','corner','pos',{(-period/2),0},'rot','0');
    %spacer
    layer
    g16=geomcomp([g16,g1],'ns',{'R16','CO1'],'sf','R16-CO1','edge','all');
    g21=geomcomp([g1,g2],'ns',{'CO1','CO2'],'sf','CO2-CO1','edge','all');
    g22=geomcomp([g21,g16],'ns',{'CO2','R16'],'sf','CO2+R16','edge','all');

    %cleaning up and merging the boundaries
    g9=geomedit(g22);
    g9([4])={[]};
    g9{2}=beziercurve2((-period/2),(xnanowire/2)],[0,0],[1,1]);
    g22=geomedit(g22,g9);

    g9=geomedit(g22);
    g9([12])={[]};
    g9{10}=beziercurve2((xnanowire/2),(period/2)],[0,0],[1,1]);
    g22=geomedit(g22,g9);
end
%
g23=rect2((2*filletradius),(2*filletradius),'base','corner','pos',{(xnanowire/2),0},'rot','0'); %rounding at base
g24=fillet(g23,'radii',filletradius,'point',[1]);
g25=geomcomp([g23,g24],'ns',{'CO23','CO24'],'sf','CO23-CO24','edge','all');
g26=mirror(g25,[xnanowire/2,0],[1,0]);
g26=move(g26,[-xnanowire,0]);

g27=geomcomp([g26,g25,g1],'ns',{'CO26','CO25','CO1'],'sf','CO26+CO25+CO1','edge','all');
%nanowire finished
g22=geomcomp([g22,g27],'ns',{'CO22','CO27'],'sf','CO22-CO27','edge','all');
%trim casing

g9=geomedit(g27);
g9([2])={[]};
g9{1}=beziercurve2((-xnanowire/2-filletradius),(xnanowire/2)],[0,0],[1,1]);
g27=geomedit(g27,g9);

g9=geomedit(g27);
g9([4])={[]};
g9{1}=beziercurve2((-xnanowire/2-filletradius),(xnanowire/2+filletradius)],[0,0],[1,1]);
filletradius,(xnanowire/2+filletradius)],[0,0],[1,1]);
g27=geomedit(g27,g9);

%Performing checks to ensure that the final structure will be valid
if filletradius > dwo3
    g28=rect2((2*filletradius-dwo3),(2*filletradius-dwo3),'base','corner','pos',{(xnanowire/2+dwo3),dwo3}),'rot','0'); %rounding at base
    g29=fillet(g28,'radii',(filletradius-dwo3),'point',[1]);
    g30=geomcomp([g28,g29],'ns',{'CO28','CO29'],'sf','CO28-CO29','edge','all');
    g31=mirror(g30,[xnanowire/2+dwo3],0],[1,0]);
    g31=move(g31,[-xnanowire-2*dwo3,0]);
    g22=geomcomp([g22,g30,g31],'ns',{'CO22','CO30','CO31'],'sf','CO22+CO30+CO31','edge','all');
    %nanowire
    else

    g28=rect2((2*filletradius),(2*filletradius),'base','corner','pos',{(xnanowire/2+dwo3),dwo3}),'rot','0'); %rounding at base
    g29=fillet(g28,'radii',filletradius,'point',[1]);
    g30=geomcomp([g28,g29],'ns',{'CO28','CO29'],'sf','CO28-CO29','edge','all');
    g31=mirror(g30,[xnanowire/2+dwo3],0],[1,0]);
    g31=move(g31,[-xnanowire-2*dwo3,0]);
    g22=geomcomp([g22,g30,g31],'ns',{'CO22','CO30','CO31'],'sf','CO22+CO30+CO31','edge','all');
    %nanowire

    g9=geomedit(g22);
    g9([6])={[]};
    g9{5}=beziercurve2((-xnanowire/2),(xnanowire/2)],[1,1]);
    g22=geomedit(g22,g9);

    g9=geomedit(g22);
    g9([9])={[]};
    g9{8}=beziercurve2((xnanowire/2),(xnanowire/2)],[filletradius,(xnanowire/2)],[1,1]);
    g22=geomedit(g22,g9);
end

```

```

'hmaxedge', [1, meshmaxedge, 2, meshmaxedge, 3, meshmaxedge, 4, meshmaxedge, 5, meshmaxedge, 6, meshmaxedge, 7, meshmaxedge, 8, meshmaxedge, 9, meshmaxedge, 10, meshmaxedge, 11, meshmaxedge, 12, meshmaxedge, 13, meshmaxedge, 14, meshmaxedge, 15, meshmaxedge, 16, meshmaxedge, 17, meshmaxedge, 18, meshmaxedge, 19, meshmaxedge, 20, meshmaxedge, 21, meshmaxedge, 22, meshmaxedge, 23, meshmaxedge, 24, meshmaxedge, 25, meshmaxedge, 26, meshmaxedge, 27, meshmaxedge, 28, meshmaxedge, 29, meshmaxedge, 30, meshmaxedge, 31, meshmaxedge, 32, meshmaxedge ], ...
'point', [], ...
'edge', [1, 3, 5, 7, 9, 26, 28], ... %first mesh the boundaries for PBCs
'ubdomain', []];
- we wish to copy the meshes to the corresponding bdy

% Copy boundary mesh - ensure opposing boundaries have identical
% mesh (Improves performance of periodic boundary condition)

fem.mesh=meshcopy(fem, ...
'source', 28, ...
'target', 32, ...
'direction', 'auto', ...
'mcase', 0);

fem.mesh=meshcopy(fem, ...
'source', 26, ...
'target', 31, ...
'direction', 'auto', ...
'mcase', 0);

fem.mesh=meshcopy(fem, ...
'source', 9, ...
'target', 21, ...
'direction', 'auto', ...
'mcase', 0);

fem.mesh=meshcopy(fem, ...
'source', 7, ...
'target', 20, ...
'direction', 'auto', ...
'mcase', 0);

fem.mesh=meshcopy(fem, ...
'source', 5, ...
'target', 19, ...
'direction', 'auto', ...
'mcase', 0);

fem.mesh=meshcopy(fem, ...
'source', 3, ...
'target', 18, ...
'direction', 'auto', ...
'mcase', 0);

fem.mesh=meshcopy(fem, ...
'source', 1, ...
'target', 17, ...
'direction', 'auto', ...
'mcase', 0);

% Initialize remaining mesh
fem.mesh=meshinit(fem, ...
'hmax', meshmaxglobal, ...
'hcurve', 0.4, ...
'hgrad', 1.4, ...
'htutoff', 0.005, ...
);

```

```

gactive=rect2(period, (yactive+dw03), 'base', 'corner', 'pos', {(-
period/2), 0}, 'rot', 0); %active
gcathode=rect2(period, (ycathode), 'base', 'corner', 'pos', {(-period/2), (-
ycathode)}, 'rot', 0); %cathode
gincomedbottom=rect2(period, (yincmedbottom), 'base', 'corner', 'pos', {(-
period/2), (dw03+yactive)}, 'rot', 0);
gincomedtop=rect2(period, (yincmedtop), 'base', 'corner', 'pos', {(-
period/2), (dw03+yactive+yincmedbottom)}, 'rot', 0);
stoppML=rect2(period, (ytopPML), 'base', 'corner', 'pos', {(-
period/2), (dw03+yactive+yincmedbottom+yincmedtop)}, 'rot', 0);

fnanoparticle=rect2(xnanowire, ynanowire, 'base', 'corner', 'pos', [-
nanowire/2, nwelectrodespacing]);

fnanoparticle=fillet(fnanoparticle, 'radii', 2e-9, 'point', [1, 2, 3, 4]);
factive=newrect2(period, nwelectrodespacing, 'base', 'corner', 'pos', [-
period/2, 0]);
factive=catgeom=rect2(period, yactive, 'base', 'corner', 'pos', [-
period/2, 0]);

domaincomp=geomcomp({stoppML, gincomedtop}, 'ns', {'R1', 'R2'}, 'sf', 'R1+R2', 'edge', 'none');
%, 'repairtol', 1.0E-10
if isitflat==0

domainbottom=geomcomp({gactive, gincomedbottom, gcathode, fnanoparticle, factive, new, factive
scatgeom}, 'ns', {'R3', 'R4', 'R5', 'R6', 'R7', 'R8'}, 'sf', 'R3+R4+R5+R6+R7+R8', 'edge', 'none')
;
else
domainbottom=geomcomp({gactive, gincomedbottom, gcathode, factive, new, factive, scatgeom}, 'ns
', {'R1', 'R2', 'R3', 'R4', 'R5'}, 'sf', 'R1+R2+R3+R4+R5', 'edge', 'none');
end

% Create assembly - (to do with internal boundary conditions)
clear s {domainbottom, domaincomp};
s.objs={ 'CO1', 'CO2' };

fem.draw=struct('s', s);
fem.geom=geomgroup(fem, 'imprint', 'off', ...
'paircand', {'CO1', 'CO2'}, ...
'repairtol', 1.0E-10);

% figure, geomplot(fem, 'edgelabels', 'on') %inspecting geometry
%% Mesh - now form the mesh. Define maximum sizes on domain and domain
%% boundary
meshmaxglobal=20e-9;
meshmaxedge=5e-9;
% Initialize mesh
if isitflat==0 %for structured case

fem.mesh=meshinit(fem, ...
'hmax', meshmaxglobal, ...
'hcurve', 0.4, ...
'hgrad', 1.4, ...
'htutoff', 0.005, ...
);

```



```

pair.import = 1;
pair.pport = powerin;
pair.type = 'port';
if isitTM=0
    pair.usermodetype = 'TE';
    pair.E0 = {{0;0;5}}; %TE
else
    pair.usermodetype = 'TM';
    pair.H0 = {{0;0;5}}; %TM
end
pair.curofforbeta = 'cutoff';
pair.pair = 'Pair 1';
bnd.pair = pair;

appl.bnd = bnd;
%
% bnd.inport = {0,0,0,0,0,1};
% bnd.type =
% {'H0','cont','periodic','periodic','periodic','periodic','periodic','period
ic'}; %port out, cont, per glass
% i=PWC, 2=cont, 3=per toppML, 4=per inmedtop, 5=per inmedbottom,
% 6=per act, 7=per active new, 8=per silv, 9=per activescatgeom
bnd.index = {0,0,1,2,3,4,5,6,7};
bnd.ind = [8,1,7,2,9,....
2,6,2,5,2,....
1,8,7,9,6,....
5,4,1,3,2,....
1,4,3];

clear pair
pair.import = 1;
pair.pport = powerin;
pair.type = 'port';
if isitTM=0
    pair.usermodetype = 'TE';
    pair.E0 = {{0;0;5}}; %TE
else
    pair.usermodetype = 'TM';
    pair.H0 = {{0;0;5}}; %TM
end
pair.curofforbeta = 'cutoff';
pair.pair = 'Pair 1';
bnd.pair = pair;

appl.bnd = bnd;
end

clear equ %domain settings - refractive index values
equ.coordOn = {{0;0},{0;0},{0;0},{0;0},{0;0},{0;0}};
equ.n = {'Johnsonagi(wave0)-
j*johnsonag(wave0)',1.4,1.4,1.4,'denmlerpcdtbpc70bmm(wave0)-
j*denmlerpcdtbpc70bmm(wave0)'}; %dummy polymer
% i=silv, 2= glass, 3= SI, 4=PML, 5=dummy polymer
equ.stype = {'none','none','none','none','none','none'};
equ.matparams = {'n','n','n','n','n','n'};

if isitflat=0 %structured!!!
    equ.ind = [1,5,5,2,1,2,4]; %polymer-metal
clear pair

```

```

pair{1}.type= 'identity';
pair{1}.name= 'Pair 1';
pair{1}.src.dl = [11];
pair{1}.src.operator = 'src2dst_ip2';
pair{1}.dst.dl = [27];
pair{1}.dst.operator = 'dst2src_ip2';
bnd.pair = pair;

fem.bnd = bnd;

clear pair
pair{1}.type= 'identity';
pair{1}.name= 'Pair 1';
pair{1}.src.dl = [6,20];
pair{1}.src.operator = 'src2dst_ip1';
pair{1}.dst.dl = [21,24];
pair{1}.dst.operator = 'dst2src_ip1';
pnt.pair = pair;

fem.pnt = pnt;

% %flat!!!
% equ.ind = [1,5,5,2,2,4]; %polymer-metal-with Si scatterer

clear pair
pair{1}.type= 'identity';
pair{1}.name= 'Pair 1';
pair{1}.src.dl = [11];
pair{1}.src.operator = 'src2dst_ip2';
pair{1}.dst.dl = [18];
pair{1}.dst.operator = 'dst2src_ip2';
bnd.pair = pair;

fem.bnd = bnd;

clear pair
pair{1}.type= 'identity';
pair{1}.name= 'Pair 1';
pair{1}.src.dl = [6,12];
pair{1}.src.operator = 'src2dst_ip1';
pair{1}.dst.dl = [13,16];
pair{1}.dst.operator = 'dst2src_ip1';
pnt.pair = pair;

fem.pnt = pnt;

end

appl.equ = equ;
appl.var = {'nu','le9',...
'lamda0','wave0'};
fem.appl{1} = appl;
fem.frame = {'ref'};
fem.border = 1;
clear units;
units.basesystem = 'SI';
fem.units = units;

% ODE Settings %performing assembly and then solving
% system

```

```

clear ode
clear units;
units.basesystem = 'SI';
ode.units = units;
fem.ode=ode;

% Multiphysics
fem=multiphysics(fem);

% Extend mesh
fem.xmesh=meshxend(fem);

% Solve problem
fem.sol=femstatic(fem, ...
'complexfun','on',...
'solcomp',{'Hz','Ez'},...
'outcomp',{'Hz','Ez'},...
'blocksize','auto',...
'pname','wave0',...
'plist',{'colon'(wavemin,((wavemax-wavemin)/(wavevals-1)),wavemax)},...
'oldcomp',{'});

% Plot solution
% Plot solution
for plotsol=1:wavevals
% Print energy dissipation
postplot(fem, ...
'tridata',{'(0.5*(2*pi*2.998e8)/wave0)*(-
1)*imag(epsilong_rfweh)*epsilon0_rfweh*(normE_rfweh)^2',...
'},... %Plot LOGe of the energy dissipation
'trimap','Rainbow',...
'solnum',plotsol, ...
'axis',[(-period/2),(period/2),-yactive,2.5*yactive]);
title({'Dissipated Energy [W/m^2]. Wavelength
(m)=',num2str(wavemin+(plotsol-1)*((wavemax-wavemin)/(wavevals-1)))});
print -djpeg -r150 outputpic

NewFileName=[Absorption-rate-period-',num2str(round(1e9*period)),'nm-
wavelength',num2str(round(1e9*(wavemin+(plotsol-1)*((wavemax-wavemin)/(wavevals-1))))),
'nm','.jpg']; %concatenate the filename
copyfile('outputpic.jpg',NewFileName)
movefile(NewFileName,NewDirectoryName);
delete outputpic.jpg
close
end

%POST-PROCESSING. Now we have the solution (value of E throughout
%domain) Perform calculations to extract useful quantities.
for kk=1:wavevals
wavelength0=wavemin+(kk-1)*((wavemax-wavemin)/(wavevals-1));
reflmat(kk,1)=wavemin+(kk-1)*((wavemax-wavemin)/(wavevals-1));
if isitflat=0 %structured!
% Integrate
refltot=postint(fem,'nPoav_rfweh',...
'unit','W/m',...
'recover','off',...
'dl',[29],...
'edim',1,...
'solnum',kk);
end
end

reflmat(kk,(jj+1))=reflmat(1,1); %
electrodeabsmat(kk,1)=wavemin+(kk-1)*((wavemax-wavemin)/(wavevals-1));
I3=postint(fem,'0.5*(2*pi*2.998e8)/wave0)*(-
1)*imag(epsilong_rfweh)*epsilon0_rfweh*(normE_rfweh)^2',... %expression for
absorption obtained from Ferry 2010
'unit','N',...
'recover','off',...
'dl',[1],...
'solnum',kk);
% I3=postint(fem,'Qav_rfweh',...
'unit','N',...
'recover','off',...
'dl',[1,4],...
'solnum',kk);
electrodeabsmat(kk,(jj+1))=I3(1,1);

if kk==(wavevals-1) && j==Nperiodsteps
end

nanostruonlyabsmat(kk,1)=wavemin+(kk-1)*((wavemax-wavemin)/(wavevals-
1));
I5=postint(fem,'0.5*(2*pi*2.998e8)/wave0)*(-
1)*imag(epsilong_rfweh)*epsilon0_rfweh*(normE_rfweh)^2',... %expression for
absorption obtained from Ferry 2010
'unit','N',...
'recover','off',...
'dl',[6],...
'solnum',kk);
% I3=postint(fem,'Qav_rfweh',...
'unit','N',...
'recover','off',...
'dl',[1,4],...
'solnum',kk);
nanostruonlyabsmat(kk,(jj+1))=I5(1,1);

activeabsmat(kk,1)=wavemin+(kk-1)*((wavemax-wavemin)/(wavevals-1));
I4=postint(fem,'0.5*(2*pi*2.998e8)/wave0)*(-
1)*imag(epsilong_rfweh)*epsilon0_rfweh*(normE_rfweh)^2',...
'unit','N',...
'recover','off',...
'dl',[2,3,4],... %for a polymer filled domain 2 (where the
spacer usually is)
'solnum',kk);
% I4=postint(fem,'Qav_rfweh',...
'unit','N',...
'recover','off',...
'dl',[2,3],...
'solnum',kk);
activeabsmat(kk,(jj+1))=I4(1,1);

%check about losses through the sides
leakabsmat(kk,1)=wavemin+(kk-1)*((wavemax-wavemin)/(wavevals-1));
out1=postint(fem,'nPoav_rfweh',... %flux through side 1
'unit','W/m',...
'recover','off',...
'dl',[1,3,5,7,9,26,28],...
'edim',1,...
'solnum',kk);
out14=postint(fem,'nPoav_rfweh',...

```

```

        reflmat(kk,jj+1)=reflmat(kk,jj+1)/(powerin);

        end %loop over wavelength

    end %loop over period

    inputparams=zeros(2,Nperiodsteps);
    inputparams(1,:)=periodvals(1,:);
    for kk=1:Nperiodsteps
        for inputparams(2,kk)=periodvals(1,kk); %outputs the absolute spacing of the
            features %inputparams(2,kk)=2*periodvals(1,kk);

            end
            %export files into directory for that NPwidth value.
            Directoryname=['testoutput\xnanowire-' num2str(round(1e9*xnanowirevals(jii)))
                '.m'];
            dlwrite('inputparams.txt',inputparams, 'delimiter', '\t', 'precision',
                3);
            mvmovefile('inputparams.txt',Directoryname);
            dlwrite('reflectance.txt',reflmat, 'delimiter', '\t', 'precision',
                7);
            mvmovefile('reflectance.txt',Directoryname);
            dlwrite('electroabsorption.txt',electrodesabmat, 'delimiter', '\t',
                'precision', 7);
            mvmovefile('electroabsorption.txt',Directoryname);
            dlwrite('nanostruonly.txt',nanostruonlyabamat, 'delimiter', '\t', 'precision',
                7);
            mvmovefile('nanostruonly.txt',Directoryname);
            dlwrite('activeabsorption.txt',activeabsmat, 'delimiter', '\t', 'precision',
                7);
            mvmovefile('activeabsorption.txt',Directoryname);
            % dlwrite('incidentflux.txt',incenergymat, 'delimiter', '\t', 'precision',
                7);
            mvmovefile('incidentflux.txt',testoutput);
            dlwrite('leaks.txt',leaksabamat, 'delimiter', '\t', 'precision',
                7);
            mvmovefile('leaks.txt',Directoryname);
            %saving the content of the mfile
            FileName = fullfile('m');
            copyfile(FileName,'complete-code-copy.txt');
            NewFileName=[FileName 'complete-code-copy.txt']; %concatenate the filename
            copyfile('complete-code-copy.txt', NewFileName)
            mvmovefile(NewFileName,Directoryname);

        end %loop over xnanowire
    end
end

```

```

        'unit','W/m', ...
        'recover','off', ...
        'dl',[17,18,19,20,21,31,32], ...
        'edim',1, ...
        'solnum',kk);
    leaksabamat(kk,(jj+1))=out1(1,1)-out14(1,1); %choose which side needs
    to be examined
    else %flat!!!
        refltot=postint(fem,'nPoav_rfweh', ... %Flux through the PM
            'unit','W/m', ...
            'recover','off', ...
            'dl',[20], ...
            'edim',1, ...
            'solnum',kk);
        reflmat(kk,(jj+1))=refltot(1,1); %
        electrodesabmat(kk,1)=wavemin+(kk-1)*((wavemax-wavemin)/(wavevals-1));
        I3=postint(fem,0.5*(2*pi*2.998e8)/wave0)*(-
            1)*imag(epsil0_rfweh)*epsil0_rfweh*(normE_rfweh)^2, ...
            'unit','N', ...
            'recover','off', ...
            'dl',[1], ...
            'solnum',kk);
        electrodesabmat(kk,(jj+1))=I3(1,1);

        activeabsmat(kk,1)=wavemin+(kk-1)*((wavemax-wavemin)/(wavevals-1));
        I4=postint(fem,0.5*(2*pi*2.998e8)/wave0)*(-
            1)*imag(epsil0n_rfweh)*epsil0n_rfweh*(normE_rfweh)^2, ...
            'unit','N', ...
            'recover','off', ...
            'dl',[2,3,4], ...
            'solnum',kk);
        activeabsmat(kk,(jj+1))=I4(1,1);

        %check about losses through the sides
        leaksabamat(kk,1)=wavemin+(kk-1)*((wavemax-wavemin)/(wavevals-1));
        out1=postint(fem,'nPoav_rfweh', ... %Flux through side 1
            'unit','W/m', ...
            'recover','off', ...
            'dl',[1,3,5,7,9,17,19], ...
            'edim',1, ...
            'solnum',kk);
        out14=postint(fem,'nPoav_rfweh', ...
            'unit','W/m', ...
            'recover','off', ...
            'dl',[12,13,14,15,16,22,23], ...
            'edim',1, ...
            'solnum',kk);
        leaksabamat(kk,(jj+1))=out1(1,1)-out14(1,1); %choose which side needs
        to be examined
    end %is it flat?

    %Normalise to incident power
    electrodesabmat(kk,jj+1)=electrodesabmat(kk,jj+1)/(powerin);
    nanostruonlyabamat(kk,jj+1)=nanostruonlyabamat(kk,jj+1)/(powerin);
    activeabsmat(kk,jj+1)=activeabsmat(kk,jj+1)/(powerin);
    leaksabamat(kk,jj+1)=leaksabamat(kk,jj+1)/(powerin);
end

```

Bibliography

- [1] D. Abbott. Keeping the energy debate clean: How do we supply the world's energy needs? *Proceedings of the Ieee*, 98(1):42–66, 2010. 537BQ Times Cited:13 Cited References Count:116.
- [2] Bundesministerium für Umwelt, Naturschutz und Reaktorsicherheit. Erneuerbare Energien in Zahlen, 2011.
- [3] *U.S. Energy Information Administration*. Electric power monthly, with data for june 2011., 2011.
- [4] R. Tidball, J. Bluestein, N. Rodriguez, and S. Knoke. Cost and performance assumptions for modeling electricity generation technologies, p 107. Technical report, NREL, 2010.
- [5] T. M. Razykov, C. S. Ferekides, D. Morel, E. Stefanakos, H. S. Ullal, and H. M. Upadhyaya. Solar photovoltaic electricity: Current status and future prospects. *Solar Energy*, 85(8):1580–1608, 2011.
- [6] G. Dennler, M. C. Scharber, and C. J. Brabec. Polymer-fullerene bulk-heterojunction solar cells. *Advanced Materials*, 21(13):1323–1338, 2009. 436RM Times Cited:566 Cited References Count:138.
- [7] J. H. Lee, S. Cho, A. Roy, H. T. Jung, and A. J. Heeger. Enhanced diode characteristics of organic solar cells using titanium suboxide electron transport layer. *Applied Physics Letters*, 96(16), 2010. 587UY Times Cited:9 Cited References Count:15.
- [8] J. D. Servaites, M. A. Ratner, and T. J. Marks. Organic solar cells: A new look at traditional models. *Energy & Environmental Science*, 4(11):4410–4422, 2011. 837YE Times Cited:0 Cited References Count:125.
- [9] Carsten Deibel and Vladimir Dyakonov. Polymer-fullerene bulk heterojunction solar cells. *Reports on Progress in Physics*, 73(9):096401, 2010.

- [10] Konarka. Konarka's power plastic achieves world record 8.3% efficiency certification from national energy renewable laboratory (nrel), www.konarka.com, accessed feb. 2012. Technical report.
- [11] National renewable energy laboratory (nrel), golden, co, 2011.
- [12] Loke-Yuen Wong, Rui-Qi Png, F. B. Shanjeera Silva, Lay-Lay Chua, D. V. Maheswar Repaka, Shi-Chen, Xing-Yu Gao, Lin Ke, Soo-Jin Chua, Andrew T. S. Wee, and Peter K. H. Ho. Interplay of processing, morphological order, and charge-carrier mobility in polythiophene thin films deposited by different methods: Comparison of spin-cast, drop-cast, and inkjet-printed films. *Langmuir*, 26(19):15494–15507, 2010.
- [13] H. R. Philipp and E. A. Taft. Optical constants of silicon in the region 1 to 10 ev. *Physical Review*, 120(1):37–38, 1960. PR.
- [14] Halls J. J. M. and R. H. Friend. *Clean Electricity from Photovoltaics*, volume 1, chapter Organic Photovoltaic Devices, page 377. Imperial College Press, London, 2001.
- [15] C. W. Tang. Two-layer organic photovoltaic cell. *Applied Physics Letters*, 48(2):183–185, 1986.
- [16] G. Yu, J. Gao, J. C. Hummelen, F. Wudl, and A. J. Heeger. Polymer photovoltaic cells: Enhanced efficiencies via a network of internal donor-acceptor heterojunctions. *Science*, 270(5243):1789–1791, 1995.
- [17] Steffan Cook, Han Liyuan, Akihiro Furube, and Ryuzi Katoh. Singlet annihilation in films of regioregular poly(3-hexylthiophene): Estimates for singlet diffusion lengths and the correlation between singlet annihilation rates and spectral relaxation. *The Journal of Physical Chemistry C*, 114(24):10962–10968, 2010.
- [18] Larry W. Barbour, Ryan D. Pensack, Maureen Hegadorn, Sergei Arzhantsev, and John B. Asbury. Excitation transport and charge separation in an organic photovoltaic material: Watching excitations diffuse to interfaces. *The Journal of Physical Chemistry C*, 112(10):3926–3934, 2008.
- [19] Charles L. Braun. Electric field assisted dissociation of charge transfer states as a mechanism of photocarrier production. *The Journal of Chemical Physics*, 80(9):4157–4161, 1984.
- [20] Carsten Deibel, Thomas Strobel, and Vladimir Dyakonov. Origin of the efficient polaron-pair dissociation in polymer-fullerene blends. *Physical Review Letters*, 103(3):036402, 2009. PRL.

-
- [21] John R. Tumbleston, Doo-Hyun Ko, Edward T. Samulski, and Rene Lopez. Analyzing local exciton generation profiles as a means to extract transport lengths in organic solar cells. *Physical Review B*, 82(20):205325, 2010. PRB.
- [22] S. H. Park, A. Roy, S. Beaupre, S. Cho, N. Coates, J. S. Moon, D. Moses, M. Leclerc, K. Lee, and A. J. Heeger. Bulk heterojunction solar cells with internal quantum efficiency approaching 100%. *Nature Photonics*, 3(5):297–U5, 2009. 447UY Times Cited:284 Cited References Count:41.
- [23] Yanming Sun, Gregory C. Welch, Wei Lin Leong, Christopher J. Takacs, Guillermo C. Bazan, and Alan J. Heeger. Solution-processed small-molecule solar cells with 6.7%. *Nature Materials*, 11(1):44–48, 2012. 10.1038/nmat3160.
- [24] A. Wagenpfahl, D. Rauh, M. Binder, C. Deibel, and V. Dyakonov. S-shaped current-voltage characteristics of organic solar devices. *Physical Review B*, 82(11), 2010. 647ZC Times Cited:16 Cited References Count:44.
- [25] Ricky B. Dunbar, Holger C. Hesse, Dominik S. Lembke, and Lukas Schmidt-Mende. Light-trapping plasmonic nanovoid arrays. *Physical Review B*, 85(3):035301, 2012. PRB.
- [26] Stefan Alexander Maier. *Plasmonics: Fundamentals and Applications*. Springer, 2007.
- [27] P. B. Johnson and R. W. Christy. Optical-constants of noble-metals. *Physical Review B*, 6(12):4370–4379, 1972. O3462 Times Cited:3855 Cited References Count:42.
- [28] J. A. Dionne, L. A. Sweatlock, H. A. Atwater, and A. Polman. Planar metal plasmon waveguides: frequency-dependent dispersion, propagation, localization, and loss beyond the free electron model. *Physical Review B*, 72(7), 2005. 960BF Times Cited:111 Cited References Count:34.
- [29] Kretschm.E and H. Raether. Radiative decay of non radiative surface plasmons excited by light. *Zeitschrift Fur Naturforschung Part a-Astrophysik Physik Und Physikalische Chemie*, A 23(12):2135, 1968. C4288 Times Cited:950 Cited References Count:12.
- [30] A. Bouhelier and G. P. Wiederrecht. Surface plasmon rainbow jets. *Opt. Lett.*, 30(8):884–886, 2005.
- [31] G. Leveque and O. J. F. Martin. Optimization of finite diffraction gratings for the excitation of surface plasmons. *Journal of Applied Physics*, 100(12), 2006. 121LA Times Cited:19 Cited References Count:24.

- [32] W. L. Barnes, T. W. Preist, S. C. Kitson, and J. R. Sambles. Physical origin of photonic energy gaps in the propagation of surface plasmons on gratings. *Physical Review B*, 54(9):6227–6244, 1996. Vg949 Times Cited:269 Cited References Count:43.
- [33] I. R. Hooper and J. R. Sambles. Dispersion of surface plasmon polaritons on short-pitch metal gratings. *Physical Review B*, 65(16), 2002. 547GQ Times Cited:28 Cited References Count:16.
- [34] H. A. Atwater and A. Polman. Plasmonics for improved photovoltaic devices. *Nature Materials*, 9(3):205–213, 2010. 557WN Times Cited:11 Cited References Count:92.
- [35] Huffman D.R. Bohren, C.F. *Absorption and Scattering of Light By Small Particles*. Wiley-Interscience, New York, 1983.
- [36] G. Mie. Beiträge zur optik trüber medien, speziell kolloidaler metallösungen. *Annalen Der Physik*, 3:377–445, 1908.
- [37] T. A. Kelf, Y. Sugawara, R. M. Cole, J. J. Baumberg, M. E. Abdelsalam, S. Cintra, S. Mahajan, A. E. Russell, and P. N. Bartlett. Localized and delocalized plasmons in metallic nanovoids. *Physical Review B*, 74(24):–, 2006. 121ZP Times Cited:54 Cited References Count:28.
- [38] F. Monestier, J. J. Simon, P. Torchio, L. Escoubas, F. Florya, S. Bailly, R. de Bettignies, S. Guillerez, and C. Defranoux. Modeling the short-circuit current density of polymer solar cells based on p3ht : Pcbm blend. *Solar Energy Materials and Solar Cells*, 91(5):405–410, 2007. 140PH Times Cited:30 Cited References Count:20.
- [39] W. Shockley and H. J. Queisser. Detailed balance limit of efficiency of p-n junction solar cells. *Journal of Applied Physics*, 32(3):510–519, 1961. 3759B Times Cited:942 Cited References Count:46.
- [40] E. Yablonovitch. Statistical ray optics. *Journal of the Optical Society of America*, 72(7):899–907, 1982. Nv728 Times Cited:176 Cited References Count:9.
- [41] Howard R. Stuart and Dennis G. Hall. Thermodynamic limit to light trapping in thin planar structures. *J. Opt. Soc. Am. A*, 14(11):3001–3008, 1997.
- [42] Dennis M. Callahan, Jeremy N. Munday, and Harry A. Atwater. Solar cell light trapping beyond the ray optic limit. *Nano Letters*, 12(1):214–218, 2011.
- [43] E. A. Schiff. Thermodynamic limit to photonic-plasmonic light-trapping in thin films on metals. *Journal of Applied Physics*, 110(10), 2011. 860JD Times Cited:0 Cited References Count:26.

- [44] Y. Sugawara, T. A. Kelf, J. J. Baumberg, M. E. Abdelsalam, and P. N. Bartlett. Strong coupling between localized plasmons and organic excitons in metal nanovoids. *Physical Review Letters*, 97(26), 2006. 121OQ Times Cited:52 Cited References Count:23.
- [45] Mahmoud A. Mahmoud, Adam J. Poncheri, Ronnie L. Phillips, and Mostafa A. El-Sayed. Plasmonic field enhancement of the exciton⁺exciton annihilation process in a poly(p-phenyleneethynylene) fluorescent polymer by ag nanocubes. *Journal of the American Chemical Society*, 132(8):2633–2641, 2010.
- [46] A. P. Kulkarni, K. M. Noone, K. Munechika, S. R. Guyer, and D. S. Ginger. Plasmon-enhanced charge carrier generation in organic photovoltaic films using silver nanoprisms. *Nano Letters*, 10(4):1501–1505, 2010. 581WU Times Cited:1 Cited References Count:41.
- [47] T. Tromholt, E. A. Katz, B. Hirsch, A. Vossier, and F. C. Krebs. Effects of concentrated sunlight on organic photovoltaics. *Applied Physics Letters*, 96(7):–, 2010. 558PX Times Cited:0 Cited References Count:18.
- [48] J. Weickert, R. B. Dunbar, H. C. Hesse, W. Wiedemann, and L. Schmidt-Mende. Nanostructured organic and hybrid solar cells. *Advanced Materials*, 23(16):1810–1828, 2011. 763HT Times Cited:0 Cited References Count:188.
- [49] S. Colodrero, A. Mihi, L. Haggman, M. Ocana, G. Boschloo, A. Hagfeldt, and H. Miguez. Porous one-dimensional photonic crystals improve the power-conversion efficiency of dye-sensitized solar cells. *Advanced Materials*, 21(7):764–+, 2009. 412PX Times Cited:21 Cited References Count:25.
- [50] M. Niggemann, M. Riede, A. Gombert, and K. Leo. Light trapping in organic solar cells. *Physica Status Solidi a-Applications and Materials Science*, 205(12):2862–2874, 2008. Sp. Iss. SI 392MP Times Cited:1 Cited References Count:52.
- [51] S. Dal Zilio, K. Tvingstedt, O. Inganas, and M. Tormen. Fabrication of a light trapping system for organic solar cells. *Microelectronic Engineering*, 86(4-6):1150–1154, 2009. 461NG Times Cited:1 Cited References Count:14.
- [52] P. Peumans, V. Bulovic, and S. R. Forrest. Efficient photon harvesting at high optical intensities in ultrathin organic double-heterostructure photovoltaic diodes. *Applied Physics Letters*, 76(19):2650–2652, 2000. 309QB Times Cited:310 Cited References Count:17.

- [53] J. Müller, B. Rech, J. Springer, and M. Vanecek. Tco and light trapping in silicon thin film solar cells. *Solar Energy*, 77(6):917–930, 2004. 883RY Times Cited:79 Cited References Count:71.
- [54] M. K. Nazeeruddin, A. Kay, I. Rodicio, R. Humphrybaker, E. Muller, P. Liska, N. Vlachopoulos, and M. Gratzel. Conversion of light to electricity by cis-x2bis(2,2'-bipyridyl-4,4'-dicarboxylate)ruthenium(ii) charge-transfer sensitizers (x = cl-, br-, i-, cn-, and scn-) on nanocrystalline tio2 electrodes. *Journal of the American Chemical Society*, 115(14):6382–6390, 1993. Lt173 Times Cited:2491 Cited References Count:45.
- [55] Z. S. Wang, H. Kawauchi, T. Kashima, and H. Arakawa. Significant influence of tio2 photoelectrode morphology on the energy conversion efficiency of n719 dye-sensitized solar cell. *Coordination Chemistry Reviews*, 248(13-14):1381–1389, 2004. 862ET Times Cited:195 Cited References Count:29.
- [56] J. H. Yoon, S. R. Jang, R. Vittal, J. Lee, and K. J. Kim. Tio2 nanorods as additive to tio2 film for improvement in the performance of dye-sensitized solar cells. *Journal of Photochemistry and Photobiology a-Chemistry*, 180(1-2):184–188, 2006. 041WI Times Cited:29 Cited References Count:25.
- [57] S. Pillai and M. A. Green. Plasmonics for photovoltaic applications. *Solar Energy Materials and Solar Cells*, 94(9):1481–1486, 2010. Sp. Iss. SI 635CN Times Cited:4 Cited References Count:41.
- [58] S. Pillai, K. R. Catchpole, T. Trupke, and M. A. Green. Surface plasmon enhanced silicon solar cells. *Journal of Applied Physics*, 101(9), 2007. 169BO Times Cited:256 Cited References Count:28.
- [59] K. Nakayama, K. Tanabe, and H. A. Atwater. Plasmonic nanoparticle enhanced light absorption in gaas solar cells. *Applied Physics Letters*, 93(12):–, 2008. 356SY Times Cited:34 Cited References Count:17.
- [60] D. Derkacs, S. H. Lim, P. Matheu, W. Mar, and E. T. Yu. Improved performance of amorphous silicon solar cells via scattering from surface plasmon polaritons in nearby metallic nanoparticles. *Applied Physics Letters*, 89(9):–, 2006. 080GT Times Cited:69 Cited References Count:14.
- [61] J. L. Wu, F. C. Chen, Y. S. Hsiao, F. C. Chien, P. L. Chen, C. H. Kuo, M. H. Huang, and C. S. Hsu. Surface plasmonic effects of metallic nanoparticles on the performance of polymer bulk heterojunction solar cells. *Acs Nano*, 5(2):959–967, 2011. 724CN Times Cited:0 Cited References Count:57.

- [62] A. J. Morfa, K. L. Rowlen, T. H. Reilly, M. J. Romero, and J. van de Lagemaat. Plasmon-enhanced solar energy conversion in organic bulk heterojunction photovoltaics. *Applied Physics Letters*, 92(1):–, 2008. 250FA Times Cited:29 Cited References Count:34.
- [63] S. S. Kim, S. I. Na, J. Jo, D. Y. Kim, and Y. C. Nah. Plasmon enhanced performance of organic solar cells using electrodeposited ag nanoparticles. *Applied Physics Letters*, 93(7):–, 2008. 345QC Times Cited:19 Cited References Count:25.
- [64] J. H. Lee, J. H. Park, J. S. Kim, D. Y. Lee, and K. Cho. High efficiency polymer solar cells with wet deposited plasmonic gold nanodots. *Organic Electronics*, 10(3):416–420, 2009. 444SM Times Cited:8 Cited References Count:27.
- [65] W. J. Yoon, K. Y. Jung, J. W. Liu, T. Duraisamy, R. Revur, F. L. Teixeira, S. Sengupta, and P. R. Berger. Plasmon-enhanced optical absorption and photocurrent in organic bulk heterojunction photovoltaic devices using self-assembled layer of silver nanoparticles. *Solar Energy Materials and Solar Cells*, 94(2):128–132, 2010. 552LH Times Cited:0 Cited References Count:39.
- [66] S. H. Lim, D. Derkacs, and E. T. Yu. Light scattering into silicon-on-insulator waveguide modes by random and periodic gold nanodot arrays. *Journal of Applied Physics*, 105(7):–, 2009. 453SX Times Cited:2 Cited References Count:21.
- [67] N. C. Lindquist, W. A. Luhman, S. H. Oh, and R. J. Holmes. Plasmonic nanocavity arrays for enhanced efficiency in organic photovoltaic cells. *Applied Physics Letters*, 93(12):–, 2008. 356SY Times Cited:7 Cited References Count:19.
- [68] R. A. Pala, J. White, E. Barnard, J. Liu, and M. L. Brongersma. Design of plasmonic thin-film solar cells with broadband absorption enhancements. *Advanced Materials*, 21(34):3504–+, 2009. 501KH Times Cited:13 Cited References Count:34.
- [69] N. C. Panoiu and R. M. Osgood. Enhanced optical absorption for photovoltaics via excitation of waveguide and plasmon-polariton modes. *Optics Letters*, 32(19):2825–2827, 2007. 225EM Times Cited:11 Cited References Count:15.
- [70] Y. G. Wei, C. Xu, S. Xu, C. Li, W. Z. Wu, and Z. L. Wang. Planar waveguide-nanowire integrated three-dimensional dye-sensitized solar cells. *Nano Letters*, 10(6):2092–2096, 2010. 606TB Times Cited:0 Cited References Count:21.
- [71] M. D. Brown, T. Suteewong, R. S. S. Kumar, V. D’Innocenzo, A. Petrozza, M. M. Lee, U. Wiesner, and H. J. Snaith. Plasmonic dye-sensitized solar cells using core-shell metal-insulator nanoparticles. *Nano Letters*, 11(2):438–445, 2011. 717LZ Times Cited:13 Cited References Count:38.

- [72] B. P. Rand, P. Peumans, and S. R. Forrest. Long-range absorption enhancement in organic tandem thin-film solar cells containing silver nanoclusters. *Journal of Applied Physics*, 96(12):7519–7526, 2004. 876FR Times Cited:113 Cited References Count:44.
- [73] D. H. Wang, D. Y. Kim, K. W. Choi, J. H. Seo, S. H. Im, J. H. Park, O. O. Park, and A. J. Heeger. Enhancement of donor-acceptor polymer bulk heterojunction solar cell power conversion efficiencies by addition of au nanoparticles. *Angewandte Chemie-International Edition*, 50(24):5519–5523, 2011. 782GR Times Cited:1 Cited References Count:37.
- [74] D.H. Wang, K.H. Park, J.H. Seo, J. Seiffter, J.H. Jeon, J.K. Kim, J.H. Park, O.O. Park, and A.J. Heeger. Enhanced power conversion efficiency in pcdtbt:pc70bm bulk heterojunction photovoltaic devices with embedded silver nanoparticle clusters. *Advanced Energy Materials*, 2011.
- [75] H. H. Shen, P. Bienstman, and B. Maes. Plasmonic absorption enhancement in organic solar cells with thin active layers. *Journal of Applied Physics*, 106(7):–, 2009. 508FT Times Cited:2 Cited References Count:28.
- [76] D. Duche, P. Torchio, L. Escoubas, F. Monestier, J. J. Simon, F. Flory, and G. Mathian. Improving light absorption in organic solar cells by plasmonic contribution. *Solar Energy Materials and Solar Cells*, 93(8):1377–1382, 2009. 465HQ Times Cited:6 Cited References Count:17.
- [77] V. Bastys, I. Pastoriza-Santos, B. Rodriguez-Gonzalez, R. Vaisnoras, and L. M. Liz-Marzan. Formation of silver nanoprisms with surface plasmons at communication wavelengths. *Advanced Functional Materials*, 16(6):766–773, 2006. 032YI Times Cited:60 Cited References Count:47.
- [78] Jun Yang, Jingbi You, Chun-Chao Chen, Wan-Ching Hsu, Hai-ren Tan, Xing Wang Zhang, Ziruo Hong, and Yang Yang. Plasmonic polymer tandem solar cell. *Acs Nano*, 5(8):6210–6217, 2011.
- [79] F. J. Haug, T. Soderstrom, O. Cubero, V. Terrazzoni-Daudrix, and C. Ballif. Plasmonic absorption in textured silver back reflectors of thin film solar cells. *Journal of Applied Physics*, 104(6):–, 2008. 361HS Times Cited:11 Cited References Count:48.
- [80] P. R. Evans, R. Kulloock, W. R. Hendren, R. Atkinson, R. J. Pollard, and L. M. Eng. Optical transmission properties and electric field distribution of interacting 2d silver nanorod arrays. *Advanced Functional Materials*, 18(7):1075–1079, 2008. 293RD Times Cited:7 Cited References Count:38.

- [81] R. H. Franken, R. L. Stolk, H. Li, C. H. M. van der Werf, J. K. Rath, and R. E. I. Schropp. Understanding light trapping by light scattering textured back electrodes in thin film n-i-p-type silicon solar cells. *Journal of Applied Physics*, 102(1):–, 2007. 189WC Times Cited:16 Cited References Count:26.
- [82] V. E. Ferry, L. A. Sweatlock, D. Pacifici, and H. A. Atwater. Plasmonic nanostructure design for efficient light coupling into solar cells. *Nano Letters*, 8(12):4391–4397, 2008. 382UK Times Cited:38 Cited References Count:34.
- [83] S. I. Na, S. S. Kim, J. Jo, S. H. Oh, J. Kim, and D. Y. Kim. Efficient polymer solar cells with surface relief gratings fabricated by simple soft lithography. *Advanced Functional Materials*, 18(24):3956–3963, 2008. 392GH Times Cited:9 Cited References Count:31.
- [84] K. Tvingstedt, N. K. Persson, O. Inganäs, A. Rahachou, and I. V. Zozoulenko. Surface plasmon increase absorption in polymer photovoltaic cells. *Applied Physics Letters*, 91(11):–, 2007. 210RT Times Cited:30 Cited References Count:21.
- [85] J. Zhu, C. M. Hsu, Z. F. Yu, S. H. Fan, and Y. Cui. Nanodome solar cells with efficient light management and self-cleaning. *Nano Letters*, 10(6):1979–1984, 2010. 606TB Times Cited:7 Cited References Count:30.
- [86] V. E. Ferry, M. A. Verschuuren, H. B. T. Li, E. Verhagen, R. J. Walters, R. E. I. Schropp, H. A. Atwater, and A. Polman. Light trapping in ultrathin plasmonic solar cells. *Optics Express*, 18(13):A237–A245, 2010. 613VG Times Cited:2 Cited References Count:35.
- [87] L. M. Chen, Z. R. Hong, G. Li, and Y. Yang. Recent progress in polymer solar cells: Manipulation of polymer: Fullerene morphology and the formation of efficient inverted polymer solar cells. *Advanced Materials*, 21(14-15):1434–1449, 2009. 442UO Times Cited:252 Cited References Count:144.
- [88] Neil D. Treat, Michael A. Brady, Gordon Smith, Michael F. Toney, Edward J. Kramer, Craig J. Hawker, and Michael L. Chabinyc. Interdiffusion of pcbm and p3ht reveals miscibility in a photovoltaically active blend. *Advanced Energy Materials*, 1(1):82–89, 2011.
- [89] H. Hoppe and N. S. Sariciftci. Organic solar cells: An overview. *Journal of Materials Research*, 19(7):1924–1945, 2004. 834NQ Times Cited:803 Cited References Count:220.
- [90] Chen Tao, Shengping Ruan, Guohua Xie, Xiangzi Kong, Liang Shen, Fanxu Meng, Caixia Liu, Xindong Zhang, Wei Dong, and Weiyu Chen. Role of tungsten oxide in inverted polymer solar cells. *Applied Physics Letters*, 94(4):043311, 2009.

- [91] V P Parkhutik and V I Shershulsky. Theoretical modelling of porous oxide growth on aluminium. *Journal of Physics D: Applied Physics*, 25(8):1258, 1992.
- [92] O. Jessensky, F. Muller, and U. Gosele. Self-organized formation of hexagonal pore arrays in anodic alumina. *Applied Physics Letters*, 72(10):1173–1175, 1998.
- [93] A. P. Li, F. Muller, A. Birner, K. Nielsch, and U. Gosele. Hexagonal pore arrays with a 50-420 nm interpore distance formed by self-organization in anodic alumina. *Journal of Applied Physics*, 84(11):6023–6026, 1998. 137RN Times Cited:668 Cited References Count:17.
- [94] A. R. Despic and V. P. Parkhutik. *Modern Aspects of Electrochemistry*, volume 20. Plenum, New York, 1989.
- [95] W. Lee, R. Ji, U. Gosele, and K. Nielsch. Fast fabrication of long-range ordered porous alumina membranes by hard anodization. *Nature Materials*, 5(9):741–747, 2006. 101HL Times Cited:253 Cited References Count:45.
- [96] T. Pfadler. *Plasmonics in nanostructured organic solar cells* (master’s thesis), Ludwig-Maximilians University, Munich, 2012.
- [97] Woo Lee, Roland Scholz, Kornelius Nielsch, and Ulrich Gösele. A template-based electrochemical method for the synthesis of multisegmented metallic nanotubes. *Angewandte Chemie International Edition*, 44(37):6050–6054, 2005.
- [98] D. C. Duffy, J. C. McDonald, O. J. A. Schueller, and G. M. Whitesides. Rapid prototyping of microfluidic systems in poly(dimethylsiloxane). *Analytical Chemistry*, 70(23):4974–4984, 1998. 143VW Times Cited:1766 Cited References Count:80.
- [99] J. Zhao, A. Swinnen, G. Van Assche, J. Manca, D. Vanderzande, and B. Van Mele. Phase diagram of p3ht/pcbm blends and its implication for the stability of morphology. *Journal of Physical Chemistry B*, 113(6):1587–1591, 2009. 404EU Times Cited:16 Cited References Count:39.
- [100] Bruker Corporation. <http://www.bruker-axs.com/tappingmode.html>, accessed: 02/02/2012.
- [101] Nanotools (R). <http://www.nanotools.com/afm-probes/ebd/high-aspect-ratio/mc60-for-veeco-dx/>, accessed: 02/02/2012.
- [102] National Renewable Energy Laboratory. <http://rredc.nrel.gov/solar/spectra/am1.5/>, accessed: 02/02/2012.

- [103] V. Shrotriya, G. Li, Y. Yao, T. Moriarty, K. Emery, and Y. Yang. Accurate measurement and characterization of organic solar cells. *Advanced Functional Materials*, 16(15):2016–2023, 2006.
- [104] R. M. Cole, J. J. Baumberg, F. J. Garcia de Abajo, S. Mahajan, M. Abdelsalam, and P. N. Bartlett. Understanding plasmons in nanoscale voids. *Nano Letters*, 7(7):2094–2100, 2007. 188NK Times Cited:42 Cited References Count:21.
- [105] T. Holmgaard and S. I. Bozhevolnyi. Theoretical analysis of dielectric-loaded surface plasmon-polariton waveguides. *Physical Review B*, 75(24), 2007. 184EX Times Cited:79 Cited References Count:32.
- [106] C. G. Khoury, S. J. Norton, and T. Vo-Dinh. Investigating the plasmonics of a dipole-excited silver nanoshell: Mie theory versus finite element method. *Nanotechnology*, 21(31), 2010. 626JC Times Cited:2 Cited References Count:41.
- [107] A. Wei, D. P. Lyvers, J. M. Moon, A. V. Kildishev, and V. M. Shalaev. Gold nanorod arrays as plasmonic cavity resonators. *Acs Nano*, 2(12):2569–2576, 2008. 388MJ Times Cited:13 Cited References Count:43.
- [108] *The Elliptic Equation. Mathworks, R2011b Documentation, Partial Differential Equation Toolbox.* <http://www.mathworks.de/help/toolbox/pde/ug/f8955.html>. Accessed 2012.02.15.
- [109] A. J. Moule and K. Meerholz. Minimizing optical losses in bulk heterojunction polymer solar cells. *Applied Physics B-Lasers and Optics*, 86(4):721–727, 2007. 142TY Times Cited:23 Cited References Count:25.
- [110] J.J. Baumberg. “plasmon-enhanced photo voltaic cell”, 2006.
- [111] T. V. Teperik, V. V. Popov, F. J. G. de Abajo, M. Abdelsalam, P. N. Bartlett, T. A. Kelf, Y. Sugawara, and J. J. Baumberg. Strong coupling of light to flat metals via a buried nanovoid lattice: the interplay of localized and free plasmons. *Optics Express*, 14(5):1965–1972, 2006. 020LF Times Cited:22 Cited References Count:23.
- [112] N. N. Lal, B. F. Soares, J. K. Sinha, F. Huang, S. Mahajan, P. N. Bartlett, N. C. Greenham, and J. J. Baumberg. Enhancing solar cells with localized plasmons in nanovoids. *Optics Express*, 19(12):11256–11263, 2011. 794AI Times Cited:0 Cited References Count:30.

Bibliography

- [113] S. Y. Chou, P. R. Krauss, and P. J. Renstrom. Imprint of sub-25 nm vias and trenches in polymers. *Applied Physics Letters*, 67(21):3114–3116, 1995. Tf574 Times Cited:1176 Cited References Count:6.
- [114] S. Y. Chou, P. R. Krauss, and P. J. Renstrom. Imprint lithography with 25-nanometer resolution. *Science*, 272(5258):85–87, 1996. Ud597 Times Cited:1110 Cited References Count:10.
- [115] R. M. Cole, Y. Sugawara, J. J. Baumberg, S. Mahajan, M. Abdelsalam, and P. N. Bartlett. Easily coupled whispering gallery plasmons in dielectric nanospheres embedded in gold films. *Physical Review Letters*, 97(13), 2006. 089HZ Times Cited:25 Cited References Count:15.
- [116] P. Boland, K. Lee, and G. Namkoong. Device optimization in pcpdtt:pcbm plastic solar cells. *Solar Energy Materials and Solar Cells*, 94(5):915–920, 2010. 592CX Times Cited:4 Cited References Count:38.
- [117] G. Dennler, K. Forberich, T. Ameri, C. Waldauf, P. Denk, C. J. Brabec, K. Hingerl, and A. J. Heeger. Design of efficient organic tandem cells: On the interplay between molecular absorption and layer sequence. *Journal of Applied Physics*, 102(12), 2007. 246DL Times Cited:24 Cited References Count:25.
- [118] Ricky B. Dunbar, Thomas Pfadler, and Lukas Schmidt-Mende. Highly absorbing solar cells - a survey of plasmonic nanostructures. *Opt. Express*, 20(S2):A177–A189, 2012.
- [119] W. Wiedemann, L. Sims, A. Abdellah, A. Exner, R. Meier, K. P. Musselman, J. L. MacManus-Driscoll, P. Muller-Buschbaum, G. Scarpa, P. Lugli, and L. Schmidt-Mende. Nanostructured interfaces in polymer solar cells. *Applied Physics Letters*, 96(26):–, 2010. 620QM Times Cited:0 Cited References Count:20.
- [120] H. C. Hesse, D. Lembke, L. Dossel, X. Feng, K. Mullen, and L. Schmidt-Mende. Nanostructuring discotic molecules on ito support. *Nanotechnology*, 22(5):–, 2011. 698GI Times Cited:0 Cited References Count:33.
- [121] M. Aryal, F. Buyukserin, K. Mielczarek, X. M. Zhao, J. M. Gao, A. Zakhidov, and W. C. Hu. Imprinted large-scale high density polymer nanopillars for organic solar cells. *Journal of Vacuum Science & Technology B*, 26(6):2562–2566, 2008. 379GV Times Cited:23 Cited References Count:23.
- [122] X. M. He, F. Gao, G. L. Tu, D. Hasko, S. Huttner, U. Steiner, N. C. Greenham, R. H. Friend, and W. T. S. Huck. Formation of nanopatterned polymer blends in photovoltaic

- devices. *Nano Letters*, 10(4):1302–1307, 2010. 581WU Times Cited:8 Cited References Count:30.
- [123] A. Liebsch. Surface-plasmon dispersion of ag. *Physical Review Letters*, 71(1):145–148, 1993. Lk368 Times Cited:99 Cited References Count:26.
- [124] M. Rocca. Low-energy eels investigation of surface electronic excitations on metals. *Surface Science Reports*, 22(1-2):p45, 1995. Rd390 Times Cited:104 Cited References Count:197.
- [125] H. Hoppe, N. S. Sariciftci, and D. Meissner. Optical constants of conjugated polymer/fullerene based bulk-heterojunction organic solar cells. *Molecular Crystals and Liquid Crystals*, 385:233–239, 2002. 624FZ Times Cited:12 Cited References Count:11.
- [126] J. P. Berenger. A perfectly matched layer for the absorption of electromagnetic-waves. *Journal of Computational Physics*, 114(2):185–200, 1994. Pj462 Times Cited:3307 Cited References Count:11.
- [127] N. M. B. Perney, J. J. Baumberg, M. E. Zoorob, M. D. B. Charlton, S. Mahnkopf, and C. M. Netti. Tuning localized plasmons in nanostructured substrates for surface-enhanced raman scattering. *Optics Express*, 14(2):847–857, 2006. 008AG Times Cited:75 Cited References Count:15.
- [128] J. Braun, B. Gompf, G. Kobiela, and M. Dressel. How holes can obscure the view: Suppressed transmission through an ultrathin metal film by a subwavelength hole array. *Physical Review Letters*, 103(20):–, 2009. 520RT Times Cited:14 Cited References Count:25.
- [129] J. F. Zhu, M. Xue, H. J. Shen, Z. Wu, S. Kim, J. J. Ho, A. Hassani-Afshar, B. Q. Zeng, and K. L. Wang. Plasmonic effects for light concentration in organic photovoltaic thin films induced by hexagonal periodic metallic nanospheres. *Applied Physics Letters*, 98(15), 2011. 750XF Times Cited:0 Cited References Count:19.
- [130] M. Handloser, R.B. Dunbar, A. Wisnet, P. Altpeter, C. Scheu, L. Schmidt-Mende, and A. Hartschuh. Influence of metallic and dielectric nanowire arrays on the photoluminescence properties of p3ht thin films. *Nanotechnology (submitted)*, 2012.
- [131] Alexandre Bouhelier, Michael R. Beversluis, and Lukas Novotny. Characterization of nanoplasmonic structures by locally excited photoluminescence. *Applied Physics Letters*, 83(24):5041–5043, 2003.

- [132] Stefan Trotzky, Theo Hoyer, Wilfried Tuszynski, Christoph Lienau, and Jürgen Parisi. Femtosecond up-conversion technique for probing the charge transfer in a p3ht : Pcbm blend via photoluminescence quenching. *Journal of Physics D: Applied Physics*, 42(5):055105, 2009.
- [133] H. Becker, S. E. Burns, and R. H. Friend. Effect of metal films on the photoluminescence and electroluminescence of conjugated polymers. *Physical Review B*, 56(4):1893–1905, 1997. PRB.
- [134] Joelle A. Labastide, Mina Baghgar, Irene Dujovne, B. Harihara Venkatraman, David C. Ramsdell, Dhandapani Venkataraman, and Michael D. Barnes. Time- and polarization-resolved photoluminescence of individual semicrystalline polythiophene (p3ht) nanoparticles. *The Journal of Physical Chemistry Letters*, 2(17):2089–2093, 2011.
- [135] M. Aryal, K. Trivedi, and W. C. Hu. Nano-confinement induced chain alignment in ordered p3ht nanostructures defined by nanoimprint lithography. *Acs Nano*, 3(10):3085–3090, 2009. 510QR Times Cited:29 Cited References Count:34.
- [136] M. Knez, K. Nielsch, and L. Niinistö. Synthesis and surface engineering of complex nanostructures by atomic layer deposition. *Advanced Materials*, 19(21):3425–3438, 2007.
- [137] C. C. D. Wang, W. C. H. Choy, C. H. Duan, D. D. S. Fung, W. E. I. Sha, F. X. Xie, F. Huang, and Y. Cao. Optical and electrical effects of gold nanoparticles in the active layer of polymer solar cells. *Journal of Materials Chemistry*, 22(3):1206–1211, 2012. 877WF Times Cited:0 Cited References Count:40.
- [138] D. D. S. Fung, L. F. Qiao, W. C. H. Choy, C. D. Wang, W. E. I. Sha, F. X. Xie, and S. L. He. Optical and electrical properties of efficiency enhanced polymer solar cells with au nanoparticles in a pedot-pss layer. *Journal of Materials Chemistry*, 21(41):16349–16356, 2011. 831LW Times Cited:2 Cited References Count:44.
- [139] H. J. Snaith, N. C. Greenham, and R. H. Friend. The origin of collected charge and open-circuit voltage in blended polyfluorene photovoltaic devices. *Advanced Materials*, 16(18):1640–+, 2004. 867BC Times Cited:64 Cited References Count:22.
- [140] K. Kim and D. L. Carroll. Roles of au and ag nanoparticles in efficiency enhancement of poly(3-octylthiophene)/c-60 bulk heterojunction photovoltaic devices. *Applied Physics Letters*, 87(20), 2005. 983PC Times Cited:23 Cited References Count:26.

- [141] J. Y. Lee and P. Peumans. The origin of enhanced optical absorption in solar cells with metal nanoparticles embedded in the active layer. *Optics Express*, 18(10):10078–10087, 2010. 594TD Times Cited:3 Cited References Count:15.
- [142] C. H. Kim, S. H. Cha, S. C. Kim, M. Song, J. Lee, W. S. Shin, S. J. Moon, J. H. Bahng, N. A. Kotov, and S. H. Jin. Silver nanowire embedded in p3ht: Pcbm for high-efficiency hybrid photovoltaic device applications. *Acs Nano*, 5(4):3319–3325, 2011. 753CJ Times Cited:0 Cited References Count:41.
- [143] T. W. Ebbesen, H. J. Lezec, H. F. Ghaemi, T. Thio, and P. A. Wolff. Extraordinary optical transmission through sub-wavelength hole arrays. *Nature*, 391(6668):667–669, 1998. Yw872 Times Cited:2560 Cited References Count:17.
- [144] R. Wannemacher. Plasmon-supported transmission of light through nanometric holes in metallic thin films. *Optics Communications*, 195(1-4):107–118, 2001. 457JT Times Cited:79 Cited References Count:27.
- [145] C. Cocoyer, L. Rocha, L. Sicot, B. Geffroy, R. de Bettignies, C. Sentein, C. Fiorini-Debuisschert, and P. Raimond. Implementation of submicrometric periodic surface structures toward improvement of organic-solar-cell performances. *Applied Physics Letters*, 88(13), 2006. 028CW Times Cited:21 Cited References Count:15.
- [146] C. J. Min, J. Li, G. Veronis, J. Y. Lee, S. H. Fan, and P. Peumans. Enhancement of optical absorption in thin-film organic solar cells through the excitation of plasmonic modes in metallic gratings. *Applied Physics Letters*, 96(13):–, 2010. 578EC Times Cited:10 Cited References Count:17.
- [147] N. Papanikolaou. Optical properties of metallic nanoparticle arrays on a thin metallic film. *Physical Review B*, 75(23), 2007. 184EW Times Cited:22 Cited References Count:44.
- [148] M. A. Sefunc, A. K. Okyay, and H. V. Demir. Plasmonic backcontact grating for p3ht:pcbm organic solar cells enabling strong optical absorption increased in all polarizations. *Optics Express*, 19(15):14200–14209, 2011. 794EF Times Cited:0 Cited References Count:29.
- [149] *Comsol Multiphysics Users Manual*. v.3.5.
- [150] W. Wang, S. M. Wu, K. Reinhardt, Y. L. Lu, and S. C. Chen. Broadband light absorption enhancement in thin-film silicon solar cells. *Nano Letters*, 10(6):2012–2018, 2010. 606TB Times Cited:16 Cited References Count:23.

Bibliography

- [151] J. Frischeisen, Q. A. Niu, A. Abdellah, J. B. Kinzel, R. Gehlhaar, G. Scarpa, C. Adachi, P. Lugli, and W. Brutting. Light extraction from surface plasmons and waveguide modes in an organic light-emitting layer by nanoimprinted gratings. *Optics Express*, 19(1):A7–A19, 2011. 702SJ Times Cited:0 Cited References Count:28.
- [152] *Stamps for Nanoprint Lithography & Microcontact Printing*. Sigma Aldrich. *Materials science products*. <http://www.sigmaaldrich.com/materials-science/material-science-products.html?TablePage=9539079> Accessed 2012.02.17.
- [153] V. D. Mihailetschi, L. J. A. Koster, J. C. Hummelen, and P. W. M. Blom. Photocurrent generation in polymer-fullerene bulk heterojunctions. *Physical Review Letters*, 93(21), 2004. 872PU Times Cited:232 Cited References Count:20.
- [154] V. Shrotriya, Y. Yao, G. Li, and Y. Yang. Effect of self-organization in polymer/fullerene bulk heterojunctions on solar cell performance. *Applied Physics Letters*, 89(6), 2006. 072RN Times Cited:74 Cited References Count:22.

Acknowledgements

First and foremost, I would like to thank Lukas Schmidt-Mende for supervising me. I am especially grateful that he gave me the freedom to design and carry out my own project. Although it was challenging at times, it made it all the more rewarding at the end. I am equally grateful that, despite being busy, he always made time for meetings to discuss the project status and new experiments.

I would like to thank Prof. Jochen Feldmann, Prof. Jörg Kotthaus and Prof. Thomas Bein for kindly granting me, along with other members of my group, access to equipment and instruments in their labs. Without this, much of the work in this thesis would not have been possible. I thoroughly enjoyed my collaborations and research visits with Dr. Udo Bach's group at the University of Monash, Melbourne, and with Prof. Jeremy Baumberg's group at the University of Cambridge. Special thanks go to the International Doctorate Program for NanoBioTechnology and the Centre of NanoScience for funding me.

I was lucky enough to have two great students during my Ph.D. Thank you Dominik. Thank you Thomas. It was a pleasure working with both of you. To all of the members of the group: Holger, Wolfgang, Sun, Lothar, Jonas, Claudia, Dominik, Thomas, Jinhu, Fenggu, Michael, Jacek, Severin, Sandra and Sarah: it has been a pleasure to work with you over these past years.

And a special thanks goes to Lukas, Dr. Ben Whelan, Jonas and Thomas, all who have read large sections of this thesis and provided valuable feedback.

Erklärung

Ich erkläre hiermit, dass ich meine Doktorarbeit mit dem Titel

**"Using metallic nanostructures to trap
light and enhance absorption in
organic solar cells"**

selbständig verfasst, sowie keine anderen als die angegebenen Quellen und
Hilfsmittel benutzt habe.

München, den April 4, 2012

(Ricky Dunbar)